Regulation of inhibitory synaptic connections and distal neuronal complexity by the Ste20-like kinase Slk

Dissertation

zur

Erlangung des Doktorgrades (Dr. rer. nat.)

der

Mathematisch-Naturwissenschaftlichen Fakultät

der

Rheinischen Friedrich-Wilhelms-Universität Bonn

vorgelegt von

Anne Quatraccioni

aus

Erlenbach a.Main

Bonn 2022

Angefertigt mit Genehmigung der Mathematisch-Naturwissenschaftlichen Fakultät
der Rheinischen Friedrich-Wilhelms-Universität Bonn

1. Gutachterin: Prof. Dr. Susanne Schoch McGovern
2. Gutachter: Prof. Dr. Walter Witke

Tag der Promotion: 18.11.2022
Erscheinungsjahr: 2022

Index

1 Summary 1

2 Introduction 2

2.1 Phosphorylation as a dynamic modification 2

2.2 Phosphorylation in neurons 3

2.2.1 Phosphorylation of the cytoskeleton and cytoskeletal-associated proteins 3

2.2.2 Regulation of synaptic function by phosphorylation 5

2.2.3 Phosphorylation in neurodegenerative and cognitive disorders 7

2.2.4. Phosphorylation in malformations of cortical development 8

2.2.5 Phosphorylation in epilepsy 9

2.2.6 Kinase inhibitors 9

2.3 Protein-protein interactions 10

2.4. Ste20-like serine/threonine-protein kinase 11

2.4.1 Slk in non-neuronal cells 12

2.4.2 Slk in neurons 16

2.4.3 Known protein-protein interactions of Slk 19

2.5 Aims of the project 22

3 Methods 24

3.1 Molecular biology 24

3.1.1 Polymerase chain reaction 24

3.1.2 Transformation of bacteria 25

3.1.3 DNA isolation 25

3.1.4 Test digest and sequencing 25

3.1.5 Protein purification from bacteria 25

3.2 Cell culture 26

3.2.1 HEK293T cell cultivation and transfection 26

3.2.2 rAAV preparation 27

3.2.3 Lentivirus preparation 27

3.2.4 Preparation of cultured cortical neurons 28

3.3 Biochemical methods 28
3.3.1 Immunocytochemistry 28
3.3.2 CoIP with cell-expressed proteins 28
3.3.3 CoIP with whole-brain lysate 29
3.3.4 Coomassie for mass spectrometry 30
3.3.5 Coomassie and Western Blot 30
3.3.6 *In vitro* kinase reactions 30
3.4 Mass spectrometric experiments 31
3.4.1 Phosphoproteomics 31
3.4.2 Mass spectrometric identification of biotinylated proteins in neurons 33
3.4.3 Mass spectrometric analysis of co-immunoprecipitated proteins 34
3.4.4 Mass spectrometric analysis of protein phosphorylation after *in vitro* kinase reactions 35
3.5. Animal experiments 36
3.5.1 *In utero* electroporation 36
3.5.2 Viral injections 37
3.5.3 Telemetric EEG and video monitoring 37
3.5.4 Multi-well MEA recordings 38
3.5.5 scRNAseq 38
3.6 Analysis 39
3.6.1 Dendrite tracing with Imaris 39
3.6.2 Quantification of fluorescence intensity in synapses and dendrites 39
3.6.3 MEA analysis 40
3.6.4 scRNAseq analysis 40
3.6.5 Bioinformatic analysis of phosphoproteomics data 41
3.6.6 KinSwing analysis 41
3.6.7 Bioinformatic analysis of BioID data 42
3.6.8 Bioinformatic analysis of CoIP data 42
3.6.9 Annotation analysis 42
3.6.10 Statistical analysis 43

4 Results 44
4.1 Further characterization of Slk knockdown model 44
4.1.1 No effect of Slk knockdown during adulthood on dendrite morphology 44
4.1.2 No spontaneous seizure activity after focal Slk knockdown 45
4.1.3 Reduced adaptation of neuronal firing behavior after Slk knockdown 46
4.1.4 Influence of Slk knockdown on surrounding cells 53
4.2 Mechanism of Slk effects 61
4.2.1 No change in abundance of known Slk interactors at inhibitory synapses 61
4.2.2 Reduced F-actin in dendrites after Slk knockdown 65
4.3 Identification of interaction partners of Slk by proteomics studies 67
4.3.1 Identifying changes in phosphorylation after Slk knockdown 67
4.3.2 Identifying proteins proximal to Slk in neurons (BioID) 75
4.3.3 Identifying binding partners of Slk (CoIP) 78
4.3.4 Proteins identified in multiple proteomics studies 81
4.4 Verification of interaction partners from proteomics studies 86
4.4.1 Grlf1 phosphorylation 86
4.4.2 Verification of binding partners of Slk (CoIP) 88
4.4.3 Verification of phosphorylation substrates of Slk by *in vitro* kinase reactions 90
5 Discussion 97
5.1 Preferential importance of Slk during neuronal development 97
5.2 Influence of Slk knockdown on cellular networks 97
5.2.1 No epileptic activity after Slk knockdown 97
5.2.2 Altered gene expression in neighboring neurons and microglia 99
5.3 Protein-protein interactions related to inhibitory synapse function 101
5.3.1 Known Slk interactors at inhibitory synapses 101
5.3.2 Possible mechanisms of Slk action at inhibitory synapses based on the results of the proteomics experiments 103
5.3.3 Potential upstream pathways involved in inhibitory synapse development 105
5.4 Potential mechanisms for Slk-dependent regulation of dendrite branching 107
5.5. Slk as a fine-tuner of neuronal morphology 110

5.6 Slk in the context of diseases 111
5.7 Outlook 116
6 Appendix 117
6.1 Contributions 117
6.2 Abbreviations 117
6.2.1 General abbreviations 117
6.2.2 Gene abbreviations 120
6.3 Material 127
6.3.1 Equipment 127
6.3.2 Software / databases 129
6.3.3 Reagents / chemicals / enzymes 130
6.3.4 Cell culture media / reagents 132
6.3.5 Consumables 132
6.3.6 Kits 133
6.3.7 Primary antibodies 134
6.3.8 Secondary antibodies 134
6.3.9 Cloning primers 135
6.3.10 Sequencing primers 140
6.3.11 Plasmids 140
6.3.12 Cells and animals 143
6.4 List of figures 144
6.5 List of tables 146
7 References 147
8 Acknowledgements 162

1 Summary

Neurons in the brain are typically defined by a characteristic morphology of the dendritic tree. Thereby, they can contact neighboring cells and communicate via excitatory and inhibitory synapses. To allow the establishment of neuronal circuits that ensure normal functions of the brain, the processes of dendrite and synapse development need to be tightly controlled. This is done via a plethora of interacting proteins within and between the developing cells. A protein that has been shown to critically influence neuronal development is the Ste20-like serine/threonine-protein kinase (Slk). Loss of Slk resulted in a simplified dendritic tree and reduced stability of specifically inhibitory synapses, which manifested in a decreased density of inhibitory synapses during postnatal development. The imbalance of excitatory and inhibitory synapses was also reflected on a functional level and impaired the electrophysiological excitation/inhibition balance.

In this study, the role and mechanism of Slk in neurons were further characterized. Slk seemed to be specifically important during development for establishing the dendritic tree while not contributing to maintaining the dendritic tree structure during adulthood.

Although a loss of Slk disturbed the excitation/inhibition balance of an individual neuron, a focal knockdown of Slk in selected neurons of cortical layers II/III did not lead to epileptic seizures or seizure-like activity. However, Slk knockdown did decrease the ability of neurons to adapt their firing behavior to external stimuli such as changed ion concentrations.

Mechanistically, Slk knockdown reduced filamentous actin in the dendrites of neurons across the whole dendritic tree. To understand how Slk influences the actin cytoskeleton, we conducted proteomics studies to identify protein interaction partners of Slk. In these studies, proteins that play a role at postsynaptic sites or are involved in cytoskeletal dynamics were detected with above-average frequency. Novel proteins that were identified to bind to Slk included Crmp1 and Prkcg, which are both involved in cytoskeletal remodeling, the synaptic vesicle protein Sv2a, and the transmembrane protein Tmeff1. Furthermore, we identified new substrates of Slk, which are the closely related kinases Mink1 and Tnik. Both kinases are known to influence dendritic outgrowth and cytoskeletal dynamics. By identifying new interaction partners of Slk in neurons, pathways underlying Slk function in neurons can be proposed. Having obtained the first data set of potential Slk downstream effectors in neurons, this provides the basis to resolve the mechanism of how Slk regulates dendritic growth and inhibitory synapse stabilization in the brain.

2 Introduction

2.1 Phosphorylation as a dynamic modification

Thirty years ago, in 1992, Edmond Fischer and Edwin Krebs were awarded the Nobel Prize in Physiology or Medicine for the characterization of a new class of proteins that were termed protein kinases (Raju, 2000). Kinases are enzymes that modify specific proteins, so-called substrates, by attaching a phosphate group (PO_4^{3-}) in a process termed phosphorylation. This posttranslational modification can alter the activity, function, conformation, or localization of the respective protein (Humphrey et al., 2015) (Fig. 1).

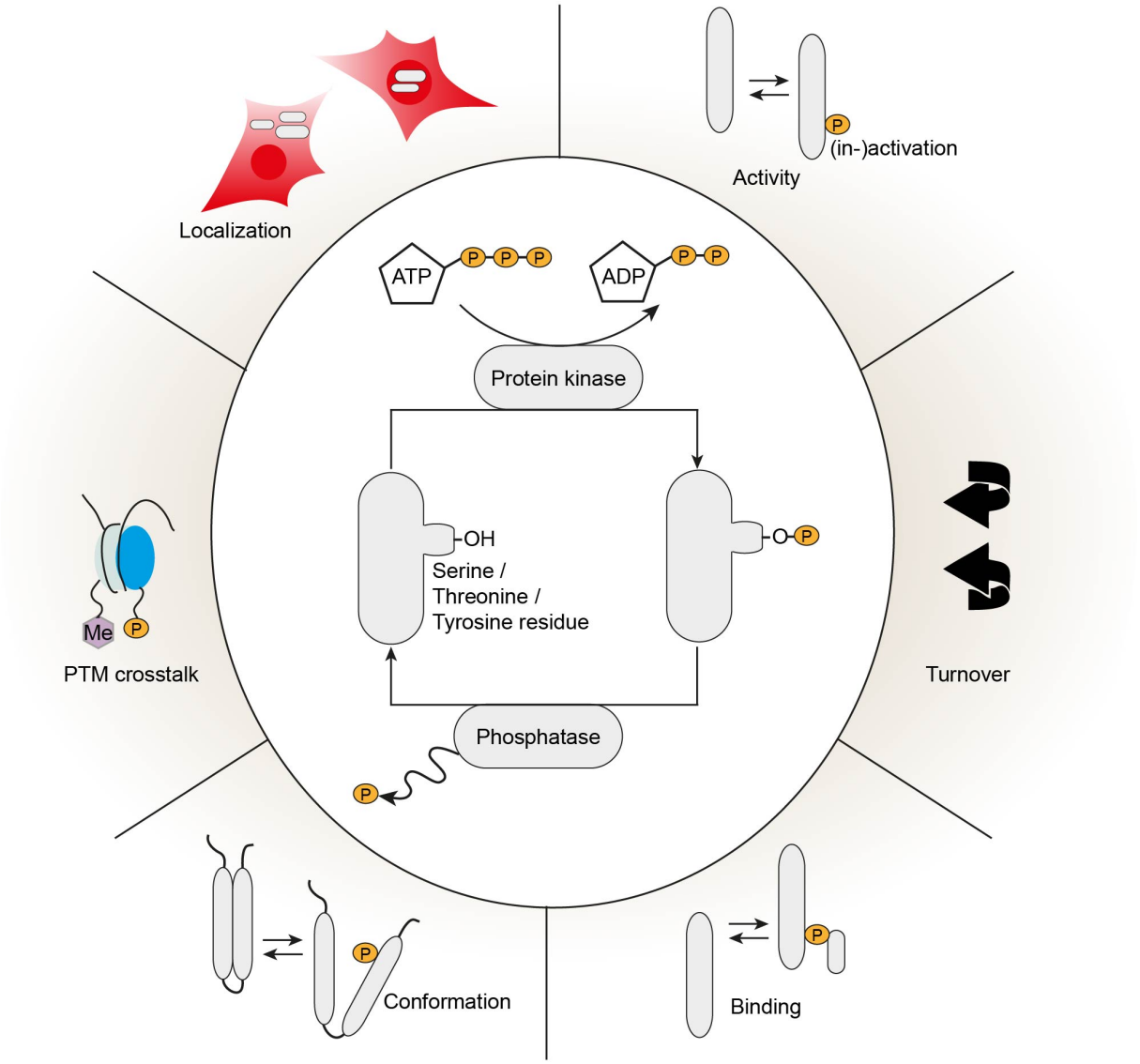


Fig. 1: Phosphorylation as a reversible process.
Kinases attach a phosphate group to a protein while phosphatases mediate the reverse reaction and remove the phosphate residue from proteins. These (de-)phosphorylation cycles allow flexible control of protein activity and protein turnover. In addition, phosphorylation can alter the binding of proteins, their conformation, interaction with other posttranslational modifications (PTM), or their localization within the cell. Modified from (Humphrey et al., 2015).

Around 500 human genes encode protein kinases and more than two-thirds of all known human proteins are a target of phosphorylation as posttranslational modification. This fact already indicates the importance of protein phosphorylation for most cellular processes including signaling mechanisms, protein synthesis, cell growth and division (Ardito et al., 2017).

Protein kinases are divided into different classes according to the amino acid residue that they modify. The three main classes include serine/threonine kinases, tyrosine kinases, and dual-specificity kinases that can phosphorylate proteins on serine (S), threonine (T), and tyrosine (Y) residues. Phosphorylation is a reversible process as antagonists of protein kinases, protein phosphatases, remove attached phosphates from proteins. This allows phosphorylation to be a very dynamic process that can be relatively fast in comparison to other cellular signaling mechanisms (Day et al 2016).

Precise and dynamic regulation of signaling is especially important for the brain, as it is a complex organ comprising up to 100 billion neurons and approximately the same number of glial cells and fulfilling essential functions ranging from motor and sensory function to cognitive performances such as memory and learning (Herculano-Houzel, 2012; von Bartheld et al., 2016). As these processes require finely tuned, rapid signal transduction within individual cells and between interacting cells, it is not surprising that phosphorylation by protein kinases plays a tremendous role in numerous brain functions.

2.2 Phosphorylation in neurons

2.2.1 Phosphorylation of the cytoskeleton and cytoskeletal-associated proteins

Already during neurodevelopmental stages, phosphorylation plays a crucial role in the formation of neurons starting from cell proliferation to differentiation, the outgrowth of the dendritic tree, the elongation of the axon, and the subsequent formation of synapses. These processes are controlled and regulated to a great extent by the cytoskeleton, which consists of microtubules, actin filaments (microfilaments), and intermediate filaments. Microtubules are the thickest cytoskeletal filaments with a diameter of 25 nm and are composed of α- and β-Tubulin heterodimers that assemble into so-called protofilaments, which combine to form the microtubule (Leterrier, 2021) (Fig. 2). Consisting of a plus (+) and a minus (-) end and thereby being a polar structure, microtubules are highly dynamic. They extend by polymerization via the addition of Tubulin-heterodimers or they shrink by depolymerization preferably at the minus end. This dynamic instability is strongly regulated by phosphorylation (Mitchison and Kirschner, 1984). Both α- and β-Tubulin are targets of phosphorylation and a phosphorylated state mainly inhibits microtubule assembly (Lasser et al., 2018). In addition, proteins regulating the microtubule cytoskeleton are a target of extensive phosphorylation. Microtubule plus-end

tracking proteins (+TIPs) include proteins such as end-binding proteins (e.g. Mapre3), which are upregulated during neurodevelopment and influence dendritic spine development, or Clasp proteins, that are important regulators of microtubule dynamics in the process of axon outgrowth (Jaworski et al., 2009). Phosphorylation of +TIPs can induce their dissociation from the plus end, or result in interactions with the actin cytoskeleton and focal adhesions (Bearce et al., 2015). Another class of microtubule regulating proteins are the Microtubule-associated proteins (Maps) that bind to microtubules and either stabilize the filaments by promoting polymerization or destabilize them by promoting depolymerization. The phosphorylation status of these proteins changes their association with the microtubules, their function, or their localization in the cell (Ramkumar et al., 2018). For instance, phosphorylated Map1b has been shown to specifically localize to growing axons where it modulates microtubule dynamics and interaction with the actin cytoskeleton (Yang et al., 2012). In contrast, phosphorylation of Map2 leads to the dissociation of the protein from microtubules and its association with the actin cytoskeleton. The ability of Map2 to crosslink the actin and microtubule cytoskeleton is especially important during the development of dendrites, showing that the regulation of the microtubule and actin cytoskeleton is highly interconnected (Ramkumar et al., 2018).

Actin filaments are the smallest cytoskeletal filaments with a diameter of 7 nm (Leterrier, 2021) (Fig. 2). They consist of actin monomers, the globular actin (G-actin), that can assemble into filamentous (F-actin) structures (Borovac et al., 2018). Similar to the microtubule cytoskeleton, phosphorylation can regulate the dynamics of F-actin assembly and disassembly. Direct phosphorylation of actin at tyrosine on position 53 (Y53) has been shown to increase the turnover rate of the actin filaments, thereby regulating dendritic spine formation (Bertling et al., 2016). Additionally, several actin binding proteins influence actin dynamics by inducing the nucleation and branching of new filaments such as the Arp2/3 complex or by increasing F-actin turnover through filament severing proteins such as the actin-depolymerizing factor (Gsn) or Cofilin-1 (Cfl1) (Konietzny et al., 2017; Tedeschi et al., 2019). The activity of Gsn/Cfl is regulated by serine phosphorylation at position 3 (S3) via the CamKII and Limk kinases while the non-phosphorylated protein is the active, actin-severing form (ben Zablah et al., 2020). In contrast, Arp2/3 needs to be phosphorylated to be able to induce nucleation of actin filaments (Leclaire et al., 2008).

The third group of cytoskeletal filaments are the intermediate filaments with a diameter of around 10 nm (Fig. 2). In neurons of the central nervous system (CNS), they are formed by neurofilament proteins, comprising Nefh (Neurofilament heavy polypeptide), Nefm (Neurofilament medium polypeptide), and Nefl (Neurofilament light polypeptide). Phosphorylation of Nefl by the cAMP-dependent protein kinase (Prka) was characterized *in vitro* and induced disassembly of neurofilaments. In contrast, phosphorylation in the tail domain of the neurofilament proteins has been discussed to influence their axonal transporting rate.

The phosphorylation status also determines the spacing of the neurofilaments. Additionally, phosphorylated neurofilament protein tails may be important for the interaction with microtubules, thereby providing a link between the different cytoskeletal components (Sihag et al., 2007; Zamoner & Pessoa-Pureur, 2017).

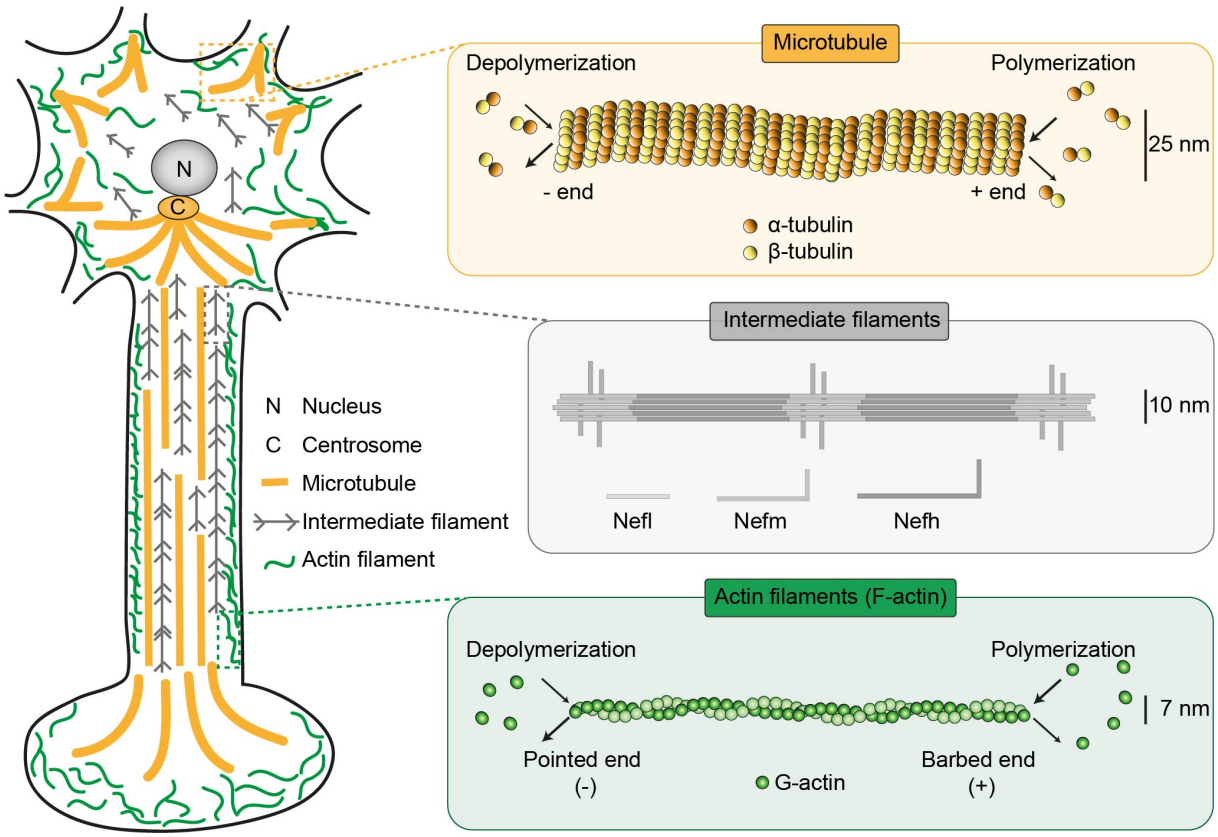


Fig. 2: Distribution of cytoskeletal elements within a neuron.
Microtubules, intermediate filaments, and actin filaments are composed of different subunits that assemble into longer filamentous structures. Modified from (Zamoner and Pessoa-Pureur, 2017; Malacrida et al., 2019).

2.2.2 Regulation of synaptic function by phosphorylation

Phosphorylation is not only essential during the development to establish the morphology of a neuron, but also crucially involved in neuronal function. Neuronal function relies on electric signals that travel along neurites and are transmitted to neighboring neurons at synapses. In the CNS, two types of synapses lead to either excitation or inhibition of the neighboring neuron. Excitation is mediated by the neurotransmitter glutamate while inhibition mainly relies on GABAergic (γ-aminobutyric acid-mediated) transmission in the brain. Synapses consist of a presynaptic part where neurotransmitter release occurs, a synaptic cleft, and the respective postsynaptic site of the contacted neighboring neuron, where the neurotransmitter binds and elicits signal transduction cascades. The postsynaptic protein composition differs between inhibitory and excitatory synapses. For excitatory synapses, the postsynaptic site is located on dendritic spines, which are small protrusions of the dendrite. In the membrane of excitatory

postsynapses, proteins such as the glutamatergic receptors (AMPA, NMDA, and metabotropic receptors), ion channels, and cell adhesion molecules are inserted. These are connected to scaffolding molecules such as Psd95, Shank, or Homer, which stabilize the synapse. Detected signals are transferred via a variety of signaling molecules including kinases, phosphatases, and GTPases (Fig. 3A). Inhibitory postsynapses on the other hand are mostly located on the dendritic shaft, the cell body, or the axon initial segment. The postsynaptic specialization contains fewer proteins compared to excitatory synapses although more proteins involved in the inhibitory postsynaptic density (iPSD) are discovered in recent years. In addition to neurotransmitter receptors (e.g. GABA receptors), the synapse contains signaling and scaffolding molecules, with Gephyrin (Gphn) being a central organizer of the inhibitory synapse (Sheng and Kim, 2011; Uezu et al., 2016) (Fig. 3B).

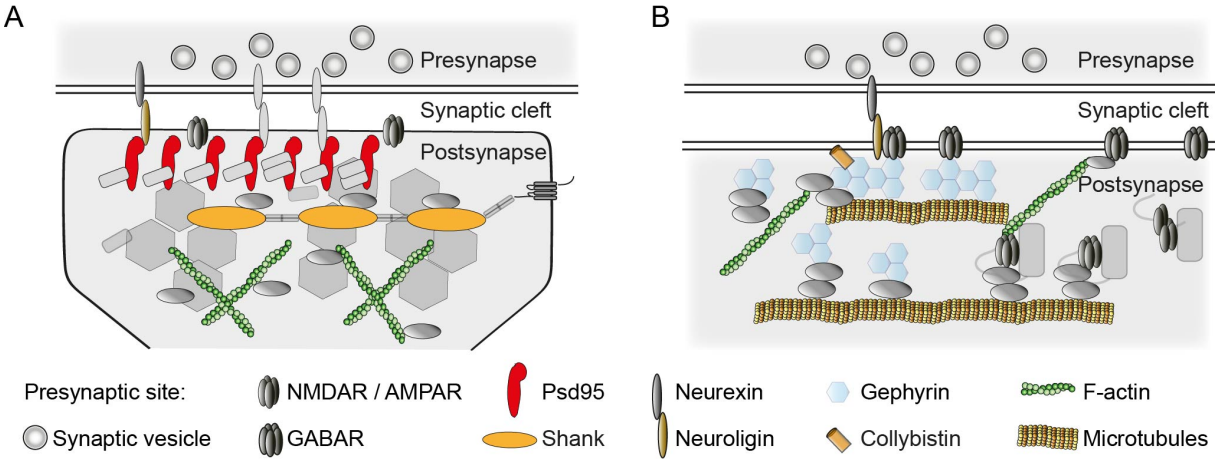


Fig. 3: Protein composition of postsynaptic sites.
(A) Excitatory synapses are localized on dendritic spines and the major scaffolding proteins include Psd95 and Shank proteins that connect the membrane to the actin cytoskeleton. (B) The protein composition of inhibitory synapses is less investigated. The main scaffolding protein is Gephyrin, which connects GABA receptors to the actin and microtubule cytoskeleton. Modified from (Sheng and Kim, 2011).

Large-scale phosphoproteomics characterization of the mouse synapse showed over 650 phosphorylation events, occurring on all major synaptic protein classes (Collins et al., 2005). Direct phosphorylation of neurotransmitter receptors has been shown to stabilize the receptor and potentiate the channel currents, thereby leading to synaptic plasticity (Lee, 2006). Another example of how synaptic function can be modulated by phosphorylation is via scaffolding molecules. Phosphorylation of Psd95 and Gephyrin scaffolding molecules regulates the stability and clustering abilities of these proteins at synapses, thereby modulating synaptic shape and morphology (Zacchi et al., 2014; Delgado et al., 2020). Interestingly, phosphorylation at the same site can even occur through different kinases and signaling pathways. Gephyrin can be phosphorylated at S270 and a phosphodeficient mutant (S270A, serine substituted by alanine at position 270) resulted in the formation of additional Gephyrin

clusters, which increased the frequency of miniature inhibitory postsynaptic currents (mIPSCs). S270 can be phosphorylated both by the Glycogen synthase kinase 3 (Gsk3) and by the Cyclin-dependent kinase 5 (Cdk5). Phosphorylation can also be mediated by the Mitogen-activated protein kinase 3 (Mapk3) at a neighboring site, S268, which decreases the size of postsynaptic Gephyrin clusters, showing that phosphorylation pathways and effects can be complex and highly interconnected (Zacchi et al., 2014; Tyagarajan et al., 2013). Bioinformatic predictions and *in vitro* phosphorylation studies also suggest that kinases phosphorylate a large number of substrates, while every substrate can be phosphorylated by many kinases (Collins et al., 2005).

2.2.3 Phosphorylation in neurodegenerative and cognitive disorders

The importance of phosphorylation in brain function is further corroborated by demonstrating the consequences of disturbed protein phosphorylation. For years, the role of aberrant phosphorylation in neurodegenerative diseases has been discussed. The most famous protein that shows changes in its phosphorylation status in neurodegenerative disorders is the Microtubule-associated protein tau (Mapt). Hyperphosphorylation of Mapt is suspected to reduce its ability to bind to microtubules and increase its capacity to aggregate and form neurofibrillary tangles, which are a pathological hallmark of Alzheimer's disease (AD) (Borovac et al., 2018; Johnson and Stoothoff, 2004; Sathe et al., 2020). Similarly, increased phosphorylation of Snca (α-Synuclein) at S129 results in protein aggregation and the formation of so-called Lewy bodies, which are found in patients suffering from Parkinson's disease (Tenreiro et al., 2014). For these two proteins, the effect of phosphorylation has been extensively studied, but they are not the only phosphoproteins dysregulated in neurodegenerative diseases. A recent study investigating the phosphoproteomics profile in the frontal and entorhinal cortex of patients with mild cognitive impairment and AD showed that phosphorylation was dysregulated for hundreds of proteins. Interestingly, alterations in the phosphorylation of proteins precede the final stage of dementia and were already found in patients with mild cognitive impairment. The majority of the identified proteins could be assigned to membrane or membrane-linked proteins, cytoskeletal and synaptic proteins, and kinases (Ferrer et al., 2021).

Often, aberrant phosphorylation affects the activity and function of the respective protein. For example, in AD mouse models and post-mortem tissue of human AD patients, phosphorylation of the Srrm2 protein at S1068 was detected. This phosphorylation prevented interaction with other proteins and the subsequent translocation to the nucleus, which in turn destabilized a second protein, Pqbp1, which influenced the splicing patterns of synapse-related genes. Pqbp1 also has a causal relationship with intellectual disability (ID), demonstrating possible links between different cognitive disorders (Tanaka et al., 2018; Okazawa, 2018). More and

more studies are being published that show how increased or decreased phosphorylation affects the function of the respective protein and how this could be linked to different diseases including ID, schizophrenia, or autism spectrum disorder (ASD) (Sepp et al., 2017; Todd and Mack, 2001; Tamura et al., 2021; Bemben et al., 2015; Yi et al., 2015). In addition to single phosphorylated proteins, also activation of pathways through phosphorylation receives increasing attention (Rosina et al., 2019; Poopal et al., 2016; Onore et al., 2017). In patients with ASD, several downstream proteins of the mammalian target of rapamycin (mTOR) pathway were stronger phosphorylated while the level of phosphorylated proteins even correlated with the severity of the disease (Rosina et al., 2019).

2.2.4. Phosphorylation in malformations of cortical development

Activation of the mTOR pathway has also been shown to be causally involved in other brain disorders. A prominent example is a group of diseases classified as mTORopathies, which are characterized by overactivation of the mTOR pathway. This pathway includes many kinases and has ubiquitous functions, controlling cellular growth, proliferation, cell survival, and protein synthesis, thereby mediating brain development and function. Overactivation of the mTOR cascade has been found in focal cortical malformations such as tuberous sclerosis (TSC), focal cortical dysplasia type IIB (FCDIIB), and gangliogliomas (GG) (Wong and Crino, 2012). TSC is an autosomal dominant disorder in which patients carry mutations in the Tsc1 or Tsc2 gene. One of the major neuropathological hallmarks are cortical lesions in form of tubers characterized by aberrant cortical lamination, dysplastic neurons, and giant cells (Juric-Sekhar and Hevner, 2019; Aronica et al., 2012). Sequence alterations of the Tsc1 gene are also often found in FCDIIB (Aronica et al., 2012). This malformation of cortical development is also characterized by disturbed cortical lamination and the presence of dysplastic and balloon cells (Crino, 2015; Orlova et al., 2010). A third mTORopathy, GGs, are glioneuronal tumors that consist of dysplastic neurons and a proliferative glial component (Blümcke and Wiestler, 2002; Cases-Cunillera et al., 2022). Although being a rare neoplasm, GGs are the most common tumors in young patients suffering from chronic focal epilepsies (Blümcke and Wiestler, 2002). Despite these different pathologies, the three disorders share a common feature, which is an aberrant activation of the mTOR pathway, resulting in enhanced phosphorylation of downstream targets such as the Ribosomal S6 protein (Rps6). Additionally, all mTORopathies are strongly associated with several neurological deficits and medically intractable epilepsy. The contribution of mTOR pathway overactivation to epileptogenesis is investigated in many animal models (Wong and Crino, 2012).

2.2.5 Phosphorylation in epilepsy

However, overactivation of the mTOR pathway is not the only phosphorylation-dependent mechanism described in epilepsy. During status epilepticus, which is defined as continuous or rapidly recurring seizures, the $GABA_A$ receptor ($GABA_AR$) was less phosphorylated at S408/9, which enhanced the endocytosis of the receptor and thus reduced the mediation of fast synaptic inhibition in the brain (Terunuma et al., 2008). Kinases have also been implicated in the progression of status epilepticus. Increasing the activity of Gsk3β via a phospho-deficient Gsk3β S9A mutant reduced the frequency of seizures induced by kainic acid in a mouse model for epilepsy. Consistent with these results, increased phosphorylation at S9 in Gsk3β which is thought to inhibit kinase activity was correlated with increased phosphorylation of the AMPA receptor subunit GluA1 in brain tissue from epilepsy patients, leading to activation of the receptor and enhanced excitation (Urbanska et al., 2019). Another kinase that is implicated in status epilepticus progression and epileptogenesis is the non-receptor Src family tyrosine kinase (SFK) Fyn. Knocking out this kinase in mice reduced the severity of the status epilepticus and the number of non-convulsive seizures. Pre-treating animals with the SFK-inhibitor saracatinib not only decreased the severity of the status epilepticus but also abolished mortality. Treatment following status epilepticus prevented the epileptogenic process in more than half of the animals and decreased seizure frequency in the remaining mice (Sharma et al., 2018), demonstrating how one kinase may be critically involved in disease onset and progression.

2.2.6 Kinase inhibitors

Kinase inhibitors such as saracatinib are increasingly becoming the focus of scientific interest and pharmaceutical drug development. Until now, kinase inhibitors are mainly approved in the treatment of cancer in peripheral tissues. Approving kinase inhibitors in disorders of the CNS has been a challenge, as the drugs have to cross the blood-brain barrier in order to reach their target proteins. Nevertheless, several kinase inhibitors are already established in clinical therapies such as alectinib, an inhibitor of the Anaplastic lymphoma kinase (Alk) in the treatment of brain metastases, or everolimus, an mTOR inhibitor used in the therapy of TSC patients (Heffron, 2016, 2018; Lechuga and Franz, 2019). Additionally, many kinase inhibitors are currently undergoing preclinical or clinical trials. Tideglusib, a Gsk inhibitor, reduced Mapt phosphorylation, neuronal death, and memory deficits in animal models of AD and went through phase II of clinical trials (Serenó et al., 2009; Lovestone et al., 2015). Saracatinib, the Fyn-inhibitor used for treating mice with status epilepticus in the above-mentioned study, has been also shown to influence neurotoxicity and Mapt phosphorylation in AD and has completed phase II of clinical trials (Fagiani et al., 2020; Sharma et al., 2018).

These examples illustrate that the importance of kinases in physiological and pathophysiological conditions is increasingly recognized, as they are key players in the regulation of signaling cascades in brain development, neuron morphology, and function.

2.3 Protein-protein interactions

Although many signaling cascades involve kinases and protein phosphorylation, signals are not only conveyed via posttranslational modifications but protein function can also be modulated by direct physical interactions with other proteins. These so-called protein-protein interactions can be stable interactions that occur for example in protein complexes. Protein complexes may either be homomeric, such as Gephyrin that self-assembles into a hexagonal lattice, or heteromeric, such as neurotransmitter receptors that are formed by different subunit proteins. To even increase complexity, monomeric and multimeric assembly can also be combined. Gephyrin, for example, does not only form homomers but also assembles with $GABA_AR$ subunits and the microtubule cytoskeleton, thereby providing an important link of the synaptic receptors to intracellular structures. The $GABA_AR$ is a typical example of a multimeric protein, as its pentameric structure is assembled from five out of sixteen different $GABA_AR$ subunits. The differential compositions of the subunits determine the properties of the receptor including sensitivity to the neurotransmitter and the opening time of the channel (Tretter et al., 2012; Olsen and Sieghart, 2009). Strong and stable interactions as they are found in the $GABA_AR$ are traditionally investigated by co-immunoprecipitations (CoIPs) by which one protein is isolated and interacting proteins will be co-purified (de Las Rivas and Fontanillo, 2010).

In addition to these stable protein-protein interactions, proteins can also interact transiently and thereby modulate a variety of cellular processes including cell cycle, apoptosis, transport, or protein folding. Proteins interact usually via specialized domains that are highly conserved. One example of such a domain is the Src homology 3 (SH3) domain that binds to sequences enriched in prolines and is often used by signaling molecules to identify their target proteins (Kurochkina and Guha, 2013). Identifying this type of more transient interactions is more challenging and requires more elaborate tools. A technique that was already successfully applied to analyze transient protein-protein interactions at inhibitory synapses is proximity-dependent biotinylation (BioID). Using this technique, a study aimed to characterize the inhibitory postsynapse, as the protein composition at these sites is less studied and understood compared to its excitatory counterpart. Therefore, a modified biotin ligase BirA* was fused to Gephyrin and two additional inhibitory postsynaptic proteins. BirA* covalently biotinylated all proteins within a distance of 10-50 nm and thereby allowed a broad characterization of the proteome at inhibitory postsynapses including weak and transient interactions (Uezu et al., 2016).

A very prominent example of protein-protein interactions that influence many processes at synapses are interactions of cell adhesion molecules. They link the pre- to the postsynaptic part and thereby not only control synapse assembly but also their maintenance and stability. Some proteins are specific to either the pre- or the postsynapse, e.g. presynaptic Neurexins that interact with postsynaptic Neuroligins, whereas other cell adhesion molecules such as Neural cell adhesion molecule (Ncam) can be found both on the pre- and the postsynaptic site. Interestingly, an altered function and expression of cell adhesion molecules have been linked to neurological diseases such as AD, ASD, or schizophrenia (X. Yang et al., 2014), demonstrating how disturbed protein interactions can drastically alter brain function.
In the last years, traditional and newly emerging methods such as BioID allowed to investigate protein-protein interactions on a large scale and to define the interactome in living organisms in healthy and pathological conditions (Lu et al., 2020; Varnaitė and MacNeill, 2016).

2.4. Ste20-like serine/threonine-protein kinase

These new and traditional methods are also used nowadays in the nervous system to investigate protein-protein interactions of a vast variety of proteins to understand their contribution to development and function in a physiological context or in the context of diseases. One kinase that has recently been discovered to play an important role in neuronal development and that may also be involved in neurodevelopmental disorders is the Ste20-like serine/threonine-protein kinase (Slk). It belongs to the family of Sterile20 (Ste20) serine/threonine kinases that were first identified in yeast as kinases involved in pheromone signaling leading to a mating response. In this context, the Ste20-kinase acts as a Map kinase kinase kinase kinase (Map4k) by phosphorylating Ste11, a Map3k, that activates Ste7, a Map2k, and finally the Map kinases Kss1 and Fus3 (Dohlman and Thorner, 2001; Strange et al., 2006; Dan et al., 2001). The Map kinase pathway is an important signaling cascade converting external stimuli such as growth factor release, cytokines, or environmental stimuli to a cellular response (Davis, 1993). In humans, the homologs of the Ste20 kinases form a large family of 28 protein kinases that can be subdivided into two major subfamilies, the p21-activated kinases (PAKs) with the conserved kinase domain at the C-terminus and the germinal-center kinases (GCKs) with the kinase domain at the N-terminus of the protein (Dan et al., 2001).
Slk belongs to the GCK V subfamily and was first discovered in guinea pig liver in 1997, shortly after which its homolog was characterized in mice (Itoh et al., 1997; Pytowski et al., 1998; Sabourin and Rudnicki, 1999). Murine Slk consists of an N-terminal catalytic kinase domain, an unstructured linker domain, and a C-terminal AT1-46 homology (ATH) domain, containing coiled-coil regions (Fig. 4A). These coiled-coil regions are important for the homodimerization of Slk and regulate the activity of the kinase (Cybulsky et al., 2017; Sabourin et al., 2000). In

the activation loop of the kinase, two phosphorylation sites have been identified at T183 and S189 that need to be auto-phosphorylated for full activation of the kinase. In the middle domain of the protein, Slk harbors a putative SH3 binding site, suggesting that Slk could interact with proteins containing SH3 domains (Cybulsky et al., 2017; Jaberi et al., 2015; Yamada et al., 2000) (Fig. 4B).

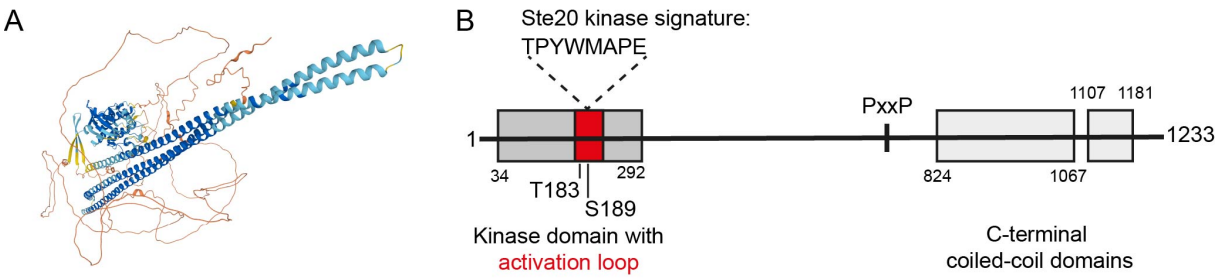


Fig. 4: Structure of Slk.
(A) Three-dimensional structure of mouse Slk (mSlk) (Sequence: UniProt (Bateman 2021)). (B) The N-terminal part of Slk harbors the kinase domain with the activation loop. At the C-terminal end, two coiled-coil domains are located (Sequence information: UniProt (Bateman et al., 2021)).

2.4.1 Slk in non-neuronal cells

Slk is expressed ubiquitously in adult tissues and specifically in muscle and neuronal lineages during development. The murine Slk was first cloned in 1999 and since then its functions were primarily characterized in non-neuronal cells (Sabourin and Rudnicki, 1999) (Fig. 5, Table 1). One of the first discovered functions of Slk was its ability to induce apoptosis, which was shown by overexpression in cultured fibroblast but also in glomerular epithelial cells of the kidney (Sabourin and Rudnicki, 1999; Cybulsky et al., 2009; Hao et al., 2006). Several studies have further characterized the apoptotic process, which appears to occur independently of kinase activity. Furthermore, apoptosis involved Jnk1 activation and was enhanced by Tp53 activation and homodimerization of Slk via its coiled-coil regions. Nevertheless, apoptosis depended mainly on the N-terminal domain of Slk, which required autophosphorylation. The process was controlled via Hsf1 and Hsp70 and signaled via Ask1 and p38 Mapk (Sabourin et al., 2000; Sabourin and Rudnicki, 1999; Cybulsky et al., 2009; Delarosa et al., 2011; Luhovy et al., 2012; Cybulsky et al., 2017; Hao et al., 2006). Not only apoptosis but also cell proliferation is regulated by Slk. In fibroblasts and myoblasts, Slk regulates the G2/M transition by activating Plk1 (Ellinger-Ziegelbauer et al., 2000). Loss of Slk resulted in a reduction of cell proliferation and an accumulation of quiescent cells, which appears to be independent of kinase activity as the same effect was observed after expression of the kinase-dead mutant Slk K63R (lysine replaced by arginine at amino acid position 63). In contrast, overexpression of Slk induced a re-entry into the cell cycle and resulted in the formation of ectopic mitotic spindles (O'Reilly et

al., 2005). At mitotic spindles, but also at the centrosome and on microtubules, Slk is colocalizing with Tubulin (Wagner and Sabourin, 2009; Wagner et al., 2002; Nadezhdina et al., 2001), which connects the function of Slk in the cell cycle with its third major function, the regulation of cytoskeletal dynamics. Loss of Slk or its kinase activity resulted in unfocused microtubule arrangement during the interphase and the centrosomes lost their ability to anchor and cap microtubules (Burakov et al., 2008). Slk phosphorylates the p150glued subunit of Dynactin (Dctn1), which targets Dynactin to the centrosome and this phosphorylation seemed to be critical for proper microtubule organization (Zhapparova et al., 2013).

In addition to microtubule organization, Slk also influences the actin cytoskeleton. Overexpression of the kinase results in the disassembly of actin stress fibers via Rac1, which seems to be mainly mediated by the ATH domain through relocalization of actin to the periphery (Wagner et al., 2002; Pytowski et al., 1998; Sabourin et al., 2000). In human airway smooth muscle cells, actin polymerization was inhibited after Slk loss by reducing Plk1 activity and thereby decreasing S272 phosphorylation of the focal adhesion-associated protein Paxillin (Pxn) (Wang et al., 2020). Paxillin and Slk colocalized at the leading edge of migrating cells but not directly at large focal adhesions. Nonetheless, Slk-induced phosphorylation of Paxillin stimulated the turnover of focal adhesions and thereby allowed the migration of cells (Quizi et al., 2013). Both the loss of Slk itself and the loss of its kinase activity impaired focal adhesion turnover and cell migration in a Fak/c-src/Mapk- or RhoA/Rock-dependent way (Wagner and Sabourin, 2009; Fokin et al., 2016).

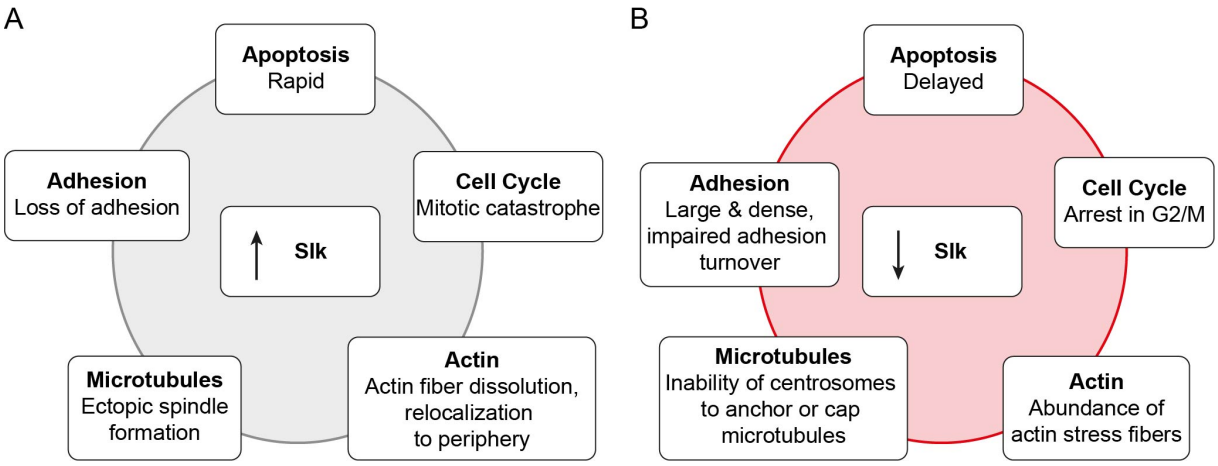


Fig. 5: Functions of Slk in non-neuronal cells.
(A) The diagram shows the effects of Slk overexpression, which demonstrates that Slk functions include regulation of apoptosis, cell cycle, adhesion, and cytoskeletal dynamics. (B) Slk knockdown induces opposite effects on apoptosis, cell cycle, adhesion, and cytoskeleton dynamics compared to overexpression of the kinase. Modified from (Al-Zahrani et al., 2013).

Migration is important during development but also plays a crucial role during tumor development. In human breast cancer, the tyrosine kinase receptor Erbb2 (also known as Neu)

is frequently overexpressed. Mammary epithelial cells that overexpressed Erbb2 were only capable of migrating efficiently in the presence of Slk whereas cancer cell invasion was inhibited by expressing kinase-dead Slk. Therefore, Slk seems to be important for the motile and invasive phenotype of Erbb2-positive breast cancer cells, which is in line with the finding of increased Slk levels in murine breast cancer cell lines (Roovers et al., 2009). In human patients with Erbb2-positive breast cancer, Slk expression is also high, and the higher the expression, the lower the survival probability of the patients. In contrast, loss of Slk accelerated tumor onset and reduced overall survival in a mouse model of Erbb2-positive breast cancer (Al-Zahrani et al., 2020). These conflicting findings show that Slk has diverse and complex roles during tumorigenesis that need further research to be fully understood.

Table 1: Known functions of Slk in different cell types and tissues.

Cell type / Tissue	Function	Observation / Effect	Reference
Fibroblasts	Cytoskeletal effects	Association with microtubules and disassembly of actin stress fibers via Rac1	(Wagner et al., 2002)
	Cell migration	Cell migration and focal adhesion turnover downstream of Fak/c-src complex	(Wagner et al., 2008)
		Control of cell motility via interaction with Ldb1 and Ldb2	(Storbeck et al., 2009)
		Enhancement of cell migration via interaction with Lmo4	(Baron et al., 2015)
		Focal adhesion turnover and cell migration via interaction with Paxillin	(Quizi et al., 2013; Wagner and Sabourin, 2009)
	Cell cycle	Regulation of cell cycle: G2/M transition	(Ellinger-Ziegelbauer et al., 2000)
		Cell proliferation and progression through M phase	(O'Reilly et al., 2005)
		Reduction of Slk activity by v-src expression	(Chaar et al., 2006)
Muscle cells	Vasodilation in vascular smooth muscle cells	Induction of vasodilation through RhoA phosphorylation	(Guilluy et al., 2008)
	Cytoskeletal effects	Contraction through actin polymerization induced by Slk	(Wang et al., 2020)

		activation of Plk1 and Paxillin phosphorylation in airway smooth muscle cells	
		Actin stress fiber assembly/disassembly	(Sabourin et al., 2000)
	Myofiber development	Influence on myoblast fusion and altered muscle organization	(Storbeck et al., 2004, 2013)
		Influence on regeneration capacity and differentiation	(Storbeck et al., 2013)
	Muscle function	Myofiber stability and force generation in skeletal muscle-specific Slk knockout mice	(Pryce et al., 2017)
	Apoptosis	Induction of apoptosis by N-terminal kinase domain	(Sabourin et al., 2000)
Epithelial cells	Cytoskeletal effects	Local enrichment of Slk and Lok in microvilli and restriction of Ezrin function to the apical domain	(Viswanatha et al., 2012)
		Regulation of apical morphology via activation of ERM proteins and RhoA	(Zaman et al., 2021)
	Epithelial-to-mesenchymal transition and cell migration	Cytoskeletal changes during Tgfβ-induced epithelial-to-mesenchymal transition and invasiveness	(Conway et al., 2017)
Kidney cells	Cytoskeletal effects	Focused microtubule arrangement	(Burakov et al., 2008, 2005)
		Microtubule organization via phosphorylation of Dctn1	(Zhapparova et al., 2013)
	Cell migration	Regulation of cell locomotion via RhoA and Dynactin subunit Dctn1	(Fokin et al., 2016)
	Apoptosis	Enhancement of apoptosis via Tp53	(Cybulsky et al., 2009)
		Enhancement of apoptosis after homodimerization via p38 Mapk and Jnk phosphorylation	(Delarosa et al., 2011)
		Promotion of apoptosis via Ask1 and p38 Mapk	(Hao et al., 2006)
	Ischemia-reperfusion injury	Enhanced Slk expression and activity after ischemia-reperfusion injury	(Cybulsky et al., 2004)
		Induction of apoptosis after ischemia-reperfusion injury	(Cybulsky et al., 2009)

	Membranous nephropathy	Increased Slk activity and Ezrin phosphorylation associated with proteinuria and podocyte injury	(Cybulsky et al., 2017)
Neurons	Development	Preferential expression during development	(Zhang et al., 2002)
Tumor	Cell invasion	Supports cell migration and invasion via destabilization of focal adhesions	(Roovers et al., 2009)
		Binding to Asap1 which promotes the formation of metastasis and increases cell motility and invasion	(Müller et al., 2010)
	Tumor development	Accelerated tumor onset and decreased survival after Slk loss in a mouse model of Erbb2/Neu-positive breast cancer	(Al-Zahrani et al., 2020)
		High Slk expression correlating with poor survival in human glioma	(Wang et al., 2018)

2.4.2 Slk in neurons

Despite the finding that Slk is preferentially expressed in muscle and neuronal lineages during development and that mice with a truncated form of Slk developed neuronal and skeletal impairments by embryonic day (E) 14.5 (Al-Zahrani et al., 2014; Zhang et al., 2002), the role of Slk in neuronal cells remained enigmatic. A study in 2002 described that Slk was mainly expressed in NeuN-positive neuronal cells and not in Gfap-positive astrocytes or Ox42-positive macrophages (Zhang et al., 2002). Nearly twenty years later, it was shown that Slk has important neuronal functions by controlling the formation of the dendritic tree and the stability of inhibitory synapses during neuronal development (Schoch et al., 2021). *In utero* electroporation (IUE) was used to knock down Slk by introducing a short hairpin RNA against Slk (shSlk) into neuronal progenitor cells at E14.5 which changed the morphology and function of the electroporated neurons. Loss of Slk decreased the amount of higher order dendrites by about 75%. Additionally, the initial normal formation of inhibitory synapses until postnatal day (P) 15 was attenuated and the neurons showed a reduced density of inhibitory synapses after P15 compared to control neurons (Fig. 6).

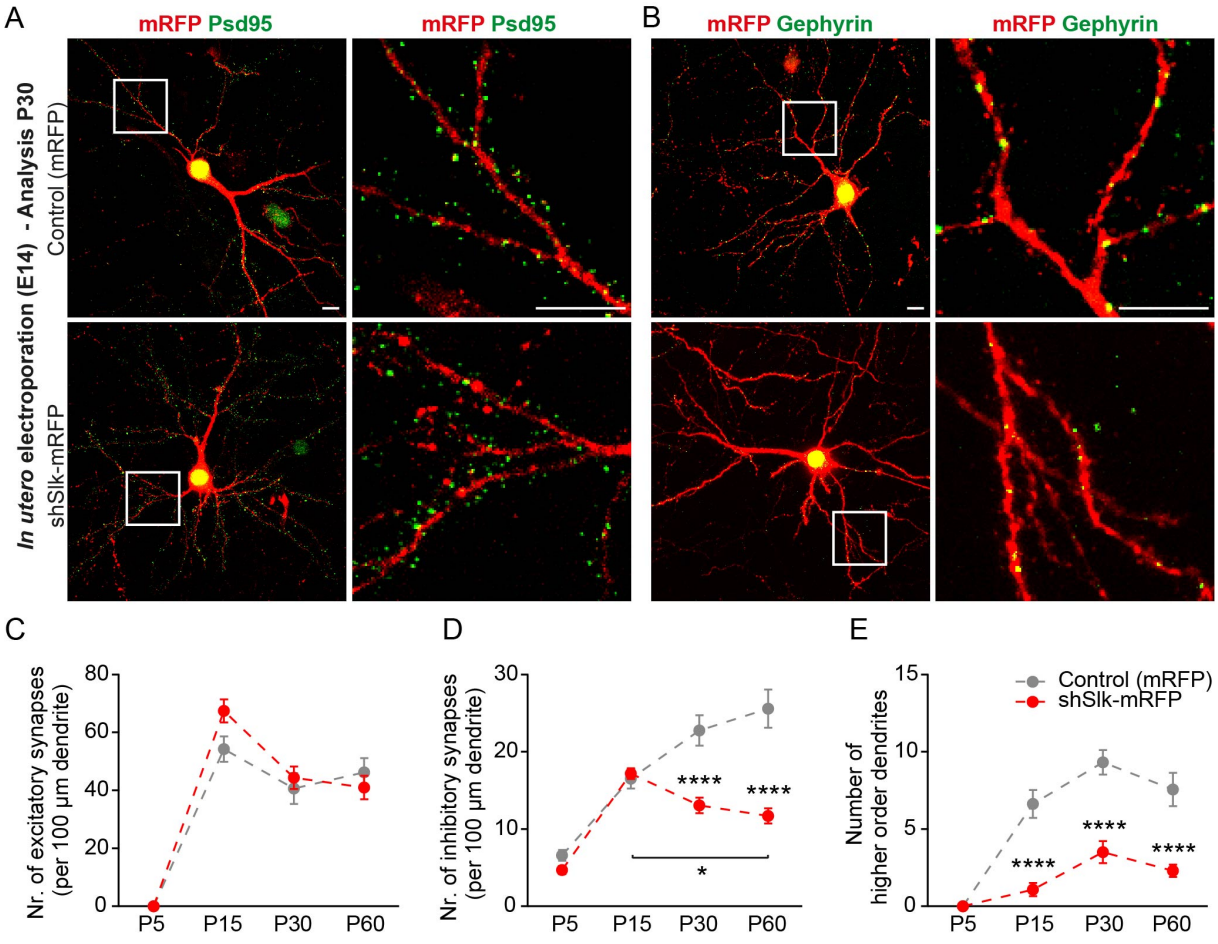


Fig. 6: Slk effects on neuron morphology.
IUE of a short hairpin RNA against Slk did not alter the density of excitatory synapses (A, C) but decreased the density of inhibitory synapses after P15 (B, D). In addition, dendritic branching was reduced, affecting specifically higher order dendrites (E). Scale bar: 10 µm. Modified from (Schoch et al., 2021).

These morphological changes were also reflected on a functional level. The capacitance of shSlk neurons was reduced, corresponding to a smaller membrane surface due to less dendritic branching. In addition, the frequency of mIPSCs was decreased, reflecting the lower density of inhibitory synapses. Interestingly, the density of excitatory synapses was not altered and the miniature excitatory postsynaptic current (mEPSC) frequency was comparable to control neurons. These findings suggest that Slk is not only important for neuronal morphology but also for the excitation-inhibition balance in neurons (Schoch et al., 2021). When this balance is disturbed, the brain cannot maintain its function, possibly manifesting in diseases such as epilepsy or ASD (Bruining et al., 2020; Jeste and Tuchman, 2015; Bozzi et al., 2018). Investigating Slk expression in cortical malformations of epilepsy-associated FCDIIB and GG revealed that Slk expression was reduced in dysplastic neurons compared to control neurons (Schoch et al., 2021) (Fig. 7). Dysplastic neurons are characterized by an aberrant dendritic branching and altered signaling (Shao et al., 2022; Mathern et al., 2000; Rossini et al., 2021).

Similarly, experimental reduction of Slk also affected dendrite branching and specifically inhibitory signaling.

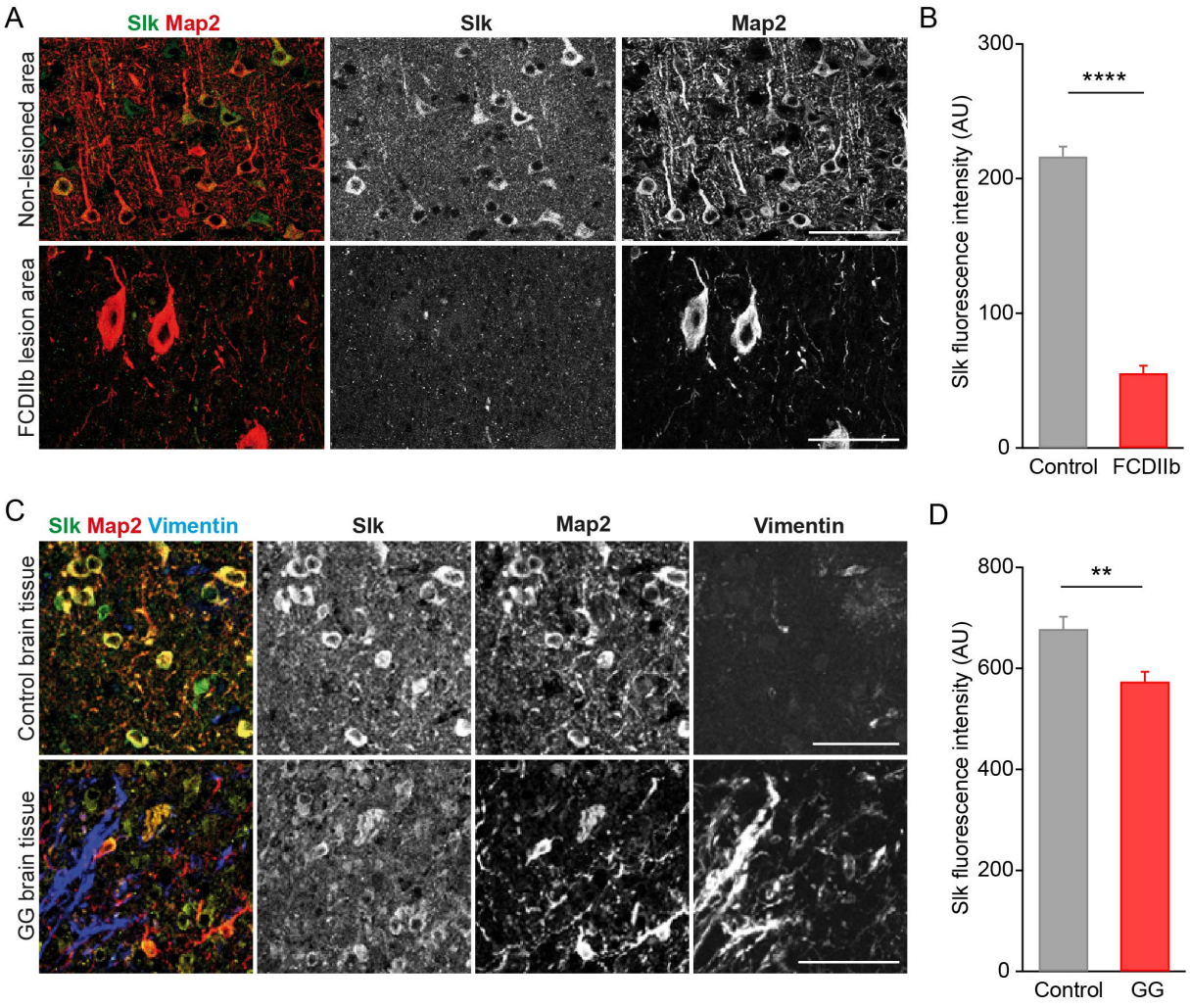


Fig. 7: Slk expression in focal cortical malformations.
The expression of Slk is reduced in dysplastic neurons of FCDIIB (A, B) and GG (C, D) patients. Scale bar: 100 µm. Modified from (Schoch et al., 2021).

Taken together, this implies that Slk could be either causally or consequentially involved in the pathogenesis of focal cortical malformations. Interestingly, another study has shown that Slk is highly expressed in human glioma tissues and cell lines while high expression is associated with poor survival of the patients. High Slk expression supported the invasion ability of glioma cells and thereby probably increased the malignancy of these tumors (Wang et al., 2018). These results suggest that overexpression as well as loss of Slk are associated with different characteristics of disease phenotypes and thereby underline the crucial role of Slk function in the brain.

2.4.3 Known protein-protein interactions of Slk

Despite or perhaps because of the diverse functions that Slk fulfills in various cell types and cellular processes, it is difficult to dissect the molecular mechanism and pathways of Slk action. As Slk is a protein kinase, many effects are likely or proven to be mediated by phosphorylation of substrate proteins (Table 2). Some phosphorylation substrates have been identified by *in vitro* kinase assays. These used Mbp, H1, and H3 proteins as generic substrates of the kinase although a physiological role of Mbp, H1, and H3 phosphorylation by Slk has never been demonstrated (Sabourin and Rudnicki, 1999; Yamada et al., 2000; Al-Zahrani et al., 2014; Potekhina et al., 2003; Delarosa et al., 2011; Pytowski et al., 1998). *In vitro* kinase reactions showed that Slk could directly phosphorylate Apoptosis signal-regulating kinase 1 (Ask1), a kinase that plays a role in the apoptosis signaling pathway (Hao et al., 2006). Similarly, the Polo-like kinase homolog (Plk1) was shown to be phosphorylated by Slk and thereby mediates cell cycle progression (Ellinger-Ziegelbauer et al., 2000; Johnson et al., 2008; Wang et al., 2020). For both kinases, phosphorylation increased their activation and thus determined further downstream mechanisms.

Cytoskeletal changes were partly initiated by Slk phosphorylation of ERM proteins, which comprise the family of Ezrin, Radixin, and Moesin proteins that are important linkers of the actin cytoskeleton to the plasma membrane (Cybulsky et al., 2017; Viswanatha et al., 2012; Machicoane et al., 2014). A possible link to the microtubule cytoskeleton might be given by phosphorylation of the p150glued subunit of Dynactin (Dctn1), which is a protein complex involved in the transport along microtubules (Zhapparova et al., 2013). At focal adhesions, Paxillin was found to be phosphorylated by Slk through *in vitro* kinase reactions although this phosphorylation could not be verified by mass spectrometry (Quizi et al., 2013). Last but not least, Slk has been shown to induce RhoA phosphorylation and thereby mediate relaxation of smooth muscle cells although it is not clear whether this phosphorylation is direct or carried out by intermediate proteins (Guilluy et al., 2008).

Table 2: Known phosphorylation substrates of Slk.

Phosphorylation substrate	Method	Reference
Apoptosis signal-regulating kinase 1 (Ask1)	*In vitro* kinase reaction	(Hao et al., 2006)
Dynactin subunit 1 (Dctn1)	*In vitro* kinase reaction	(Zhapparova et al., 2013)
ERM proteins (Ezrin (Ezr), Radixin (Rdx), Moesin (Msn))	*In vitro* kinase reaction; reduced phosphorylation in cells after Slk depletion	(Machicoane et al., 2014)

Ezrin (Ezr)	*In vitro* kinase reaction; reduced phosphorylation in cells after Slk depletion	(Cybulsky et al., 2017; Viswanatha et al., 2012)
Histone H1	*In vitro* kinase reaction	(Sabourin and Rudnicki, 1999; Potekhina et al., 2003)
Histone H3	*In vitro* kinase reaction	(Pytowski et al., 1998)
Myelin Basic Protein (Mbp)	*In vitro* kinase reaction	(Sabourin and Rudnicki, 1999; Yamada et al., 2000; Burakov et al., 2008; Potekhina et al., 2003; Delarosa et al., 2011; Pytowski et al., 1998)
Paxillin (Pxn)	*In vitro* kinase reaction	(Quizi et al., 2013)
Polo-like kinase homolog (Plk1)	Elevated phosphorylation in Slk transfected cells; *in vitro*	(Ellinger-Ziegelbauer et al., 2000; Johnson et al., 2008; Wang et al., 2020)
RhoA (Rhoa)	Elevated phosphorylation in Slk transfected cells	(Guilluy et al., 2008)
Slk (autophosphorylation)	*In vitro* kinase reaction	(Sabourin and Rudnicki, 1999; Yamada et al., 2000)

Other functions of Slk have been shown to occur independently of kinase activity, which indicates that different types of protein-protein interactions may be involved (Table 3). For example, the kinase-independent process apoptosis, which can be induced by the kinase-dead mutant, was prevented by the expression of the nucleoporin Tpr. Slk and Tpr were confirmed to be direct interaction partners in CoIP experiments (Jaberi et al., 2015). Cytoskeletal and cytoskeleton-associated proteins such as α-Tubulin and α-Actinin-4 were also co-immunoprecipitating with Slk (Jaberi et al., 2015; Wagner et al., 2002), although the exact effect of the binding is not known yet.

For other proteins, binding to Slk is known to induce a functional change. For Ldb1 and 2 proteins, binding to Slk regulated cell migration while binding to Lmo4 activated Slk kinase activity (Baron et al., 2015; Storbeck et al., 2009). In contrast, a functional link can only be suspected for other proteins. Asap1 has been shown to bind to Slk and as both proteins are upregulated in rodent tumor models and correspond with the metastatic potential, a putative functional link can be hypothesized (Müller et al., 2010). Interestingly, only one of the putative phosphorylation substrates, namely RhoA, has been demonstrated to bind to Slk (Guilluy et al., 2008; Bagci et al., 2020).

Table 3: Known binding partners of Slk.

Binding partner	Method	Reference
Arf-GAP with SH3 domain, ANK repeat and PH domain-containing protein 1 (Asap1)	CoIP	(Müller et al., 2010)
LIM domain transcription factor (Lmo4)	CoIP	(Baron et al., 2015)
LIM domain-binding proteins (Ldb1, Ldb2)	CoIP, colocalization assay	(Storbeck et al., 2009)
Nucleoprotein (Tpr)	CoIP; mass spectrometry	(Jaberi et al., 2015)
RhoA (Rhoa)	CoIP; BioID	(Guilluy et al., 2008; Bagci et al., 2020)
α-Actinin-4 (Actn4)	CoIP; mass spectrometry	(Jaberi et al., 2015)
α-Tubulin (Tuba)	CoIP	(Wagner et al., 2002)

Therefore, several protein interaction partners of Slk have been identified so far but the evidence is still very sparse and not sophisticated enough to sufficiently explain the functions of Slk in different cell types. Especially in neurons, no phosphorylation substrates and protein binding partners have yet been identified that could explain the observed effects of Slk.

2.5 Aims of the project

Protein-protein interactions are important regulators of cellular functions ranging from development to synaptic function. These include mere physical interaction but also enzymatic reactions such as phosphorylations. Phosphorylation is an important posttranslational modification that can control diverse cellular processes in neurons. Alterations in protein-protein interactions and phosphorylation patterns are found in a variety of neurodevelopmental diseases and are the focus of intensive research. Therefore, understanding protein-protein interactions in a physiological context is necessary to be able to dissect and target abnormalities in pathophysiological situations.

One protein that has been shown to be indispensable for the proper development of neurons is the protein kinase Slk. This kinase is not only necessary for distal dendritic arborization and inhibitory synapse stability but also crucial for excitation-inhibition balance in the cell. Aberrant expression of Slk was shown to be linked to tumor development and the survival rate in non-neuronal tissue but also discovered in dysplastic cells in brain specimens of FCDIIB and GG patients. This suggests a link between Slk expression and disease phenotype and therefore underlines the important role of Slk in cells.

To further investigate Slk function in neurons, we would like to characterize the model of Slk knockdown in greater detail. Therefore, we will analyze the effects of an Slk knockdown on the dendrite phenotype in adult animals to determine the critical time point of Slk action. In addition, we will characterize the electrophysiological properties of the developmental Slk knockdown by electroencephalography (EEG) and multi-well multi-electrode arrays (MEA) to answer the question if Slk knockdown induces epileptic activity. To further define the effects of Slk knockdown on the surrounding cellular network, potential changes in neighboring cells and cell types will be explored by single-cell RNA sequencing (scRNAseq).

To better understand the known functions of Slk in neurons, it is pivotal to dip into the molecular mechanism of Slk action inside the cells and explore protein-protein interactions of Slk. In a first approach, we will investigate if known mechanisms from non-neuronal cells can be translated to neuronal cells by analyzing potential Slk interactors at inhibitory synapses and in the dendrites. As the data for direct Slk phosphorylation substrates and interaction partners is sparse in non-neuronal cells and non-existent for neuronal cells, we also aim to identify Slk interactors in large-scale proteomics experiments. Therefore, phosphorylation substrates will be searched by a phosphoproteomics screen, proteins proximal to Slk will be identified by proximity-dependent biotinylation (BioID), and binding partners will be discovered by CoIP experiments. These experiments will lead to a comprehensive dataset from which promising candidates will be chosen and verified in additional experiments.

All in all, we aim to characterize and explain the function of the protein kinase Slk by completing the picture of Slk effects in neurons and by identifying protein-protein interactions that could provide explanations for the observed functions.

3 Methods

3.1 Molecular biology

It is common practice to italicize gene symbols and to use non-italicized symbols for the corresponding protein product. In addition, all letters for human genes are usually in upper case while mouse and rat genes only begin with an upper-case letter. To keep the text clear and consistent, these rules are not applied in this study. All mentioned genes and proteins will be referred to by their gene names in the following format: Slk. Full protein names corresponding to the respective gene names can be found in the Appendix in Table 16. The information if a gene or protein is of human, mouse, or rat origin can be found in the Appendix in Table 27 which lists all plasmids that were used in this study together with the information about the organism the protein was derived from. For scRNAseq and proteomics experiments, mouse genes and proteins were sequenced and analyzed.

3.1.1 Polymerase chain reaction

Protein-encoding plasmids were cloned using the In-Fusion Cloning approach. To clone new constructs, fragments to insert were amplified by polymerase chain reaction (PCR) according to Table 4 using a proofreading competent polymerase. The amplification was performed in a thermocycler with the elongation time being adjusted according to the fragment size (in basepairs (bp)). The amplified fragments were run on a 1% agarose gel and purified from the gel using the Gel DNA Recovery Kit.

Table 4: PCR protocol for amplification of insert.

PCR mixture:			**PCR protocol:**					
10	µl	5x HF Buffer	Denaturation	98	°C	30	sec	
200	µM	dNTP	Denaturation	98	°C	10	sec	35x
0.5	µM	Forward primer	Annealing	58	°C	30	sec	
0.5	µM	Reverse primer	Elongation	72	°C	60	sec/kbp	
2	U	Phusion DNA polymerase	Elongation	72	°C	10	min	
50-100	ng	DNA / cDNA		4	°C	∞		
5	%	DMSO (optional)						
		H_2O ad 50 µl						

The vector DNA was digested with the appropriate restriction enzymes as described in Table 5 for 3 h at 37°C and isolated via agarose gel electrophoresis followed by DNA purification with the Gel DNA Recovery Kit.

Table 5: Restriction digest of vector DNA and recombination with PCR fragments.

Restriction digest:			Recombination:		
2	µl	10x Buffer	100	ng	PCR fragment 1
10	U	Restriction Enzyme 1	100	ng	PCR fragment 2
10	U	Restriction Enzyme 2	100	ng	Linearized vector
1-2	µg	DNA	2	µl	5x InFusion HD Enzyme PreMix
		H_2O ad 20 µl			H_2O ad 10 µl

To combine one or multiple inserts with the digested vector, the DNA fragments and the vector were incubated at 50°C for 20 min (Table 5). A list of all the generated and used plasmids including corresponding restriction enzymes and resistance markers can be found in the Appendix in Table 27.

3.1.2 Transformation of bacteria

Subsequently, the recombination mix was transformed into 50-80 µl of Stellar competent bacteria and incubated on ice for 30-60 min. To induce the uptake of DNA, bacteria were exposed to a heat shock at 42°C for 45 sec and incubated on ice for 2 min. After adding 200 µl of LB-medium and incubating for 1 h at 37°C on a shaker, bacteria were plated onto agar plates containing the appropriate antibiotics. For retransformation of already cloned plasmids, 100 ng of DNA was transformed into 50-80 µl of E. coli DH5α using the same protocol as described above. For bacterial protein production, DNA was transformed into E. coli BL21 bacteria.

3.1.3 DNA isolation

From the agar plates, one or multiple colonies were picked and incubated in 5 ml of LB-medium supplemented with the respective antibiotics for small-scale DNA purification or in 200 ml for high-scale DNA purification. DNA was isolated using the GeneJET Plasmid Miniprep Kit or the PureLink HiPure Plasmid Filter Maxiprep Kit. For IUE and virus production, endo-free DNA was prepared with the EndoFree Plasmid Maxi Kit according to the manufacturer's instructions.

3.1.4 Test digest and sequencing

Cloned plasmids were checked by digesting the plasmid with appropriate restriction enzymes for 1 h at 37°C and additionally verified by sequencing (Eurofins Genomics).

3.1.5 Protein purification from bacteria

To purify proteins from bacteria, a transformed colony of BL21 bacteria was incubated in 40 ml of LB-medium with Ampicillin overnight at 37°C in a thermoshaker. The next day, 460 ml of

LB-medium with Ampicillin was added and further incubated until the optical density of 0.5-0.7 was reached. Protein induction was initiated by adding 0.1 mM of IPTG. 4 h later, bacteria were pelleted by centrifugation. For protein purification, bacteria were resuspended in 10 ml of PBS with lysozyme (1 mg/ml) and proteinase inhibitor and incubated for 20 min followed by ultrasound sonication for 2 min at 20% amplitude in 10 sec intervals. Cell debris was removed by a one-hour centrifugation step and the remaining lysate was incubated with 1 ml of 50% glutathione agarose slurry at 4°C for 2 h on a rotator. The beads were washed 5 times in PBS supplemented with proteinase inhibitor and finally resuspended to a 50% solution in PBS and proteinase inhibitor. For elution of the GST-tagged protein from the glutathione agarose beads, bead-bound proteins were incubated with GST-Elution Buffer for 1 h at 4°C. The eluate was saved and the elution step was repeated three times to maximize the elution efficiency. Protein concentrations were determined by Coomassie staining using a BSA standard.

3.2 Cell culture

Human embryonic kidney cells (HEK293T) and cultured cortical neurons were kept at 37°C with 5% CO_2 in a humidified incubator.

3.2.1 HEK293T cell cultivation and transfection

HEK293T cells were cultured in Dulbecco's Modified Eagle's Medium (DMEM) with pyruvate that was supplemented with 10% fetal bovine serum (FBS) and 1% penicillin/streptomycin (P/S). Cells were split every 2-3 days by washing with PBS and detaching cells with trypsin. For transfection, $1.5x10^6$ cells were seeded into 100 mm dishes. The following day, the medium was changed to Iscove's Modified Dulbecco's Medium (IMDM) supplemented with 5% FBS. 4 to 5 h later, transfection was performed using the calcium phosphate transfection method according to Table 6. For co-transfection of plasmids, the molar ratio of plasmids was calculated based on the length of the plasmids in a way that a total amount of 10 µg DNA was transfected. 48 h after plating, the medium was changed to DMEM (+ FBS + P/S), and 72 h after plating, the cells were harvested. To prepare recombinant adeno-associated virus (rAAV) crude viral extracts or purified virus, packaging plasmids were co-transfected with the respective expression plasmid according to Table 6.

Table 6: Transfection of HEK293T cells in 100 mm cell culture dishes.

Transfection mixture:			Transfection mixture for rAAV preparation:		
1.1	ml	H_2O	1	ml	H_2O
145	µl	$CaCl_2$ (2.5 M)	145	µl	$CaCl_2$ (2.5 M)
10	µg	Expression plasmid	11	µg	pFΔ6 VP179
1.6	ml	2x HEBS (50 mM HEPES, 280 mM NaCl, 1.5 mM Na_2HPO_4; pH 7.05)	2.64	µg	pNLrep / pRV1 VP180
			2.64	µg	pH21 VP181
			5.5	µg	Expression plasmid
			1.2	ml	2x HEBS

3.2.2 rAAV preparation

To prepare crude viral extracts or purified rAAVs, HEK293T cells were seeded into 100 mm cell culture dishes and transfected as described in section 3.2.1. For crude viral extract preparation, cells were harvested on day *in vitro* (DIV) 4, pelleted, and dissolved in 500 µl PBS. After three freeze-and-thaw cycles of 5 min each, cell debris was pelleted by centrifugation and the supernatant was collected to transduce cells. 5 µl were used to transduce a 24-well of cultured cortical neurons while 20 µl were used for one well of a 6-well plate. For purified rAAVs, cells were lysed by 0.5% sodium deoxycholate and 50 U/ml benzonase endonuclease. To purify and concentrate the virus, HiTrap heparin columns and Amicon Ultra Centrifugal filters were used as described in (van Loo et al., 2012).

3.2.3 Lentivirus preparation

For preparing lentiviruses, HEK293T cells were cultured in GlutaMAX-DMEM supplemented with 10% FBS and 300 µg/ml G418. Around $3x10^6$ cells were seeded in GlutaMAX-DMEM with 10% FBS in 100 mm cell culture dishes and three dishes were used per lentiviral construct. The next day, a DNA mixture and a transfection mixture were prepared, incubated for 5 min at room temperature, and then combined (Table 7). After a further incubation of 20 min, 3 ml of the combined DNA transfection mixture were added to the cells. On DIV3, cells were washed once with medium and then further incubated in fresh medium. On DIV6, lentiviruses were harvested. The supernatant of the transfected cells was filtered through a 0.45 µm PVDF filter, combined with 300 µl 60% OptiPrep Density Gradient Medium, and ultracentrifuged for 2 h with 24000 rpm at 4°C. The virus formed above the OptiPrep medium phase and was resuspended in TBS-5 (50 mM Tris-HCl, pH 7.8, 130 mM NaCl, 10 mM KCl, 5 mM $MgCl_2$). After another ultracentrifugation round for 2 h with 24000 rpm at 4°C, the pelleted virus was dried and incubated with 50 µl TBS-5 overnight at 4°C. The next day, the pellet was

resuspended, cell debris was removed by short centrifugation, and the virus was used for neuron transduction.

Table 7: Transfection of HEK293T cells for lentivirus preparation.

DNA mixture:			**Transfection mixture:**		
4.5	ml	GlutaMAX-DMEM without FBS	4.5	ml	GlutaMAX-DMEM without FBS
22.5	µg	psPAX2 (packaging plasmid)	120	µl	GenJet Plus DNA *in vitro*
15	µg	pMD2.G (VSV-G envelope-expressing plasmid)			Transfection Reagent
10	µl	Expression plasmid			

3.2.4 Preparation of cultured cortical neurons

Primary cultured cortical neurons were isolated from mouse embryos on E16-19 as described before (Zürner et al., 2011). Cells were plated at a density of 30000 cells on poly-D-lysine coated coverslips in a 24-well plate or at a density of 300000 cells per well in a 6-well plate in Basal Medium Eagle (BME) or Neurobasal Medium supplemented with B27 and L-glutamine (NB+). Neurons were transduced with crude viral extracts or lentivirus at DIV3-6 and harvested or fixed at DIV14-15.

3.3 Biochemical methods

3.3.1 Immunocytochemistry

Primary cortical neurons that were plated on coverslips in BME were transduced with 5 µl of crude viral extracts expressing hrGFP or shSlk-hrGFP. At DIV14, neurons were fixed with 4% paraformaldehyde (PFA) for 10 min. After three washing steps with PBS, cells were incubated with 0.3% TritonX-100 in PBS for 10 min, followed by incubation with blocking solution (1% BSA, 10% NGS, 1% TritonX-100 in PBS) for 2 h. Primary antibodies were diluted in blocking solution and incubated overnight at 4°C on a shaking platform. The following day, cells were washed three times with PBS and incubated with secondary antibodies in blocking solution for 1 h. After the final three washing steps with PBS, the coverslips were mounted with mowiol. A list of all used primary and secondary antibodies including the dilution factor can be found in the Appendix in Table 23 and Table 24.

3.3.2 CoIP with cell-expressed proteins

For CoIP experiments followed by immunoblotting, HEK293T cells were seeded into 100 mm dishes and transfected as described in section 3.2.1. Plasmids expressing mSlk and the respective GFP-tagged protein of interest were co-transfected in a molar ratio. On DIV4, cells

were washed in Dulbecco's Phosphate Buffered Saline (DPBS) and harvested in 300 µl of lysis buffer (50 mM HEPES, 150 mM NaCl, 1% TritonX-100, proteinase inhibitor). After an hour of incubation at 4°C on a rotator, the cell debris was removed by centrifugation. An aliquot of the supernatant was kept as input control and the remaining supernatant was added to 30 µl of GFP-Trap magnetic agarose beads. The beads were incubated with the protein lysate at 4°C for 2 h on a rotator before non-binding proteins were removed by 5 washing steps with CoIP Wash Buffer (25 mM Tris, 150 mM NaCl, 1 mM EDTA, 1% TritonX-100, 5% Glycerol; pH 7.4). After a final washing step with PBS, the magnetic beads were resuspended in 20 µl of DPBS, 6x Laemmli Buffer (375 mM Tris-HCl, 9% SDS, 50% Glycerol, 0.03% Bromophenol Blue; pH 6.8, 10% β-Mercaptoethanol) was added and the purified proteins were boiled at 95°C for 5 min. The bead-purified proteins were entirely loaded on an SDS-PAGE (sodium dodecyl sulfate-polyacrylamide gel electrophoresis) for immunoblotting together with 1% of the input.

3.3.3 CoIP with whole-brain lysate

To identify proteins that are binding to Slk, a CoIP reaction was performed with Slk purified from HEK293T cells and whole-brain lysate. The whole-brain lysate was prepared as described before (Gleichman et al., 2012). Briefly, 15-30-week-old C57BL/6 mice were decapitated and the brain was isolated. The brain was dissected in 5 ml of lysis buffer (100 mM Tris-HCl, 150 mM NaCl, 1 mM EDTA, 1% TritonX-100, 1% sodium deoxycholate, 1% N-octyl-β-D-glucopyranoside; pH 6.5 supplemented with protease inhibitor) per g of brain weight. The tissue was further mechanically dissociated with a Polytron homogenizer and a tissue grinder followed by a 3 h incubation at 4°C on a rotator. To remove cell debris, the lysate was centrifuged at 7000 g for 15 min at 4°C and ultra-centrifuged for another 30 min at 70000 g at 4°C. The supernatant was used as whole-brain lysate for CoIP experiments. To purify Slk and its respective controls, six 100 mm cell culture dishes of HEK293T cells were transfected with 10 µg of pLenti-Ef1α-mCherry-T2A-HA or pLenti-Ef1α-mCherry-T2A-mSlk-HA with the calcium phosphate method. Cells were washed with DPBS and harvested in 300 µl of lysis buffer (50 mM HEPES, 150 mM NaCl, 1% TritonX-100; pH 7.4, protease inhibitor). After 1 h of incubation at 4°C on a rotator and subsequent centrifugation to remove cell debris, an aliquot of the supernatant was taken as input control and the remaining supernatant was added to 20 µl / dish of Pierce Anti-HA magnetic beads. The beads were incubated with the lysate for 2 h at 4°C on a rotator and then washed twice with low salt buffer (50 mM HEPES, 100 mM NaCl, 0.5% TritonX-100; pH 7.4), twice with high salt buffer (50 mM HEPES, 500 mM NaCl, 0.5% TritonX-100; pH 7.4), twice with low salt buffer (50 mM HEPES, 100 mM NaCl, 0.5% TritonX-100; pH 7.4), and twice in DPBS. 650 µl of the whole-brain lysate (approximately 5 mg/ml protein concentration) was added to the beads and incubated overnight at 4°C on a rotator. The next day, beads were washed 5 times with CoIP Wash Buffer (25 mM Tris, 150 mM

NaCl, 1 mM EDTA, 1% TritonX-100, 5% Glycerol; pH 7.4) and once with DPBS before they were resuspended in DPBS and 6x Laemmli buffer (375 mM Tris-HCl, 12% SDS, 30% Glycerol; pH 6.8, 10% β-Mercaptoethanol) and boiled for 5 min at 95°C.

3.3.4 Coomassie for mass spectrometry

Samples from the CoIP experiments or the *in vitro* kinase reactions were loaded onto NuPAGE 4-12% Bis-Tris polyacrylamide gels and run in NuPAGE MOPS SDS running buffer. Gels were stained in colloidal Coomassie Brilliant Blue (RotiBlue) solution overnight (CoIP experiments) or for 10 min (*in vitro* kinase reaction) and destained with H_2O. Specific protein bands or the whole lane of proteins were cut with a sterile scalpel and subjected to mass spectrometry analysis.

3.3.5 Coomassie and Western Blot

If no subsequent mass spectrometric analysis was planned, proteins were separated on polyacrylamide gels that consisted of a resolving (6, 10, or 12%) and a 5% stacking gel. Gels were run for 3 h at 70 and 100 mA and either incubated in Coomassie solution to stain all proteins or transferred onto nitrocellulose membranes overnight at 45 mA to stain specific proteins. Membranes were blocked in 2% gelatin from cold-water fish skin in PBS for 1 h. For Grlf1 and phosphorylated Grlf1 (pGrlf1) incubation, 5% BSA in TBST was used as blocking solution. For BioID experiments, immunoblots were blocked in 2.5% BSA + 0.4% TritonX-100 in PBS. Afterward, they were incubated with the primary antibody in blocking solution for 2 h, washed three times with PBST (PBS + 0.1% Tween), and incubated with secondary antibodies for 1 h. After washing 3 times with PBST, membranes were imaged on an Odyssey imaging system. β-actin primary antibodies were co-incubated with the other primary antibody whereas for all other co-stainings, primary antibodies were incubated subsequently. Coomassie-stained gels and immunoblots were visualized and quantified with the ImageStudio and ImageStudioLite Software.

3.3.6 *In vitro* kinase reactions

For *in vitro* kinase reactions, 5 / 10 µg (5 µg for initial tests, 10 µg for final mass spectrometric analysis of Mink1, Tnik, Map4k4, Shisa7) of the GST-tagged protein or the positive control histone H3 were incubated with 50 µM of UltraPure ATP and 100 ng of full-length human Slk in 1x Kinase Assay Buffer III (reagents from Slk kinase enzyme system) at 30°C for 30 min with mixing every 10 min. To assess phosphorylation with the ADP-Glo Kinase Assay, 25 µl of ADP-Glo Reagent were added to one kinase reaction and incubated for 40 min at room temperature to deplete the remaining ATP of the reaction and convert the produced ADP into ATP. Subsequently, 50 µl of Kinase Detection Reagent were added and incubated for another

30 min. In this step, the produced ATP was used in a luciferase/luciferin reaction. The luminescence was measured with the Kinase Glo protocol of a GloMax 96 Microplate luminometer with an integration time of 0.5 sec and a delay to measurement of 2 sec.
For mass spectrometric analysis of the proteins, the proteins were denatured at 95°C for 5 min in 6x Laemmli buffer after the kinase reaction and then separated by SDS-PAGE as described in section 3.3.4. After colloidal Coomassie staining, bands were excised and analyzed by mass spectrometry.

3.4 Mass spectrometric experiments

3.4.1 Phosphoproteomics

For whole-cell phosphoproteomics analysis, primary cortical neurons were seeded at a density of 300000 cells/well in a 6-well plate. At DIV3-5, cells were transduced with 5 µl of lentivirus expressing pLVTHM-Ef1α-mRFP-H1-MCS and pLVTHM-Ef1α-mRFP-H1-shSlk or pLenti-Ef1α-mCherry and pLenti-Ef1α-mCherry-T2A-mSlk. At DIV14-15, cells were washed in DPBS, and harvested in lysis buffer (2% SDS, 50 mM Tris-HCl pH 7.4, 2 mM EGTA, 2 mM EDTA, cOmplete Protease Inhibitor Cocktail, 2 mM PMSF, 5 mM NaF, 2 mM β-Glycerophosphate, Phosphatase Inhibitor Cocktail II, PhosSTOP). The lysate was frozen on dry ice and then placed at 85°C for 10 min. After cooling the samples to room temperature, they were sonicated for 3x 10 sec with high, 3x 10 sec with low, and 3x 10 sec with high intensity. An aliquot was taken for immunoblot analysis and the remaining sample was lyophilized. Protein samples were labeled with tandem mass tag (TMT) 10-plex reagents, phosphopeptides were enriched by the TiSH method, and peptides were prepared for liquid chromatography-tandem mass spectrometry (LC-MS/MS) by a Q Exactive Plus hybrid quadrupole-orbitrap mass spectrometer as described before (Müller et al., 2022) by Mark Graham at the Children's Medical Research Institute in Westmead, Australia.
Briefly, to analyze the phosphorylation of neuronal proteins, the lyophilized samples were rehydrated with 100 µl of 10 mM TCEP. After heating the samples to 85°C for 10 min, 20 mM iodoacetamide was added and incubated for 30 min at 22°C. Proteins were precipitated by the chloroform-methanol-water protocol (Wessel and Flügge, 1984) and dried at 37°C for 1 h. Subsequently, proteins were cleaved by 4 µg of lysyl endopeptidase in 24 µl of 7.8 M Urea in 50 mM HEPES at pH 8.0 and incubated at 25°C for 8 h. Peptide digestion was performed in HEPES/NaOH pH 8.0 with 4 µg of trypsin for 4 h at 37°C. Peptide concentrations were determined by a nanophotometer measuring the absorption at 280 nm. 100 µg of peptides were tagged using TMT 10-plex reagents according to the manufacturer's instructions. The five replicates of the control and Slk knockdown condition were processed together and treated with formic acid. After vacuum concentration, samples were diluted in 1 ml of 0.1% trifluoracetic

acid followed by desalting through a Sep-Pak tC18 3 cc Vac Cartridge. The eluted volume was reduced and then dissolved in 1 M glycolic acid, 5% trifluoroacetic acid, and 80% acetonitrile. Phosphopeptides were enriched using the TiSH method followed by hydrophilic interaction chromatography fractionation with a 5 µm TSKGel Amide 80 resin leading to the collection of multi-site phosphopeptides in a single fraction and the collection of mono-phosphorylated peptides into eighteen fractions (Engholm-Keller et al., 2019).

Reversed-phase chromatography was applied with an UltiMate 3000 RSLCnano system using a 300 x 0.075 mm ReproSil Pur C18 AQ 1.9 µm resin column. Chromatography was performed at a flow rate of 250 nl/min with a column temperature of 50°C with Buffer A (0.1% formic acid) and Buffer B (0.1% formic acid, 90% acetonitrile, 9.99% H_2O; gradient: 5-25%: in 69 min, to 35%: in 8 min, to 99%: in 3 min). A Q Exactive Plus Hybrid Quadrupole-Orbitrap mass spectrometer was used with the Nanospray Flex ion Source spray at 2.3 kV, the capillary temperature at 250°C, and the S lens radio frequency level at 60. The MS scan was conducted with a resolution of 70000 full width at half maximum (m/z: 375-1500, automatic gain control target: 1000000 counts, maximum ion time: 100 msec). For MS/MS scans, maximal 11 ions exceeding 46000 counts were measured with a resolution of 35000 full width at half maximum (maximum ion time: 120 msec, automatic gain control target: 20000 counts, isolation window: 1.2 units of m/z scale, fixed first mass: m/z: 120, normalized collision energy: 34). Peptides that were charged < 2+ or > 8+ or had no assigned charge were dynamically excluded (20 sec). Additionally, around 2 µg of the non-phosphorylated (not binding to titanium dioxide) peptides were analyzed by LC-MS/MS (gradient: 5-28% buffer B in 126 min, to 35% in 10 min, to 99% in 3 min; > 50000 counts for maximum ion time: 110 msec selected for MS/MS; dynamic exclusion: 30 sec).

The raw LC-MS/MS data were analyzed with the MaxQuant v1.5.8.3 software (Tyanova et al., 2016) using the default settings (protease specificity: Trypsin/P; missed cleavages: up to 3; fixed modification: carbamidomethyl (C); variable modifications: deamidation (N, Q), oxidation (M), acetylation (protein N-termini), and phosphorylation (S, T, Y); with max. 5 modifications per peptide; minimum score for modified peptides: 40; minimum peptide length: 6; maximum peptide mass: 7000 Da). As a reference file, the fasta file of the mus musculus reference proteome was downloaded from UniProtKB (released 07/2017, 60205 entries including different protein isoforms). Together with the default contaminants file, a reversed sequence database was created to assess the false discovery rate. The false discovery rate for peptide spectrum match, protein, and modification site was set to 1%, and the same rate was applied to the dependent peptide search. All modified peptides and their respective non-modified peptides were excluded from further quantification. A second peptide search was applied with a tolerance for MS and MS/MS spectra of 4.5 ppm and 20 ppm, respectively.

3.4.2 Mass spectrometric identification of biotinylated proteins in neurons

Primary cortical mouse neurons were cultured with a density of 300000 in a 6-well plate in NB^+ medium. At DIV5-6, they were transduced with lentiviruses expressing pLenti-Ef1α-mCherry-T2A-mSlk-HA or pLenti-Ef1α-mCherry-T2A-mSlk-myc-BirA*. After the addition of 50 µM biotin for 24 h at DIV13-14, cells were washed, harvested in DPBS, pelleted, and frozen in liquid nitrogen. An aliquot was kept for immunoblotting experiments to verify successful protein expression and biotinylation.

The pellets were resuspended in 1 ml of lysis buffer (50 mM Tris-HCl pH 7.4, 500 mM NaCl, 2% TritonX-100, 0.4% SDS, 5 mM EDTA, 1 mM DTT, cOmplete Protease Inhibitor Cocktail) and sonicated with an Ultrasonics Sonifier (2 mm tip, up to 1 min, 60% amplitude). After a one-hour incubation on a shaker at 4°C, samples were centrifuged for 30 min with 20000 g at 4°C. After measuring protein concentrations with the Bio-Rad DC Protein assay, 1 mg of the cell lysate was added to 75 µl of streptavidin beads that were pre-washed three times with lysis buffer. The next day, the beads were washed with different buffers for 10 min each (2x Wash Buffer 1: 2% SDS in 50 mM HEPES pH 7.5; 1x Wash Buffer 2: 0.1% sodium deoxycholate, 1% TritonX-100, 500 mM NaCl, 1 mM EDTA, 50 mM HEPES pH 7.5; 1x Wash Buffer 3: 250 mM LiCl, 0.5% NP-40, 0.5% sodium deoxycholate, 1 mM EDTA, 10 mM Tris-HCl pH 8.1; 2x Wash Buffer 4: 50 mM NaCl, 50 mM Tris-HCl pH 7.5). Reduction and alkylation of the proteins were performed on beads by adding 300 µl of 10 mM DTT dissolved in 100 mM HEPES at 56°C for 30 min, 300 µl of 25 mM acrylamide for 30 min at RT, and 300 µl of 10 mM DTT for 10 min at room temperature. Proteins were digested overnight with 2.5 µg trypsin/mg input protein in 300 µl of 100 mM HEPES pH 8 at 37°C on a shaker. By adding 300 µl of 5% acetonitrile and 0.1% formic acid twice, peptides were eluted from the beads.

After adjusting the volume of the samples to 100 µl and the acetonitrile content to < 1%, the peptides were labeled with dimethyl as described before (Boersema et al., 2009). In short, 16 µl of 4% (v/v) formaldehyde solution (control: light = CH_2O; mSlk-BirA*: medium = CD_2O) and 16 µl of 0.6 M sodium cyanoborohydride $NaBH_3CN$ were added to each sample. After 1 h incubation with 700 rpm at room temperature, the reaction was quenched with 64 µl of 1% (v/v) NH_4OH for 15 min at room temperature. To acidify the peptides, 32 µl formic acid was added and the samples were combined and desalted with Oasis HLB cartridges. Samples were dried in a vacuum centrifuge and fractionated with a 3100 OFFGEL fractionator (12 fraction setup, no addition of glycerol to buffers, pI range: 3-10, 20 kVh) according to the manufacturer's instructions after rehydrating the IPG strips and resolubilizing the sample in 1.8 ml IPG buffer. Individual fractions were transferred to microtubes, the extraction of each well was performed by 150 µl of 0.1% trifluoroacetic acid, and finally combined with the respective fractions. To desalt the samples, C_{18} StageTips were used as described before (Rappsilber et al., 2003). Therefore, the pressing of 6 small discs of C_{18} material into 200 µl pipette tips was followed by

placing the tips into miniprep columns with pierced holes in 2 ml microtubes. Activation of C_{18} material was achieved by adding 20 µl methanol and 20 µl buffer B (80% acetonitrile, 0.5% AcOH) and washing with 20 µl of buffer A (0.5% AcOH in HPLC-water). While for OFFGEL fractionated samples, 300 µl of 0.1% trifluoroacetic acid containing the peptides were applied on the stage tips and centrifuged at 2000 g for 2 min, 20 µl of 5% acetonitrile and 5% of formic acid were added to other peptide samples, they were sonicated for 5 min and the volume was adjusted to 100 µl with HPLC-water followed by centrifugation for 2 min at 2000 g. After washing the stage tips with 100 µl of buffer A, 20 µl of buffer B was added twice to elute the peptides. Drying of the eluate in a vacuum centrifuge at 60°C was followed by resuspending the sample in 20 µl of 5% acetonitrile and 5% formic acid. A final sonification step in an ultrasonic water bath for 5 min and centrifugation for 15 min at 20000 g preceded the mass spectrometric analysis. Samples were loaded on a nano-UHPLC-Dionex Ultimate 3000 system (flow rate: 600 nl/min in 95% solvent A (0.1% formic acid) and 5% solvent B (90% acetonitrile + 0.1% formic acid), peptide separation: 230 min linear gradient: 5-35% solvent B, flow rate: 300 nl/min) coupled to an Orbit Fusion Lumos mass spectrometer (settings: m/z: 375-1500, automatic gain control: standard, maximum ion injection time: 54 msec). To fragment precursor ions, higher collision dissociation with dynamic exclusion of 60 sec was used with MS2 scans being set to rapid scan mode. The raw files were mapped against Uniprot/Trembl mouse (released 06/2019, 17019 entries) in MaxQuant 1.6.5.0 (enzyme specificity: trypsin; missed cleavages: up to 2; initial mass tolerance: ±20 ppm; final mass tolerance: ±9 ppm for precursor masses, ±0.5 Da for fragment ions; fixed modification: propionamide (cysteine); variable modifications: oxidation (methionine), and acetylation (protein N-termini); false discovery rate: 1%). The identification of biotinylated proteins was performed by Shiva Ahmadi.

3.4.3 Mass spectrometric analysis of co-immunoprecipitated proteins

Gel slices that were cut from the Coomassie gels were digested as described before (Rosenfeld et al., 1992; Jenö et al., 1995). Briefly, the slices were washed with H_2O, 50% acetonitrile, and subsequently 100% acetonitrile. After reducing the proteins with 20 mM DTT in 50 mM ammonium bicarbonate and alkylation with 40 mM acrylamide (in 50 mM bicarbonate), the slices were washed and dehydrated with acetonitrile. Subsequently, proteins were digested with 330 ng of trypsin (sequencing grade) at 37°C overnight before drying the peptide extracts in a vacuum concentrator and storing them at -20°C.

The peptides were re-dissolved in 10 µl of 0.1% formic acid (solvent A) and peptides were separated on a Dionex Ultimate 3000 RSLC nano HPLC system with the autosampler being used in µl-pickup mode. After injecting 2 µl onto a C18 analytical column (350 mm length, 75 µm inner diameter, ReproSil-Pur 120 C18-AQ, 1.9 µm), peptides were separated within 60 min on a linear gradient from 5% to 35% of 90% acetonitrile with 0.1% formic acid (solvent

B) at 300 nl/min. An Orbitrap Fusion Lumos mass spectrometer was directly coupled online to the nano HPLC. Data were acquired by scanning ions between 330 and 1600 m/z in the Orbitrap detector every 2 sec (resolution: 120000, gain control target: 400000). The internal calibration was performed with polysiloxane (m/z 445.12002). Using a top-speed method, ions were fragmented by higher energy collision-induced dissociation (1.0 Da isolation, threshold intensity: 25000, collision energy: 30%) and fragments were analyzed in the Orbitrap (R: 15000) with gain control target 50000 and maximum inject time 22 msec. For 15 sec, fragmented peptide ions were excluded from repeat analysis. Raw data were processed and analyzed with Proteome Discoverer software 2.5.0.400. Peptides were identified with an in-house Mascot server version 2.6.1 from Proteome Discoverer. Proteins were identified and classified in MS2 data using a database of common contaminants (cRAP of the Global Proteome Machine) and the murine SwissProt sequences of Uniprot (released 03/2021, 17089 sequences). Search settings included a precursor Ion m/z tolerance of 10 ppm and a fragment ion tolerance of 20 mmu (tryptic peptides; missed cleavages: up to 2; static modification of cysteines: propionamide; dynamic modifications: oxidation of methionine and acetylation of protein N-termini). Mascot results were further analyzed with the Percolator algorithm version 3.05 (Proteome Discoverer 2.5) (Käll et al., 2008). A second search was performed for spectra without high confident matches (q-value > 0.01) with semi-specific enzyme cleavage, dynamic modification of cysteines with propionamide, and serines/threonines with phosphate. The calculation of abundances was based on the sum of the areas of unique peptides extracted ion chromatograms. The mass spectrometric analysis was performed in the Mass Spectrometry Core Facility of the University of Bonn by Marc Sylvester.

3.4.4 Mass spectrometric analysis of protein phosphorylation after *in vitro* kinase reactions

Gel slices that were excised from the Coomassie gels were in-gel digested as described above in section 3.4.3. For further processing, extracts were dissolved in solvent A (10 µl 0.1% formic acid) and peptides were separated by a Dionex Ultimate 3000 RSLC nano HPLC system operated in the µl-pickup mode. To avoid losing phosphopeptides due to metal ion binding, the LC-MS system was passivated with three citrate injections (Winter et al., 2009). 2 µl of the peptides were injected on a C18 analytical column (350 mm length, 100 µm inner diameter) and peptides were separated on a linear gradient in 5-35% solvent B (90% acetonitrile, 0.1% formic acid) at 300 nl/min within 60 min. The nano HPLC was coupled online to an Orbitrap Fusion Lumos mass spectrometer, which was used for data-dependent acquisition (330-1600 m/z, scanned every 3 sec, resolution: 120000, gain control target: 400000, maximum inject time: 50 msec). For internal calibration, polysiloxane with an m/z of 445.12002 was used. Fragmentation of peptides was performed using higher-energy collision-induced dissociation

(1.0 Da isolation, threshold intensity: 30000, collision energy: 27%) and fragments were analyzed with a gain control target of 50000 and maximum inject time of 54 msec. If phospho-specific neutral loss was detected (97.9769 Da), an additional electron-transfer/higher-energy dissociation fragment spectrum was measured (1.0 Da isolation, threshold intensity: 30000, R: 30000, gain control target: 100000, maximum inject time: 54 msec). Fragmented peptide ions were excluded for 20 sec from the repeat analysis. Raw data were processed and analyzed in Proteome Discoverer software 2.5.0.400 using an in-house Mascot server version 2.6.1. MS2 data were compared to a database of common contaminants (cRAP of Global Proteome Machine) and a custom database that included the sequences of the cloned recombinant GST-tagged proteins (precursor ion m/z tolerance: 10 ppm; fragment ion tolerance: 20 ppm; tryptic peptides with up to 2 missed cleavages; static modification: propionamide; dynamic modification: oxidation of methionine, phosphorylation of serine and threonine, acetylation of protein N-termini). With the Target Decoy PSM Validator node, the spectrum confidence of the Mascot results was assessed (selection: concatenated, target FDR strict/relaxed: 0.01/0.05). Phosphorylation sites were localized using the IMP-ptmRS node while extracted ion chromatogram areas of peptides were calculated with the Minora Feature detector (default settings). To calculate protein abundance, unique peptides excluding phosphorylation peptides were summed and the abundance was normalized on the individual protein used in the respective experiment. Protein ratios were calculated with the pairwise-ratio-based method and differentially regulated proteins/peptides were detected with the background-based t-test method implemented in Proteome Discoverer. The mass spectrometric analysis was performed in the Mass Spectrometry Core Facility of the University of Bonn by Robert Hardt.

3.5. Animal experiments

All animal experiments were planned and performed in accordance with the 3R principle (replacement, reduction, refinement) and with the guidelines of the University of Bonn Medical Center Animal Care Committee and approved by the European Directive (2010/63/EU) on the protection of animals used for experimental purposes and ARRIVE guidelines. Mice were housed in a 12 h day/night cycle, in an environment controlled for humidity (55 $\pm$ 10%) and temperature (22 $\pm$ 2°C), with food and water ad libitum and nesting material. Mice were allowed to adapt to the animal facility before any treatment.

3.5.1 *In utero* electroporation

CD1 female mice were timely mated with C57BL/6 male mice and pregnant females were selected for IUE. DNA plasmids were *in utero* electroporated into CD1/C57BL/6 wild-type mice at E14.5 as described in (Szczurkowska et al., 2016).

The time-pregnant mice were anesthetized with isoflurane inhalation and injected with analgesics preoperatively (0.05 mg/kg buprenorphine and 5 mg/kg ketoprofen). The abdomen was opened and the uterus exposed. 1 µl of DNA (1.5 µg/µl) that was visualized with FastGreen (1 mg/ml) was injected into the lateral ventricles of each embryo with a glass capillary connected to a microinjector (Picospritzer). To insert the DNA into cortical progenitor cells in the motor and somatosensory cortex, 5 electric pulses with a duration of 50 msec with a 950 msec long break in between were administered via a triple-electrode using a CUY21SC Square Wave Electroporator with a voltage of 30 V.

3.5.2 Viral injections

30 to 32 days after birth, the electroporated mice were injected with a rAAV (Schoch et al., 2021). Briefly, the mice were injected with analgesics (5 mg/kg ketoprofen) and anesthetized (0.05 mg/kg fentanyl, 5 mg/kg midazolam, 0.5 mg/kg medetomidine) and holes were drilled at 1 mm posterior, -0.9/0.9 mm lateral and 1.5 mm ventral (relative to bregma). 300 nl virus were injected into both hemispheres at 3 depths (1.5/1/0.5 ventral) with a rate of 200 nl/min with a 10 µl Hamilton syringe connected to a microprocessor-controlled mini-pump. After 5 min, the needle was removed and the injection site closed. On P74, mice were sacrificed by intracardiac perfusion with 4% PFA, 150 µm thick coronal brain sections were cut on a vibratome, and the dendrite morphology was analyzed with confocal imaging.

3.5.3 Telemetric EEG and video monitoring

For telemetric EEG and video monitoring, telemetric transmitters (TA10ETA-F20) were subcutaneously implanted on the abdominal side of the animals as described before (Becker et al., 2008; Pitsch et al., 2007) and electrodes were placed in the center of the electroporated cortex which was identified based on the expression of hrGFP detected with a Dual Fluorescent Probe Flashlight Set. Therefore, *in utero* electroporated mice were treated with analgesics (5 mg/kg ketoprofen) and anesthetized (0.05 mg/kg fentanyl, 5 mg/kg midazolam, 0.5 mg/kg medetomidine) at P68-78. The reference electrode was attached above the cerebellar cortex (-6 mm posterior, 0 mm lateral, 0 mm ventral) with a stainless-steel screw. All animals received analgesic treatment after every surgery (5 mg/kg ketoprofen for 3 days). The EEG was recorded continuously with a 1 kHz sampling rate and analyzed with the NeuroScore v2.1 software by fast-Fourier transform power spectral analysis including five frequency bands (δ (0.5–4 Hz), θ (4–8 Hz), α (8–13 Hz), β (13–30 Hz), and γ (30–40 Hz)) (Pitsch et al., 2017, 2012; Becker et al., 2008). The analysis of the EEG and video monitoring was conducted by Julika Pitsch. Mice were sacrificed at P95-106 and brains were isolated after intracardiac perfusion of 4% PFA.

3.5.4 Multi-well MEA recordings

In utero electroporated mice were decapitated in deep isoflurane anesthesia between P30 and P43 and the brain was isolated. 300 µm thick brain sections were prepared on a vibratome in ice-cold artificial cerebrospinal fluid (aCSF) with high glucose (87 mM NaCl, 2.5 mM KCl, 1.25 mM NaH_2PO_4, 7 mM $MgCl_2$, 2 mM $CaCl_2$, 26 mM $NaHCO_3$, 25 mM glucose, 75 mM sucrose; pH 7.4). Slices were incubated in aCSF with high glucose for 30 min at 35°C and further incubated at room temperature in aCSF (124 mM NaCl, 3 mM KCl, 1.25 mM NaH_2PO_4, 2 mM $MgSO_4$, 2 mM $CaCl_2$, 26 mM $NaHCO_3$, 10 mM glucose; pH 7.4) for 1 h. *In utero* electroporated hemispheres were separated and placed on the electrode grid (rectangle of 64 electrodes) in a 6-well CytoView plate. The hemispheres were weighted with platinum grids to avoid displacement and either aCSF (124 mM NaCl, 3 mM KCl, 1.25 mM NaH_2PO_4, 2 mM $MgSO_4$, 2 mM $CaCl_2$, 26 mM $NaHCO_3$, 10 mM glucose; pH 7.4) or $aCSF^{low\ Mg2+,high\ K+}$ (125 mM NaCl, 5 mM KCl, 1.25 mM NaH_2PO_4, 0.5 mM $MgSO_4$, 1.5 mM $CaCl_2$, 25 mM $NaHCO_3$, 10 mM glucose; pH 7.4) were added. The plate was placed in a MEA system at 26°C with 5% CO_2. After 5 min of adaptation, the spontaneous activity of the slices was recorded for 15 min in the Neural Spikes mode with a low pass filter of 3 kHz and a high pass filter of 200 Hz. To be able to correlate the electrical activity with the corresponding brain region, images were taken after each measurement with an epifluorescent microscope.

3.5.5 scRNAseq

For scRNAseq analysis, animals were *in utero* electroporated at E14.5 with pAAV-U6-MCS-CMV/CBA-hrGFP + pAAV-U6-MCS-CMV/CBA-mRFP or pAAV-U6-shSlk-CMV/CBA-hrGFP plasmids, and sacrificed at P30. The brain was removed and cut into 300 µm sections in ice-cold DPBS with a vibratome. The *in utero* electroporated area was micro-dissected under an epifluorescent microscope and the tissue was kept in ice-cold HBSS. The tissue was dissociated using the Neural Tissue Dissociation Kit (P) according to the manufacturer's instructions. Briefly, enzymatic dissociation with papain was combined with mechanic dissociation using a GentleMACS Octo Dissociator followed by filtration through a 70 µm filter. Myelin was removed using the Myelin Removal Kit by magnetic separation through LS columns. Finally, red blood cells were removed using Red Blood Cell Removal solution for 10 min at 4°C. After a washing step with DPBS, the cell pellet was resuspended in 10 µl HBSS. Cell viability and density were determined with a Countess 2 Automated Cell Counter. Cells were prepared for scRNAseq with the Chromium NextGEM Single Cell 3' GEM, Library & Gel Bead Kit v3.1, the Chromium Chip B Single Cell Kit, and the Chromium i7 Multiplex Kit according to the manufacturer's instructions. 2000 cells were aimed to be sequenced at a sequencing depth of 100000 reads per cell. The sequencing was performed with an S2 flow

cell on a NovaSeq6000 and the library preparation and sequencing were performed by André Heimbach at the Next Generation Sequencing Core Facility of the University of Bonn.

3.6 Analysis

3.6.1 Dendrite tracing with Imaris

150 µm coronal brain sections were imaged with a laser scanning Nikon A1/Ti confocal microscope with a CFI Plan APO 20x (NA 0.75) objective. Z-stacks with 1 µm step size were acquired and the dendritic tree of the neurons was traced with the Imaris software.
Confocal z-stack images of rAAV-transduced neurons were opened in Imaris and the dendrites were traced with FilamentTracer in the manual mode in 3D. The branch hierarchy was calculated with the XTension “Filaments Branch Hierarchy” where each dendrite branch is assigned to a dendrite branch order and the statistics for dendrite order, dendrite length, and the number of dendritic branches were exported. Sholl analysis was conducted by the Imaris Software. The number of Sholl intersections was defined as the number of intersections with concentric spheres that were spaced evenly by 1 µm.

3.6.2 Quantification of fluorescence intensity in synapses and dendrites

Cultured cortical neurons were imaged with a CFI Plan APO IR 60x WI (NA 1.27) objective of the Nikon A1/Ti or the PlanAPO 63x OI (NA 1.4) objective of a Zeiss LSM700 laser scanning confocal microscope, acquiring z-stacks with 5 steps and a step size of 0.3 µm. The fluorescence intensity at inhibitory synapses was quantified with Fiji. A maximum intensity projection of the z-stack images was generated, the background was subtracted (rolling ball radius: 1/3 of pixel width of image), and Gephyrin-positive regions of interest (ROIs) were automatically detected based on the intermode threshold of 30% of the maximum fluorescence intensity. Only ROIs with a size of 2-19 px^2 were included in the analysis. To account for potential experimental differences in the acquisition of the images, fluorescent beads (TetraSpeck Microspheres) were imaged in each session and the fluorescence intensity of each replicate was normalized to the fluorescence intensity of the fluorescent beads.
To analyze the Phalloidin and acetylated Tubulin intensity in dendrites of transduced neurons, the soma of the neuron was blackened in Fiji. A maximum projection was created, the background was subtracted as described for the synapse analysis and a mask of the hrGFP-expressing dendrites was created by applying a threshold of 10% of the maximum hrGFP fluorescence intensity. The fluorescence intensity was measured either in all detected dendrites or at different distances to the soma. Therefore, the fluorescence intensity was quantified in rings around the soma that were evenly spaced at 21 µm. As for the synapse

quantification, the fluorescence intensity values were normalized to fluorescent bead intensities.

3.6.3 MEA analysis

For the analysis of spiking activity in brain slices of control and shSlk *in utero* electroporated animals, the 64 electrodes of one well of the MEA plates were classified according to the slice region. Electrodes that were contacting the *in utero* electroporated region were classified as category 1 and those contacting the border of the *in utero* electroporated region were classified as 2. All other electrodes that were contacting the slice in non-*in utero* electroporated regions counted as category 3 while electrodes outside of the brain slice were excluded from the analysis. For one slice, the number of spikes or bursts was summed per category and normalized to the number of electrodes in that category. Additionally, the proportion of spikes and bursts in that category relative to all categories was calculated per slice. Only brain slices with all electrode categories were considered for the analysis. Spikes were defined by an adaptive threshold crossing method with the threshold set to 6 standard deviations of the baseline. If at least 5 spikes with a maximum inter-spike interval of 100 ms were detected, this was defined as a burst.

3.6.4 scRNAseq analysis

The raw data from the scRNAseq were aligned to the mouse reference genome in which the sequence for hrGFP was included to be able to identify electroporated cells. The Cell Ranger pipeline demultiplexed, mapped, and quantified the unique molecular identifiers (UMIs) to generate a raw count matrix. The conversion of the raw data to the count matrix was performed by Theodoros Georgomanolis at the Cologne Center for Genomics.

The subsequent pre-processing and downstream analysis were conducted with the package Seurat 3.2.1 in R version 3.6.3. For quality control, cells were filtered according to the number of UMIs (> 600) and genes (> 300). Cells in which more than 15% of all genes were mapped to mitochondrial genes were excluded as a high proportion of mitochondrial genes might be indicative of dying cells. The filtered data were normalized, variance stabilization was performed, mitochondrial gene expression was regressed out, and the 3000 most variable features were identified using scTransform. Integration of the two conditions (Control / Slk knockdown) was based on the 3000 most variable features. Cells were clustered with a graph-based clustering approach (k-nearest neighbor graph) with 40 dimensions and a resolution of 0.8. Clusters were collapsed and annotated based on known cellular markers that were extracted from Allen Brain Map and the Mouse Brain Atlas from the Linnarsson Lab. Markers were identified for each cluster based on differential expression analysis with the Wilcoxon Rank Sum test using a $\log_2$ transformed fold change ($\log_2$FC) threshold of 0.25. Differentially

expressed genes between control and the Slk knockdown condition were analyzed with the Wilcoxon Rank Sum test using the function FindMarkers. Visualization was performed via non-linear dimensional reduction using uniform manifold approximation and projection for dimension reduction (UMAP). In all graphs, the normalized count data was plotted.

3.6.5 Bioinformatic analysis of phosphoproteomics data

MaxQuant output files of the phosphoproteomics mass spectrometry screen were analyzed with phosphoprocessR version 0.99.8 in R version 3.5.1 as described previously (Müller et al., 2022). In short, after remapping the phosphorylation sites to the fasta file, each phosphorylated site +/-7 amino acids was used to create a centered peptide sequence. Only phosphopeptides with a site localization score > 0.75 (class I) for at least one site were used for further analysis while multi-phosphorylated peptides required a score > 0.5 for additional sites in a peptide with a class I site. In the case of multiple measurements for one phosphopeptide, all measurements were summarized by the median $\log_2$ transformed intensity. If measurements mapped to more than one unique protein identifier, a multi-mapped identifier was allocated. Complete data that had no missing values across replicates were normalized (quantile normalization) (Dudoit and Fridlyand, 2002) and unwanted variation was removed via surrogate variable analysis (Leek and Storey, 2007). This was followed by principal component analysis (PCA) and hierarchical clustering to analyze the effect of the normalization and the removal of unwanted variation. To compare phosphorylation in the control and Slk knockdown condition, differential phosphorylation analysis was performed by fitting the data to a generalized linear model using Bayes shrinkage with limma version 3.36.5 (Ritchie et al., 2015). Multiple comparison correction of p-values was done with the Benjamini and Hochberg method (Benjamini and Hochberg, 1995).

3.6.6 KinSwing analysis

Using KinSwingR version 1.1.4 (http://bioconductor.org/packages/KinSwingR/) (Engholm-Keller et al., 2019), kinase motifs and matches of kinase-substrate were analyzed as described before (Müller et al., 2022). Therefore, the position weight matrices (PWMs) of 160 kinases with minimally 10 published phosphopeptides were created (log-likelihood ratio of the average frequency of amino acid residues at each position divided by background frequency). Three PWMs that were centered on S, T, or S/T combined phosphorylation sites were modeled for Slk with the buildPWM function of KinSwingR using already published and curated substrates of Slk. The viewPWM function of KinSwingR modeled each position in the kinase motif and created it as a Shannon Entropy model. The coloring of the motif amino acids followed the Shapely scheme, assigning brighter colors to polar and duller colors to non-polar amino acids. Every kinase PWM was scored for each measured phosphopeptide by the scoreSequences

function of KinSwingR. The standardized weighted proportion of substrate matches to each kinase was calculated to assess kinase activity inference. To determine statistical significance, 1000 network perturbations of PWM:substrate edges were performed as described in http://bioconductor.org/packages/KinSwingR/.

3.6.7 Bioinformatic analysis of BioID data

Further analysis of MaxQuant output files for the BioID data was done in R version 3.5.1. Allowing maximally 25% of missing values for the experimental condition, data were subjected to log_2 transformation and quantile normalization. For imputation of missing values, the k-nearest neighbor approach (Ripley, 2014) as implemented in this package (https://www.rdocumentation.org/packages/class/versions/7.3-19/topics/knn) was used and batch effects were accounted for using ComBat (Johnson et al., 2007). With limma statistics followed by Benjamini and Hochberg correction, differences between the control and the experimental condition were calculated.

3.6.8 Bioinformatic analysis of CoIP data

Proteome Discoverer output files from the mass spectrometric analysis of the CoIP experiment were analyzed in R version 3.5.1. Before further analysis, proteins with more than 25% of missing data for the experimental condition and proteins without annotation or classified as contaminants were excluded from further analysis. For the data based on the single excised bands, values were log_2 transformed and imputation of missing values was performed by the left-censored missing data approach (QRILC, implemented in imputeLCMD: https://cran.rstudio.com/web/packages/imputeLCMD/index.html).
The log_2-ratios (experimental / control condition) were normalized with cyclic loess normalization (Ballman et al., 2004). For the data based on the excised whole lane, an additional batch correction step was performed with ComBat. Differences between the conditions were assessed with limma statistics combined with multiple hypothesis correction via the Benjamini and Hochberg method (as described above). Bioinformatic analysis of the mass spectrometry data was performed by Ashley J. van Waardenberg (i-Synapse, Australia).

3.6.9 Annotation analysis

Protein lists from the different proteomics approaches were annotated with the Functional Annotation Tool of the DAVID Bioinformatics Resources 6.8.
For gene ontology (GO) analysis, biological process (GOTERM_BP_DIRECT) and cellular component (GOTERM_CC_DIRECT) terms were analyzed with a threshold count of 2, a threshold EASE of 0.1, and a multiple-comparisons adjusted p-value (padj) according to Benjamini corrections. For analysis of synaptic gene ontologies, the SynGO resource was

used. For SynGO search, all annotations were included in the evidence filters and the GSEA settings were set to a minimum gene count per term of three.
Visualizations of protein networks were performed with STRING Database Version 11.5 (Szklarczyk et al., 2021).

3.6.10 Statistical analysis

Except for the scRNAseq and the proteomics data, statistical analysis was performed using GraphPad Prism 9.1.1. Chosen statistical tests are described in the figure legend of the respective experiment and a result was considered to be significant if the p-value was lower than 0.05 ($p < 0.05$). If not defined otherwise, data are presented as the mean and standard error of the mean (SEM). Log_2 transformed expression ratios (log_2FC) were always expressed as the ratio of experimental condition by control (experimental condition / Ctrl). For scRNAseq data, statistical testing was performed within Seurat 3.2.1 in R version 3.6.3. For the phosphoproteomics, BioID, and CoIP dataset, p-values were calculated by Ashley J. van Waardenberg with a moderated t-test and corrected for multiple comparisons by the Benjamini and Hochberg method (Benjamini and Hochberg, 1995) in limma version 3.36.5.

4 Results

4.1 Further characterization of Slk knockdown model

Knocking down Slk during embryonic development alters the arborization of the dendritic tree and the density of inhibitory synapses at different postnatal stages (Schoch et al., 2021), indicating that Slk critically influences neuronal morphology. However, it is not clear yet whether Slk expression is important at a particular developmental stage or whether constant expression of Slk is required to maintain neuronal structure and function. Since Slk is expressed in neuronal lineages during development as well as in cells in adulthood (Zhang et al., 2002), both scenarios would be conceivable.

4.1.1 No effect of Slk knockdown during adulthood on dendrite morphology

To address the question if Slk is needed during development for the initial formation of the neuron or the maintenance of neuronal morphology during postnatal stages, the effect of knocking down Slk in adulthood was investigated. Animals were *in utero* electroporated with Gephyrin-FingR-EGFP at E14.5 and injected at P30 with rAAV virus expressing control mRFP or shSlk-mRFP. After six weeks, the morphology of the dendrites and the inhibitory synapse density were assessed. However, no colocalization of the Gephyrin-FingR-EGFP electroporated neurons and virus-transduced neurons could be detected, suggesting that the virus did not infect cells that were previously *in utero* electroporated. This finding was confirmed by further unrelated experiments that were performed in the laboratory by colleagues (unpublished data). As a consequence, the effect of a late knockdown of Slk could only be assessed for the dendritic phenotype by this method (Fig. 8A). The neurons that were transduced by the virus were reconstructed (Fig. 8B) and the number of dendrites was analyzed for the different dendrite orders (Fig. 8C). No difference was detected between control and shSlk-transduced neurons. Additionally, Sholl analysis showed a similar branching of control and Slk knockdown neurons (Fig. 8D) across different distances toward the soma (data presented in (Schoch et al., 2021)).

Thus, we can conclude that Slk is important for proper dendritic arborization during developmental stages but its absence in adult cortical neurons does not induce dendritic alterations.

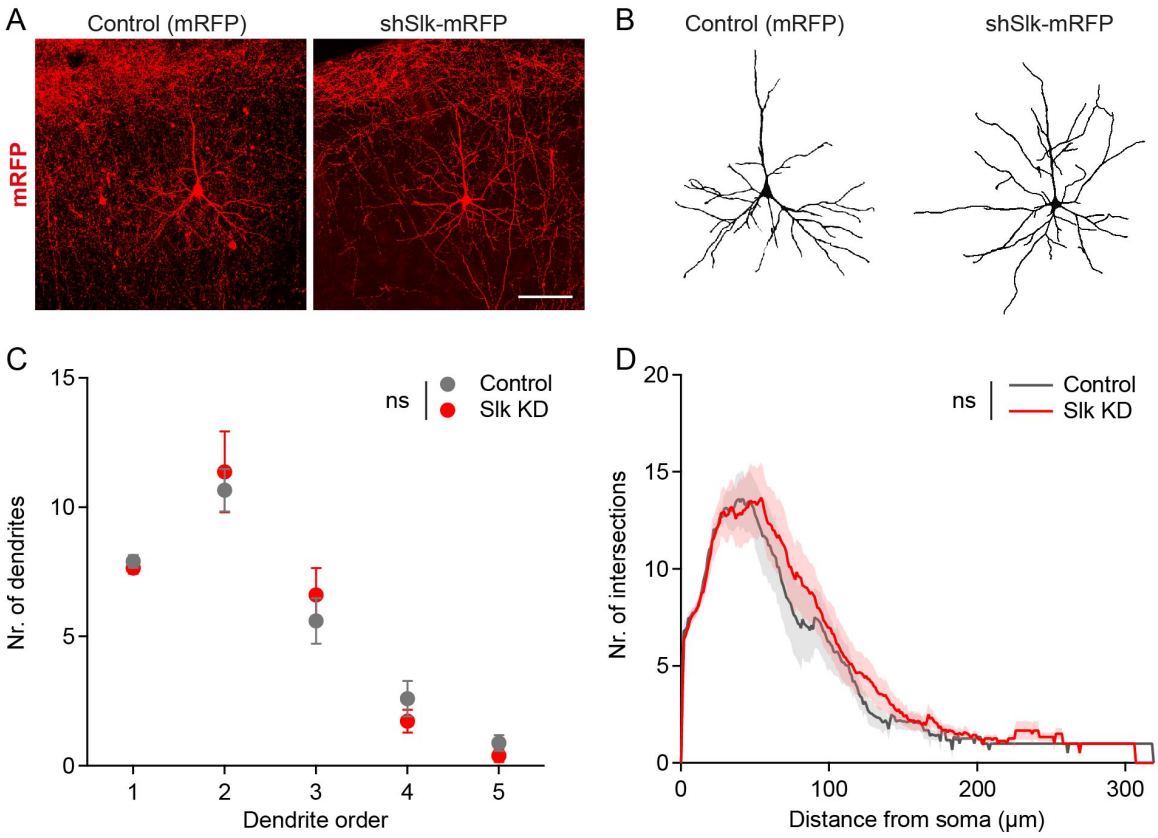


Fig. 8: No change of dendritic arborization after Slk knockdown (KD) in adulthood.
(A) Slk was knocked down in animals by viral injection of shSlk-mRFP at P30. Control animals only received a virus expressing mRFP. (B) The virally-transduced neurons were traced and reconstructed with the Imaris Software in 3 dimensions. (C) No difference in the number of different order dendrites could be detected between control and Slk KD neurons. N = 4 and N = 6 mice from different litters with n = 29 control and n = 30 Slk KD neurons; two-way RM ANOVA: Condition (Control vs. Slk KD): not significant (Interaction: p(F=0.6626; df=4, 32) = 0.6226; Dendrite order: p(F=72.89; df=1.792, 14.34) < 0.0001; Condition: p(F=0.0006046; df=1, 8) = 0.9810); Šidák's multiple comparisons test, not significant. (D) The dendritic arborization of control and Slk KD neurons was assessed by Sholl analysis and similar between the conditions. N = 4 and N = 6 mice from different litters with n = 29 control and n = 30 Slk KD neurons; two-way RM ANOVA: (C) Condition (Control vs. Slk KD): not significant (Interaction: p(F=0.6626; df=4, 32) = 0.6226; Dendrite order: p(F=72.89; df=1.792, 14.34) < 0.0001; Condition: p(F=0.0006046; df=1, 8) = 0.9810); (D) Condition (Control vs. Slk KD): not significant (Interaction: p(F=0.4322; df=319, 2552) > 0.9999; Distance from soma: p(F=75.37; df=1.516, 12.13) < 0.0001; Condition: p(F=0.3003; df=1, 8) = 0.5986); Šidák's multiple comparisons test, ns: not significant. Data shown in this figure contributed to Figure 2 in (Schoch et al., 2021).

4.1.2 No spontaneous seizure activity after focal Slk knockdown

Since Slk loss is important during development and gives rise to neurons with abnormal morphology and function, this may imply that Slk is involved in the pathogenesis of focal cortical malformations such as GG and FCDIIB, which are also characterized by the presence of dysplastic neurons with aberrant morphology. Slk was specifically found to be downregulated in these dysplastic neurons of GG and FCDIIB in biopsies of patients (Schoch et al., 2021). As these developmental malformations are highly epileptogenic and Slk knockdown shifted the excitation/inhibition balance by destabilizing inhibitory synapses, we investigated if a focal loss of Slk expression manifested in epileptic seizures. To answer this

question, mice were *in utero* electroporated at E14.5 with control (hrGFP) or Slk knockdown plasmids (shSlk-hrGFP) (Fig. 9A). The plasmids were injected into the lateral ventricles of the embryos and the DNA was electroporated into cortical progenitor cells by giving electric pulses using a triple electrode. Seventy to eighty days after birth, EEG electrodes were implanted into the electroporated area and the animals were subjected to EEG and video monitoring for a minimum of four weeks (Fig. 9B). After this time period, mice were perfused and the brain was prepared to verify that the electrode had been placed in the correct area of the cortex (Fig. 9C). Analyzing the EEG traces and the recorded video material revealed that for none of the control or Slk knockdown animals, epileptic seizures were observed (data not shown). Thus, knocking down Slk in a limited number of cells in a focal area of the cortex does not seem to be sufficient to elicit spontaneous epileptic seizures.

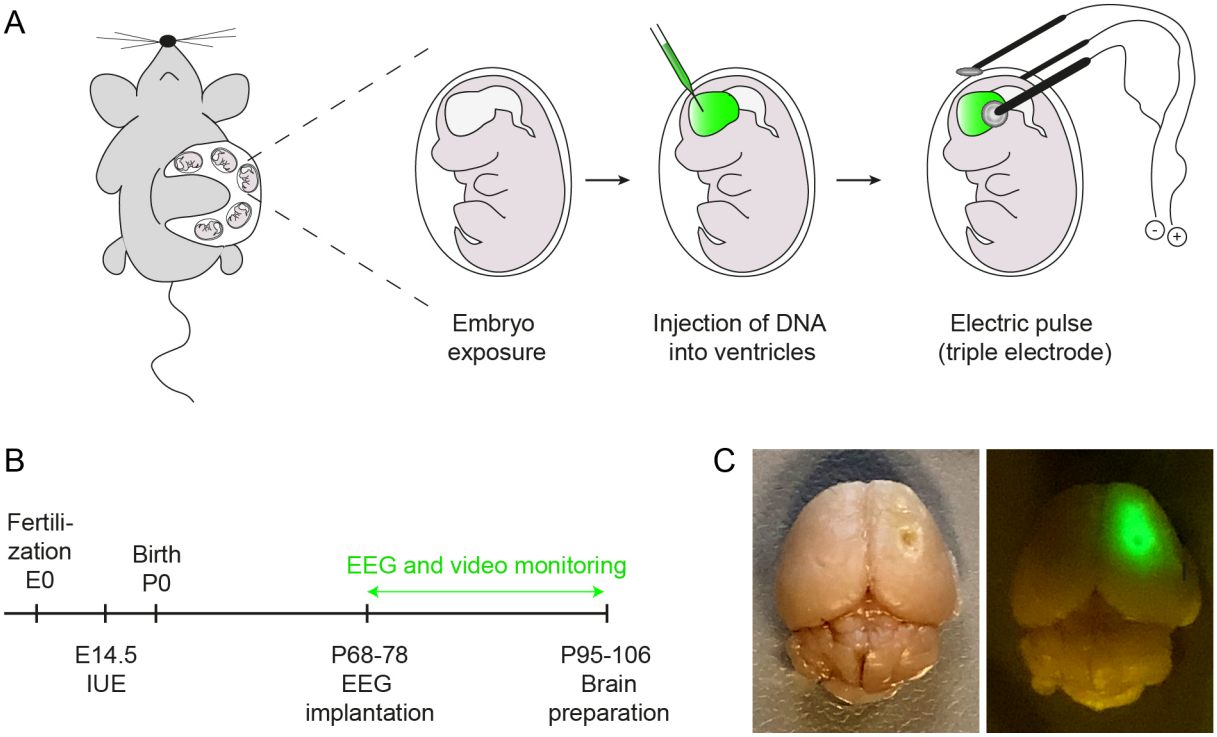


Fig. 9: Video/EEG monitoring of *in utero* electroporated mice.
(A) At E14.5, embryos were *in utero* electroporated with hrGFP or shSlk-hrGFP expressing plasmids that were injected into the ventricles and electroporated into cortical progenitor cells with a triple electrode. (B) At P68-78, EEG electrodes were implanted into the *in utero* electroporated cortex and the animals were monitored for a minimum of 28 days. (C) Example of a brain where the electrode was implanted in the *in utero* electroporated area (green) of the right hemisphere. n = 7 mice for control and n = 7 mice for Slk knockdown group.

4.1.3 Reduced adaptation of neuronal firing behavior after Slk knockdown

Even though no seizure activity was observed in EEG recordings, the reduced density of inhibitory synapses in Slk knockdown mice might nevertheless affect the firing properties of the *in utero* electroporated and neighboring neurons on a local level that cannot be detected in EEG recordings obtained from a large population of neurons. To analyze if Slk knockdown

induces changes locally, we analyzed the spontaneous activity of acute brain slices with multi-well MEA recordings. MEA recordings allow to measure the activity of a smaller population of neurons and to correlate the measured activity with the corresponding area of the slice. This technique is therefore commonly used to measure epileptogenic activity in human glioma sections, dissecting electrical activity in the tumor core from peritumoral areas (Dossi et al., 2014; Pallud et al., 2014). Transferring this approach to the Slk knockdown animals permits to analyze activity that is specific for the *in utero* electroporated area compared to the surrounding non-electroporated cortex. For this purpose, the brain was isolated at P30 from animals that were *in utero* electroporated with control or shSlk-expressing plasmids. One electroporated hemisphere of 300 µm thick slices was placed on an 8x8 square grid of electrodes and spontaneous activity was recorded for 15 minutes from the electroporated area and the surrounding non-electroporated area (Fig. 10A). Afterward, images were taken to be able to relate firing behavior to the respective brain area (Fig. 10B). Electrodes were classified as contacting the electroporated area (1), contacting the border area of the IUE (2), or contacting the non-electroporated area (3). Spikes were defined as a signal crossing the threshold of six times the standard deviation and bursts as a train of at least five spikes with a maximum inter-spike interval threshold of 100 msec (Fig. 10C).

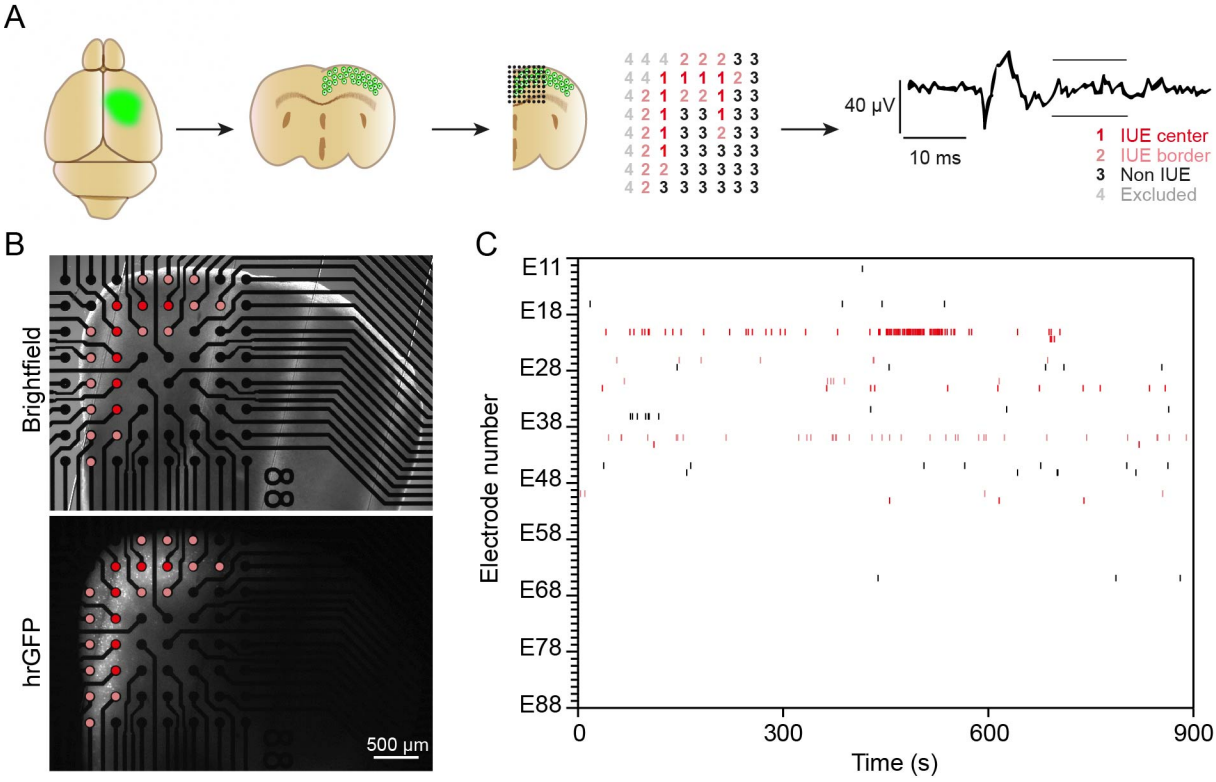


Fig. 10: Procedure of MEA recordings from acute brain slices.
(A) Mice were *in utero* electroporated at E14.5 with control or shSlk-expressing plasmids. The brain was isolated on P30 and 300 µm acute brain slices were prepared. One hemisphere of the brain was placed with the *in utero* electroporated area on a 64-electrode grid and spontaneous activity was recorded for 15 minutes. (B) Electrodes

were classified according to the fluorescence as electrodes recording from the IUE area (red), from the IUE border area (light red), or the non-electroporated area (black). (C) The number of spikes and bursts was analyzed per electrode based on the categorization of the electrode (example image). Every dash represents one recorded spike at the respective electrode.

The number of spikes per electrode for each of the defined electrode categories was quantified. For slices incubated in normal aCSF, there was no difference detected between areas or experimental conditions (Fig. 11A). In addition, the proportion of spikes per area and animal was calculated to determine which area was proportionally the most active. Again, no difference was found between the areas and conditions (Fig. 11B). Incubation of the slices in aCSF with low magnesium and high potassium ($aCSF^{lowMg2+,highK+}$) has been shown to induce epileptiform activity and ictal discharges (Khosravani et al., 2003). For control animal brain slices, $aCSF^{lowMg2+,highK+}$ increased spontaneous activity whereas the increase for Slk knockdown animals seemed to be smaller (Fig. 11C, D). A similar trend was observed when the number of bursts in aCSF and $aCSF^{lowMg2+,highK+}$ was analyzed (Fig. 11E-H). Between the conditions, no significant difference was detected, which may be partly due to high variability within and between animals.

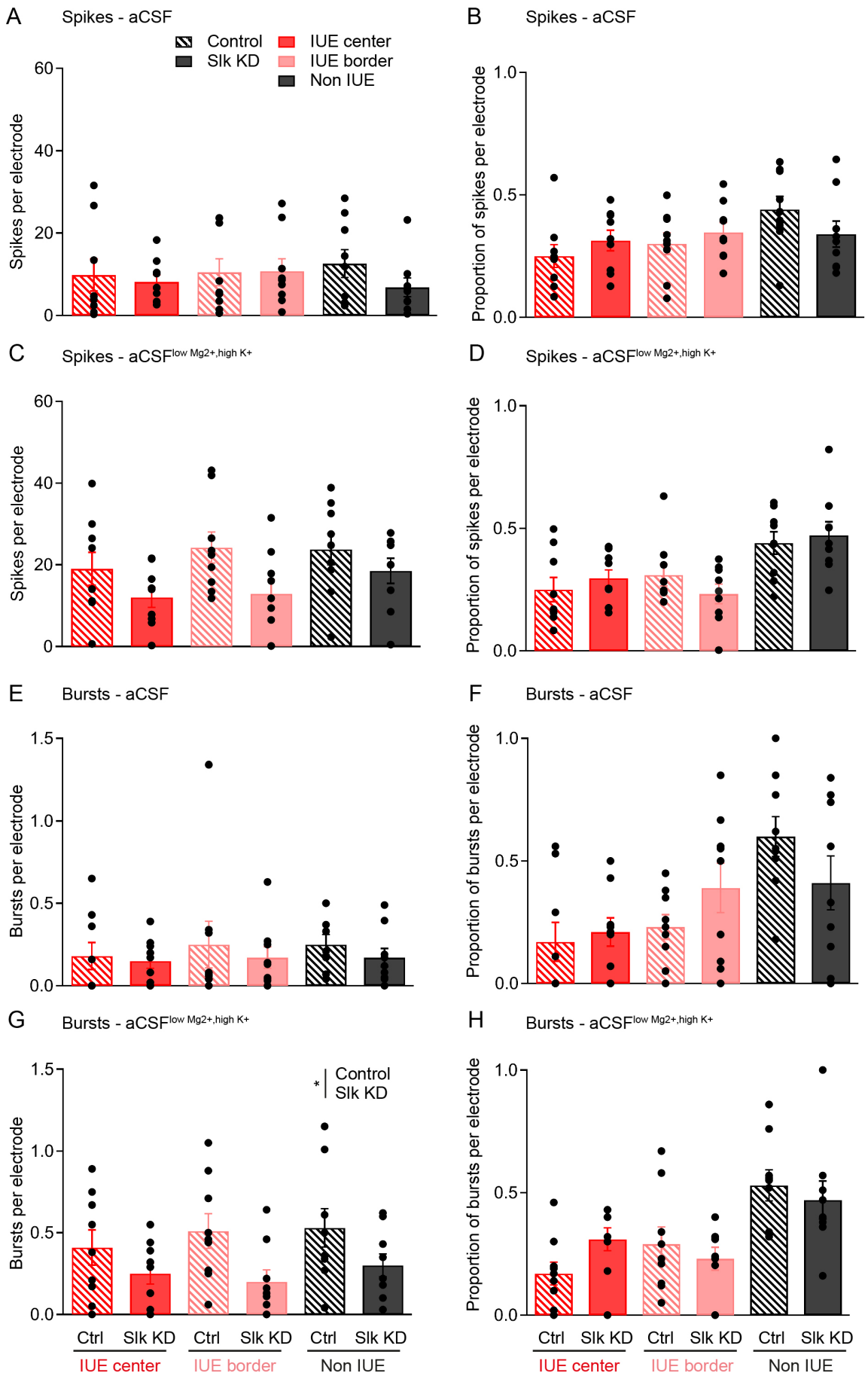

A
Spikes - aCSF
Control
Slk KD
IUE center
IUE border
Non IUE
Spikes per electrode
60
40
20
0
B
Spikes - aCSF
Proportion of spikes per electrode
1.0
0.5
0.0
C
Spikes - aCSF low Mg2+,high K+
Spikes per electrode
60
40
20
0
D
Spikes - aCSF low Mg2+,high K+
Proportion of spikes per electrode
1.0
0.5
0.0
E
Bursts - aCSF
Bursts per electrode
1.5
1.0
0.5
0.0
F
Bursts - aCSF
Proportion of bursts per electrode
1.0
0.5
0.0
G
Bursts - aCSF low Mg2+,high K+
Bursts per electrode
1.5
1.0
0.5
0.0
*
Control
Slk KD
Ctrl
Slk KD
Ctrl
Slk KD
Ctrl
Slk KD
IUE center
IUE border
Non IUE
H
Bursts - aCSF low Mg2+,high K+
Proportion of bursts per electrode
1.0
0.5
0.0
Ctrl
Slk KD
Ctrl
Slk KD
Ctrl
Slk KD
IUE center
IUE border
Non IUE

Fig. 11: No change in the number of spikes and bursts in MEA recordings of acute slices of control (Ctrl) and Slk knockdown (KD) animals.
(A) The number of spontaneous spikes that occurred within 15 minutes of recording in aCSF were quantified and normalized to the number of electrodes per category. (B) The proportional spiking activity was calculated per category for control and Slk KD animals. (C, D) The number (C) and the proportion (D) of spikes was quantified for control and Slk KD slices that were incubated in $aCSF^{lowMg2+,highK+}$. Similarly, the number and proportion of bursts were quantified per category in aCSF (E, F) and $aCSF^{lowMg2+,highK+}$ (G, H). n = 9 mice for control and n = 9 mice for Slk KD group. Two-way RM ANOVA: (A): Condition (Control vs. Slk KD): not significant (Interaction: p(F=0.9900; df=2, 32) = 0.3827; IUE area: p(F=0.2872; df=1.874, 29.98) = 0.7383; Condition: p(F=0.4729; df=1, 16) = 0.5015); (B): Condition (Control vs. Slk KD): not significant (Interaction: p(F=1.298; df=2, 32) = 0.2871; IUE area: p(F=1.820; df=1.841, 29.946) = 0.1820; Condition: p(F=1.016; df=1, 16) = 0.3285); (C): Condition (Control vs. Slk KD): not significant (Interaction: p(F=0.0.7155; df=2, 32) = 0.4966; IUE area: p(F=2.346; df=1564, 25.03) = 0.1262; Condition: p(F=4.018 df=1, 16) = 0.0622); (D): Condition (Control vs. Slk KD): not significant (Interaction: p(F=0.8343; df=2, 32) = 0.4434; IUE area: p(F=7.289; df=1.879, 30.06) = 0.0031; Condition: p(F=0.3718; df=1, 16) = 0.5506); (E): Condition (Control vs. Slk KD): not significant (Interaction: p(F=0.09214; df=2, 32) = 0.9122; IUE area: p(F=0.2730; df=1.329, 21.26) = 0.6727; Condition: p(F=0.6666; df=1, 16) = 0.4262); (F): Condition (Control vs. Slk KD): not significant (Interaction: p(F=1.617; df=2, 32) = 0.2144; IUE area: p(F=5.0000; df=1.732, 27.71) = 0.0174; Condition: p(F=0.9505; df=1, 16) = 0.3441); (G): Condition (Control vs. Slk KD): * $p < 0.05$ (Interaction: p(F=0.6406; df=2, 32) = 0.5336; IUE area: p(F=0.7636; df=1.844, 29.50) = 0.4651; Condition: p(F=5.353; df=1, 16) = 0.0343); (H): Condition (Control vs. Slk KD): not significant (Interaction: p(F=1.218; df=2, 32) = 0.3092; IUE area: p(F=7.923; df=1.673, 26.76) = 0.0031; Condition: p(F=0.6076; df=1, 16) = 0.4471; Šidák's multiple comparisons test, not significant.

Defects in neuronal firing behavior can sometimes only be detected when the system is challenged. Therefore, we directly compared the spiking and bursting behavior of control and Slk knockdown brain slices being incubated in aCSF to $aCSF^{lowMg2+,highK+}$ to see if enhanced activity would induce a shift of spiking or bursting activity. However, no significant difference in the proportional spiking and bursting could be detected in the IUE area, the IUE border, or the non-electroporated area between the different solutions for control animals (Fig. 12A, B) or animals with focal Slk knockdown (Fig. 12C, D).

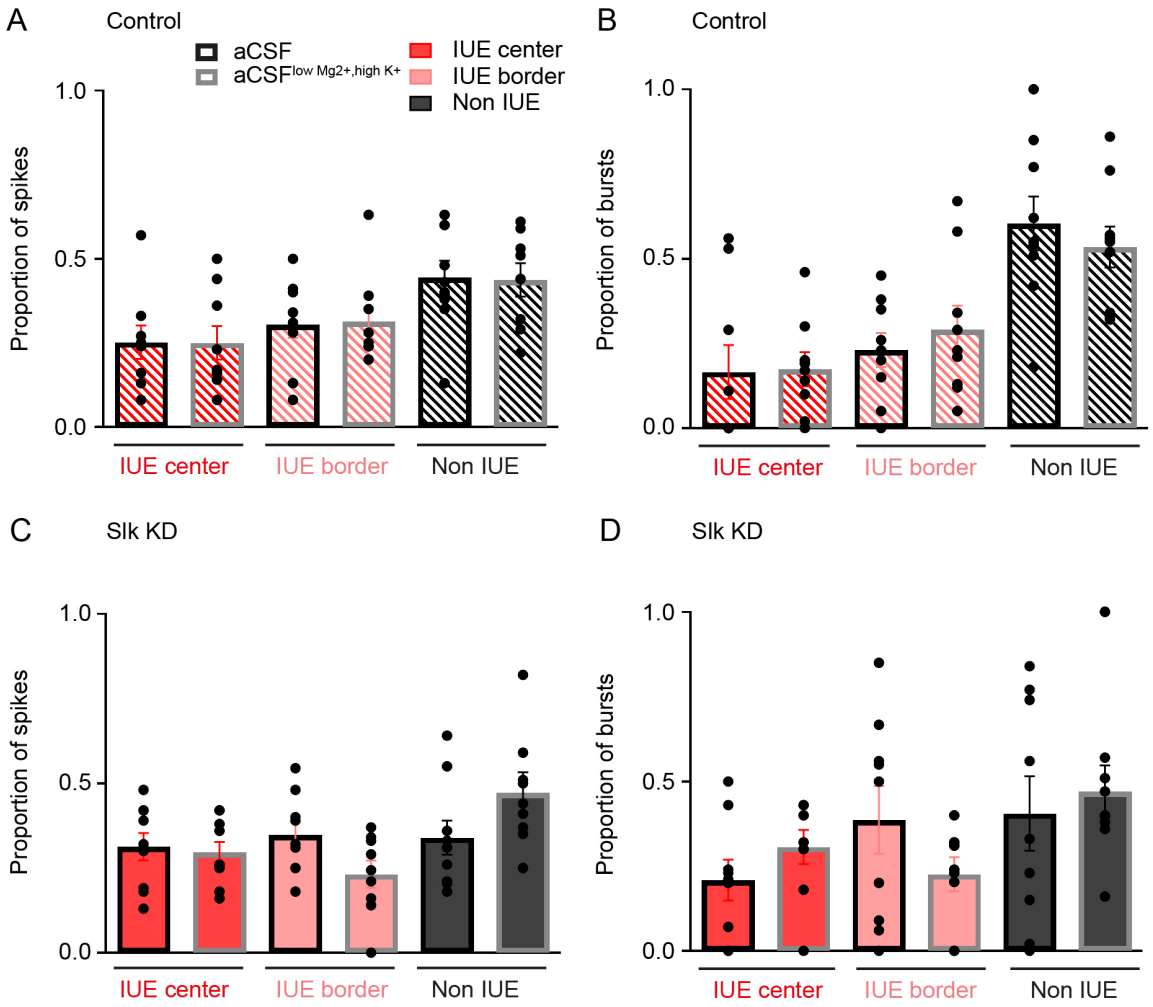


Fig. 12: Effect of epileptiform aCSF$^{lowMg2+,highK+}$ on control and Slk knockdown (KD) brain slices.
(A, B) The proportional spiking and bursting activity for the categories IUE center, IUE border, and non-electroporated area was compared for slices being incubated in normal aCSF and aCSF$^{lowMg2+,highK+}$. No significant difference was detected for control animals. (C, D) No difference in the proportional spiking and bursting activity could be detected between the areas or the solutions for Slk KD animals. n = 9 mice for control and n = 9 mice for Slk KD group. Two-way RM ANOVA: (A): Solution (aCSF vs. aCSF$^{lowMg2+,highK+}$): not significant (Interaction: p(F=0.007607; df=2, 32) = 0.9924; IUE area: p(F=5.712; df=1.971, 31.53) = 0.0079; Solution: p(F=0.20000; df=1, 16) = 0.6607); (B): Solution (aCSF vs. aCSF$^{lowMg2+,highK+}$): not significant (Interaction: p(F=0.3319; df=2, 32) = 0.7200; IUE area: p(F=13.31; df=1.912, 30.59) < 0.0001; Solution: p(F=0.3077; df=1, 16) = 0.5868); (C): Solution (aCSF vs. aCSF$^{lowMg2+,highK+}$): not significant (Interaction: p(F=2.671; df=2, 32) = 0.0846; IUE area: p(F=2.652; df=1.609, 25.74) = 0.0994; Solution: p(F=0.3676; df=1, 16) = 0.5528); (D): Solution (aCSF vs. aCSF$^{lowMg2+,highK+}$): not significant (Interaction: p(F=1.099; df=2, 32) = 0.3455; IUE area: p(F=1.890; df=1.472, 23.55) = 0.1800; Solution: p(F=0.07765; df=1, 16) = 0.7841); Šidák's multiple comparisons test, not significant.

In general, incubation with aCSF$^{lowMg2+,highK+}$ elevated spiking and bursting robustly by two-fold in control animals for almost all categories (Fig. 13A, B). For animals with focal Slk knockdown, the effect of aCSF$^{lowMg2+,highK+}$ was only seen in the non-electroporated area for spiking activity. Spiking and bursting activity in the IUE center and border area could not be significantly elevated using aCSF$^{lowMg2+,highK+}$.

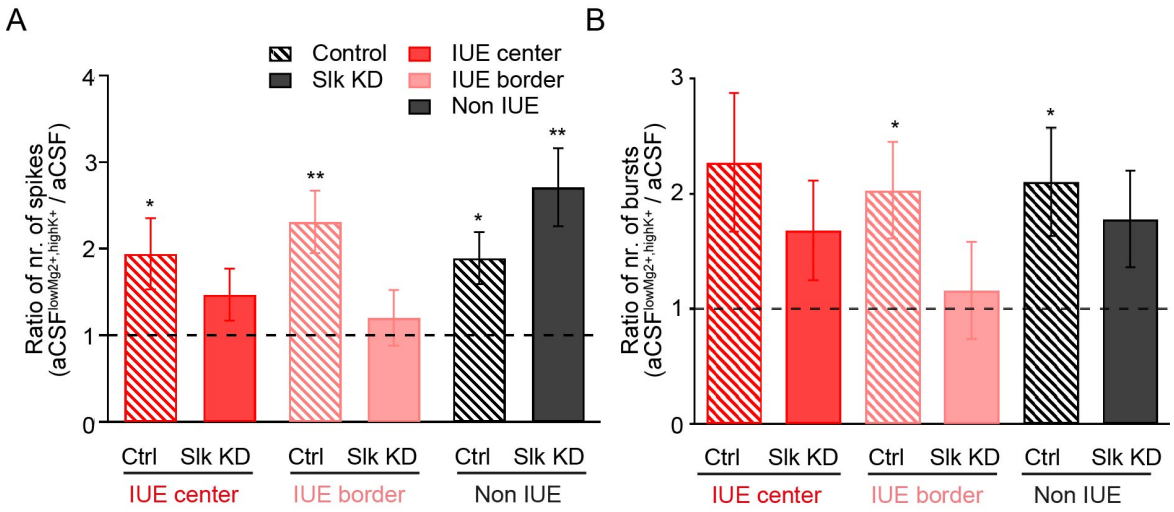


Fig. 13: Increased activity in aCSF$^{lowMg2+,highK+}$ predominantly in control (Ctrl) brain slices.
Comparing the number of spikes (A) and bursts (B) in the different categories showed that incubation of control brain slices with aCSF$^{lowMg2+,highK+}$ stably increased spiking and bursting behavior by two-fold compared to normal aCSF. In focal Slk knockdown (KD) brain slices, incubation with aCSF$^{lowMg2+,highK+}$ did not increase spiking and bursting in the IUE center and IUE border areas of the slice. n = 9 mice for control and n = 9 mice for Slk KD group. One sample t-test: (A) Ctrl IUE center: p(t=2.311, df=8) = 0.0496; Slk KD IUE center p(t=1.567, df=8) = 0.1558; Ctrl IUE border p(t=3.606, df=8) = 0.0069; Slk KD IUE border p(t=0.6186, df=8) = 0.5534; Ctrl Non IUE p(t=2.934, df=8) = 0.0189; Slk KD Non IUE: p(t=3.800, df=8) = 0.0052; (B) Ctrl IUE center: p(t=2.117, df=8) = 0.0672; Slk KD IUE center p(t=1.594, df=8) = 0.1497; Ctrl IUE border p(t=2.472, df=8) = 0.0386; Slk KD IUE border p(t=0.3780, df=8) = 0.7153; Ctrl Non IUE p(t=2.357, df=8) = 0.0462; Slk KD Non IUE: p(t=1.872, df=8) = 0.0981; * $p < 0.05$; ** $p < 0.01$.

In general, spontaneous activity *ex vivo* is quite low which is the reason why challenging the system with epileptogenic aCSF$^{lowMg2+,highK+}$ could reveal subtle differences between the conditions. The fact that no significant differences could be detected between control and focal Slk knockdown animals when comparing spiking and bursting behavior directly might be due to the high variability between animals within the same group. This could be explained by several factors. With IUE at E14.5, it is possible to reliably target the same area of the cortex, namely layer II/III of the motor and somatosensory cortex (Szczurkowska et al., 2016; Taniguchi et al., 2012). However, the extent of the *in utero* electroporated area and the density of the electroporated cells vary between animals and are not identical as they are in genetically modified animals. Therefore, a certain extent of variability in the spiking and bursting behavior can be attributed to the animal model itself, in addition to the technical variability of the experiment.

However, despite the limitations of the animal model and the technique, Slk knockdown by IUE appears to restrict the ability of neurons to increase their firing behavior in response to external stimuli.

4.1.4 Influence of Slk knockdown on surrounding cells

In malformations of cortical development, the role and involvement of the perilesional area are widely discussed. Although appearing macroscopically normal, alterations have been described in this area presenting a possible explanation that surgical resection does not always result in the complete elimination of epilepsy (Aronica et al., 2012; Andrade and da Costa Leite, 2011). As a knockdown of Slk leads to developmental alterations in dendritic branching and inhibitory synapse density, it could be that the morphologically aberrant cells also influence their environment and neighboring cells. One technique to characterize different cell types and individual cells is scRNAseq. This method allows to analyze the transcriptome profile of single cells and to classify them based on their molecular profile into different cell types and states (Zeisel et al., 2015). To analyze if Slk knockdown affects and alters neighboring cells and other cell types, a scRNAseq experiment was performed. Animals were *in utero* electroporated at E14.5 with control plasmids (hrGFP + mRFP) or the Slk knockdown plasmid (shSlk-hrGFP). At P30, brains were removed and the *in utero* electroporated area was micro-dissected (Fig. 14A). The tissue was dissociated enzymatically and mechanically which resulted in a cell suspension with a predominant proportion of dead cells and debris (Fig. 14B). Therefore, additional purification steps were included to remove myelin and red blood cells. 78-95% of the remaining cells were viable and were further used for scRNAseq (Fig. 14C).

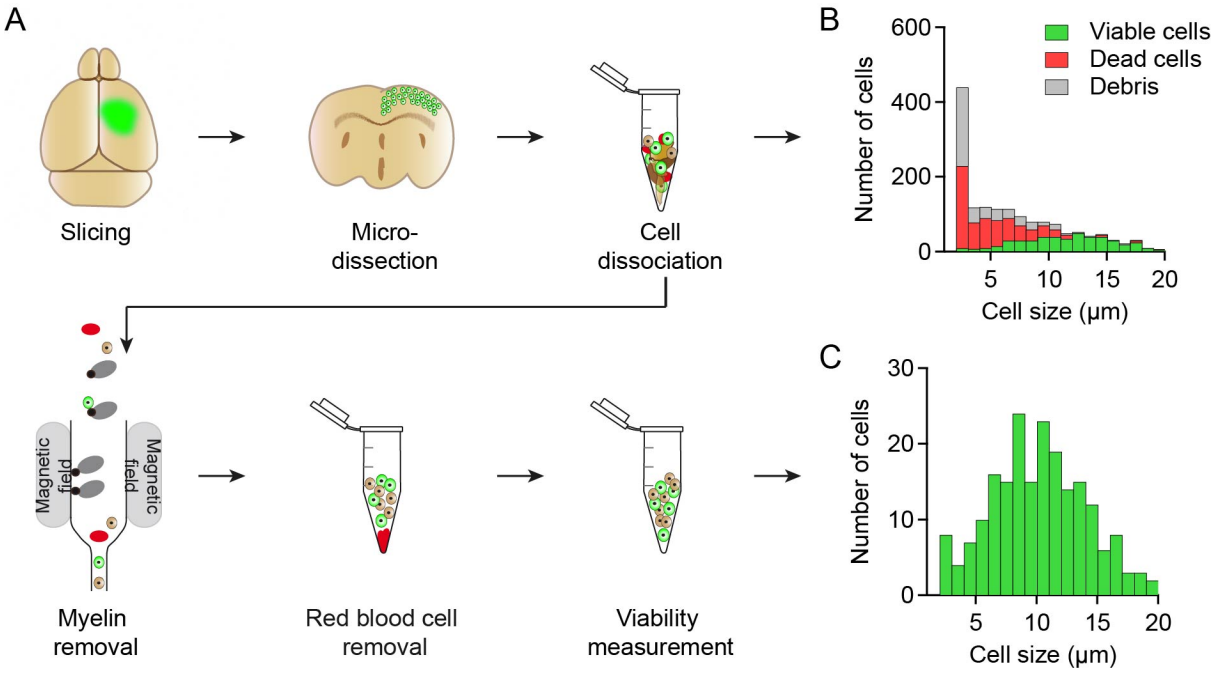


Fig. 14: Preparation of a viable cell suspension for scRNAseq analysis.
(A) Brains of *in utero* electroporated animals were removed and the *in utero* electroporated area was micro-dissected. The cells were dissociated enzymatically with papain digestion and mechanically using the gentleMACS Octo Dissociator. (B) Example image of a viability measurement after cell dissociation. The cell suspension consisted of many dead cells and debris, showing only a small proportion of viable cells. (C) Additional removal of

myelin and red blood cells decreased the proportion of dead cells and debris which can be seen in an exemplary graph of the cell viability over cell size.

The cells were sequenced with the droplet-based method of 10x Genomics and the sequences were aligned to the mouse genome complemented with the hrGFP sequence. During quality control, cells were filtered based on their gene and RNA molecule (UMI) counts, and on the proportion of mitochondrial genes, which was used as an indicator for healthy cells. After clustering, the identities of cell clusters were determined based on identifying known cell type markers from published scRNAseq studies in our dataset (Fig. 15A, B). In a second complementary approach, marker genes that were specific to the cell clusters in our dataset were identified and compared to published markers (Fig. 15C). This two-directional marker identification allowed the cell type annotation of the different clusters.

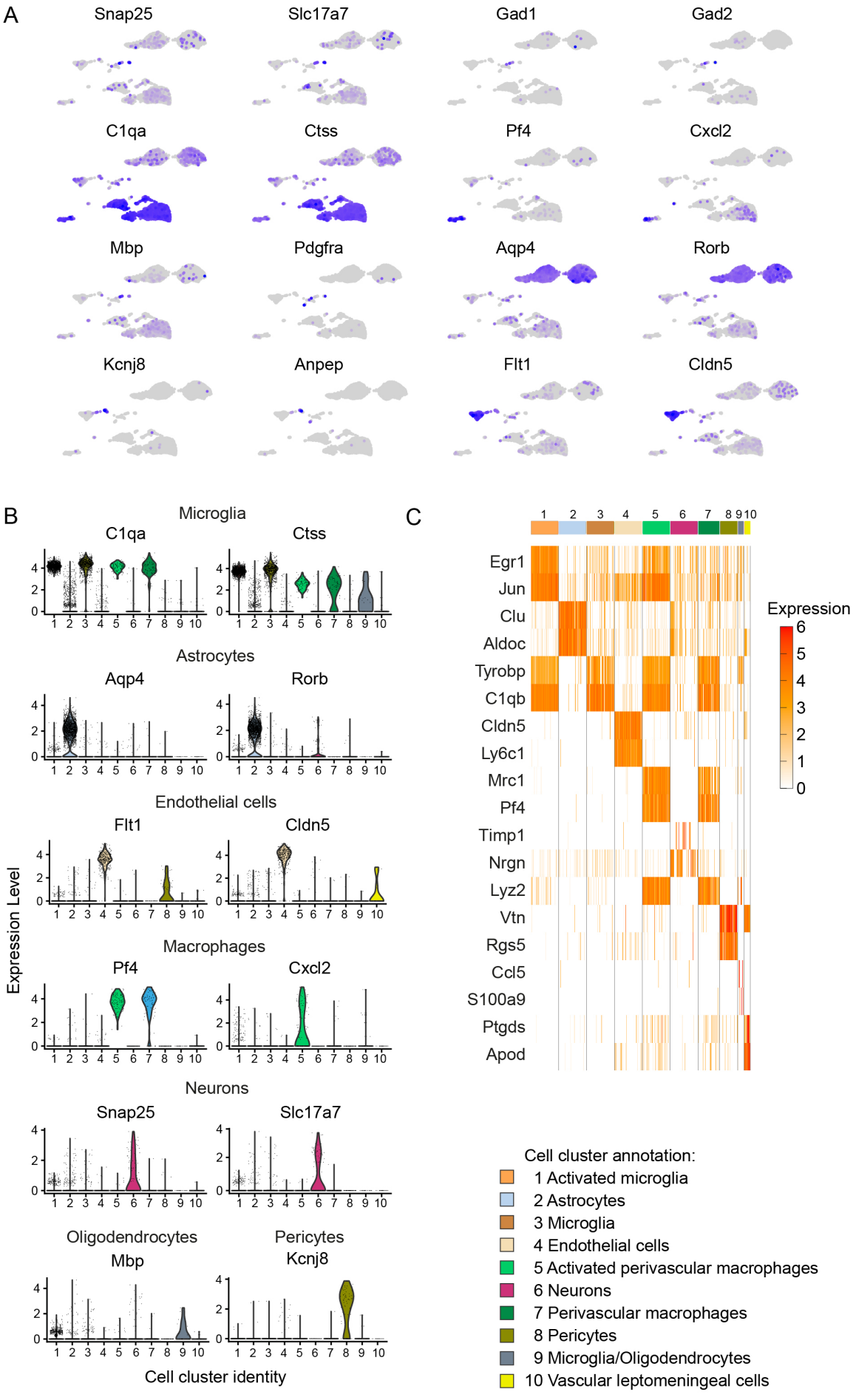

A
Snap25
Slc17a7
Gad1
Gad2
C1qa
Ctss
Pf4
Cxcl2
Mbp
Pdgfra
Aqp4
Rorb
Kcnj8
Anpep
Flt1
Cldn5
B
Microglia
C1qa
Ctss
Astrocytes
Aqp4
Rorb
Endothelial cells
Flt1
Cldn5
Macrophages
Pf4
Cxcl2
Neurons
Snap25
Slc17a7
Oligodendrocytes
Mbp
Pericytes
Kcnj8
Expression Level
Cell cluster identity
C
Egr1
Jun
Clu
Aldoc
Tyrobp
C1qb
Cldn5
Ly6c1
Mrc1
Pf4
Timp1
Nrgn
Lyz2
Vtn
Rgs5
Ccl5
S100a9
Ptgds
Apod
Expression
Cell cluster annotation:
1 Activated microglia
2 Astrocytes
3 Microglia
4 Endothelial cells
5 Activated perivascular macrophages
6 Neurons
7 Perivascular macrophages
8 Pericytes
9 Microglia/Oligodendrocytes
10 Vascular leptomeningeal cells

Fig. 15: Marker identification in the cell clusters of the scRNAseq dataset.
(A) UMAP visualizations of all sequenced cells show different cell clusters that are based on the 3000 most variable genes. Cell-type specific markers from published scRNAseq studies were found in different clusters of our dataset. Cells with high gene expression are displayed in purple. (B) Violin plots of known cell type markers show preferential expression of the markers in specific clusters. (C) In a reverse approach, gene markers that are specific to one cluster were identified in our dataset and compared to published cell type markers for cell-type annotation. The heatmap shows the top two strongest differentially expressed genes for each cluster compared to all other clusters.

When splitting the cluster visualization into control and Slk knockdown condition, it is apparent that more cells remained in the Slk knockdown condition after quality control compared to the control condition although the same number of cells was aimed to be sequenced for both conditions (Fig. 16A). The expression of Slk among all cell types was higher in subpopulations of glial, vascular, and endothelial cells compared to neurons (Fig. 16B). When we isolated the neuronal cell cluster and plotted the Slk expression, Slk expression was only detected in very few cells (Fig. 16C). This could be either due to technical reasons as scRNAseq data contains many genes with zero counts (Jiang et al., 2022; Choi et al., 2020) or to biological reasons as it was shown that Slk expression is highest during development and decreases during neural stem cell differentiation (Zhang et al., 2002). Surprisingly, only one hrGFP-expressing neuron could be identified (Fig. 16C). This was unexpected as the micro-dissection of the *in utero* electroporated tissue was performed based on hrGFP fluorescence. Fluorescent cells were still detected during the cell viability measurement in which on average 15% of the analyzed cells were hrGFP positive. Therefore, we would have expected to see around 1020 hrGFP-positive cells out of the 6801 cells in total that survived the quality control and filtering. This surprising finding might suggest that *in utero* electroporated cells are more sensitive, especially when compared to glial cells, and are somehow lost on the way from cell viability control to the actual sequencing of the cells. The observation that before quality control and filtering 73 hrGFP-expressing cells were detected, supports the idea that the genetically modified cells are of lower quality and thus might be more sensitive to degeneration.
Although we could not analyze cells with Slk knockdown directly, there was still the possibility to analyze the surrounding cells, which had been the main goal of the scRNAseq experiment. As only the *in utero* electroporated region has been micro-dissected, all sequenced cells are necessarily neighbors or in the same environment as the Slk knockdown cells. As Slk knockdown cells have less inhibitory postsynapses and fewer higher order dendrites where usually mainly excitatory postsynapses are located, we would expect an altered network and cell-cell connections in the Slk knockdown condition compared to the control condition. This might involve cell-cell connections via synaptic sites or non-synaptic cell-cell junctions.

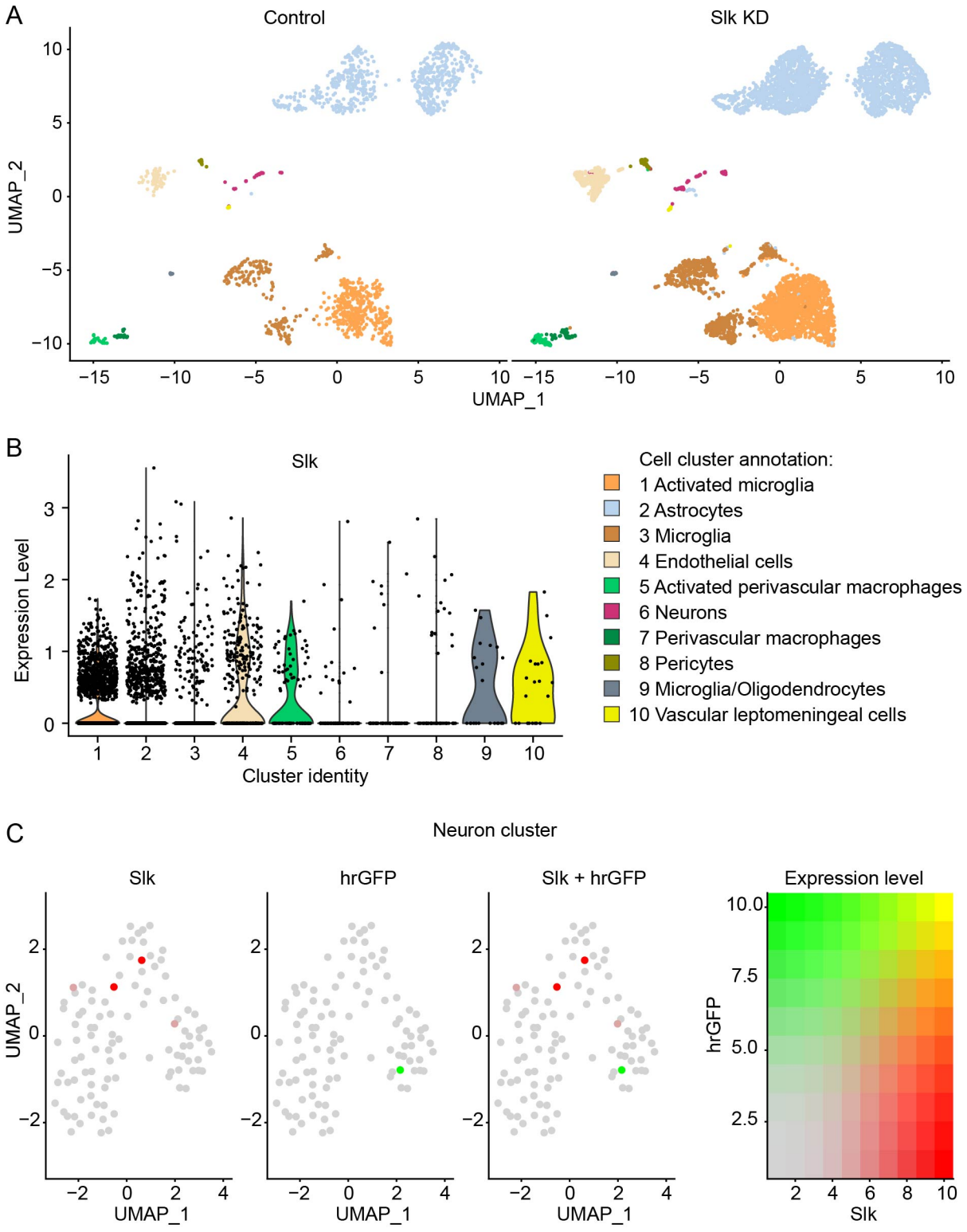


Fig. 16: Clustering and cell-type annotation of the sequenced cells.
(A) UMAP plots show the different annotated cell type clusters for control and focal Slk knockdown (KD) animals. Each dot corresponds to one cell and all of the four replicates are plotted together. (B) Expression of Slk was mainly detected in non-neuronal cell types. (C) The UMAP plots show all the cells of the neuronal cell cluster. Only a few cells express Slk and only one cell expresses hrGFP, which is a marker for the *in utero* electroporated cells.

All identified cell types were found in the control and in the focal Slk knockdown animals and for both conditions, the largest proportion of cells was of glial origin, mostly corresponding to astrocytes and microglia (Fig. 17A). No significant differences in the proportion of cells in a specific cell type were observed between the control and the Slk knockdown condition.

A differential gene analysis between neurons of the Slk knockdown animals compared to the control condition revealed 48 genes that were significantly altered in their expression by at least 1.5-fold in one or more cell type clusters (Fig. 17B). The majority of differential expression was detected in neurons and immune cells. As the Slk knockdown is specific for neurons and could potentially alter the interaction with non-affected neurons, the main effect would be expected for neurons. Interestingly, the expression for all differentially expressed neuronal genes was reduced in the Slk knockdown condition compared to control.

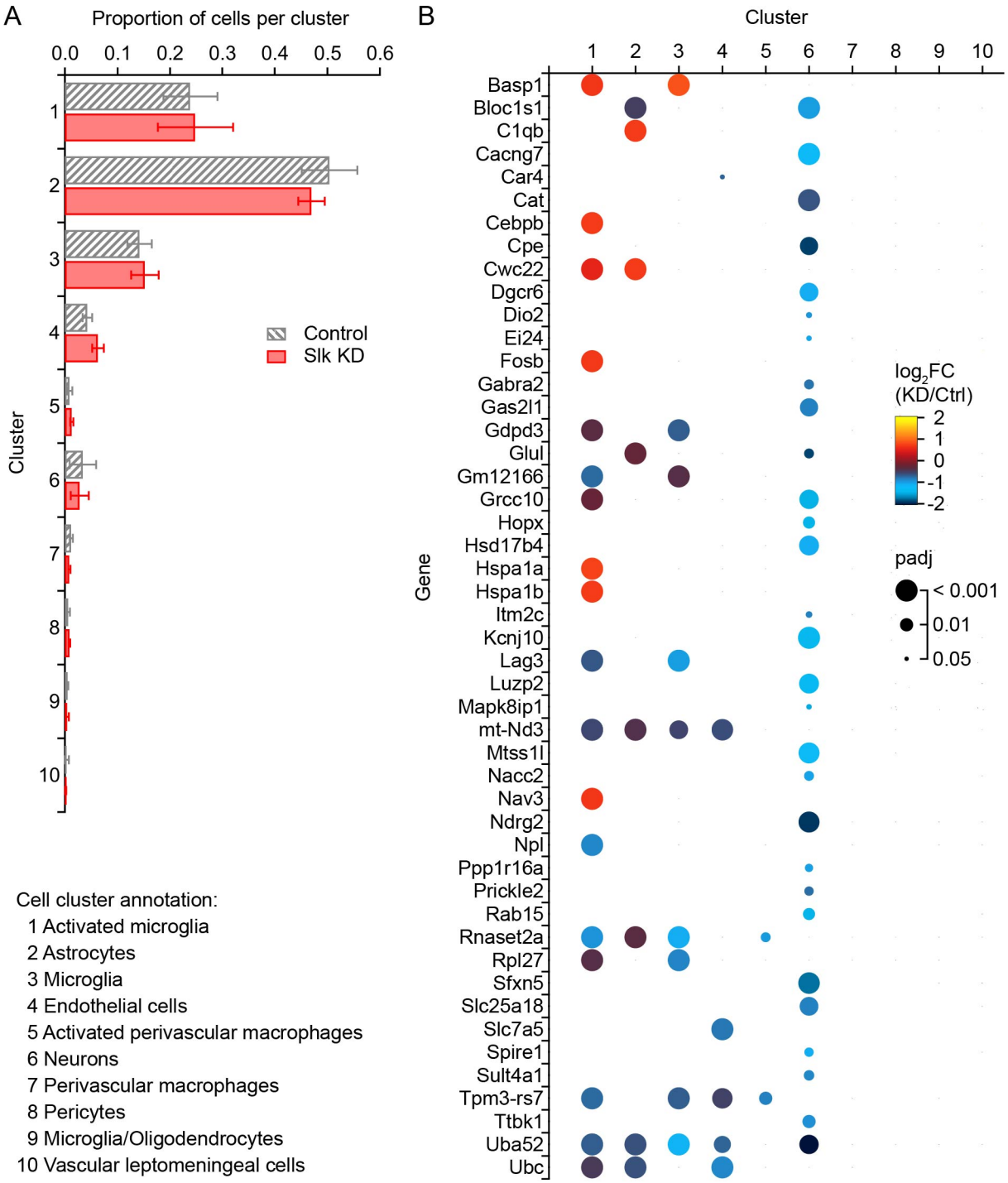


Fig. 17: scRNAseq cell cluster characterization.
(A) The proportion of cells is plotted for the control (Ctrl) and the focal Slk knockdown (KD) condition. In both conditions, most sequenced cells are annotated as microglia or astrocytes. Two-way RM ANOVA: Condition (Ctrl vs. Slk KD): not significant (Interaction: p(F=0.1352; df=9, 54) = 0.9985; Cell type: p(F=65.15; df=1.507, 9.041) < 0.0001; Condition: p(F=1.174; df=1, 6) = 0.3202; Šidák's multiple comparisons test, not significant. (B) Genes that are significantly differentially expressed in at least one cell cluster are plotted in alphabetical order (log_2FC > |0.58| & padj < 0.05 in at least one cluster).

Among the lower expressed genes were genes involved in cytoskeletal functions (Gas2l1, Mtss1l, Spire1, Ttbk1), genes involved in synaptic processes (Gabra2, Prickle2, Glul, Rab15), and genes important for neurite growth (Ndrg2, Mapk8ip1, Mtss1, Spire1, Prickle2) (Fig. 18A). These differences in gene expression in non-electroporated neurons might be a first hint that Slk knockdown does not only affect the morphology and function of the affected neurons but also influences neighboring neurons.

Apart from neurons, gene expression was also noticeably altered in microglia. The strongest upregulation in Slk knockdown compared to control microglia was found in proinflammatory genes (Hspa1a, Hspa1b, Cebpb, Fosb) (Fig. 18B). This might suggest a different activation of a subset of microglia in animals with a focal Slk knockdown.

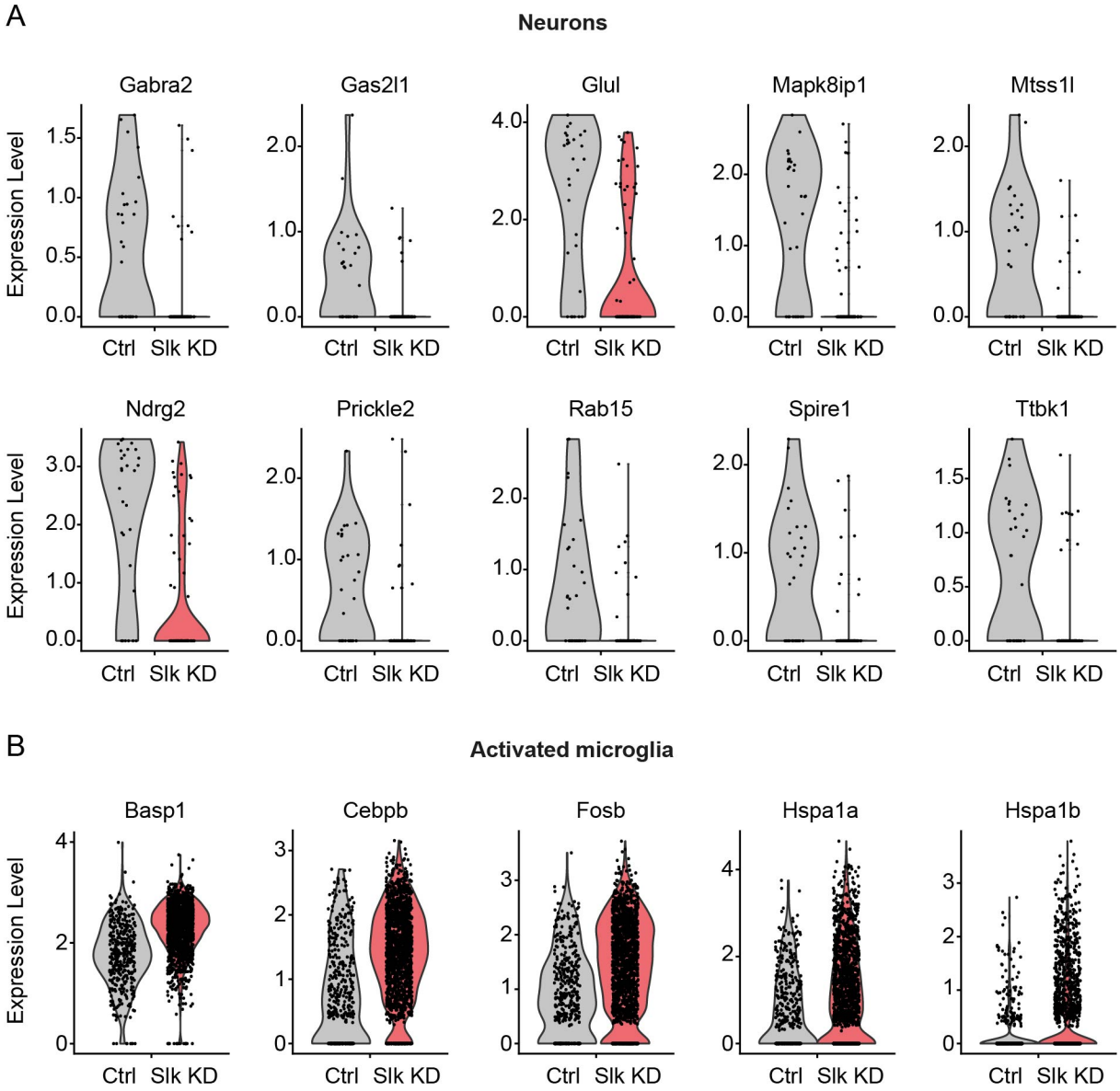


Fig. 18: Differential gene expression in scRNAseq dataset.
(A) The expression of genes that are important for cytoskeletal or synaptic function or implicated in neurite growth was reduced in neurons in the local environment of Slk knockdown (KD) neurons. Padj < 0.05 & $\log_2$FC < -0.58 in the neuron cluster. (B) Genes implicated in inflammatory responses were upregulated in microglia of focal Slk KD animals compared to control. Padj < 0.05 & $\log_2$FC > 0.58 in the activated microglia cluster.

As synaptic pruning and synapse elimination by immune cells in the brain are increasingly recognized in normal brain development and diseases such as schizophrenia and ASD (Andoh et al., 2019; Paolicelli et al., 2011), the differential gene expression in microglia cells between control and Slk knockdown mice might suggest a role of microglia in processes that occur as a consequence of Slk knockdown.

4.2 Mechanism of Slk effects

4.2.1 No change in abundance of known Slk interactors at inhibitory synapses

The previous experiments further characterized the influence of Slk on cellular development, morphology, and function of cells. However, they do not explain how Slk influences neuronal functions. To be able to understand how Slk affects cell morphology and function on a mechanistic level, the pathway of Slk inside the cell was investigated. Until now, no molecular mechanisms and pathways of Slk function inside neurons are known.

As Slk reduces the stability of inhibitory synapses, several potential mechanisms would explain this phenomenon. The destabilization could result from changes in the cytoskeletal stability or changes in the link to the extracellular matrix (ECM). In non-neuronal cells, Slk had already been described to influence cytoskeletal dynamics and the stability of focal adhesions that link the cytoskeleton to the ECM. Reduction of Slk levels impaired the focal adhesion turnover probably via the Fak-Paxillin pathway (Wagner and Sabourin, 2009; Quizi et al., 2013). Furthermore, increased Slk levels induced the disassembly of actin stress fibers, and reduced Slk levels disrupted the ability of centrosomes to anchor or cap microtubules (Sabourin et al., 2000; Wagner et al., 2002; Burakov et al., 2005, 2008).

Therefore, in a first attempt to uncover the molecular mechanism of Slk, proteins known to be influenced by Slk in non-neuronal cells were investigated at inhibitory synapses in neurons (Fig. 19A). Cultured cortical neurons were transduced with crude viral extracts to knock down Slk, which reduced Slk protein expression by 98% (Fig. 19B), and then stained for the protein of interest (Fig. 20).

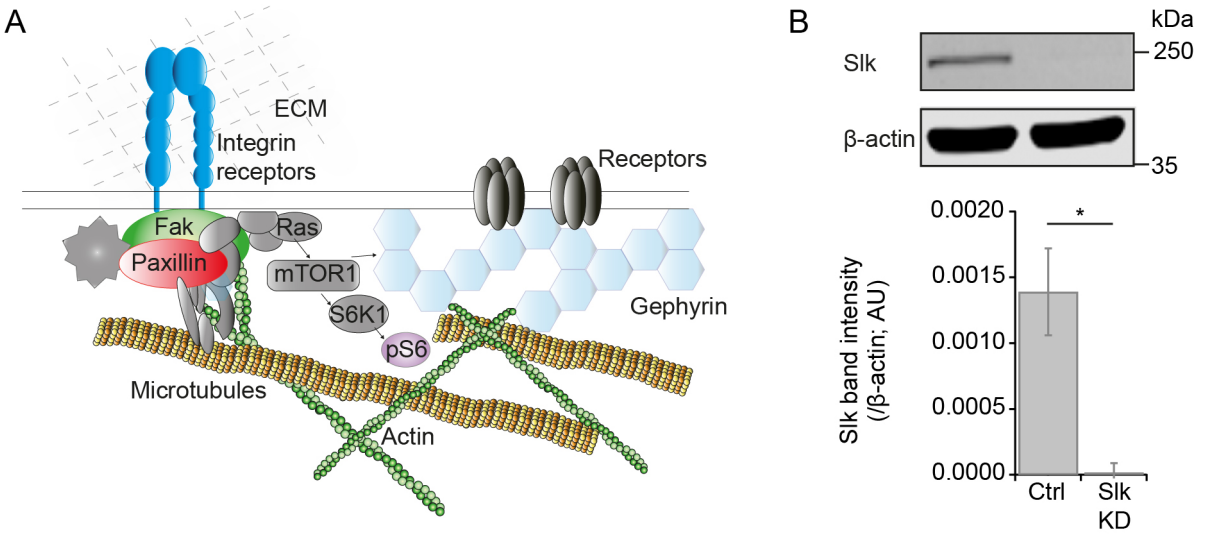


Fig. 19: Investigation of cytoskeleton-/scaffold-associated proteins at inhibitory synapses in cultured neurons with Slk knockdown (KD).
(A) Candidate proteins at inhibitory synapses that have been described in non-neuronal cells to contribute to Slk function. The postsynaptic scaffold protein Gephyrin forms a molecular lattice that connects the postsynaptic receptors to the cytoskeleton. Focal adhesions including Fak and Paxillin link the extracellular space to the intracellular cytoskeleton and transmit signals to the intracellular space that get transmitted via intracellular pathways like the mTOR pathway. mTOR pathway activation, in turn, induces Gephyrin polymerization and clustering. (B) The candidate proteins were investigated in cultured cortical neurons after transduction with hrGFP or shSlk-hrGFP expressing rAAV crude viral extracts. Knocking down Slk via viral transduction reduced Slk expression by 98%, which was confirmed by immunoblotting (arbitrary units (AU)). n = 4. Paired t-test: p(t=4.172, df=3) = 0.0251; * p < 0.05.

To investigate focal adhesions, Fak and Paxillin were stained directly (Fig. 20B, C). The cytoskeleton was analyzed by staining with Phalloidin, visualizing filamentous, polymerized actin, and acetylated Tubulin antibodies to visualize stabilized microtubules (Fig. 20A, D).
To be able to identify inhibitory synapses, the inhibitory postsynaptic scaffold molecule Gephyrin was stained. As Gephyrin is the main postsynaptic scaffold protein, also changes in its composition and submembranous lattice could induce degeneration of inhibitory synapses. One pathway that has been described to be crucially involved in the molecular organization of Gephyrin is the mTOR pathway. Activation of the mTOR pathway results in increased Gephyrin clustering (Wuchter et al., 2012). To analyze if mTOR pathway activation is altered in Slk knockdown neurons, we stained for the phosphorylated S6 protein (pS6), which is commonly used as an indicator for mTOR pathway activation (Liu et al., 2014; L. Yang et al., 2014) (Fig. 20E).

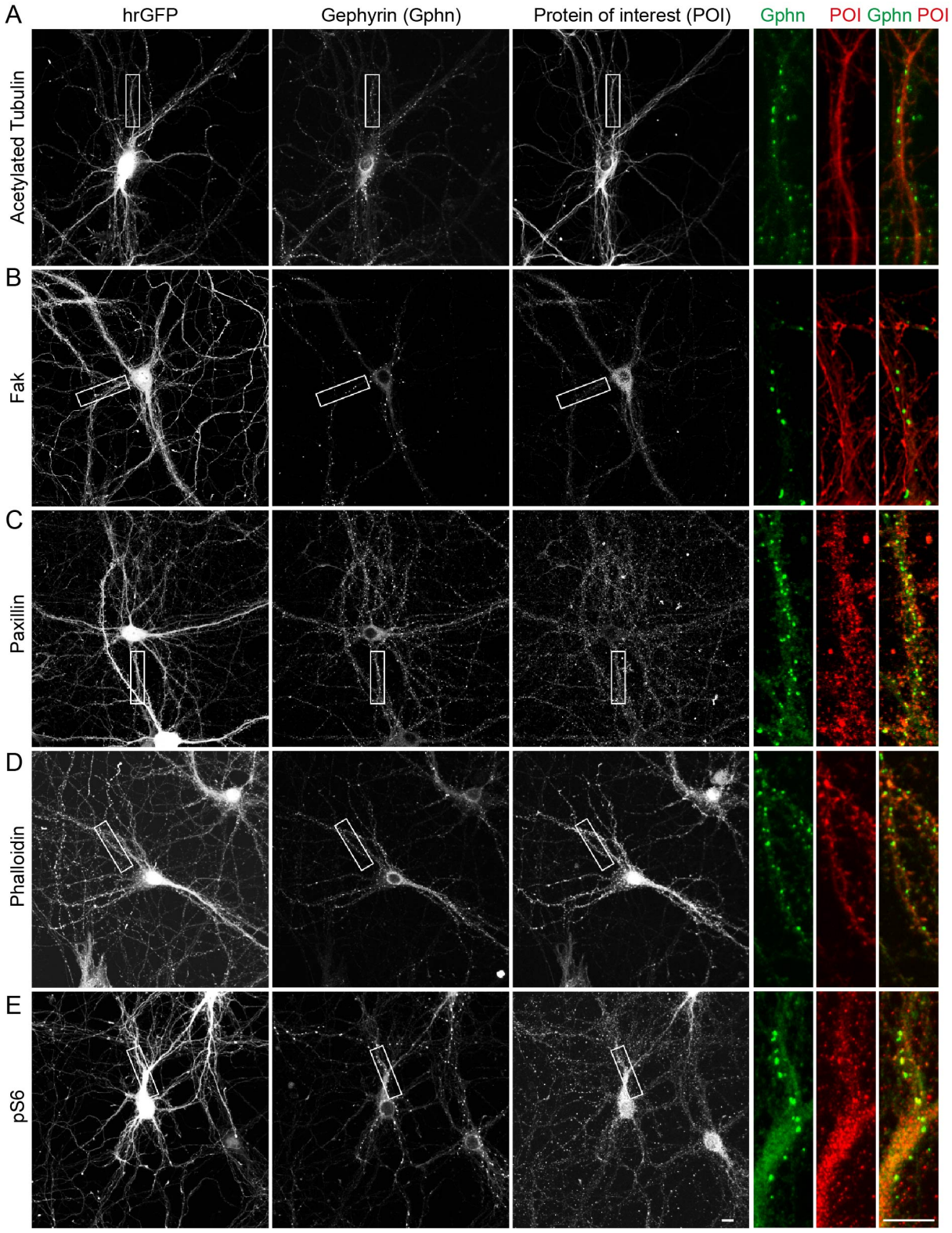


Fig. 20: Immunocytochemistry of cultured cortical neurons.
Neurons were transduced with either hrGFP or shSlk-hrGFP crude viral extracts and stained against Gephyrin and either acetylated Tubulin (A), Fak (B), Paxillin (C), Phalloidin (D), or pS6 (E). Scale bar 10 µm.

For all of the different stainings, there was no difference in the Gephyrin fluorescence intensity between control and Slk knockdown synapses (Fig. 21A). Similarly, no difference was detected

for the candidate proteins investigated (Fig. 21B). As a possible degeneration of inhibitory synapses could be accompanied or preceded by a reduction in the size of the inhibitory synapse, we also quantified the synapse sizes (Fig. 21C). The frequency distributions of control and Slk knockdown synapse sizes overlapped completely, showing that Slk does not seem to influence synapse size in cultured cortical neurons (Fig. 21D).

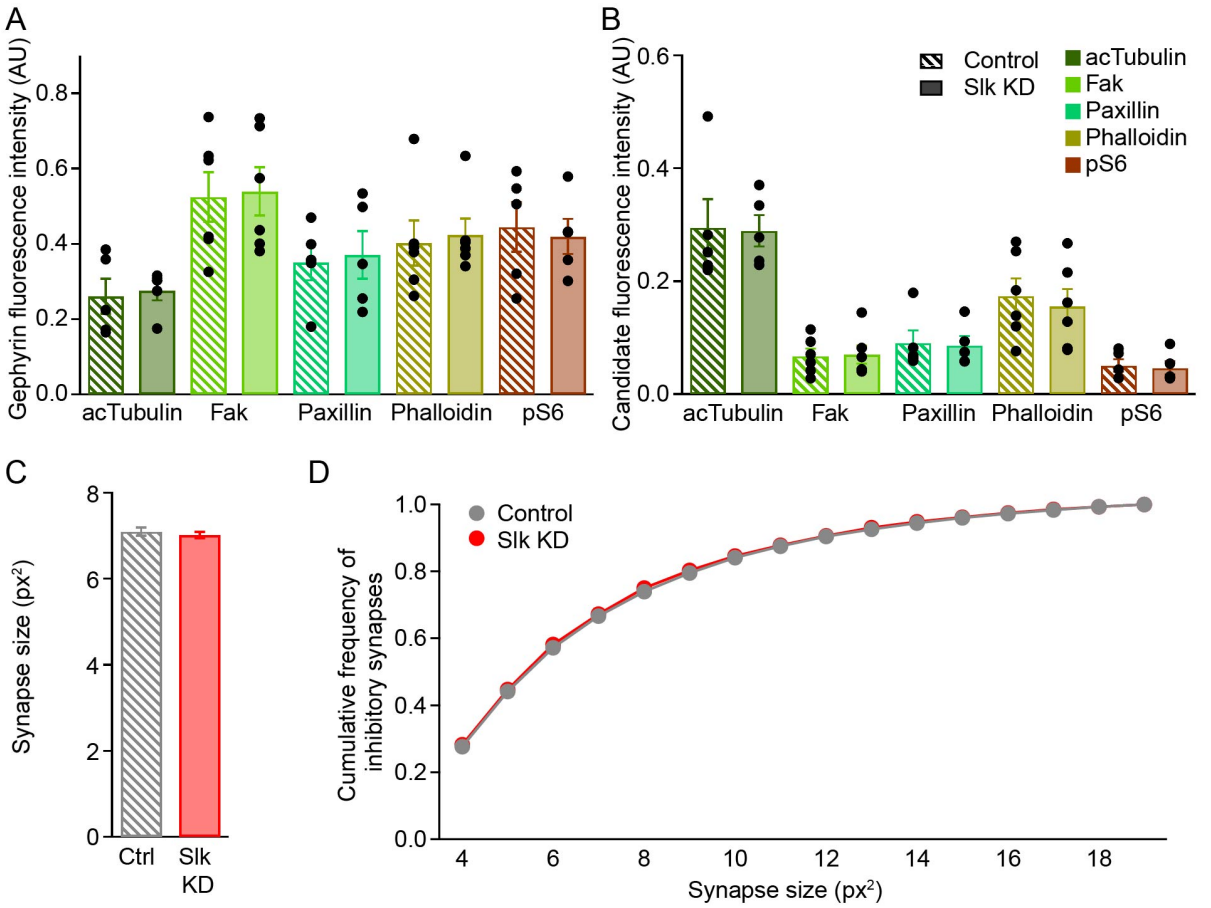


Fig. 21: No change in candidate proteins at inhibitory synapses in control and Slk knockdown (KD) neurons. Cultured cortical neurons were stained at DIV14 for different candidate proteins. (A) The fluorescence intensity of Gephyrin was analyzed in each of the different stainings. No significant difference could be found between control neurons and Slk KD cells. (B) There was also no significant change in the fluorescence intensity of acetylated Tubulin, Fak, Paxillin, Phalloidin, or pS6 at inhibitory synapses between control and Slk KD cells. (C) The size of inhibitory synapses does not change between control and Slk KD neurons. (D) The frequency distribution of inhibitory synapse sizes was comparable between control and Slk KD neurons showing that Slk also does not influence synapse size in cultured cortical neurons (arbitrary units (AU)). N = 5-6 neuronal cultures with n = 3-6 images per condition. Two-way RM ANOVA: Condition (Control vs. Slk KD) not significant (A): (Interaction: p(F=0.3138; df=4, 22) = 0.8657; Protein of interest: p(F=3.386 df=4, 22) = 0.0265; Condition: p(F=0.3777; df=1, 22) = 0.5451; (B): (Interaction: p(F=0.2064; df=4, 22) = 0.9321; Protein of interest: p(F=16.05; df=4, 22) < 0.0001; Condition: p(F=0.5760; df=1, 22) = 0.4559 (D): (Interaction: p(F=1.570; df=15, 60) = 0.1102; Synapse size: p(F=459.9; df=15, 60) < 0.0001; Condition: p(F=1.000; df=1, 4) = 0.3739); Šidák's multiple comparisons test, not significant. Paired t-test: (C): p(t=0.0292, df=26) = 0.3619.

4.2.2 Reduced F-actin in dendrites after Slk knockdown

Even though Slk does not seem to influence known interactors from non-neuronal cells in inhibitory synapses of neurons, it could still be possible that Slk interacts with these structures in other parts of the neuron. Slk knockdown specifically affected distal dendritic arborization, which points to structural alterations. As the cytoskeleton is the key player in dendrite outgrowth, cellular morphology, and stability, we next investigated if Slk affects actin or microtubule dynamics in neuronal dendrites.

Therefore, cultured cortical neurons were transduced with hrGFP or shSlk-hrGFP rAAV crude viral extracts and then stained for acetylated Tubulin to assess stabilized microtubules and for Phalloidin which labels F-actin (Fig. 22A, B). The fluorescence intensity of acetylated Tubulin in the dendrites was comparable between control and Slk knockdown neurons (Fig. 22C) and did not change between dendrites that were more proximal and dendrites that were more distal from the soma (Fig. 22D). However, there was a significant reduction in the amount of F-actin in Slk knockdown compared to control neurons (Fig. 22E). As Slk is mainly important for the proper formation of the distal dendritic tree, it might be that the actin cytoskeleton is differently affected depending on whether dendrites are more proximal or more distal to the soma. To investigate that, the fluorescence intensity of Phalloidin was analyzed in evenly spaced rings around the soma. Surprisingly, the reduction of F-actin in Slk dendrites was stable across the assessed rings and therefore independent of the distance to the soma (Fig. 22F).

As a consequence, Slk seems to have a stabilizing effect on the actin cytoskeleton, leading to more F-actin in the dendrites of neurons.

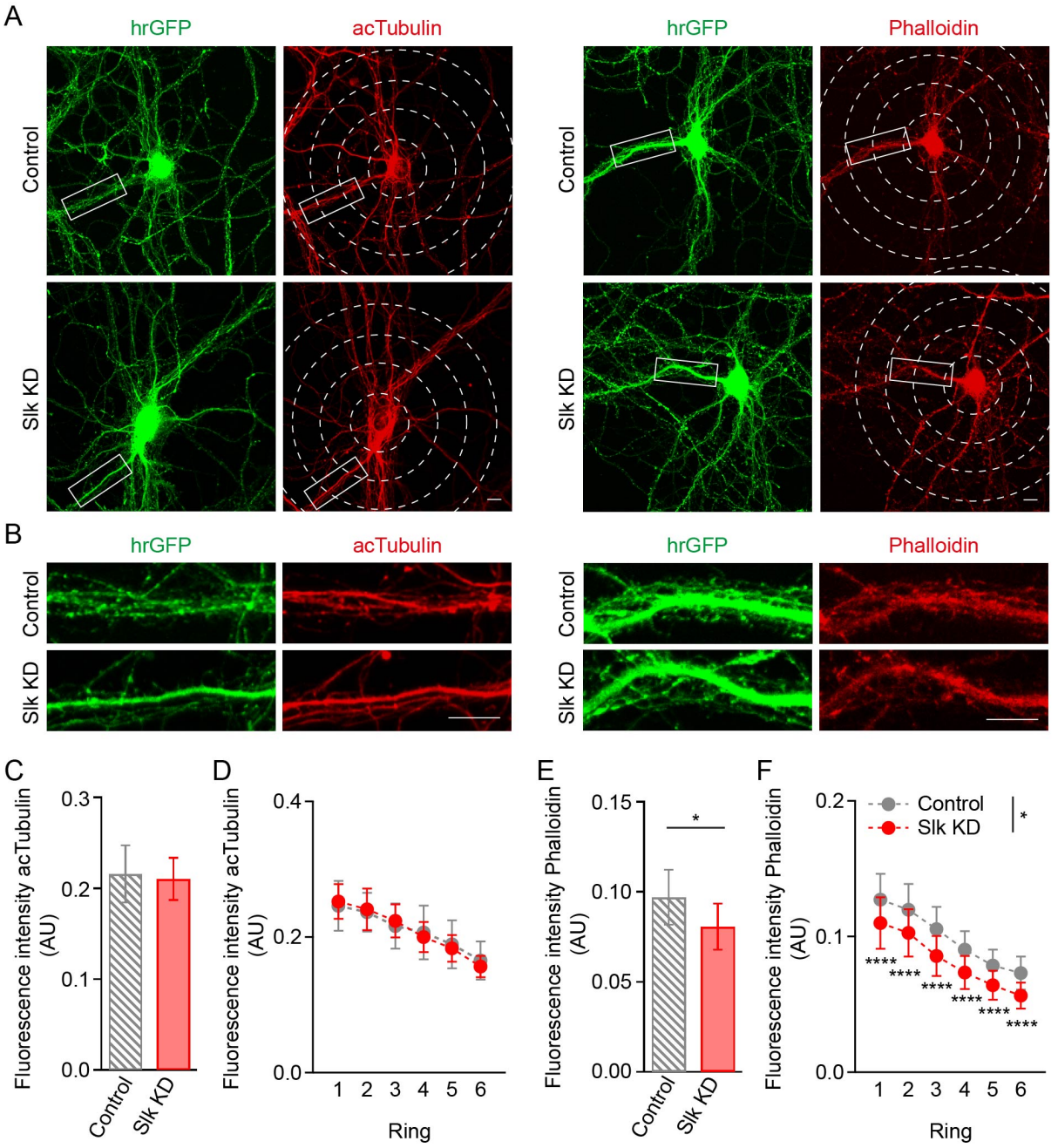


Fig. 22: Cytoskeletal changes in dendrites after Slk knockdown (KD).
(A) Cultured cortical neurons were transduced with rAAV crude viral extracts (hrGFP or shSlk-hrGFP) and stabilized microtubules were stained with acetylated Tubulin while F-actin was visualized with Phalloidin. Scale bar: 10 µm. (B) Neurites of the cells from panel A are shown in greater magnification. Scale bar: 10 µm. (C) No significant difference in the fluorescence intensity of acetylated Tubulin reflecting the amount of stabilized microtubules was detected. (D) The fluorescence intensity of acetylated Tubulin in dendrites was comparable between control and Slk KD neurons irrespective of distance to the soma. (E) The fluorescence intensity of Phalloidin in the dendrites was significantly lower in Slk KD compared to control neurons. (F) This reduction of F-actin was independent of distance from the soma, which is shown by the quantification of fluorescence intensity in rings around the soma (ring spacing: 0.21 µm) (arbitrary units (AU)). N = 5-6 independent neuronal cultures with n = 4-6 images per condition. Ratio paired t-test; (C): p(t=1.705, df=3) = 0.1633; (E): p(t=3.393, df=5) = 0.0194; * p < 0.05. Two-way RM ANOVA: (D): Condition (Control vs. Slk KD) not significant (Interaction: p(F=0.5369; df=5, 20) = 0.7460; Dendrite distance: p(F=50.78 df=5, 20) < 0.0001; Condition: p(F=0.0007113; df=1, 4) = 0.9800; Šidák's multiple comparisons test: not significant; (F): Condition (Control vs. Slk KD) * p < 0.05 (Interaction: p(F=0.4638; df=5, 25) = 0.7994; Dendrite distance: p(F=30.19; df=5, 25) < 0.0001; Condition: p(F=11.36; df=1, 5) = 0.0199; Šidák's multiple comparisons test: **** p < 0.0001.

4.3 Identification of interaction partners of Slk by proteomics studies

4.3.1 Identifying changes in phosphorylation after Slk knockdown

Even though there was a first hint that Slk can influence the actin cytoskeleton, it is still not clear how and through which protein interactions this is mediated intracellularly. To be able to analyze protein-protein interactions of Slk in neurons in an unbiased way and on a large scale, we conducted three different proteomics approaches. The first one was a phosphoproteomics screen to identify potential phosphorylation substrates of Slk. As Slk is a serine/threonine kinase, many effects in neurons will likely be mediated via phosphorylation of substrate proteins. To identify these, cultured cortical control neurons were transduced with a virus expressing a control fluorescent protein, shSlk to knock down Slk expression, or Slk to overexpress the protein. At DIV14, the cells were lysed and the phosphorylation status of the proteins was analyzed by LC-MS/MS (Fig. 23A). The viral transduction of neurons resulted in a two-fold increase for the overexpression (Fig. 23B) and a robust 93% decrease in Slk expression levels for the knockdown condition (Fig. 23C).

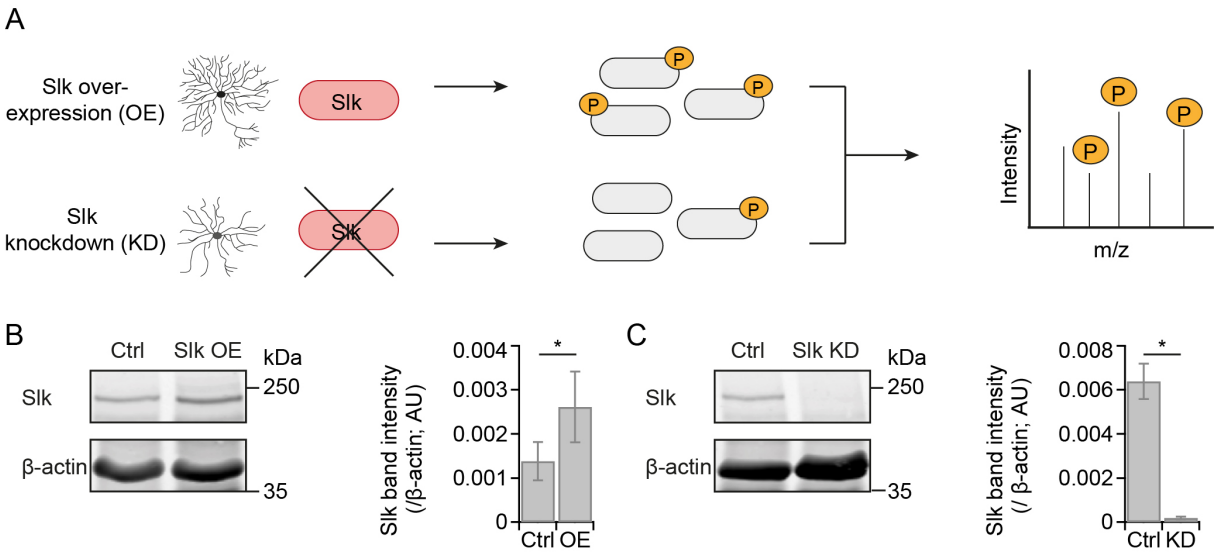


Fig. 23: Screen for phosphorylation substrates of Slk in neurons.
(A) Cultured cortical neurons were transduced with lentivirus expressing mCherry or mCherry-2A-Slk to overexpress Slk and mRFP or shSlk-mRFP to knock down Slk expression. At DIV14, neurons were lysed, proteins were enriched for phosphoproteins and these were analyzed by LC-MS/MS. (B) Transduction of neurons with mCherry-2A-Slk increased Slk expression two-fold which was confirmed by immunoblotting. (C) Knocking down Slk by transduction of shSlk reduced Slk expression by 93% in immunoblotting experiments (arbitrary units (AU)). n = 5. Paired t-test; (B): p(t=3.178, df=4) = 0.0336; (C): p(t=3.890, df=4) = 0.0177; * p < 0.05.

When analyzing the phosphorylation profile of the proteins, we were interested in the changes between control and overexpression or control and knockdown condition, as these phosphorylations are either directly executed by Slk or at least mediated and influenced by Slk. By plotting the first dimensions of a PCA, there was no clear separation between control

and overexpression samples (Fig. 24A) while control and Slk knockdown samples were clustered by condition (Fig. 24B). For the overexpression condition, the phosphorylation of only three proteins was significantly different compared to the control condition (Fig. 24C). After knocking down Slk, 1060 phosphorylation sites were differentially regulated. 512 phosphorylation sites were less phosphorylated in the knockdown condition, which makes them potential direct phosphorylation sites of Slk (Fig. 24D). A similar number of sites, 548, were stronger phosphorylated after Slk knockdown which suggests an indirect involvement of Slk. Among the strongest differentially phosphorylated sites were cytoskeletal proteins such as Map1b and Nefh, proteins that are known to influence the outgrowth of dendrites such as Igf2bp1, Chl1, Nav1, and Crmp1, and also synaptic proteins such as Sv2a.

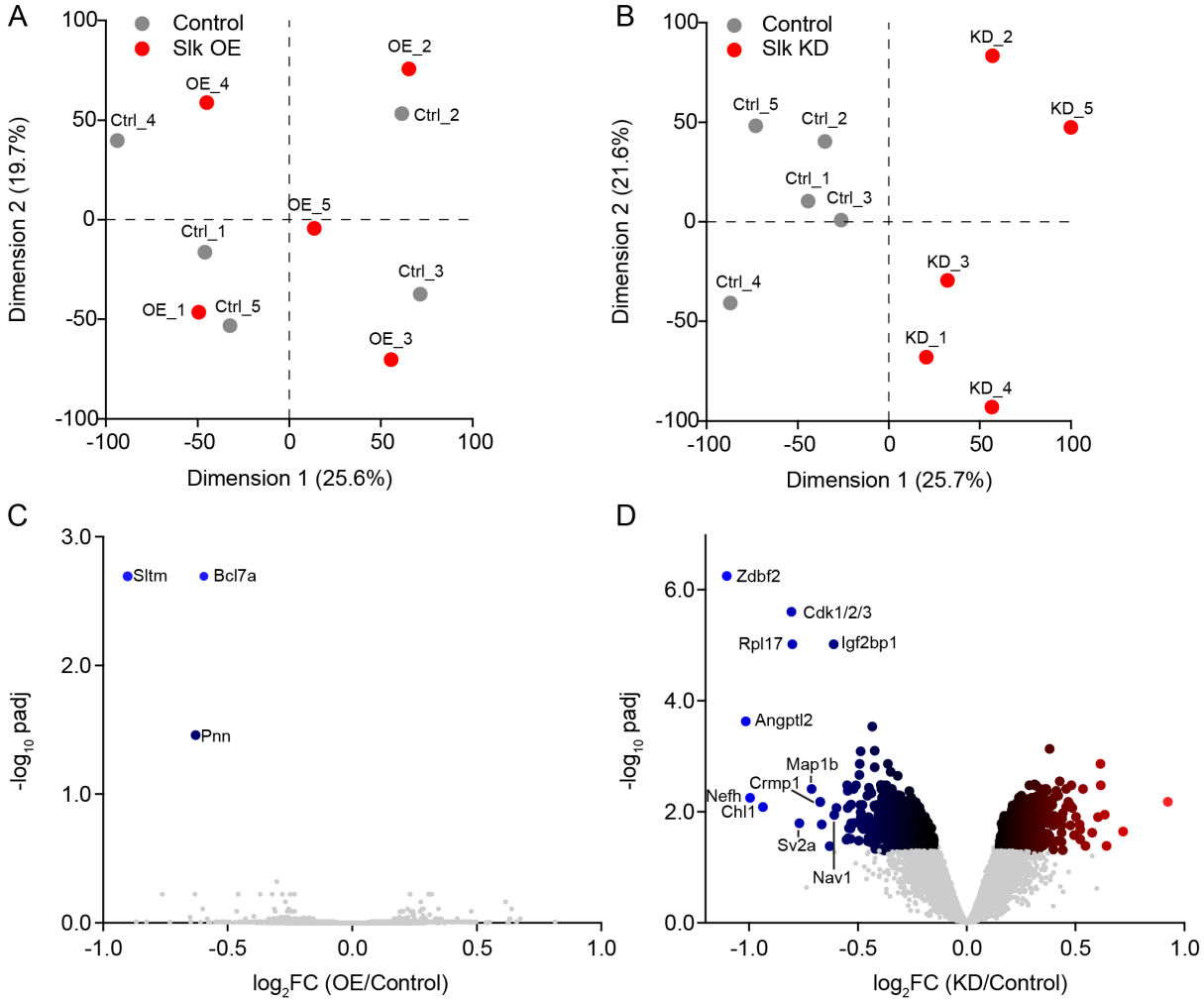


Fig. 24: Phosphorylation profile of cultured cortical neurons after Slk overexpression or knockdown.
(A) Overexpressing Slk in cultured cortical neurons did not result in a clear separation of the phosphorylation pattern between control (Ctrl) and overexpression (OE) samples. (B) Samples from control and shSlk-transduced neurons (KD) are separated in the PCA plot after analyzing the phosphorylation status of proteins. (C) In the overexpression condition, only three proteins were significantly differentially phosphorylated compared to control samples. (D) After Slk KD, the volcano plot shows significantly regulated phosphorylation sites (black), that either are less phosphorylated (blue) or more phosphorylated (red) in the KD compared to the control condition. n = 5.

All sites with reduced phosphorylation in the Slk knockdown condition could potentially be regulated directly by Slk while increased phosphorylation suggests an indirect mechanism of Slk via other kinases and phosphatases. Both, direct and indirect mechanisms could give hints about cellular locations and functions that Slk is involved in. Therefore, proteins with significantly regulated phosphorylation sites were annotated both for their cellular localization and their function. Proteins with increased and decreased phosphorylation were highly enriched for synaptic proteins, specifically those at the postsynaptic density. Furthermore, proteins important at cell junctions and for the cytoskeleton were amongst the significantly enriched terms (Fig. 25A). Functionally, proteins were involved in important processes of nervous system development, synaptic processes, and also cytoskeletal dynamics (Fig. 25B). As the enrichment for synaptic structures and functions underlines the previous results of Slk effects at synapses, a more detailed analysis of the proteins was conducted to specify synaptic location and function. Many of the regulated proteins were part of membrane components (M) in the presynaptic and the postsynaptic part (Fig. 25C). This suggests that after Slk knockdown, phosphorylation patterns change predominantly at membranous structures that form the border of the cell and at the same time are the place where connections are made to extracellular structures and neighboring cells. The functions of the analyzed proteins are either organization (SO) and assembly (SA) mainly of postsynaptic structures, or processes involved in chemical synaptic transmission (CS) such as synaptic vesicle cycle (VC) or regulation of postsynaptic neurotransmitter levels (NR) (Fig. 25D).

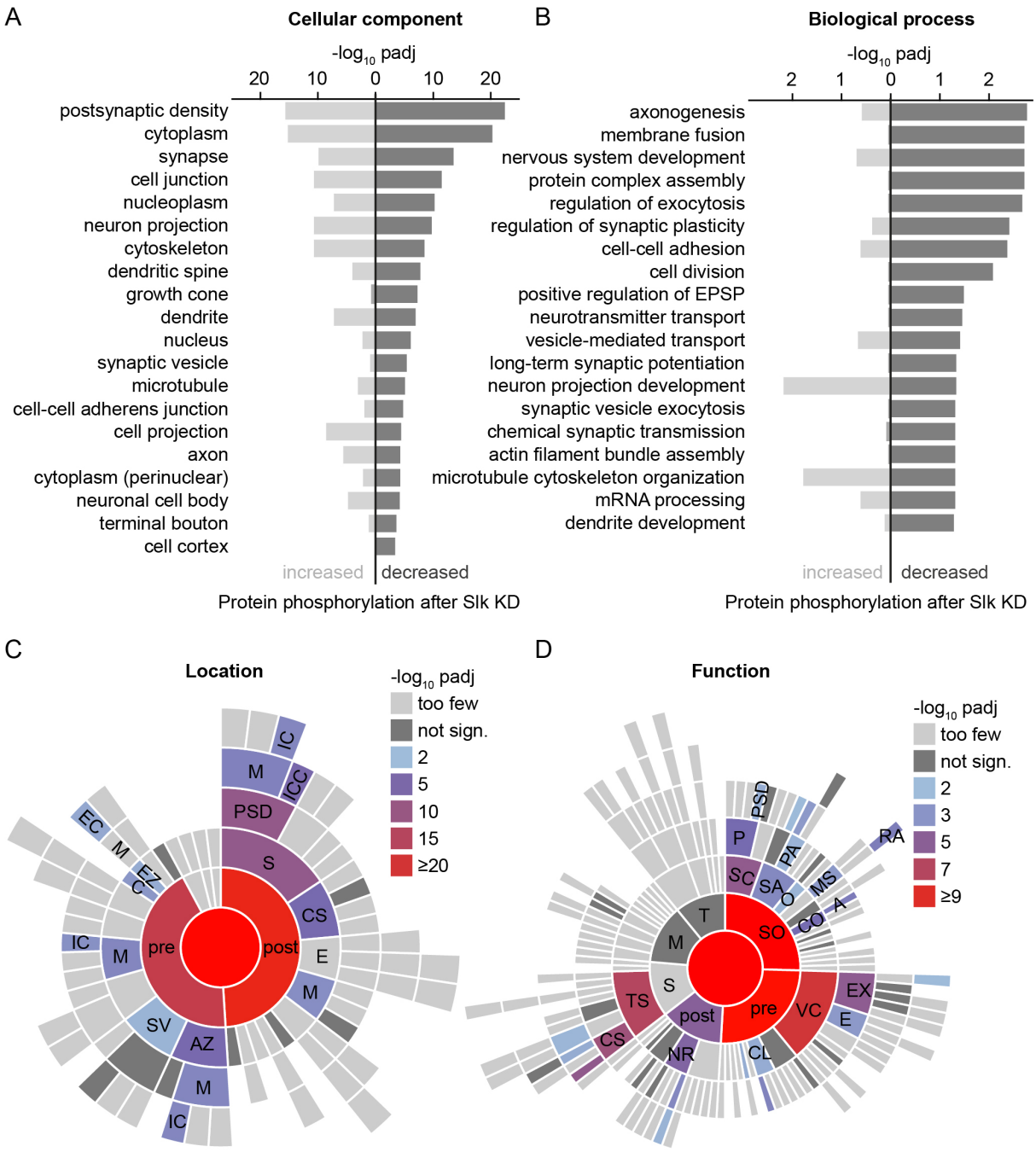


Fig. 25: Annotation of significantly differentially phosphorylated proteins after Slk knockdown (KD). Significantly differentially phosphorylated proteins (phosphorylation sites with padj < 0.05 & $\log_2$FC > |0.15|) were annotated according to their localization (A) in cells and the function (B) they are involved in. All significantly enriched terms for phosphorylation sites with decreased phosphorylation in Slk KD are visualized in descending order (dark gray). As the strongest enrichment was found for proteins at postsynaptic densities, a SynGO analysis was conducted to specify the locations (C) and functions (D) of the proteins at synaptic sites. (C) AZ: active zone, C: cytosol, CS: cytoskeleton, E: endosome, M: membrane, IC: integral component, ICC: intracellular component, EC: extrinsic component, EZ: endocytic zone, PSD: postsynaptic density, S: postsynaptic specialization. (D) SO: synapse organization, pre: presynaptic process, post: postsynaptic process, S: signaling, M: metabolism, T: transport, SC: structural constituent of synapse, P: structural constituent of postsynapse, SA: synapse assembly, PA: postsynaptic specialization assembly, TS: transsynaptic signaling, VC: vesicle cycle, CS: chemical synaptic transmission, NR: regulation of postsynaptic membrane neurotransmitter receptor levels, CL: regulation of presynaptic cytosolic calcium levels, E: synaptic vesicle endocytosis, EX: synaptic vesicle exocytosis, CO: postsynaptic cytoskeleton organization, MS: modification of postsynaptic structure, RA: regulation of modification of postsynaptic actin cytoskeleton, A: postsynaptic actin cytoskeleton organization.

Among the differentially phosphorylated proteins, proteins that are binding to specific structures, proteins, or protein domains are upregulated (Fig. 26A). Among the most significantly enriched terms are microtubule and actin binding, again suggesting a link between Slk and the cytoskeleton. Interestingly, proteins binding to microtubules show both increased and decreased phosphorylation after Slk knockdown, while proteins binding to actin are predominantly less phosphorylated in the knockdown condition which could suggest a more direct effect of Slk on the actin cytoskeleton.

Many of the microtubule binding proteins are involved in microtubule polymerization and depolymerization and two of them negatively regulate Tubulin deacetylation (Fig. 26B). However, in the experiment in which acetylated Tubulin was quantified in cultured cortical control and Slk knockdown neurons, we did not find a difference in the intensity of acetylated Tubulin. Of the actin binding proteins, one-third of them are regulating actin polymerization and one-third are involved in organizing cellular projections (Fig. 26C). These results could be nicely correlated to our previous finding of reduced F-actin levels in the dendrites of Slk knockdown neurons and suggest a function of Slk in the polymerization of the actin cytoskeleton.

The analysis of differentially regulated sites after Slk knockdown gave an idea about neuronal functions and processes that Slk is involved in. A next interesting question was to identify proteins that are directly phosphorylated by Slk and that are therefore immediate interaction partners of Slk. Even though reduced phosphorylation after Slk knockdown could be an indication that Slk itself is participating in phosphorylating that site, there are other possibilities as well. Slk could also activate other kinases directly and indirectly or inhibit phosphatases. If that activation/inhibition is missing in neurons with reduced Slk levels, less phosphorylation of the respective phosphorylation site will be observed as well.

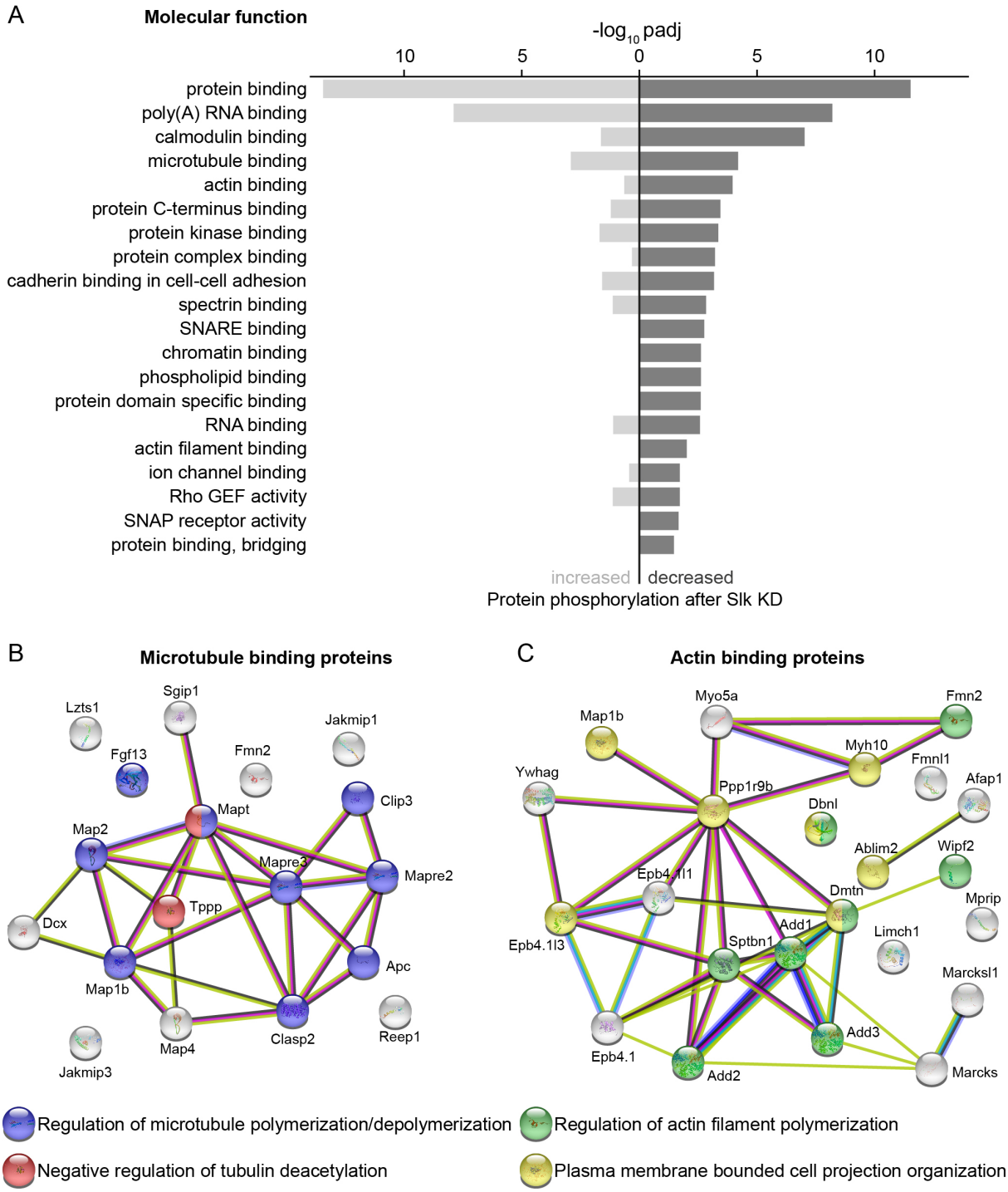


Fig. 26: Annotation of the molecular function of differentially phosphorylated proteins after Slk knockdown (KD).
(A) Proteins with phosphorylation sites that had a padj < 0.05 & $\log_2$FC > |0.15| were functionally annotated. There was a significant enrichment of proteins that bind to different structures and domains. (B) Microtubule binding proteins extracted from (A) were mostly regulating polymerization and depolymerization of microtubules. (C) Actin binding proteins were involved in regulating actin filament polymerization and organizing cell projections. Visualization: STRING database.

To be able to narrow down the number of potential direct substrates of Slk, a phosphorylation motif was created based on published known phosphorylation substrates of Slk. Surprisingly,

Slk seemed to have different motif preferences depending on whether a serine or threonine was phosphorylated. Therefore, different putative motifs were created based on the phosphorylated amino acid. For serine phosphorylation, Slk seemed to prefer polar uncharged amino acids (serine/glutamine) in combination with the basic amino acid arginine (Fig. 27A) while for threonine phosphorylation, basic amino acids (arginine/lysine) were dominating (Fig. 27B). In addition, a combined motif of the S and T phosphorylation site was created (Fig. 27C).

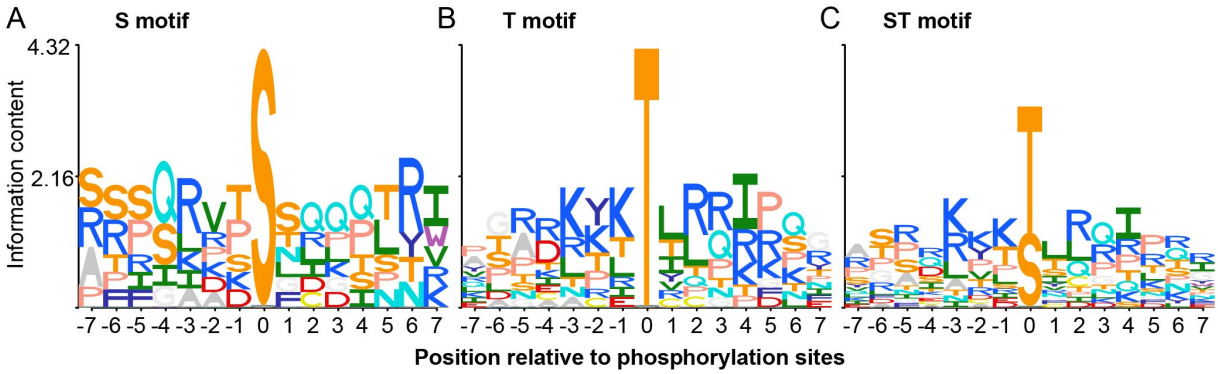


Fig. 27: *In vitro* phosphorylation motifs of Slk.
Phosphorylation motifs were computed based on known phosphorylation substrates. Amino acid preferences surrounding the phosphorylated amino acid depend on if serine or threonine is phosphorylated. The motif of the phosphorylated amino acid plus seven flanking amino acids on both sides was computed for serine (A), threonine (B), and serine/threonine combined (C).

The Slk motifs were integrated with 159 other known kinase phosphorylation motifs and for each of the detected phosphorylation sites in the mass spectrometry screen, the probability that a given kinase would phosphorylate this site was calculated. Among the 531 significantly regulated phosphorylation sites that were less phosphorylated in the Slk knockdown condition, 54 sites were fitting to at least one of the computed Slk motifs (Fig. 28). For some of the proteins such as Mink1/Tnik/Map4k4, the site fits predominantly the phosphorylation motif of specifically Slk, but for other proteins such as Mapre2, the phosphorylation site would also fit the motif of multiple other kinases.

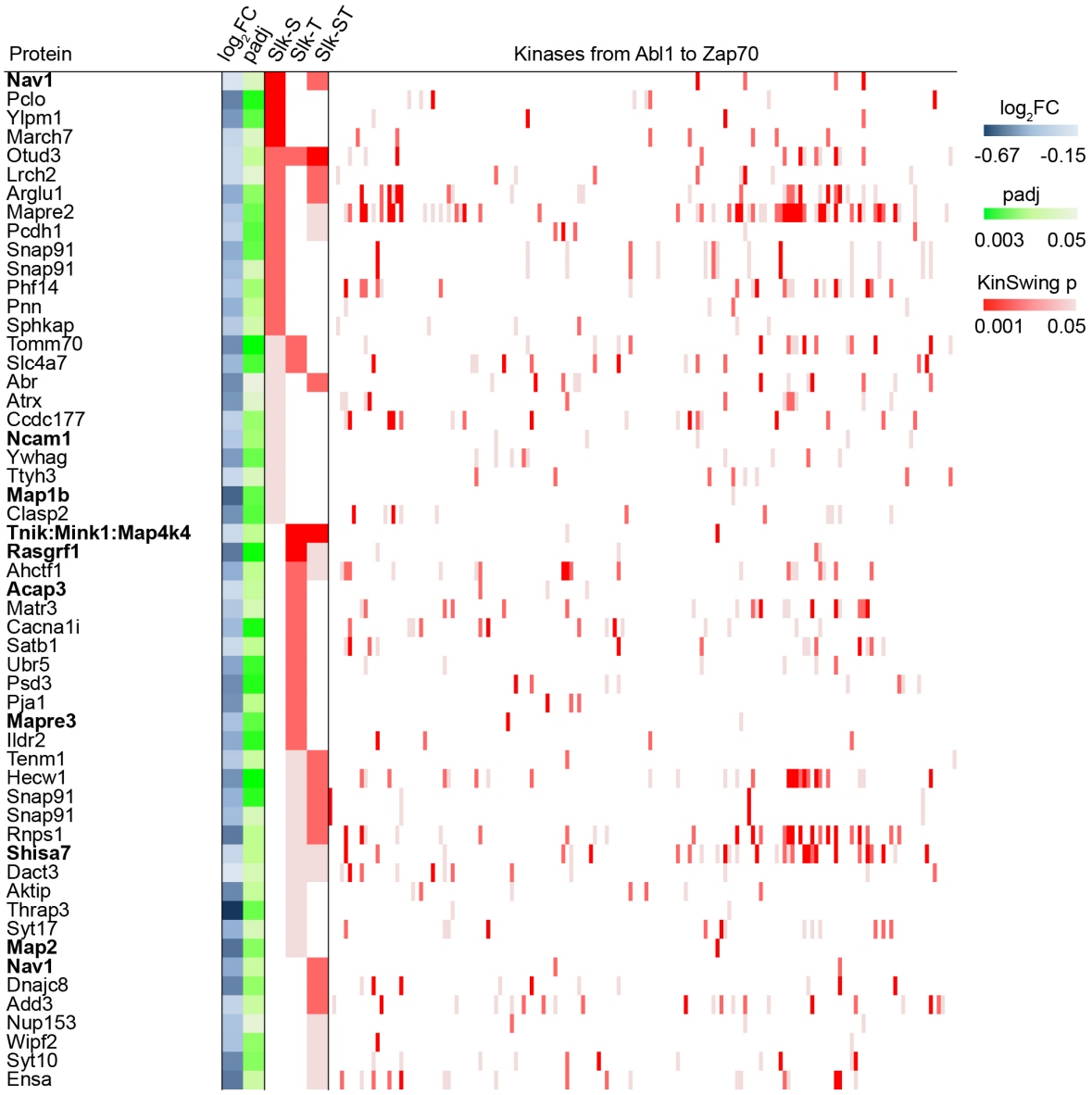


Fig. 28: KinSwing analysis of measured phosphorylation sites.
The probability that a particular kinase phosphorylated a site detected in the mass spectrometric experiments was calculated. All phosphorylation sites that were significantly less phosphorylated in Slk knockdown ($log_2FC < -0.15$ & padj < 0.05) and had a KinSwing p < 0.05 for one of the Slk phosphorylation motifs were plotted in this table. In addition, potential phosphorylation of these motifs by other kinases was included.

Many of the proteins with phosphorylation sites that are similar to the Slk motif, regulate the organization of cellular components, cell communication, or the cytoskeleton. Around one-third correspond to proteins that are part of structures involved in cell-cell or cell-matrix communication such as cell junctions and synapses (Fig. 29A). Interestingly, most of the synaptic proteins are classified as postsynaptic proteins, maybe underlining a stronger involvement of potential Slk interactions at postsynaptic sites. The great majority of the proteins with an Slk phosphorylation motif are already annotated phosphoproteins. Three out of them are not only phosphoproteins but also have kinase activity themselves (Fig. 29B).

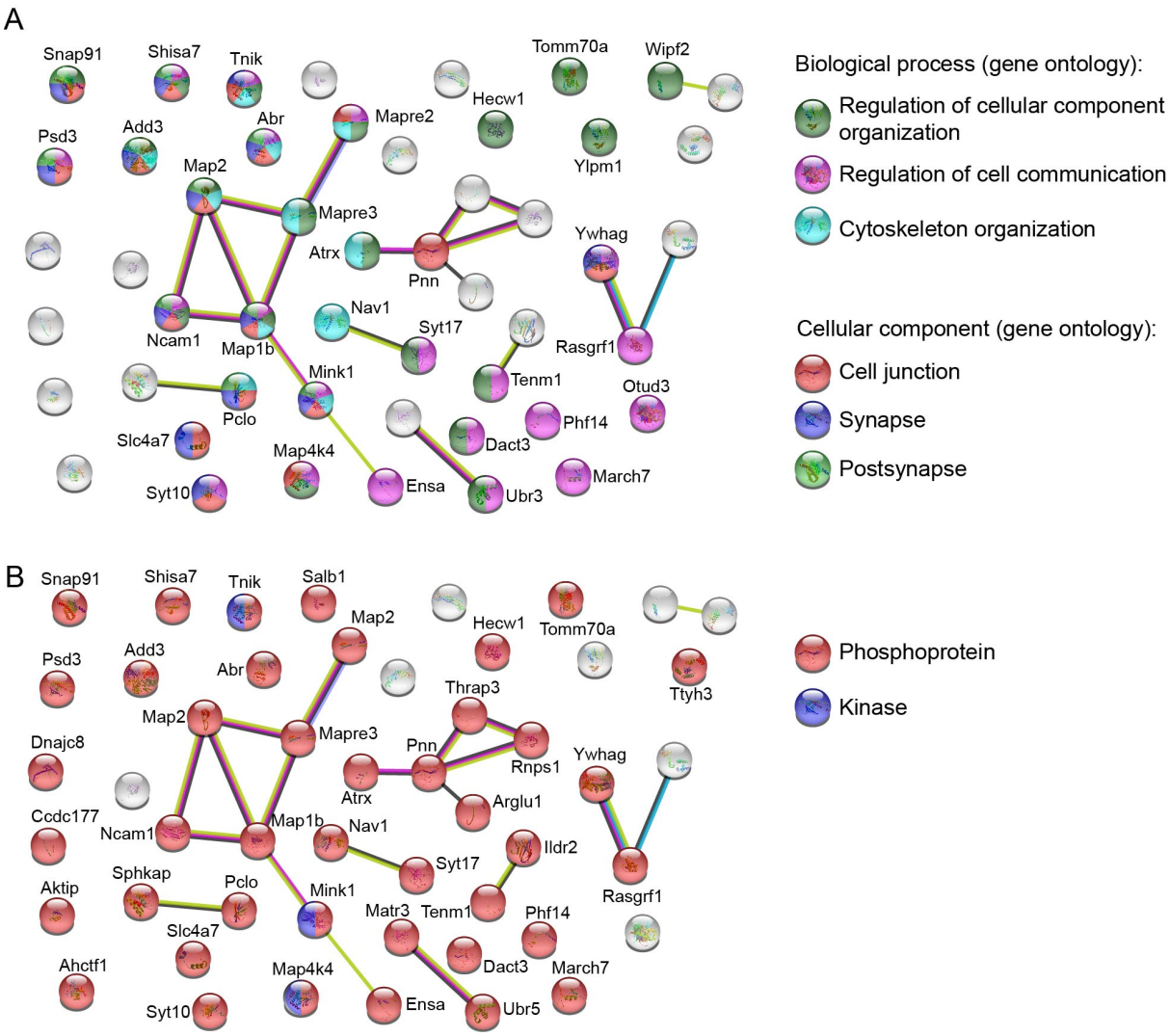


Fig. 29: Classification of proteins with phosphorylation sites matching the computed Slk motifs.
(A) String analysis showed that proteins participate in different biological processes and that many proteins are part of cellular junctions or synapses. (B) Most of the proteins are already classified as phosphoproteins. Three of the proteins have kinase functions themselves, thereby suggesting a possible cascade of signal transduction. Visualization: STRING database.

Thereby, the screen for phosphoproteins after Slk knockdown revealed many possible direct phosphorylation substrates of Slk in addition to pointing to direct and indirect phosphorylation cascades that Slk might be involved in.

4.3.2 Identifying proteins proximal to Slk in neurons (BioID)

As some of the effects of Slk in non-neuronal cells are independent of its kinase activity, protein-protein interactions of Slk might also hint toward the mechanism of the kinase in neurons. One method that is highly sensitive and can detect physiologically relevant and at the same time weak or transient interactions is proximity-dependent biotinylation. This technique uses a modified biotin ligase BirA R118G (BirA*) that is fused to the protein of interest. After the addition of biotin, the biotin ligase starts to biotinylate the lysine residues of proteins in

close proximity, which has been shown to reach a radius of around 10 nm (Kim et al., 2014). BirA* was cloned in a lentiviral expression vector together with a fluorescent reporter protein (Fig. 30A). In addition, a fusion protein of Slk and BirA* was created in the same vector to be able to characterize proteins proximal to Slk (Fig. 30B).

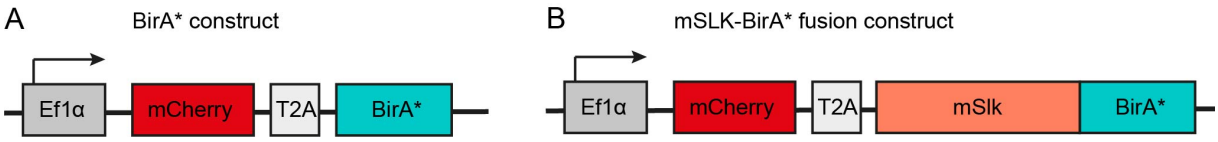


Fig. 30: Cloning of BirA* expression constructs for proximity-dependent biotinylation experiments.
(A) BirA* was cloned into a lentiviral expression vector that also expresses mCherry. A T2A peptide links mCherry and BirA* and leads to the separation of the two proteins during translation. (B) An Slk-BirA* fusion protein was cloned in the same lentiviral vector.

To test the functionality of the generated constructs, the plasmids were transfected into HEK293T cells. 24 hours before harvesting, the medium was supplemented with different concentrations of biotin. In the control condition, the addition of biotin did not increase the biotinylation of proteins (Fig. 31A). When BirA* was expressed in the cells, the addition of biotin induced the biotinylation of a variety of proteins of different sizes. For the fusion protein Slk-BirA*, mainly large proteins got biotinylated. The biotinylation activity of both constructs, BirA* alone and the fused Slk-BirA* construct, was significantly induced by adding biotin (Fig. 31B). To transfer the experiment to cultured neurons, lentivirus expressing Slk as a control or Slk-BirA* together with the fluorescent protein mCherry were prepared. Transduced neurons were biotinylated for 24 hours before harvesting. The strongest biotinylated proteins in neurons were carboxylases that have biotinylated subunits (Bramwell, 1987) and that are found in the control and the Slk-BirA* condition. Apart from that, an increase in biotinylated proteins was mainly detected for proteins with high molecular weight (Fig. 31C). After having confirmed that biotinylation occurs in neurons as well, neuronal cell lysates were prepared for the mass spectrometry experiment. Therefore, the neurons were transduced with Slk or Slk-BirA* expressing lentiviruses, biotinylated for 24 hours, and then lysed. The biotinylated proteins were purified and analyzed by LC-MS/MS (Fig. 31D).

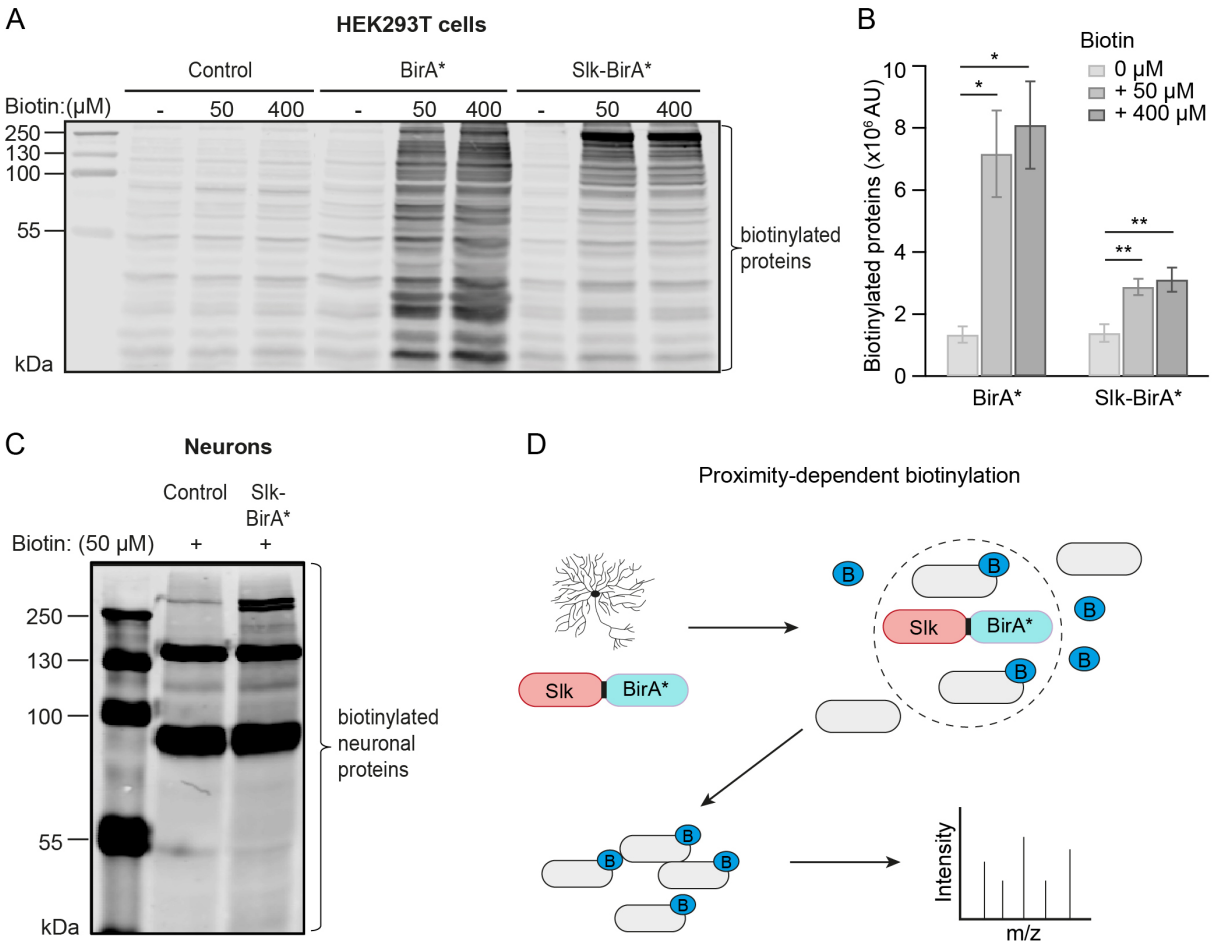


Fig. 31: Proximity-dependent biotinylation in cultured HEK293T cells and primary neurons.
(A) HEK293T cells were transfected with the BirA*-expressing constructs or a control construct that only expressed the fluorescent protein. After biotinylation for 24 hours, cells were harvested and lysed. Immunoblotting of the lysate with streptavidin showed strong biotinylation of proteins for the BirA* construct. The Slk-BirA* fusion protein strongly biotinylated especially large proteins. (B) The amount of biotinylation observed in the immunoblot of (A) was quantified for the different conditions (arbitrary units (AU)). (C) Neurons were transduced with pLenti-mCherry-T2A-Slk (control) or pLenti-mCherry-T2A-Slk-BirA* expressing lentivirus and biotinylated for 24 hours before harvesting. Immunoblotting with streptavidin points to proteins with high molecular weight to be biotinylated by Slk-BirA*. (D) Neurons which were transduced with control or Slk-BirA* expressing lentivirus were biotinylated and harvested at DIV14-16. Biotinylated proteins were purified and analyzed by LC-MS/MS. Mass spectrometric analysis was done in collaboration with Shiva Ahmadi. n = 4 HEK293T cultures and n = 4 neuronal cultures. Two-way RM ANOVA: (B): (Interaction: p(F=15.66; df=2, 12) = 0.0005; Treatment: p(F=44.58; df=1.061; 6.364) = 0.0004; Condition: p(F=8.463; df=1, 6) = 0.0270); Holm-Šidák's multiple comparisons test: BirA*: 0 vs. 50 µM: p = 0.0203; 0 vs. 400 µM: p = 0.0203; Slk-BirA*: 0 vs. 50 µM: p = 0.0080; 0 vs. 400 µM: p = 0.0080; * p < 0.05; ** p < 0.01.

The control and the Slk-BirA* condition were detected in separate clusters by PCA analysis while the replicates of the same condition were found in one cluster (Fig. 32A). 197 proteins were significantly enriched in the Slk-BirA* condition (padj < 0.05) and 17 were more than two-fold enriched ($log_2FC > 1$) compared to controls (Fig. 32B). Among the highest enriched proteins is Slk itself, which can be interpreted as a positive control. As Slk is known to act as a dimer (Cybulsky et al., 2017), biotinylation of Slk was expected. The strongest enriched protein was Kidins220, which is an ankyrin repeat-rich membrane-spanning protein. Knockdown of Kidins220 in primary hippocampal neurons reduced the complexity of dendritic

arbors (Chen et al., 2012). This finding could be replicated by knocking down Kidins220 through IUE, which not only impaired dendritic branching but also neuronal migration (Chen et al., 2012). In another study, Kidins220 was shown to interact with Tubulin and several microtubule-regulating proteins such as Map1a, Map1b, and Map2 (Higuero et al., 2010). Another protein that was enriched in the Slk-BirA* condition, Hook3, is also interacting with the microtubule cytoskeleton. This protein is an adaptor that binds to Dynein and Dynactin complexes and activates the transport of cargo toward the minus end of microtubules (Kendrick et al., 2019; Schroeder and Vale, 2016). Talin1 (Tln1), too, is functioning as an adaptor protein that is important at focal adhesions. At these extracellular–intracellular contact points, Talin1 binds to integrin subunits and links them to other components of focal adhesions such as Vinculin and Fak and the actin cytoskeleton (Desiniotis and Kyprianou, 2011; Calderwood et al., 1999; Jin et al., 2015). Apart from Slk, the kinase Prkcg is among the stronger enriched proteins. Prkcg is important for dendrite development and synaptic function through its phosphorylation activity (Winkler et al., 2020).

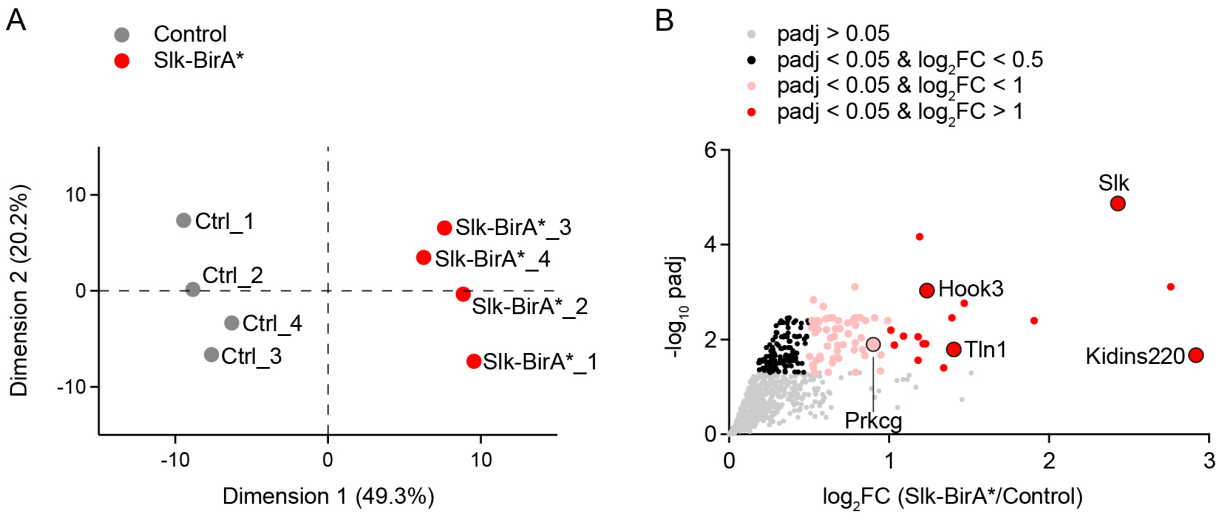


Fig. 32: BioID analysis.
(A) Mass spectrometric detection of biotinylated proteins in control (Ctrl) versus Slk-BirA* transduced neurons resulted in two distinguishable groups in the PCA plot. (B) The volcano plot marks proteins that are significantly enriched in the Slk-BirA* condition in red. n = 4.

By these proximity-dependent labeling experiments, we identified several proteins that might be involved in the Slk pathway as they fulfill cellular functions that could be related to Slk function in neurons.

4.3.3 Identifying binding partners of Slk (CoIP)

One advantage of the proximity-dependent labeling approach is the fact that also weak and transient interactions between proteins can be detected. This is especially interesting given

the fact that Slk as a protein kinase will presumably establish many kinase-substrate contacts that usually do not involve strong binding (Lee et al., 2017). However, the BioID experiment does not differentiate between direct and strong binding partners and weak or even only neighboring interactions as the amount of biotinylation does not solely depend on the quality of interaction but also on the available lysine side chains of the protein, where the biotin is attached (Roux et al., 2018).

Therefore, the next step on the way to shed light on the pathway of Slk in neurons was to identify direct binding partners of Slk by CoIP. To this end, proteins from whole-brain lysate were incubated with Slk purified from HEK293T cells and the proteins that co-immunoprecipitated with Slk were visualized by a Coomassie-stained SDS gel (Fig. 33A). For mass spectrometric identification of proteins, five bands that were exclusively appearing in the CoIP with Slk and not in the control, indicating specific binding to Slk, were excised (Fig. 33B). To be able to also identify proteins that were binding weaker to Slk, the whole lanes of co-immunoprecipitated proteins were excised in a second approach and analyzed by mass spectrometry.

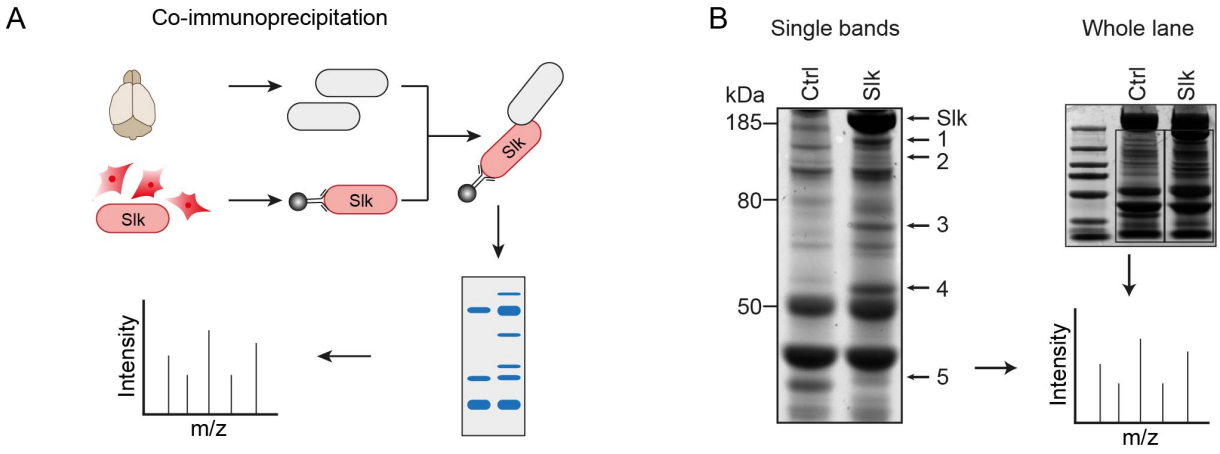


Fig. 33: CoIP of brain proteins with Slk.
(A) The scheme depicts the workflow, starting with the preparation of protein lysates from mouse brains that were incubated with Slk purified from HEK293T cells. After CoIP, proteins were separated on an SDS-gel and visualized by Coomassie staining. (B) Bands that were only visible in the CoIP with Slk and not in the control condition, indicating proteins that specifically bind to Slk, were excised and analyzed by mass spectrometry. In addition, the whole lane of all proteins was excised for control and Slk co-immunoprecipitated proteins, and analyzed by mass spectrometry. n = 4.

In total, 842 proteins were found to be significantly and at least twofold more enriched after CoIP with Slk compared to control (Fig. 34A). 142 even were more than 8-fold enriched in comparison to control ($log_2FC > 3$). Around 18% of the significantly enriched proteins were annotated as cytoskeletal proteins, while 10% were annotated as cell adhesion proteins. Likewise, 10% of the proteins were attributed to the postsynapse. When we compared the proteins with protein complexes that were described to be found at excitatory postsynaptic

densities (ePSDs) and inhibitory postsynaptic densities (iPSDs) (Uezu et al., 2016), around 2% could be attributed to the ePSD while twice as much, around 4%, were iPSD specific.
For the analysis of the single excised bands, 679 different proteins could be identified (Fig. 34B). 60% of all the proteins were identified in band 1, which corresponds to a band at the size of around 130 kDa. The finding that many large proteins seem to be binding to Slk corresponds to the BioID results, which also implied that Slk might be surrounded primarily by proteins with a large molecular weight. More than half of the proteins that were identified in the single bands were also detected in the whole lane approach (Fig. 34C). The fourteen most enriched proteins in both approaches included cell surface proteoglycans (Gpc6, Gpc1, Gpc5), proteins involved in translation (Rars, Ngdn), transmembrane proteins (Nrxn3, Tmeff1, Tmeff2), and the kinases Tnik and Mink1 (Fig. 34D).

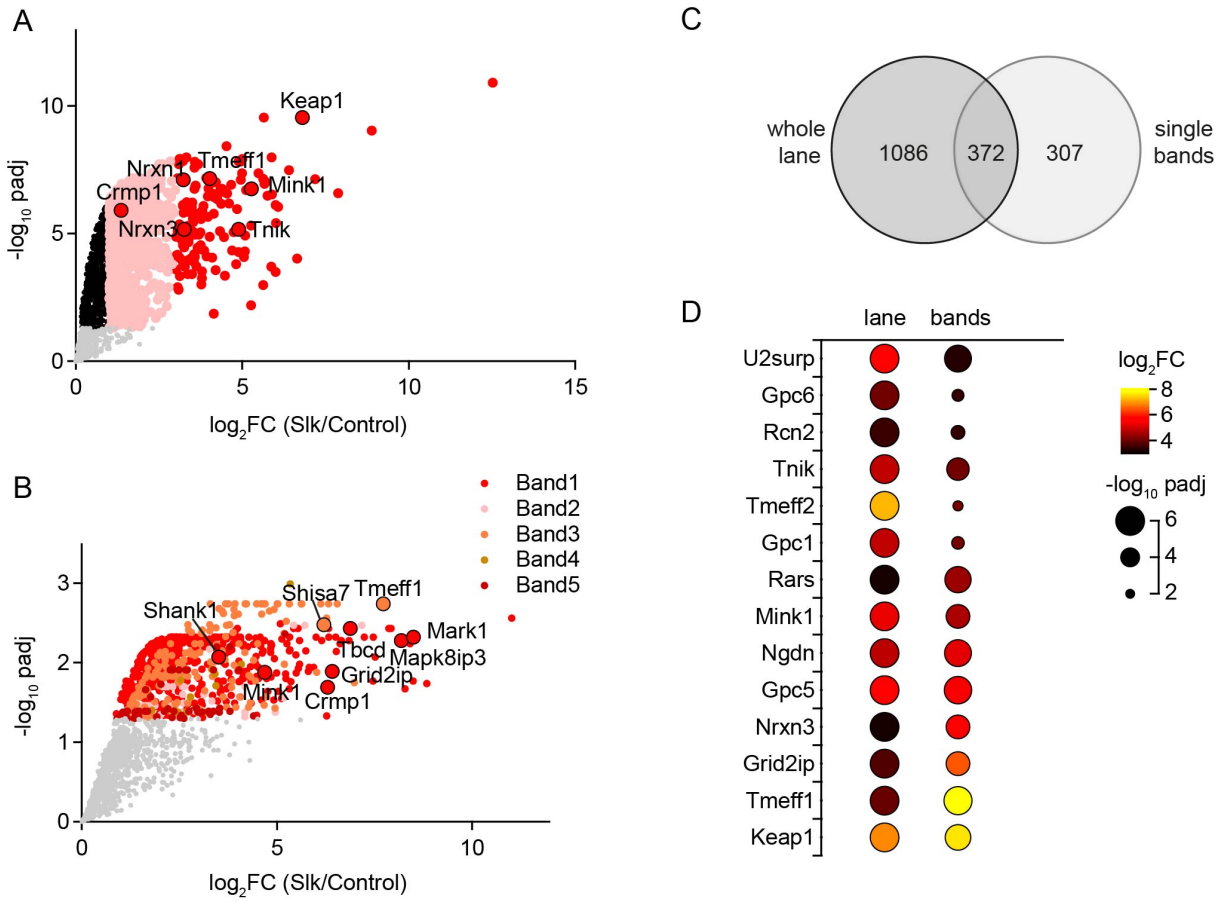


Fig. 34: Mass spectrometric analysis of co-immunoprecipitated proteins.
(A) Proteins of the whole lane of the Coomassie gel were analyzed by mass spectrometry. 1458 proteins were significantly enriched (padj < 0.05) after CoIP with Slk compared to control. (B) Five different bands were excised from the Coomassie after CoIP with Slk and analyzed by mass spectrometry. 679 unique proteins were significantly enriched. (C) 372 proteins were identified both in the whole lane analysis and in the single excised bands. (D) 14 out of these proteins had a $log_2FC > 3$ in both approaches.

4.3.4 Proteins identified in multiple proteomics studies

As proteins that are phosphorylated by Slk will also be proximal to Slk and potentially even bind to Slk, it was interesting to analyze proteins that were identified in more than one of the proteomics approaches. Over 200 proteins were identified to be binding to Slk in one of the CoIP approaches and being differentially phosphorylated after Slk knockdown (Fig. 35A). 80 proteins were identified to be proximal and binding to Slk (Fig. 35B) and 22 were proximal to Slk and differentially phosphorylated (Fig. 35C). 6 proteins (Table 8) were identified in all of the proteomics approaches (Fig. 35D).

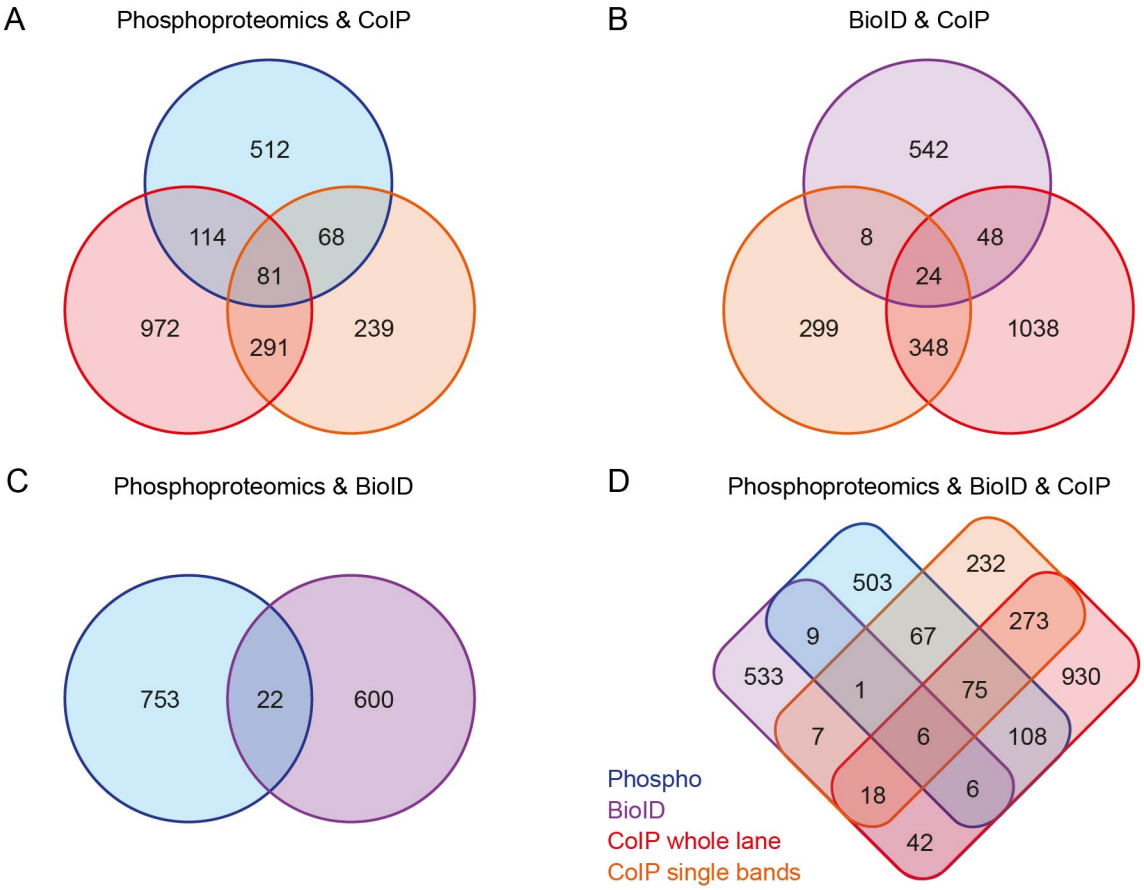


Fig. 35: Overlap of the three different proteomics approaches.
Differentially phosphorylated proteins were identified by phosphoproteomics, proximal proteins by BioID, and binding proteins by CoIP experiments coupled with mass spectrometry. (A) Around 200 proteins were binding to Slk and found to be differentially phosphorylated after Slk knockdown. (B) 80 proteins that were proximal to Slk in the BioID experiments were found to also bind to Slk in the CoIP. (C) 22 proteins were proximal to Slk and differentially phosphorylated after Slk knockdown. (D) The Venn diagram shows the number of proteins that are found in all of the different approaches. Phosphoproteomics: padj < 0.05; BioID + CoIP: padj < 0.05 & $\log_2$FC > 0.

Two out of these six proteins showed reduced phosphorylation after Slk knockdown, namely Ddx17, an RNA helicase that is involved in DNA repair (Fortuna et al., 2021), and Kpnb1 (Importin subunit β) that is involved in nuclear protein import for example of histone proteins (Apta-Smith et al., 2018). Ap3d1, Pacs1, and Prkcg all increased the phosphorylation after Slk

knockdown, which indicates that none of them is a direct substrate of Slk. Ap3d1 is a subunit of the AP-3 complex that transports proteins from the cell body towards neurites and synapses (Larimore et al., 2011). A homozygous mutation in the Ap3d1 protein was identified in a patient with neurodevelopmental delay and generalized seizures (Ammann et al., 2016). Prkcg is a brain-specific isoform of the protein kinase C. One of its substrates are γ-Protocadherins which regulate dendritic branching (Garrett et al., 2012). Treatment with a Prkcg activator decreased dendritic branching in wild-type neurons (Keeler et al., 2015). In Purkinje cells, Prkcg controls the outgrowth of dendrites via phosphorylation of Crmp2 (Winkler et al., 2020). However, Prkcg is not only important for dendrite branching but also for synapse development as Prkcg binds to the $GABA_AR$ and is inversely correlated with its activity (Bright and Smart, 2013; Meier et al., 2003). Therefore, Prkcg could be involved in the pathway of Slk function as it was repeatedly discovered to interact with Slk and mediates similar functions. However, it is not a direct substrate of Slk and therefore not a direct downstream candidate.

Table 8: Proteins that were found in all of the proteomics approaches.
Phosphoproteomics: padj < 0.05; BioID + CoIP: padj < 0.05 & $log_2FC > 0$.

Protein	Phosphoproteomics		BioID	CoIP	
	Phosphorylation site	log_2FC	log_2FC	Single bands: log_2FC	Whole lane: log_2FC
Ap3d1	S760; S784	0.18; 0.22	0.37	2.70	0.78
Ddx17	S520	-0.31	0.19	2.13	0.76
Kpnb1	S12	-0.22	0.27	1.76	1.01
Pacs1	S491	0.27	0.66	4.24	1.43
Prkcg	S322	0.33	0.90	2.22	1.37
Slk	S340; S666	-0.99; -0.92	2.43	9.50	8.44

Apart from the proteins that were detected in all proteomics studies, we also verified that previously described interactors of Slk were found in one or more of the proteomics screens. Among the proteins that were already described in the literature to interact with Slk were the postsynaptic scaffold protein Shank3 and Asap1, a protein that stimulates metastasis formation and tumor cell motility and invasion (Müller et al., 2010) (Table 9). The fact that already described Slk interactors were found in our proteomics datasets provides validation to our data.

Table 9: Comparison of proteomics results with known substrates and interaction partners of Slk.
Padj < 0.05.

Protein	Reference	Phosphoproteomics		BioID	CoIP	
		Phosphorylation site	log_2FC	log_2FC	Single bands: log_2FC	Whole lane: log_2FC
Actn4	(Jaberi et al., 2015)					0.96
Asap1	(Müller et al., 2010)	S732	0.28			1.16
Eftud2	(Malinová et al., 2017)					1.09
Fgb	(Huttlin et al., 2017)					1.57
Gtf2e2	(Huttlin et al., 2017)					1.26
Hgs	(Pourhaghighi et al., 2020)					0.76
Hist1h1c	(Potekhina et al., 2003)			0.37		
Hist1h1d	(Potekhina et al., 2003)			0.38		1.35
Jnk / Mapk8	(Luhovy et al., 2012)					0.69
Keap1	(Hast et al., 2014)				7.51	6.8
Map4	(Wan et al., 2015)	T657 / S667; S899 / S841	0.25 / 0.5 / -0.18		1.65	0.79
Mbp	(Burakov et al., 2005)	S250	-0.31		1.89	
Nono	(Havugimana et al., 2012)					0.62
Nsfl1c	(Wan et al., 2015)	S114 / S140	-0.20 / -0.37			
Shank3	(Li et al., 2017, 2016)	S387 / S1073 / S1577	0.31 / 0.38 / 0.32		2.35	

A second validation step was to identify proteins in more than one of the proteomics approaches, thereby increasing the likelihood of being a true interactor. Interestingly, the overlap between binding proteins and proteins being differentially phosphorylated (CoIP and phosphoproteomics) was larger than the overlap between proximal and differentially phosphorylated proteins (BioID and phosphoproteomics). Usually, kinase-substrate interactions are low-affinity, transient bindings that are hard to discover by CoIP experiments

(Lee et al., 2017). However, for Slk, there might be a substantial overlap between binding and phosphorylated proteins.

To have a closer look at the proteins that were found both in the CoIP and phosphoproteomics experiments, GO analysis was conducted. The overlapping proteins were mainly involved in binding to the cytoskeleton or part of the cytoskeleton (Fig. 36A). Furthermore, proteins with guanine nucleotide exchange factor (GEF) activity were significantly enriched.

The greatest enrichment regarding the cellular localization of these proteins was found for the postsynaptic density. Also here, many proteins were identified as cytoskeletal proteins or linked to the cytoskeleton (Fig. 36B).

To be able to discover direct phosphorylation substrates of Slk, the great overlap of proteins being differentially phosphorylated after Slk knockdown and proteins that were binding to Slk offered the chance to further narrow down the number of potential substrates. All proteins that are less phosphorylated after Slk knockdown could theoretically be phosphorylated by Slk. If this protein is additionally also binding to Slk, this could be another hint of a direct interaction such as a substrate-kinase interaction.

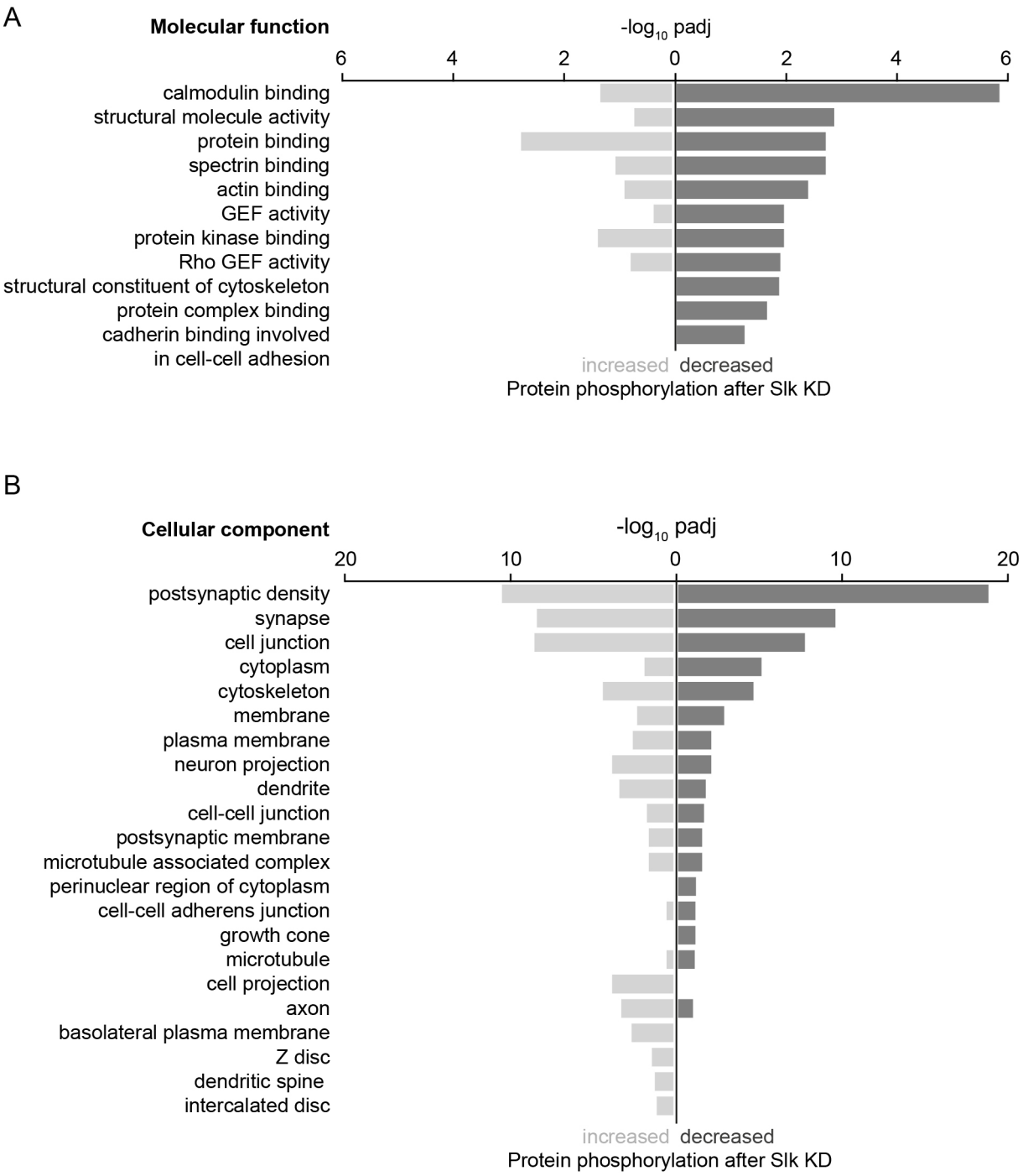


Fig. 36: GO analysis of proteins identified in phosphoproteomics and CoIP experiments.
(A) Proteins that were identified in the CoIP and phosphoproteomics experiments were analyzed for their molecular function. (B) Similarly, enrichment of the overlapping proteins regarding their cellular localization was analyzed. Phosphoproteomics: padj < 0.05 & CoIP whole lane + single bands: padj < 0.05 & $log_2FC > 0$. All enriched GO terms with padj < 0.05 are displayed.

45 proteins were detected that are strongly binding to Slk and less phosphorylated after Slk knockdown (Fig. 37A). Many of them are described to be found at synaptic sites, often specifically at postsynaptic densities (Fig. 37B). Cytoskeletal proteins and proteins with

guanine nucleotide exchange factor (GEF) / GTPase activating-protein (GAP) activity are also among the top candidates.

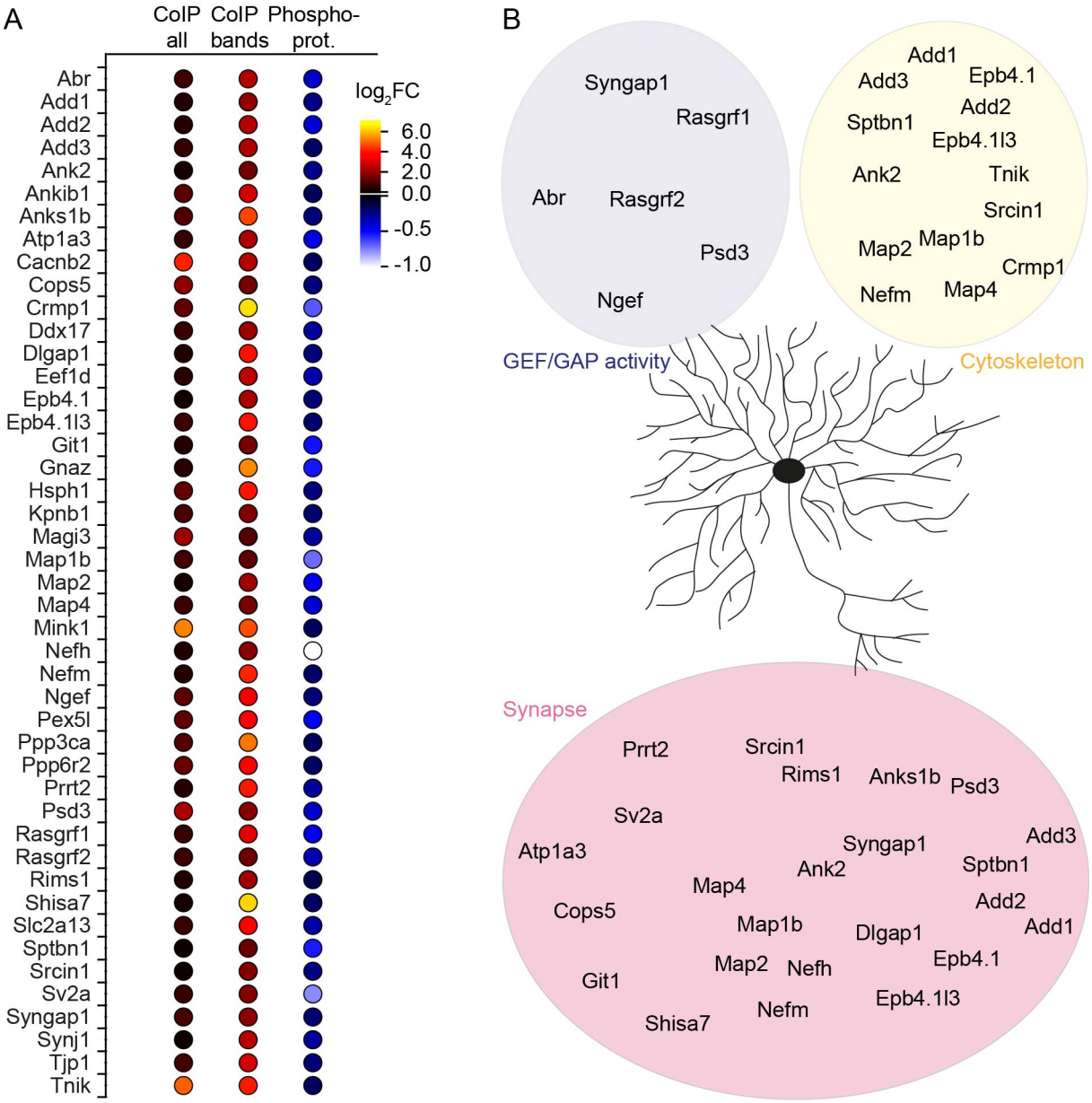


Fig. 37: Proteins that are binding to Slk and less phosphorylated after Slk knockdown.
(A) 45 proteins were identified in the CoIP and phosphoproteomics experiments. (B) The identified proteins are found at synapses or associated with the cytoskeleton. In addition, there was enrichment for proteins with GEF activity. Phosphoproteomics: padj < 0.05 & log_2FC < -0.15; CoIPs: padj < 0.05 & log_2FC > 0.

4.4 Verification of interaction partners from proteomics studies

4.4.1 Grlf1 phosphorylation

As we had previously observed that Slk knockdown results in decreased F-actin levels in dendrites of cultured neurons, one of the proteins that are involved in cytoskeletal dynamics

and were differentially phosphorylated after Slk knockdown could provide a mechanistic explanation for the F-actin decrease. RhoA controls F-actin polymerization and this GTPase has been described to interact with Slk in non-neuronal cells. In our data, we did not find differential phosphorylation or binding of RhoA to Slk. But we did identify a GTPase-activating protein, Grlf1, that supports the GTP hydrolysis to convert active RhoA-GTP into inactive RhoA-GDP (Fig. 38A), which then results in F-actin depolymerization. Grlf1, which is also called p190RhoGAP, was phosphorylated stronger after Slk knockdown at Y1105, which is known to be an activating phosphorylation (Hernández et al., 2004; Shen et al., 2008). Additionally, Grlf1 was also binding to Slk in the CoIP experiment (Table 10).

Table 10: Identification of Grlf1 in phosphoproteomics and CoIP experiments.
Padj < 0.05.

Protein	Phosphoproteomics		CoIP
	Phosphorylation site	log_2FC	Whole lane: log_2FC
Grlf1	Y1105	0.34	2.09

Therefore, the aim was to verify the phosphorylation that was previously identified by mass spectrometry in immunoblotting experiments, as a phospho-specific antibody detecting Y1105 phosphorylation was commercially available. In cultured cortical neurons, Slk was knocked down by transduction with shSlk-mRFP expressing lentivirus. At DIV14, neurons were harvested and the immunoblot was performed against Grlf1, the phosphorylated pGrlf1 Y1105, and the housekeeping gene β-actin (Fig. 38B). However, no significant difference in the phosphorylation between control and Slk knockdown neurons could be detected (Fig. 38C).

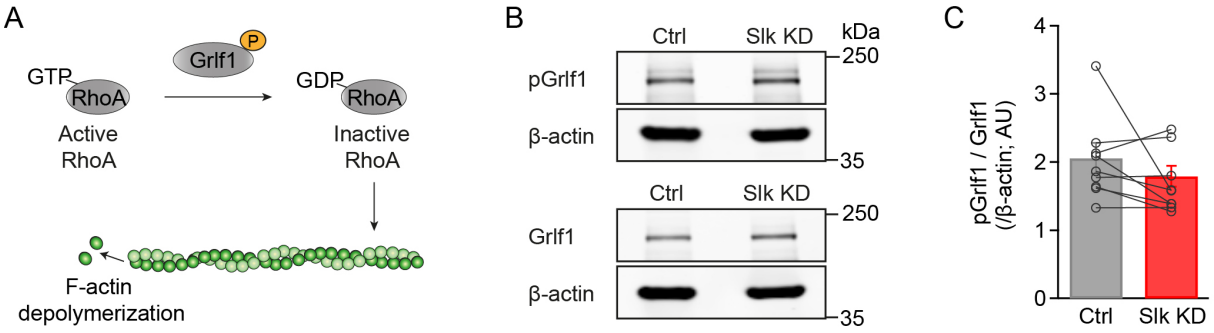


Fig. 38: No change of Grlf1 phosphorylation after Slk knockdown (KD) in cultured cortical neurons.
(A) Grlf1 is a GTPase-activating protein that upon Y1105 phosphorylation inactivates RhoA, which results in F-actin depolymerization. (B) Cultured cortical neurons were transduced with mRFP or shSlk-mRFP at DIV3-5 and harvested at DIV14 for immunoblotting experiments against Grlf1 and pGrlf1 Y1105. (C) Quantification of the band intensity of pGrlf1 and Grlf1 did not show a significant difference between control (Ctrl) and Slk KD neurons. Band intensity was normalized to β-actin (arbitrary units (AU)). n = 9. Paired t test: p(t=1.526, df=8) = 0.1655.

Thus, the 25% increase in phosphorylation after Slk knockdown that was detected by mass spectrometry could not be verified by immunoblotting experiments. This might be due to

different sensitivities of the methods but could potentially be also attributed to the specificity of the antibody. Although it was used to detect altered Grlf1 phosphorylation in another study (Yu et al., 2017), it could be that the specificity of the antibody to detect only phosphorylated Y1105 is not sufficient to identify a small increase in phosphorylation. Furthermore, it could be also possible that the increase detected by mass spectrometry was caused by biological variation and is not attributable directly to Slk knockdown.

4.4.2 Verification of binding partners of Slk (CoIP)

In a next step, we wanted to verify some of the proteins that were identified in the CoIP experiments as binding partners of Slk. In the CoIP proteomics experiment, proteins were analyzed that were co-purified with Slk. For the verification experiments, a reverse approach was chosen, where the GFP-tagged protein of interest was isolated and co-purification of Slk was checked by immunoblotting (Fig. 39A). As a negative control, GFP alone was used. In total, 14 GFP-tagged proteins were used for these experiments that had been shown to be binding to Slk in the CoIP mass spectrometry screen (Table 11).

Table 11: Proteins chosen for CoIP verification experiments.
Proteins that were identified in the phosphoproteomics screen to be differentially phosphorylated after Slk knockdown and in the CoIP screen to be binding to Slk were chosen for additional verification experiments. Gephyrin, Nav2, and Igf2bp1 were not binding to Slk in the CoIP experiments, while Shank2 and Tmeff1 were not significantly phosphorylated after Slk knockdown. Padj < 0.05.

Protein	Phosphoproteomics		CoIP	
	Phosphorylation site	log_2FC	Single bands: log_2FC	Whole lane: log_2FC
Crmp1	S518; S522 S518; S521	-0.67 -0.42	6.29	1.35
Gephyrin	T265; S270	-0.21	-	-
Igf2bp1	S181	-0.61	-	-
Map4k4	T180 S547 S558; S561 S708	-0.18 0.14 0.24 0.27	2.73	-
Mink1	T181 S537 T609 S706 T861	-0.18 0.16 0.17 0.29 0.44	4.69	5.27
Nav1	S58 S148 S510 S582	-0.23 -0.61 -0.29 -0.22	-	-

	S651 S1258	-0.16 -0.19		
Prkcg	S322	0.33	2.22	1.37
Shank1	S413 S1931	0.17 - 0.27	3.51	-
Shank2		-	2.06	-
Shank3	S387 S1073 S1577	0.31 0.38 0.32	2.35	-
Shisa7	S250	-0.19	6.2	0.28
Sv2a	S106	-0.77	1.82	0.74
Tmeff1		-	7.72	4.02
Tnik	T181 S711	-0.18 0.23	4.13	4.89

In addition, Gephyrin, Nav1, and Igf2bp1, which were not detected in the CoIP experiments but showed reduced phosphorylation after Slk knockdown, were tested. As expected, Slk was co-purified for all of the tested proteins except for the negative control GFP, Gephyrin, and Igf2bp1 (Fig. 39B). For Nav1, there seemed to be a small fraction of Slk being co-purified although it had not been detected in the mass spectrometric data. The strongest band was observed for Map4k4 and Tmeff1, the latter also being strongly enriched in the mass spectrometry experiments.

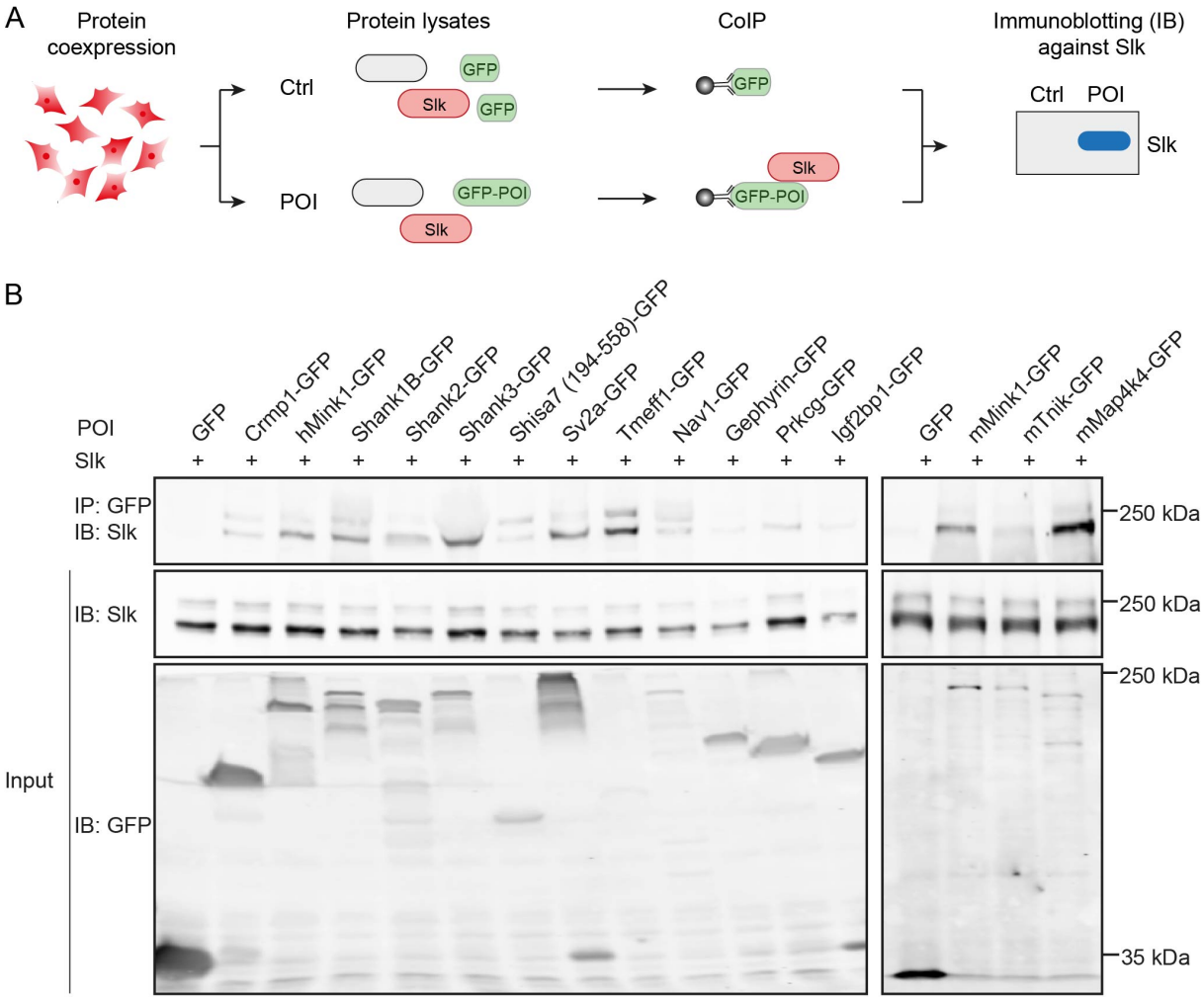


Fig. 39: CoIP with candidate proteins followed by immunoblotting.
(A) Slk and the candidate protein of interest (POI) were co-expressed in HEK293T cells. After HEK293T cell lysis, the GFP-tagged POI was immunoprecipitated with magnetic beads. A potential co-purification of Slk was checked by immunoblotting against Slk. (B) After the immunoprecipitation (IP) of the GFP-tagged proteins, it was analyzed if Slk was co-immunoprecipitated by immunoblotting (IB) against Slk. n = 5, exemplary blot shown.

4.4.3 Verification of phosphorylation substrates of Slk by *in vitro* kinase reactions

Having identified these new binding partners of Slk, it would be interesting to see if there is a direct functional link between these proteins and Slk. Therefore, we wanted to verify if proteins that were binding to Slk were also phosphorylated by the kinase. To select probable phosphorylation candidates, proteins with putative Slk phosphorylation motifs based on the KinSwing analysis were selected. In addition, we included proteins that had the strongest reduction in phosphorylation after Slk knockdown and that might play a role in neurons. Fragments of the candidate proteins that included the phosphorylation site of interest were cloned into the pGEX-GST vector and the GST-tagged proteins were purified from bacteria. Successful purification was confirmed by Coomassie staining (Fig. 40A). Subsequently, the protein fragments were incubated *in vitro* with Slk and ATP to allow potential phosphorylation.

The phosphorylation events were measured with the ADP-Glo Kinase Assay, which takes the generation of ADP as an indirect measure of kinase activity. In the first step, the remaining ATP from the kinase reaction is depleted, followed by a conversion of the produced ADP into ATP. The ATP is then used by a luciferase/luciferin reaction to generate luminescence, which is a correlate of kinase activity (Fig. 40B).

As a positive control, the reaction was established with the known Slk substrate histone H3. There was consistent phosphorylation of H3 measured in several replicates (Fig. 40C). As the negative control reaction without Slk accounts for the background of the reaction and reflects naturally occurring ATP-to-ADP decay, this reaction was subtracted to obtain the luminescent values that correspond to ATP turnover by the kinase. A substantial ADP production by Slk is already observed without the substrate H3. This might mainly account for the auto-phosphorylation activity of Slk. When the substrate H3 is added to the reaction, the ADP production doubles, which reflects both autophosphorylation of Slk and substrate phosphorylation (Fig. 40D). After establishing a positive control for the *in vitro* kinase reaction, the kinase reaction was conducted with the GST-tagged protein fragments (Fig. 40E, F). As a control without substrate, purified GST alone was used. In contrast to the positive control H3, ADP production in the reaction without substrate was lower than in the reaction without Slk. Therefore, it was not possible to differentiate between autophosphorylation and substrate phosphorylation in the reaction with the substrate. To exclude that the agarose beads to which the GST-tagged proteins were bound were confounding the reaction, trials with eluted proteins were run (Fig. 40G, H). However, an unequivocal conclusion about autophosphorylation and potential substrate phosphorylation was still not possible. For this reason, the evaluation method of the *in vitro* kinase reactions was changed from the ADP-Glo assay to mass spectrometry. Analysis by mass spectrometry also provides the additional advantage that not only phosphorylation can be detected but also the exact phosphorylation site is determined.

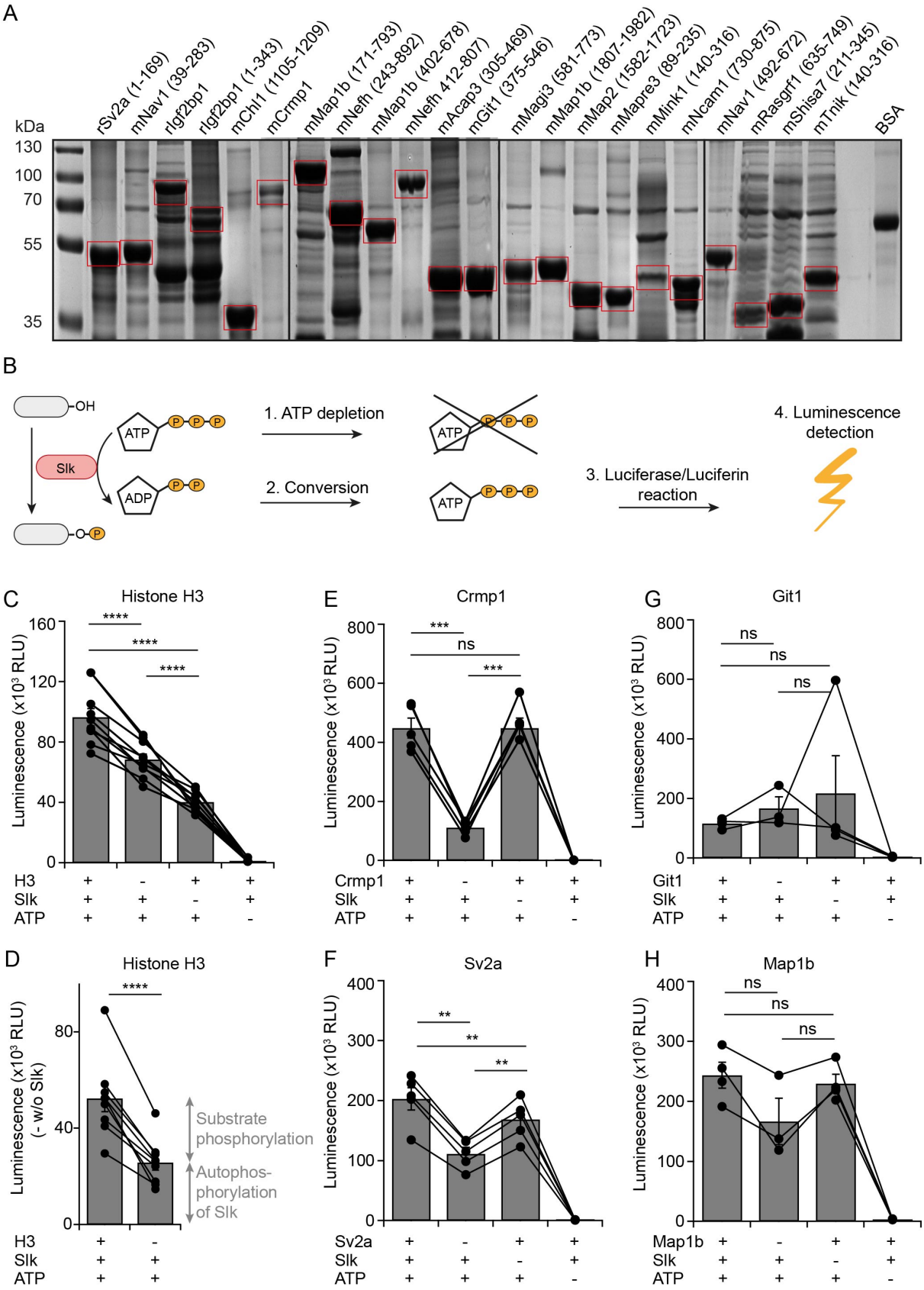


Fig. 40: *In vitro* kinase reactions with potential candidate substrates of Slk.
(A) Candidate proteins from the phosphoproteomics mass spectrometry experiments were cloned into the pGEX-GST vector and purified from bacteria. Coomassie staining verified the successful purification (BSA concentration: 5 µg). (B) *In vitro* kinase reactions were carried out by adding ATP and Slk to the potential substrate protein. To detect phosphorylation events, ADP production was measured by a luminescence reaction using the ADP-Glo

Kinase Assay. Generated luminescent signals positively correlate with the amount of ADP generated during the kinase reaction. (C) A positive control for the kinase reactions was established with the known substrate histone H3. Luminescence in the reaction with all components exceeds the luminescent signals detected in the negative controls without the substrate, without Slk, or without ATP. (D) The luminescent signal of the reaction without Slk (w/o Slk) was subtracted from the other reactions as this value corresponds to ATP decay that occurs independently of kinase activity. The remaining signal can be attributed to kinase activity and is split into autophosphorylation and substrate phosphorylation. (E+F) The bead-bound candidate proteins Crmp1 and Sv2a were tested by *in vitro* kinase reactions. The luminescent signals in the reaction without Slk exceeded the signals in the reaction without the substrate, which did not allow to differentiate between potential substrate phosphorylation and autophosphorylation. (G+H) Git1 and Map1b were eluted from the agarose beads and subjected to kinase reactions. The luminescent signal in the kinase reaction with all the components did not surpass the negative controls (relative luminescent units (RLU)). n = 10 replicates for (C)+(D); n = 5 for (E)+(F); n = 4 for (G)+(H). One-way RM ANOVA: (C): (Conditions: p(F=172.2; df=1.319, 11.87) < 0.0001; Individual (between rows): p(F=2.210; df=9, 27) = 0.0538 (E): (Conditions: p(F=139.5; df=1.1.708, 6.833) < 0.0001; Individual (between rows): p(F=1.833; df=4, 12) = 0.1875; (F): (Conditions: p(F=114; df=1.216, 4.864) = 0.0001; Individual (between rows): p(F=6.891; df=4, 12) = 0.0040; (G) Mixed-effects model: p = 0.2567; (H) Mixed-effects model: p = 0.0019. Holm-Šidák's multiple comparisons test: ns: not significant, ** p < 0.01, *** p< 0.001, **** p < 0.0001. Paired t test: (D) p(t=8.445, df=9) < 0.0001; **** p < 0.0001.

In an initial screening experiment, all cloned GST-tagged proteins were subjected to *in vitro* kinase reactions and subsequently analyzed by mass spectrometry. From the 23 investigated phosphorylation sites, phosphorylation could be detected in six (Table 12). In three out of these six, the phosphorylation was only detected in the reaction with Slk and not in the negative control without Slk, pointing to direct phosphorylation by Slk.

Table 12: Mass spectrometric screen of candidate proteins after *in vitro* kinase reactions with Slk.
Proteins, which had a differentially phosphorylated site in the phosphoproteomics screen, were investigated by *in vitro* kinase reactions followed by mass spectrometry if they were directly phosphorylated by Slk. In a subset, the previously identified phosphorylation site could be detected. For Mink1, Shisa7, and Tnik, the phosphorylation could only be detected in the reaction with the kinase and not in the negative control. n = 1.

Construct	**Phosphoproteomics**			***In vitro* kinase reaction**	
	Phosphorylation site	$log_2FC < -0.58$	Potential KinSwing motif	Phosphopeptide detected	Only in + Slk condition
mAcap3 (305-469)	T381		+		
mChl1 (1105 - 1209)	S1148	+			
mCrmp1	S518; S522	+			
mGit (375-546)	S419			+	
mMagi3 (581-773)	S702				
mMap1b (171-793)	S561; S565	+			
mMap1b (1807-1982)	S1856		+		
mMap1b (402-678)	S561; S565	+			
mMap2 (1582-1723)	S1654		+		
mMapre3 (89-235)	T161		+	+	

mMink1 (140-316)	**T181**		+	+	+
mNav1 (39-283)	S148				
mNav1 (492-672)	S510; S651		+	+	
mNcam1 (730-875)	S770; S774		+		
mNefh (243-892)	S523	+			
mNefh (412-807)	S523	+			
mRasgrf1 (635-749)	T718		+		
mShisa7 (211-345)	**S250**		+	+	+
mTnik (140-316)	**T181**		+	+	+
rSv2a (1-169)	S106	+			
rIgf2bp1	S181	+			

In addition to the known phosphorylation sites, also sites that were not detected or not significantly differentially phosphorylated in the phosphoproteomics experiment were found to be phosphorylated by Slk in the *in vitro* kinase reactions (Table 13).

Table 13: New phosphorylation sites identified by *in vitro* kinase reactions followed by mass spectrometric analysis.
Three of them were previously detected in the phosphoproteomics screen although there had been no significant difference in the phosphorylation between control and Slk knockdown neurons.

Construct	***In vitro* kinase reaction**	**Phosphoproteomics**		
	Phosphorylation site(s)	Phosphopeptide detected	log_2FC	padj
mMap1b (1807-1982)	T1836			
mNav1 (39-283)	S93	+	-0.16	0.36
mNav1 (39-283)	S197	+	0.15	0.35
mNav1 (39-283)	S202	+	-0.06	0.40
mNav1 (39-283)	T95, T141, S143, S175, T264			
mNav1 (492-672)	S607, S627, T630			
mNefh (243-892)	S431, T432			
mRasgrf1 (635-749)	T735, S745			
mTnik (140-316)	T187, S264			

The proteins, that were less phosphorylated in the phosphoproteomics experiment after Slk knockdown and that were found to be phosphorylated by Slk in the mass spectrometry screen after the *in vitro* kinase reactions, were further investigated. These included the kinases Mink1, Tnik, Map4k4, and the transmembrane protein Shisa7 (Fig. 41).

The kinases are Ste20 family kinases and belong to the GCK IV family. All three kinases regulate Jnk signaling in neurons in response to stress (Larhammar et al., 2017). The kinase domains are highly homologous and the analyzed phosphorylation site is part of the activation loop for all three kinases (Fig. 41). Shisa7 is a transmembrane protein that is localized at excitatory and inhibitory synapses (Schmitz et al., 2017; Han et al., 2019). At inhibitory synapses, Shisa7 regulates the trafficking and function of $GABA_A$ receptors. CRISPR-Cas mediated knockout of Shisa7 specifically decreased the frequency but not the amplitude of mIPSCs (Han et al., 2019).

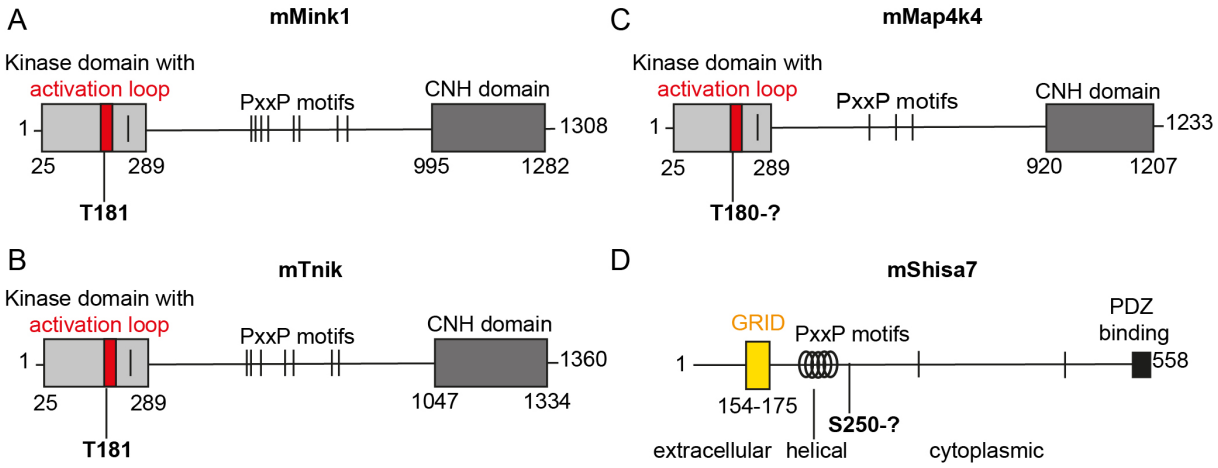


Fig. 41: Structures and phosphorylation sites of the four candidate substrates of Slk.
Four proteins showed reduced phosphorylation after Slk knockdown. These proteins were subjected to *in vitro* kinase reactions and the phosphorylation was analyzed by subsequent mass spectrometry analysis. Slk was able to phosphorylate the kinases Mink1 (A) and Tnik (B) at T181 in the activation loop of the kinase domain. No phosphorylation could be detected for Map4k4 at position T180 (C) and no difference in phosphorylation between control and kinase reaction could be detected for Shisa7 (D). n = 4. CNH: citron homology domain, Pxxp: SH3-domain binding motif, GRID: $GABA_AR$ interacting domain.

Phosphorylation analysis by mass spectrometry showed that Mink1 and Tnik are phosphorylated by Slk at T181 (Fig. 41A, B). No phosphorylation was detected for T180 in Map4k4 so it is not clear if this is due to technical detection limitations or if Slk does not phosphorylate Map4k4 (Fig. 41C). For Shisa7, phosphorylation at S250 was detected but no difference was found between the control reaction without Slk and the kinase reaction with Slk (Fig. 41D). Further experiments will be needed to elucidate if Map4k4 and Shisa7 can be phosphorylated by Slk.

The identified phosphorylation of Mink1 and Tnik was already described in the literature. The phosphorylation site at threonine T181 is located in the activation loop of the kinase and,

together with T187 phosphorylation, is required for full activation of Tnik (Wang et al., 2016). Interestingly, a knockdown of Mink1 and Tnik by RNA interference reduced dendritic branching in cultured neurons (Hussain et al., 2010). Tnik has also been shown to disrupt F-actin in a fibroblast cell line (Fu et al., 1999).

Thus, we identified two proteins, the two kinases Mink1 and Tnik, that can be directly phosphorylated by Slk and whose function could mediate some of the observed effects of Slk in neurons.

5 Discussion

5.1 Preferential importance of Slk during neuronal development

It is undeniable that the protein kinase Slk has important functions in non-neuronal and neuronal cells. Mice with a complete knockout of the Slk gene are not viable, demonstrating the importance of the kinase for biological functions (Pryce et al., 2017). Even the expression of a truncated form of Slk with reduced phosphorylation efficiency resulted in the death of embryos by E14.5, demonstrating the necessity of Slk kinase activity for development (Al-Zahrani et al., 2014). In neurons, Slk is especially important for branching of the distal dendritic tree and inhibitory synapse development (Schoch et al., 2021). As synapses and dendrites are highly dynamic structures that are regulated up into adulthood (Lin and Koleske, 2010; Tailby et al., 2005), Slk could be either important during development for proper formation of dendrites and synapses or during adulthood in keeping and maintaining these structures. Our experiments in which Slk was knocked down at an adult stage confirmed the first hypothesis. A late knockdown did not result in a changed dendritic arbor compared to control mice, implying that Slk is first and foremost important while the dendritic tree is formed rather than when it is maintained. This finding complements the previous publications demonstrating that Slk is indispensable during development by showing that it critically contributes to the formation of morphologically healthy neurons during brain development.

5.2 Influence of Slk knockdown on cellular networks

5.2.1 No epileptic activity after Slk knockdown

As structure often also determines function (Chklovskii, 2004), the effects of Slk on the morphology of neurons have functional correlates. Decreasing Slk expression resulted in a decreased frequency of mIPSCs (Schoch et al., 2021) and a reduced amplitude of IPSCs, thereby shifting the excitation-inhibition balance of the neuron (Royero, 2022). However, it was not clear yet if Slk knockdown also impaired network activity, eventually leading to hyperexcitability of the network due to impaired inhibition. As Slk expression was decreased in dysplastic neurons of GG and FCDIIB (Schoch et al., 2021), two malformations of cortical development that are highly epileptogenic, a connection of Slk with hyperexcitability was plausible. However, EEG recordings of mice with focal Slk knockdown did not show spontaneous seizure activity. Therefore, Slk loss does not seem to be the primary cause for epileptic activity in malformations of cortical development. Still, we cannot rule out that Slk affects network activity to an extent that cannot be picked up by EEG recordings. Although the EEG electrode was placed right in the *in utero* electroporated brain area, it will sample from a large population of neurons from which the majority is non-electroporated. A technique that

allows to sample from a smaller population of neurons and to additionally correlate the activity with the location it originates from are MEA recordings. They are frequently used with human slices from different tumors (Dossi et al., 2014; Pallud et al., 2014) to study the epileptogenic behavior of the different areas of the tumor. To elicit epileptic seizure-like activity in human brain slices, the system needs to be challenged by a solution with increased potassium and reduced magnesium, which might be explained by the fact that on slice level, all connections to other brain areas are lost (Dossi et al., 2014). MEA recordings of brain slices of mice electroporated with shSlk constructs did not show a significantly different activity than brain slices of control animals. However, while challenging control slices with epileptogenic $aCSF^{lowMg2+,highK+}$ doubled the activity in electroporated and non-electroporated areas, no significant increase in activity could be detected for Slk knockdown brain slices in the *in utero* electroporated area. This points to subtle differences in the electrophysiological behavior of a network with interspersed Slk knockdown neurons. Interestingly, a mouse model for GG demonstrated reduced activity in the tumor core region, which could also not be elevated by $aCSF^{lowMg2+,highK+}$ (Cases-Cunillera et al., 2022). Also in human glioma, the tumor core was found to be silent whereas interictal-like discharges were elicited by the surrounding peri-tumoral tissue (Pallud et al., 2014). Similarly, in a mouse model of FCD using an mTOR mutation, mice developed spontaneous seizures but the hyperexcitability originated from neurons neighboring the neurons with the mutation. The neurons carrying the mutation were actually the ones that were less excitable (Koh et al., 2021). The result that a focal Slk knockdown altered the response of the neuronal network when challenged with external stimuli, is also supported by previous results. These showed that chemically-induced seizures were more severe in mice with focal Slk knockdown, induced by IUE, compared to controls while the seizure onset was comparable in both groups (Robens, 2016). As a reduction of Slk expression alone is not sufficient to elicit epileptic seizure-like activity but increases the severity of seizures that are induced by external causes, Slk may be regarded as a disease-modulating factor. Several studies suggest that certain genes and gene variants alone are not sufficient to induce epilepsy but significantly elevate the risk of developing epilepsy after acquired brain damage including traumatic brain injury, tumors, and malformations. Accordingly, only the minority of epilepsy cases can be attributed to a solely genetic or acquired cause but it is often an interplay between different genetic and acquired factors that results in an epileptic phenotype (Kang et al., 2019; Steinlein, 2008; Perucca and Scheffer, 2021; Berkovic et al., 2006).

The findings that Slk knockdown alone does not elicit epileptic seizures but alters the responses of the neuronal network towards external stimuli both on slice level and *in vivo* indicate that Slk might be a modifying factor in malformations associated with epilepsy, which

is neither necessary nor sufficient to induce an epileptic phenotype as it is typical for multifactorial disorders.

5.2.2 Altered gene expression in neighboring neurons and microglia

Not only the MEA recordings but also the results of the scRNAseq dataset pointed to a possible influence of Slk knockdown neurons on neighboring cells. In mice, neurons in the neighborhood of Slk knockdown cells expressed cytoskeletal, synaptic, and neurite growth-related genes to a lower degree than neurons from control mice. Expression of the Ndrg2 gene for example is elevated during neurite outgrowth and overexpression results in neurite outgrowth (Schonkeren et al., 2019). Knockdown of Mtss1, Spire1, and Prickle2 were described to decrease dendrite branching (Sowers et al., 2013; Yu et al., 2016; Ferreira et al., 2014). In addition, several cytoskeleton-associated genes were downregulated. Spire1 is an actin nucleation protein and knockdown in neurons from Drosophila decreased levels of F-actin (Ferreira et al., 2014). Gas2l1 links the microtubule and actin cytoskeleton, which results in the local stabilization of F-actin (Sánchez-Huertas and Herrera, 2021; Willige et al., 2019). Interestingly, several of these proteins have been also implicated in tumor development. Ndrg2 and Mtss1 are potential tumor suppressor genes and the expression of Ndrg2 was decreased in glioma tissue while a reduced expression of Mtss1 was associated with poor outcomes in glioblastoma (Schonkeren et al., 2019; Zhang and Qi, 2015). Additionally, the expression of synaptic genes was decreased in neurons in the neighborhood of Slk knockdown cells. Gabra2 encodes the α2 subunit of the $GABA_A$ receptor. Knocking out Gabra2 in mice reduced the frequency of mIPSCs while not affecting the amplitude and also the density of Gephyrin clusters (de Groot et al., 2017; Panzanelli et al., 2011). Several Gabra2 variants have been associated with developmental delay and severe epilepsy in patients (Butler et al., 2018). Not only gene expression related to inhibitory synapses but also to excitatory synapses was affected. Prickle2 localizes to excitatory postsynapses and associates with Psd95. Knockout of Prickle2 reduced synapse number, the size of the postsynaptic density, and also the frequency of PSCs. Moreover, mice with Prickle2 knockout showed alterations in their behavior resembling ASD phenotypes (Sowers et al., 2013). Taken together, the scRNAseq data suggest that Slk knockdown neurons could induce gene alterations in neighboring neurons that might result in changes in neurite growth, cytoskeletal dynamics, and synapse organization. Interestingly, these potential changes resemble partly the morphological and functional alterations observed in Slk knockdown neurons. So far, we can only speculate how Slk knockdown neurons could induce these changes in surrounding neurons. As Slk knockdown neurons present with fewer dendritic branches and fewer inhibitory synapses, direct connections to the surrounding neurons will be reduced, which could directly alter the development of these neurons. However, also multicellular signaling could be involved. It is

known that dendritic and synaptic development is tightly controlled by a close interaction of neurons, astrocytes, and microglia. Microglia are brain-resident immune cells that play a role in the clearing of cell debris and the secretion of inflammatory molecules after brain injury (Paolicelli et al., 2011; Andoh et al., 2019). However, they also are indispensable for normal brain development as they are involved in the pruning of dendrites and synapses during postnatal development. This includes the engulfment of weak or less active synapses and therefore contributes to the refinement and maturation of synaptic structures (Paolicelli et al., 2011). Aberrant synaptic pruning has been implicated in various neurodevelopmental diseases such as ASD, AD, epilepsy, or schizophrenia (Andoh et al., 2019; Datta et al., 2020; Koyama and Ikegaya, 2015; Goikolea-Vives and Stolp, 2021). A proposed molecular pathway for synapse elimination by microglia involves the complement component C1q. Upon secretion of C1q, the factor binds to synapses and tags them for subsequent engulfment by microglial cells (Andoh et al., 2019; Lewis, 2021; Riccomagno & Kolodkin, 2015). Expression of C1q was demonstrated to be increased in patients with ASD, AD, and epilepsy associated with mesial temporal lobe epilepsy or FCD (Datta et al., 2020; Koyama and Ikegaya, 2015; Andoh et al., 2019). In the cells surrounding Slk knockdown neurons, C1q expression was elevated in astrocytes. This could tag neighboring synapses and initiate their elimination by microglia. Activated microglia cells in the Slk knockdown mice displayed an increased expression of several genes implicated in inflammatory responses. Hspa1 encodes the heat shock 70 kDa protein and was shown to initiate both pro- and anti-inflammatory responses. Its expression increases after brain injury such as ischemic stroke and increased expression of Hspa1 enhanced the seizure susceptibility in mice (von Rüden et al., 2018; Dukay et al., 2019). Cebpb and Fosb both are transcription factors that have a proinflammatory role. They especially mediate inflammation and activation of microglia after excitotoxicity and contribute to excitotoxic damages (Ndoja et al., 2020; Cortes-Canteli et al., 2008). In addition, genes that are characteristic of a resting state of microglia were significantly downregulated in Slk knockdown compared to control mice. This included Serinc3, a gene that is downregulated in disease-associated microglia, and Grn, which reduces the inflammatory response of microglia (Andoh et al., 2019; Ronning et al., 2019). Thus, a subset of activated microglia cells seems to differentially express genes related to inflammation and cell activation in Slk knockdown mice compared to controls. This might suggest that in Slk knockdown animals, the loss of inhibitory synapses after P15 is mediated by excessive synaptic elimination by microglia cells. In a recent study, synaptic pruning via a complement-dependent mechanism was specifically investigated for inhibitory synapses. After depletion of microglia, the number of connections between excitatory neurons and parvalbumin-positive interneurons increased. This increase occurred after synaptogenesis was completed, which implies a role of microglia in inhibitory synapse refinement and maturation (Lewis, 2021). The reduction of inhibitory synapses in Slk

knockdown neurons seems to be specific for synapses between excitatory neurons and parvalbumin-positive interneurons and starts after the initial formation of synapses between P15 and P30 (Royero, 2022; Schoch et al., 2021). The increased expression of proinflammatory and activity-inducing genes in microglia of animals with a focal Slk knockdown could be correlated to an excessive synaptic pruning activity, which then could reduce the number of inhibitory synapses between excitatory neurons and parvalbumin-positive interneurons. Thus, excessive synaptic pruning could be one potential explanation for the loss of inhibitory connections observed after Slk knockdown (Fig. 42). Synapse elimination can depend on transsynaptic interactions between neurons and microglia. Knockout of the $GABA_BR$ in microglia reduced the expression of genes important for synaptic pruning and phagocytosis, suggesting the GABA-$GABA_BR$ axis as a strong candidate for the interaction of interneurons and microglia (Lewis, 2021). In our model, Slk is knocked down specifically in excitatory neurons that lose their inhibitory input during development. This might imply that Slk knockdown alters inhibitory postsynapses, which could result in signals activating microglia. Alternatively, a change in the postsynapse could translate to presynaptic changes on interneurons, which might alter the functionality of the synapse. Non-functional synapses then would be recognized by microglia and eliminated. However, so far, no targets or pathways of Slk inside the neuron are known that could explain which changes occur at inhibitory postsynapses, that result in altered transsynaptic signaling to neurons or glial cells. Therefore, several experiments were conducted in this study to elucidate the mechanism of Slk.

5.3 Protein-protein interactions related to inhibitory synapse function

5.3.1 Known Slk interactors at inhibitory synapses

In a first attempt to identify mechanisms that could explain inhibitory postsynapse elimination after Slk knockdown in the neuron itself, proteins that were known to interact with Slk in non-neuronal cells were investigated at inhibitory synapses. These included Fak, Paxillin, pS6, and the actin and microtubule cytoskeleton, as these could theoretically induce the observed changes. In non-neuronal cells, Slk influenced the stabilization of focal adhesion by phosphorylating Paxillin and thereby altering the accumulation of Fak (Quizi et al., 2013; Wang et al., 2020; Wagner et al., 2008; Roovers et al., 2009). In Slk-LacZ fusion embryos, levels of Paxillin, Fak, and Tubulin were reduced (Al-Zahrani et al., 2014). In neurons, the equivalent to focal adhesions are the so-called point contacts, which are cell-matrix adhesion complexes in growth cones. These point contacts consist of focal adhesion-related proteins such as β1-Integrins, Fak, Paxillin, and Vinculin. Activation of integrin receptors by extracellular cues induces autophosphorylation of Fak and activation of downstream molecules. Altered Fak signaling in neuronal cultures enhanced neurite growth and synapse formation by decreasing

the motility of the growth cone and increasing branching (Ribeiro et al., 2013; Myers and Gomez, 2011; Ferrer-Ferrer and Dityatev, 2018). Phosphorylation of Paxillin by Fak can activate Grlf1, which decreases RhoA activity and induces actin disassembly (López-Colomé et al., 2017). The role of the actin cytoskeleton in the formation of inhibitory synapses is controversial. While one study shows that depolymerizing actin did not affect the distributions of $GABA_AR$ and Gephyrin (Allison et al., 2000), other studies discovered a signaling pathway that influences F-actin and inhibitory synapse maintenance. The Git1/Pak signaling pathway promotes inhibitory synapse integrity and stability via F-actin, implying an important role of F-actin in the stabilization and maintenance of inhibitory synapses (Smith et al., 2014).

Slk is known to affect the cytoskeleton and overexpression can induce the disassembly of actin stress fibers and F-actin (Wang et al., 2020; Sabourin et al., 2000; Pytowski et al., 1998; Woychyshyn et al., 2020). Slk also interacted with F-actin binding proteins such as α-Actinin and the ERM proteins (Jaberi et al., 2015; Viswanatha et al., 2012; Machicoane et al., 2014). Additionally, Slk was found to colocalize and co-immunoprecipitate with α-Tubulin, and knockdown of Slk resulted in unfocused microtubule assembly (Wagner et al., 2002, 2008; Burakov et al., 2005, 2008). Expression of the C-terminal fragment of Slk increased acetylated Tubulin indicating stabilized microtubules in a kidney cell line (Burakov et al., 2008). The microtubule cytoskeleton also has important functions at inhibitory synapses. It provides the scaffold for transport proteins such as Kinesins that mediate for example the transport of $GABA_AR$ and Gephyrin. A knockout of these motor proteins impaired inhibitory signal transmission and resulted in spontaneous epileptic seizures. Depolymerizing microtubules interfered with the transport of Gephyrin and changed Gephyrin cluster sizes, numbers, and the signal intensity of Gephyrin (Fan and Lai, 2022; Maas et al., 2009). Gephyrin is a Tubulin-binding protein that is the major scaffold at inhibitory postsynapses by connecting $GABA_AR$ to the cytoskeleton. Removing endogenous Gephyrin reduced $GABA_AR$ and also affected the density of presynaptic vesicular GABA transporter clusters leading to reduced mIPSC amplitude and frequency (Marchionni et al., 2009). Gephyrin clustering is strongly controlled by phosphorylation (Tretter et al., 2012). A pathway implicated in Gephyrin clustering is the mTOR pathway. Inactive mTOR associates with Gephyrin and upon activation releases the protein, which increases clustering. Clustering is supported by reduced phosphorylation at S270, as active mTOR represses Gsk3β, the kinase responsible for S270 phosphorylation (Wuchter et al., 2012; Tyagarajan et al., 2011).

Thus, Paxillin, Fak, the mTOR pathway, and the actin/microtubule cytoskeleton would be interesting candidates to mediate Slk effects in neurons. However, we did not see a difference in the fluorescence intensity of Paxillin and Fak at inhibitory synapses. Additionally, we could not detect an increase in mTOR signaling or cytoskeletal stabilization at inhibitory synapses. Gephyrin cluster size and intensity were also not changed, indicating that there is no direct

influence of Slk on Gephyrin protein level or clustering. From these results, we could conclude that these pathways are not influenced in cultured neuronal cells at inhibitory synapses. However, as we only assessed fluorescence intensity, we would only observe relative changes in protein expression or clustering. Therefore, we cannot exclude changes on different levels such as activation/inactivation or phosphorylation status.
To identify potential novel pathways and protein interactors that could mediate Slk effects in neurons, we took a more unbiased approach. To discover proteins that interact with Slk in neurons, several proteomics approaches were designed to identify proteins in close proximity to Slk, proteins binding to Slk, and proteins phosphorylated by Slk.

5.3.2 Possible mechanisms of Slk action at inhibitory synapses based on the results of the proteomics experiments

In recent years, the proteome of the inhibitory synapse was increasingly characterized by proximity-dependent labeling or genetically modified mice approaches (Uezu et al., 2016; Nakamura et al., 2016). Many of the known inhibitory synapse proteins such as Gephyrin and Nlgn2, but also proteins with previously unknown involvement in inhibitory synapses such as Sv2a or Prkcg were identified in our proteomics studies. Two-thirds of all proteins that were co-immunoprecipitating with the $GABA_AR$ were identified in our proteomics studies (Nakamura et al., 2016). This suggests that Slk plays an important role in the protein network of the iPSD. For a majority of these proteins, their function at inhibitory synapses is still hardly explored. However, for some proteins, a functional link to inhibitory synaptic transmission has been established. A knockout of Sv2a, which is originally known as a protein at the ePSD, reduces both the amplitude and frequency of spontaneous IPSCs (Bartholome et al., 2017). Knockout animals suffer from severe seizures and Sv2a is an established target of antiepileptic drugs such as levetiracetam (Ohno and Tokudome, 2017; Lynch et al., 2004). The scaffold protein Shank3 is also known to be part of ePSDs and it is actually not found at inhibitory synapses. Nevertheless, mice lacking exon 9 present with normal mEPSCs but a reduced mIPSC frequency suggesting a functional impact of Shank3 on inhibitory synaptic transmission (Lee et al., 2015). A third protein that was originally identified at excitatory synapses is Shisa7. In contrast to Shank3, Shisa7 is now known to localize to inhibitory synapses as well where it interacts with $GABA_AR$. It controls the abundance of the receptor at synapses and influences kinetics of the channel deactivation by directly binding to subunits of the $GABA_AR$. Knocking out Shisa7 resulted in a specific reduction of the mIPSC frequency but not the amplitude, similar to the effects of Slk knockdown in neurons. In addition, Shisa7 modulates the effects of the benzodiazepine diazepam, which is a positive allosteric modulator of $GABA_AR$ (Han et al., 2019). Since 2020, it is officially approved as a nasal spray to treat epileptic seizures in the United States (Cornett et al., 2021). Shisa7 seems to be especially important for exocytosis

but not for endocytosis of $GABA_AR$ (Han et al., 2019). Phosphorylation at S405 by Prka induces the activity of Shisa7, while a phospho-deficient mutant reduced the surface expression of $GABA_AR$ and synaptic inhibition. In addition, Shisa7 S405A knock-in mice showed behavioral alterations associated with neurodevelopmental disorders (Wu et al., 2022). In our studies, we discovered another phosphorylation site, S250, whose phosphorylation is reduced after Slk loss. If the effects of S250 phosphorylation on the activity of Shisa7 and the localization of $GABA_AR$ parallel the effects of S405 phosphorylation by Prka needs to be determined in future studies.

Other promising candidates for Slk interactions include cell-cell adhesion molecules. The neural-specific adhesion molecule Ncam1 was less phosphorylated at S770/774 after Slk knockdown at a site that fits the Slk phosphorylation motif but the subsequent *in vitro* experiments confirmed no direct phosphorylation by Slk. Phosphorylation at S774 is important for signal transduction and a phosphodeficient mutant has been shown to decrease neurite outgrowth (Pollscheit et al., 2012), making it an interesting candidate for the dendrite phenotype induced by Slk. During synaptogenesis, Ncam is also indispensable and is involved in pruning perisomatic inputs from parvalbumin-positive basket interneurons. Loss of Ncam specifically increased the density of perisomatic inhibitory boutons on pyramidal neurons in layer II/III, which fits the recent discovery that Slk specifically affects synapses with parvalbumin-positive interneurons, which preferentially form perisomatic synapses (Royero, 2022; Duncan et al., 2021). In addition, Ncams are proposed as targets for microglia during synaptic pruning as they are specifically expressed on newly formed neurons (Ekdahl, 2012).

Another pathway that has been described in detail to contribute to inhibitory synapse stabilization is the Git1/βPix/Rac1/Pak pathway. Git1 and βPix interact with the GTPase Rac1, which in turn activates the Pak kinase, a known actin regulator. Knocking down Git1 or βPix decreased $GABA_AR$ and the Gephyrin cluster area and also reduced the number of $GABA_AR$ at the neuronal surface. Functionally, mIPSC amplitudes and frequencies were diminished while mEPSCs were not affected. The reduction of $GABA_AR$ could be rescued by the F-actin-stabilizing drug jasplakinolide. Accordingly, Git1 and βPix knockdown decreased the number of inhibitory synapses containing F-actin (Smith et al., 2014). βPix is a GEF that not only regulates actin polymerization at inhibitory synapses but also during dendritic branching (López Tobón et al., 2018). In general, many of the GEFs and GAPs identified in this study are involved in cytoskeletal dynamics, but βPix is the one with the best-described effect on inhibitory synapses. However, it cannot be ruled out that the effect of Slk on inhibitory synapses is not only mediated via βPix but also via other GEFs/GAPs whose functions at inhibitory synapses are not studied in detail yet. Git1 and βPix were identified as Slk binding proteins in our CoIP experiments and Git1, βPix, and Pak all showed reduced phosphorylation after Slk

loss, suggesting Slk to be upstream of this pathway. But which pathway could be upstream of Slk, inducing these effects at inhibitory synapses?

5.3.3 Potential upstream pathways involved in inhibitory synapse development

Based on the proteins that were identified in the different proteomics screens, different possible explanations for an upstream mechanism of Slk-dependent inhibitory synapse stabilization would be plausible.

The development and stabilization of synapses are dependent on transsynaptic signaling complexes such as the Neurexin/Neuroligin, Ephrin/Ephs, and Semaphorin/Plexin protein pairs. Especially the Semaphorin/Plexin pathway has been shown to be important for the stabilization of inhibitory synapses. The transmembrane receptor Plexin consists of an extracellular domain that binds to the Semaphorin ligands, while the intracellular domain has an intrinsic GAP function that subsequently interacts with Ras-like GTPases via several signaling pathways. Inactive Ras leads to the decrease of Phosphoinositide 3-kinase activity, which reduces Akt phosphorylation and thereby its activation. This in turn reduces the phosphorylation of Gsk3β and as the phosphorylation is inhibiting, this activates the kinase and thereby increases the phosphorylation of downstream molecules such as Crmp2. The GAP activity of the Plexins can also inactivate the Rho-GTPase RhoA, which results in actin depolymerization. However, by interacting with GEFs, Plexin activation can induce actin cytoskeleton polymerization via activation of Rho-GTPases (RhoA, Rac1). This results in subsequent activation of kinases such as Rock, Pak, or Limk1 and finally in the phosphorylation of Cofilin, thereby hindering the actin-depolymerizing activity of Cofilin (Ridley, 2006).

Interestingly, Plexin-B2 signaling controls both excitatory and inhibitory synapse development, while Plexin-B1 is specific for inhibitory synapses (McDermott 2018). Treatment of hippocampal neurons with soluble Semaphorin 4D that signals through Plexin-B1 in the postsynaptic excitatory neuron results in an increase in the density of inhibitory synapses (McDermott et al., 2018). Experiments in organotypic brain slices revealed that Semaphorin 4D is not inducing de novo formation of inhibitory synapses but rather stabilizes already formed synapses and thereby increased synapse density by 25% (Frias et al., 2019). In general, inhibitory synapses are quite dynamic, and about one-fifth are not stable, which means that they are constantly appearing and disappearing over time (Schuemann et al., 2013). On a molecular level, Semaphorin 4D-dependent synapse stabilization increased the number of Gephyrin-positive puncta but did not increase the size or the fluorescence intensity of these puncta (Frias et al., 2019). This would be in line with our observation that Slk knockdown in cultured cortical neurons did not change the fluorescence intensity or the size of Gephyrin-positive puncta. This could be a first hint that Slk might be a downstream effector of

Semaphorin 4D/Plexin-B1 signaling in neurons. Besides, many signaling proteins of the Plexin pathway were identified in the proteomics screens we conducted. Both Plexins, Plexin-B1 and Plexin-B2, co-immunoprecipitated with Slk as well as several downstream proteins including Pak5, Plcg1, Crmp2, and catalytic and regulatory subunits of the Phosphoinositide 3-kinase (Pik3r1, Pik3r4, Pik3c3). In the BioID experiments, Pak5 and Rap2b have been identified to be proximal to Slk. Reduced phosphorylation could be detected for Gsk3β and Pak1. These results suggest that Slk could be downstream of Plexin but upstream of Gsk3β and Pak1, as Slk seems to either directly or indirectly influence their phosphorylation status. If Slk is part of this pathway, a knockdown of Slk would disrupt Semaphorin 4D/Plexin signaling during development and thereby decrease inhibitory synapse stabilization and subsequently their density. As Slk did not seem to be important for the initial steps of inhibitory synapse formation, but for stabilizing and maintaining their density after P15, this would be in line with the results reported for Semaphorin 4D effects on inhibitory synapse formation. Interestingly, in Caenorhabditis elegans the Tnik ortholog Mig-15 was shown to act downstream of Plexin activation to control synapse formation (Chen et al., 2018). Tnik was identified as a binding partner of Slk and a direct phosphorylation substrate. Further experiments will be needed to investigate if Tnik activation by Slk is controlled by the Plexin pathway also in mammalian neurons.

Plexin-activation dependent effects on inhibitory synapses are thought to be mediated via actin cytoskeletal changes (Frias et al., 2019). Interestingly, Plexin activation can result both in actin polymerization or depolymerization depending on the co-activated proteins. Activation of the Plexin-B1-Erbb2 receptor complex resulted in activation of RhoA leading to actin polymerization while Plexin-B1-Met receptor co-activation inactivates RhoA and thereby initiates opposing effects (Sun et al., 2012; Swiercz et al., 2008). However, when we investigated the actin cytoskeleton by determining F-actin amounts at inhibitory synapses, we did not find a significant difference between control and Slk knockdown neurons. This result might argue against a specific involvement of actin polymerization for Slk-dependent inhibitory synapse stabilization. However, keeping in mind that Slk knockdown did reduce F-actin in dendrites, there might be other explanations why we do not see a difference at inhibitory synapses. One explanation could be technical in nature. The inhibitory postsynaptic scaffold defined by Gephyrin clustering is quite small in size (0.35-0.45 µm in diameter (Fossati et al., 2016)) and the resolution limit of confocal microscopy is around 0.24 µm (for a wavelength of 568 nm). As the size of the investigated structure is only marginally larger than the resolution limit, this might have prevented us from seeing potential changes in the actin cytoskeleton at the synapses. Approaching this question with super-resolution microscopy that overcomes the resolution limit of conventional microscopy could further shed light on the question if actin cytoskeletal dynamics occur at inhibitory synaptic sites. Moreover, it could be possible that Slk

influences the velocity of actin remodeling, which would also not be detected by analyzing F-actin amounts at a certain timepoint. A time-lapse approach to visualize actin dynamics over time could be a suited method to answer this question in the future.

5.4 Potential mechanisms for Slk-dependent regulation of dendrite branching

In contrast, in dendrites of Slk knockdown neurons, we could detect a reduced amount of F-actin pointing to cytoskeletal changes induced by the loss of Slk but the exact mechanism of controlling actin polymerization is not known yet. In the proteomics experiments, a plethora of proteins regulating cytoskeletal parameters was detected to be interacting with Slk. After Slk knockdown, many cytoskeletal proteins were differentially phosphorylated, with the strongest changes on Nav1, Crmp1, Map1b, and Igf2bp1. All of them have been described to be involved in neurite outgrowth or elongation. Nav1 is a microtubule plus-end tracking protein (+TIP) that crosslinks microtubules and actin filaments (Sánchez-Huertas and Herrera, 2021). Its role in neurite outgrowth is suggested to be mediated by interaction with the RhoGEF Trio and subsequent Rac1 activation (van Haren et al., 2014). Map1b is also suggested to crosslink the actin and microtubule cytoskeleton and thereby contribute to neurite elongation (Teng et al., 2001; Cueille et al., 2007). The phosphorylation sites in Igf2bp1 and Crmp1 that were less phosphorylated following Slk knockdown are already described in the literature. A phosphodeficient S181A mutant of Igf2bp1 reduced the dendritic branching of cultured neurons similar to a knockdown of the protein (Urbanska et al., 2017). The upstream kinase responsible for phosphorylating S181 is unknown. However, Slk does not seem to be the direct upstream kinase, as the *in vitro* kinase reactions did not confirm any phosphorylation of Igf2bp1 by Slk. Igf2bp1 was also not binding to Slk in the CoIP experiments, suggesting that phosphorylation of Igf2bp1 at S181 may only be indirectly mediated by Slk. For Crmp1, Slk knockdown resulted in reduced phosphorylation of S518/S522. Also here, Slk does not seem to be the direct kinase as no phosphorylation could be detected in the *in vitro* kinase reactions. Crmp1 is primarily phosphorylated by Cdk5 and Dyrk2 at S522, leading to the phosphorylation of a secondary site, S518 by Gsk3β. The phosphorylation enhances the binding of Crmp1 to Filamin-A which is an actin binding protein (Nakamura et al., 2020). Interestingly, also Gsk3β phosphorylation was significantly altered after Slk knockdown. The phosphorylation at S21 was reduced (log_2FC = -0.36, padj = 0.03) but the effect of this phosphorylation is not investigated yet. Both, Gsk3β and Crmp1 were also identified in the CoIP experiments and were binding to Slk. This suggests that Slk might be upstream of Gsk3β signaling, leading to Gsk3β phosphorylation, thereby inducing Crmp1 phosphorylation, which results in altered binding to Tubulin (Nakamura et al., 2020). Crmp1 associates also with the actin cytoskeleton

and binds Ena/VASP proteins, thereby accelerating the elongation of actin filament barbed ends (Yu-Kemp et al., 2017). Enhanced phosphorylation increases the interaction with Filamin-A, an F-actin organizer, and thereby enables remodeling of the actin cytoskeleton, which could play a role in dendritic outgrowth (Nakamura et al., 2020) (Fig. 42).

Furthermore, a pathway via the cell adhesion molecule Ncam would be plausible as well. As mentioned above, the phosphorylation site that was identified in our phosphoproteomics screen is implicated in Ncam activation. Additionally, Slk binds to Ncam, which in turn can bind to Pak1 kinase, which also showed reduced phosphorylation after Slk knockdown. Ncam activation induces Pak1 activity in growth cones, inducing actin polymerization and thereby neurite growth (Li et al., 2013).

A third pathway how Slk could influence the actin cytoskeleton and thereby neurite outgrowth is via the GCK IV kinases Mink1, Tnik, and Map4k4. Phosphorylation of these kinases was reduced after Slk knockdown, their phosphorylation site fits the substrate motif of Slk, and Mink1 and Tnik were confirmed to be phosphorylated directly by Slk through *in vitro* kinase reactions. The identified phosphorylation site T181 is located in the activation loop and for Tnik, both phosphorylation at T181 and T187, are needed for full kinase activity (Wang et al., 2016). As these three kinases are closely related and the amino acid composition of the activation loop is identical, it could be deduced that the activation of Mink1 and Map4k4 might also require phosphorylation of these threonine residues.

Knocking down Mink1 and Tnik in cultured neurons reduced dendritic arborization. However, it is not clear if the dendritic arborization depends on kinase activity, as overexpression of wild-type or kinase-dead Mink1 did not change dendrite branching (Hussain et al., 2010). Therefore, it could be possible that the effect on neurite branching is not mediated by phosphorylating substrates but by acting as a scaffold to assemble protein complexes. A Tnik effect that is dependent on its kinase activity is cell rounding in cell lines, which is explained by a disruption of F-actin (Wang et al., 2011; Fu et al., 1999). Among the few described potential substrates of Tnik are important cytoskeletal regulators such as the Ena/VASP proteins, Fmnl2, and Mtss1l (Wang et al., 2016). In our phosphoproteomics dataset, the described Tnik phosphorylation sites of the Ena/VASP protein Enah and Mtss1l had a tendency to be less phosphorylated after Slk knockdown (log_2FC= -0.27, p = 0.09 and log_2FC = -0.21, p = 0.10). For both proteins, the reduced phosphorylation was not significant, but this could be due to the fact that it is further downstream of Slk action and possibly also influenced by additional Slk-independent pathways. Mtssl1 upregulates the activity of the Arp2/3 complex, which is important for the assembly of F-actin (Kawabata Galbraith et al., 2018). Enah associates with the barbed end of actin filaments and promotes actin polymerization by antagonizing filament capping proteins and by recruiting Profilin, an actin polymerization enhancing protein (Krause et al., 2003). The Enah homolog Ena in Drosophila also stimulates actin assembly and thereby

promotes the formation of dendritic branches (Li et al., 2005; Winkelman et al., 2014). Neutralizing the function of Ena/VASP reduced bundled F-actin and the number of neurites whereas overexpression increased the number of primary neurites and F-actin bundles (Lebrand et al., 2004). Enah is known to be regulated by phosphorylation, especially by Prka, which activates the protein (Loureiro et al., 2002). The effect of the phosphorylation T696 detected in our screen is unknown so far. In neurons, we observed reduced phosphorylation (= putative reduced activation) of Mink1, Tnik, and Map4k4 after Slk knockdown and at the same time saw a reduced amount of F-actin in dendrites and a decreased dendritic branching. This is partially contradictory to the previous studies where Tnik activation resulted in disruption of F-actin. There might be several possible explanations for that. First of all, the effects of the kinases in neurons may be different than in other cell types. Enah, which is a potential substrate of Tnik (Wang et al., 2016), is recruiting Profilin to the actin cytoskeleton and in the brain, there is an isoform (Profilin 2) that is exclusive to the nervous system. Profilin 2 differs from Profilin 1 in the affinity for actin and also binds to different proteins (Witke, 2004), making it possible that the outcome of the Tnik downstream cascade in neurons differs from the one in non-neuronal cells. Additionally, it might be possible that the actin dynamics change over time during development. We analyzed the F-actin in dendrites of DIV14 neurons, where the dendritic tree is already formed (Wilson et al., 2020). It might be that the actin dynamics are differently controlled by Slk in growth cones of developing neurites compared to already formed dendritic structures. In addition, potential phosphorylation of Enah by Tnik could increase actin polymerization, as other phosphorylation sites also activate protein function. Therefore, future studies are needed to elucidate the effects of Mink1 and Tnik phosphorylation by Slk and how this phosphorylation impacts the actin cytoskeleton and neurite outgrowth (Fig. 42).

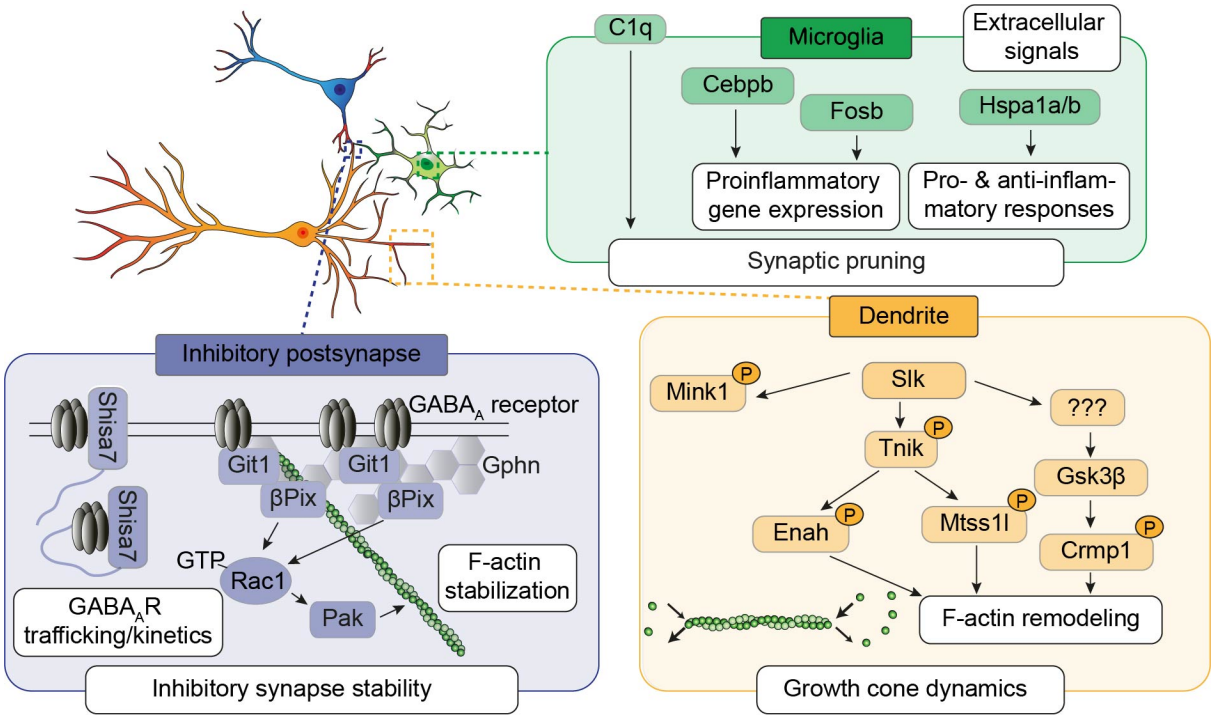


Fig. 42: Potential mechanisms of Slk action in neurons based on proteomics experiments.
Slk plays an important role in the dendrite growth of cortical neurons and the stabilization of inhibitory synapses formed with neighboring inhibitory neurons. Microglia cells are involved in synapse pruning, which might be exacerbated by a loss of Slk.

5.5. Slk as a fine-tuner of neuronal morphology

In general, Slk seems to be important for the late phase of network integration and maturation, as it specifically affects the maintenance of inhibitory synapses and distal neurite compartments that form last. In contrast, proteins that control dendritic arborization during the early postnatal stages affect different morphological parameters. Knockdown of the transcription factor Satb2 by IUE for example resulted in pyramidal neurons with fasciculated dendrites that crossed with dendrites of the same neuron (Kise and Schmucker, 2013). This does not naturally occur as neurons have elaborate mechanisms, which ensure self-avoidance meaning that dendrites of the same neurons do not cross or contact each other, thereby allowing for optimal coverage of a receptive field by the dendritic tree (Kise and Schmucker, 2013; Hoersting and Schmucker, 2021; Stürner et al., 2022).

Studies that modeled the dendritic tree showed that dendrites are characterized by a fractal branching behavior, allowing the formation of complex morphologies underlying the gigantic networks between different cells and cell types (Smith et al., 2021; Read Montague and Friedlander, 1991; Caserta et al., 1990, 1995). Interestingly, the structure of the dendritic tree was sufficient to characterize the connections and predict synapse formation with neighboring cells, thereby emphasizing the importance of the dendritic morphology for network establishment and function (van Ooyen et al., 2014; Hill et al., 2012; Smith et al., 2021).

These findings might suggest that Slk is especially important in the final morphological steps that lead to normal integration of the neurons into the surrounding network.

5.6 Slk in the context of diseases

Abnormal neurite development is associated with many neurodevelopmental disorders, including ASD, ID, or schizophrenia (Hu et al., 2020; Hoersting and Schmucker, 2021; Wong, 2008; Rossini et al., 2021; Mitsogiannis et al., 2021). There are Ste20 kinases that are known to influence neurite development and which are already implicated in neurodevelopmental disorders. For instance, the Ste20 kinase Taok2 controls dendritic development and synaptic connectivity by influencing F-actin dynamics, and Taok2 is a known ASD risk gene (Hu et al., 2020; Richter et al., 2018; de Anda et al., 2012). Therefore, a potential involvement of Slk in diseases might be plausible, especially given the dendritic and synaptic function of Slk.

A link between Slk and diseases was already shown in non-neuronal cells as Slk is important for tumor cell characteristics (Al-Zahrani et al., 2020; Müller et al., 2010; Sharma et al., 2016; Wang et al., 2018). In neurons, Slk is not directly connected to specific diseases yet. However, Slk expression was found to be reduced in dysplastic neurons of GG and FCDIIB, two malformations of cortical development (Schoch et al., 2021). This could suggest a link of Slk expression to these disorders, but so far it is not dissolved if it might be a causal or a consequential link. The fact that GG and FCDIIB are very complex disorders further complicates the search for a link of Slk in these diseases. Lesions can co-occur and there is a strong association of GG with FCDs (Cossu et al., 2013). GG and FCDIIB are not only strongly associated with intractable epilepsy, but also often associated with other impairments. Up to 30% of all children with epilepsy are also diagnosed with ASD (Jeste and Tuchman, 2015). Among the ASD patients, epilepsy was most prominently found in those diagnosed with ID (Woolfenden et al., 2012). It is not clear whether ASD and ID are a consequence of brain impairments caused by epilepsy or if these disorders coincide because of common underlying mechanisms. For both, epilepsy and ASD, the most prominent feature is a dysregulation of the excitation/inhibition balance (Jeste and Tuchman, 2015). This can either be due to an impairment of inhibition such as reduced levels of GABA receptor subunits or to overactivation of excitatory signaling (Bozzi et al., 2018).

In GG and FCDIIB, a reduction of Slk expression was selectively found in dysplastic neurons of the lesion, which is modeled by the IUE approach where Slk is only reduced in selected neurons. Our experiments in mice imply that the reduction of Slk in dysplastic neurons of GG and FCDIIB probably does not cause the high epileptogenicity of these malformations. However, this does not exclude that Slk might be a contributing or modulating factor for the epileptic phenotype and the comorbidities of the disorders.

In the literature, mutations of the Slk gene in humans have been linked to other neurodevelopmental diseases (Fig. 43A). In a study by Anazi and colleagues, Slk was identified as one of 14 novel candidate genes for ID (Anazi et al., 2017). The identified 1414G>T mutation results in a premature stop codon between the kinase domain and the C-terminal coiled-coil domains of Slk (G472*). Symptoms included neurological deficits such as a global developmental delay and hydrocephalus but also hepatomegaly and generalized muscle weakness. Although no experimental link between this mutation and the symptoms has been shown, Slk is known to play a role in neuronal, liver, and muscle development, thereby being an interesting candidate gene. A second Slk mutation has been identified in a screen for novel ASD clinical variants (Jiang et al., 2013). This mutation, C2695T, leads to an amino acid substitution at position 899 (R899C) in the coiled-coil domains of Slk. The patient was diagnosed with ASD but except for intelligence quotient and behavior impairments, no other medical condition was diagnosed.

Both described mutations affect the C-terminal part of Slk. While the G472* stop mutation in the ID patient leads to a truncated form of Slk without the coiled-coil domains, the R899C mutation in the ASD patient results in a single amino acid exchange in the coiled-coil domains. These coiled-coil domains are described to mediate dimerization of Slk and are also important for its kinase activity. In a study, point mutations were introduced that disrupted the N- and C-terminal coiled-coil domain structures (Cybulsky et al., 2017). The I878G mutation that disrupts the N-terminal coiled-coil domains reduced both homodimerization and kinase activity of Slk. Prediction of the coiled-coil domain structures by the Paircoil2 algorithm shows that this I878G mutation changes the prediction of one of the first coiled-coil domains compared to the wild-type Slk version (Fig. 43B, C). Similarly, the R899C mutation that was found in the ASD patient, changes the prediction of the same coiled-coil domain (Fig. 43D). The G472* stop mutant of the ID patient leads to a premature stop codon, which completely abolishes the C-terminal coiled-coil domains. Studies with different Slk domains showed that deletion of the C-terminus of Slk (Slk^{1-950}) did not impact kinase activity. However, a stronger truncation (Slk^{1-373}) strongly enhanced kinase activity (Sabourin et al., 2000). Therefore, although no experimental link between the Slk mutations and the ID and ASD pathology has been proven yet, it is probable that Slk is involved, as both mutations lead to structural changes in the Slk protein that will, according to experimental studies, also affect Slk function.

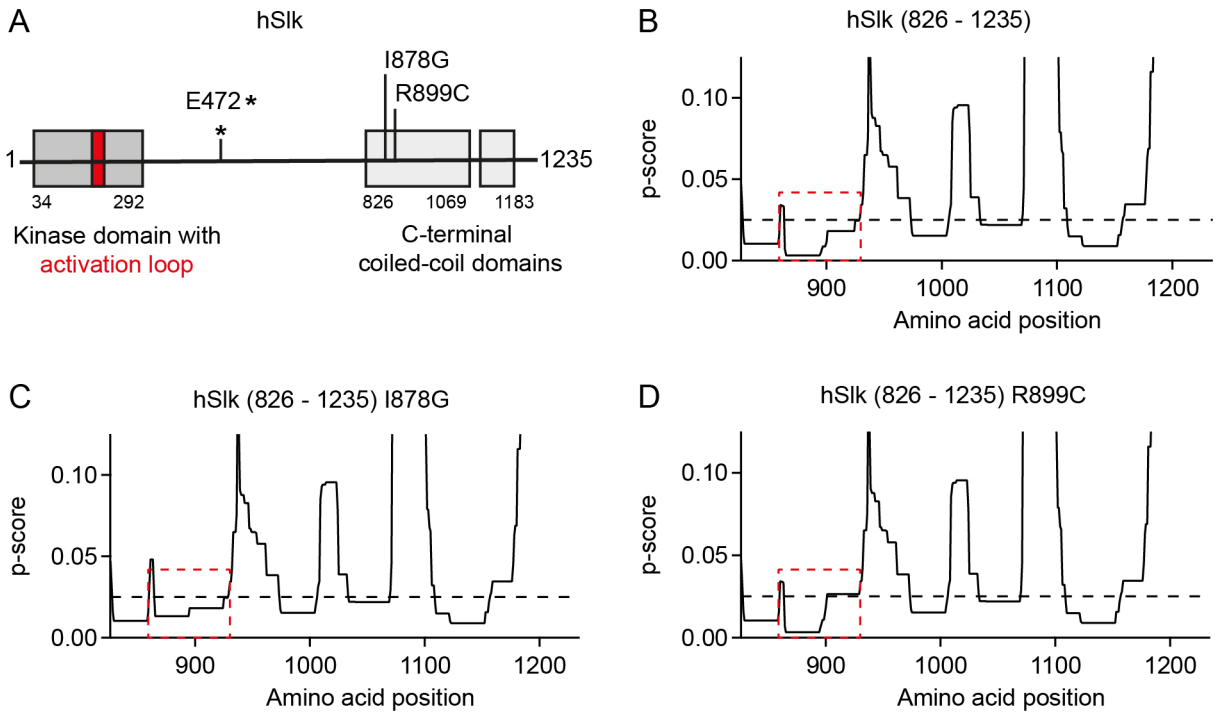


Fig. 43: Mutations in hSlk leading to a disruption of the coiled-coil domains.
(A) Structure of hSlk with the N-terminal kinase domain and the C-terminal coiled-coil domains based on information from UniProt. Mutations described in patients are indicated. (B) Prediction of coiled-coil structures in the C-terminus of human wild-type Slk with Paircoil2. (C) The I878G mutation that was described by Cybulsky and colleagues (Cybulsky et al., 2017) disrupts the second predicted coiled-coil structure. (D) The R899C mutation that was described in a patient with ASD also disrupts the second predicted coiled-coil structure (Jiang et al., 2013). Paircoil2: lower p-score = greater likelihood of coiled-coil. $p < 0.025$: predicted to be in a coiled-coil structure (McDonnell et al., 2006).

In animal models, especially mutations in synaptic genes were shown to induce ASD and/or epilepsy. Typical ASD models are generated by Shank3 or Mecp2 mutations. Knockouts of Mecp2 and Shank3 mutants lacking exon 9 resulted in a reduction of mIPSCs, which goes in line with a decrease of inhibitory synapses (Zhang et al., 2008; Lee et al., 2015).

Interestingly, both Mecp2 and Shank3 were identified in our proteomics screen to interact with Slk in the CoIP experiments. For Mecp2, also reduced phosphorylation of S424 was detected after Slk knockdown, suggesting a potential direct or indirect functional regulation of this protein by Slk. Shank3 was also differentially phosphorylated on multiple amino acids after Slk knockdown. In addition, we verified that Shank3 could indeed bind to Slk. One potential domain that could possibly mediate this interaction is the SH3 domain of Shank3 as Slk is known to have a putative SH3 binding site. Interestingly, deleting exon 9 from Shank3 results in a premature stop codon before the SH3 domain, thereby abolishing all binding with this domain (Lee et al., 2015).

Many genetic risk loci involved in neurodevelopmental diseases are shown to impact structural plasticity, among them synaptic genes such as Shank3, but also cell adhesion molecules such as Nrxn1 and Nlgn3 or GTPase modulating proteins such as the GAP Syngap1 and the GEFs

Trio and Kalrn. Whole exome sequencing studies have shown that more than 15% of all newly identified genetic variants belong to a class of GEFs/GAPs and cell adhesion molecules (Forrest et al., 2018). Our proteomics studies also identified many proteins whose phosphorylation is influenced by Slk activation or that are binding to Slk to be cell adhesion molecules or GEFs/GAPs. Additionally, 16 out of 25 risk genes that were summarized in a study to affect structural plasticity in neurodevelopmental disorders were identified in our proteomics studies (Forrest et al., 2018) (Table 14).

Table 14: Neurodevelopmental risk genes affecting structural plasticity.
Most of the proteins were detected in our proteomics studies to interact with Slk or Slk signaling (padj < 0.05). ASD: autism spectrum disorder; BD: bipolar disorder; DD: developmental disorder; ID: intellectual disability; SZ: schizophrenia. Modified from (Forrest et al., 2018).

Gene or copy number variant	Type of effect on spines and/or dendrites	Disease association	Proteomics study	
			Phospho-proteomics	CoIP
Cell adhesion				
Nrxn1	Spine stability	SZ, ASD	+	+
Nlgn3	Spine density	ASD		+
Cntnap2	Spine and dendrite stability	ID, ASD		
Dscam	Dendrite and spine development	ASD		
Pcdh10	Spine density	ASD, SZ		
Glutamate receptors				
Gria1	Spine size	SZ, ID, ASD	+	
Prrt2	Spine density	Epilepsy	+	+
Cacng2	Dendritic arborization	ID	+	
Grin2a	Dendritic arborization	SZ, epilepsy	+	
Grin2b	Spine density	ASD		
Scaffold proteins				
Shank3	Dendrite and spine development	ASD	+	+
Ank3	Spine size and density and activity-dependent spine enlargement	BD	+	+
Dlg4	Spine density and size; activity-dependent structural plasticity	ASD and/or ID		+
Dlgap1	Spine size	ASD and/or ID	+	+
Cask	Spine density and size	ASD and/or ID, DD		

Calcium signaling				
Cacna1c	Spine density	BD, SZ		
Cacnb4	Spine density	SZ	+	
Camk2b	Activity-dependent spine formation and dendritic arborization	ID		+
Camk2a	Activity-dependent spine formation	ASD, ID		+
GTPase signaling				
Syngap1	Spine formation, development, and activity-dependent structural plasticity	ID, DD, ASD	+	+
Trio	Dendrite development and activity-dependent structural plasticity	ASD and/or ID	+	
Kalrn	Spine morphogenesis and activity-dependent structural plasticity	DD	+	
Nf1	Spine development and activity-dependent structural plasticity	ID		
Arhgef6	Dendrite development and spine density	ID		
Ophn1	Dendrite and spine development	ID, DD		

This together with the fact that mutations or different expression of Slk have been identified in neurodevelopmental disorders is a very strong indication that Slk could be involved in the context of diseases. Neurodevelopmental disorders such as epilepsy, ID, and ASD arise from aberrant neural circuits that impact the function of the brain and thereby manifest often in seizures, cognitive delays or malfunctions, and social impairments. The proper shaping of neural circuitry is executed during different critical periods of neurodevelopment that are critically dependent on environmental cues and activity. While first synaptic connections are formed in excess, the early postnatal period is important for pruning of neurite processes and subsequent pruning of synapses to stabilize active and eliminate less active synapses (Goikolea-Vives and Stolp, 2021; Riccomagno and Kolodkin, 2015; Lewis, 2021). This results in a balance of excitation and inhibition that allows for higher cognitive processes. Slk is critically involved in the pruning of dendrites and the stabilization of synapses contributing to a balance between excitation and inhibition and thereby to normal circuit formation. Thus, Slk in the brain has been linked to different neurodevelopmental disorders, although further research is needed to clarify the concrete role of Slk in these diseases.

5.7 Outlook

In this study, we further characterized the influence of Slk on neuronal development and identified potential mechanisms and interaction partners of Slk. scRNAseq experiments revealed that the progressive decline of inhibitory synapses after Slk knockdown could be mediated by microglial activation and excessive synaptic pruning. Inside the Slk knockdown neuron, different protein interactions could be responsible for the destabilization of inhibitory synapses and the reduction in dendritic branching. In dendrites, Slk affects the stability of F-actin and many cytoskeletal and cytoskeleton-associated proteins have been identified to interact with Slk in the proteomics studies. Additionally, several proteins were verified to bind to Slk and two of them were demonstrated to be direct phosphorylation substrates of Slk. Future studies could focus on the effect of the identified Slk interactions to further dissect the mechanism of Slk in neurons.

Additionally, it would be interesting to determine how strongly aberrant Slk function contributes to the pathology in neurodevelopmental disorders. Understanding the exact contribution of Slk to disease context would also allow to test therapeutic treatments targeting this kinase. In recent years, kinase inhibitors being able to target Slk are developed, optimized, and characterized (Asquith et al., 2020; Serafim et al., 2021). Parallel progress in the understanding of Slk-dependent processes in disease and further improvement of Slk kinase inhibitors might allow for studies with Slk as a treatment target.

Thirty years after awarding the Nobel Prize for describing protein phosphorylation by kinases, we increasingly appreciate the importance of kinases in health and disease conditions. This study focused specifically on characterizing the function and the mechanism of one kinase, Slk, in neurons. In another thirty years, the role of Slk might be understood in even greater detail and this information might be possibly used to target Slk as one treatment option in neurodevelopmental disorders.

6 Appendix

6.1 Contributions

Mass spectrometric analysis was conducted in collaboration with Dr. Shiva Ahmadi (AG Winter, University of Bonn) for the BioID experiments, with Dr. Mark Graham (Children's Medical Research Institute, Australia) for phosphoproteomics experiments or with the Mass Spectrometry Core Facility of the University of Bonn (Dr. Robert Hardt, Dr. Marc Sylvester). Bioinformatic analysis of the proteomics data was performed by Dr. Ashley J. van Waardenberg (i-Synapse, Australia). scRNA sequencing was performed at the Next Generation Sequencing Core Facility of the University of Bonn (Dr. André Heimbach). Raw count matrices were extracted by Dr. Theodoros Georgomanolis (Cologne Center for Genomics). Cultured cortical neurons were prepared by Sabine Opitz (AG Schoch/Becker, University of Bonn). EEG analysis was performed by Dr. Julika Pitsch (AG Schoch/Becker, University of Bonn).

6.2 Abbreviations

6.2.1 General abbreviations

Table 15: Abbreviations that are used in this study.

Abbreviation	Explanation
+TIP	Plus-end tracking protein
A	Alanine
aCSF	Artificial cerebrospinal fluid
AD	Alzheimer's disease
ADP	Adenosine diphosphate
AMPA	α-amino-3-hydroxy-5-methyl-4-isoxazole propionic acid
ASD	Autism spectrum disorder
ATH domain	AT1-46 homology domain
ATP	Adenosine triphosphate
AU	Arbitrary units
BioID	Proximity-dependent biotin identification
BirA*	E. coli biotin ligase BirA (R118G)
BME	Basal Medium Eagle
bp	Basepair
BSA	Bovine serum albumin
CMV	Cytomegalovirus
CNH domain	Citron homology domain
CNS	Central nervous system
CoIP	Co-immunoprecipitation
Ctrl	Control
Da	Dalton

DIV	Day *in vitro*
DMEM	Dulbecco's Modified Eagle's Medium
DMSO	Dimethyl sulfoxide
dNTP	Deoxyribonucleotide triphosphate
DPBS	Dulbecco's Phosphate Buffered Saline
DTT	Dithiothreitol
E	Embryonic day
ECM	Extracellular matrix
EEG	Electroencephalography
EGFP	Enhanced green fluorescent protein
Ena/VASP protein family	Enabled/vasodilator-stimulated phosphoprotein protein family
ePSD	Excitatory postsynaptic density
EPSP	Excitatory postsynaptic potential
ERM protein family	Ezrin, Radixin, Moesin protein family
F-actin	Filamentous actin
FBS / FCS	Fetal bovine serum / Fetal calf serum
FCD	Focal cortical dysplasia
fw	Forward
G-actin	Globular actin
GABA	γ-aminobutyric acid
$GABA_AR$	$GABA_A$ receptor
GAP	GTPase activating protein
GCK	Germinal-center kinase
GEF	Guanine nucleotide exchange factor
GG	Ganglioglioma
GO	Gene ontology
GST	Glutathione-S-transferase
H	Histone
h	Human
HA	Hemagglutinin
HEBS	HEPES-buffered saline
HEK293T	Human embryonic kidney cell line 293T
HPLC	High-performance liquid chromatography
hrGFP	Humanized Renilla reniformis green fluorescent protein
ICC	Immunocytochemistry
ID	Intellectual disability
IMDM	Iscove's Modified Dulbecco's Medium
iPSD	Inhibitory postsynaptic density
IPTG	Isopropyl-β-D-thiogalactopyranosid
IUE	*In utero* electroporation
K^+	Kalium ion
KD	Knockdown
LC-MS/MS	Liquid chromatography - tandem mass spectrometry
log_2FC	log_2 transformed fold change
m	Mouse
mCherry	Monomeric Cherry (red fluorescent protein)

MCS	Multiple cloning site
MEA	Multi-electrode array
mEPSC	Miniature excitatory postsynaptic current
Mg^{2+}	Magnesium ion
mIPSC	Miniature inhibitory postsynaptic current
mRFP	Monomeric red fluorescent protein
mTOR	Mammalian target of rapamycin
NB	Neurobasal Medium
NGS	Normal goat serum
NMDA	N-methyl-D-aspartate
p	phosphorylated
P	Postnatal day
P/S	Penicillin/Streptomycin
padj	Adjusted p-value
PBS	Phosphate buffered saline
PCA	Principal component analysis
PCR	Polymerase chain reaction
PFA	Paraformaldehyde
POI	Protein of interest
PTM	Posttranslational modification
PWM	Position weight matrix
QRILC	Quantile regression imputation of left-censored data
r	Rat
rAAV	Recombinant adeno-associated virus
RE	Restriction enzyme
rev	Reverse
RLU	Relative luminescent units
ROI	Region of interest
rpm	Revolutions per minute
S	Serine
scRNAseq	Single-cell RNA sequencing
SDS	Sodium dodecyl sulfate
SDS-PAGE	Sodium dodecyl sulfate-polyacrylamide gel electrophoresis
SEM	Standard error of the mean
SFK	Src family tyrosine kinase
SH3 domain	Src homology 3 domain
shSlk	Short hairpin RNA against Slk
Ste20	Sterile20
T	Threonine
TBS	Tris-buffered saline
TiSH	TiO_2-sequential immobilized-metal affinity chromatography-hydrophilic interaction liquid chromatography
TMT	Tandem mass tag
TSC	Tuberous sclerosis
U	Unit

UMAP	Uniform Manifold Approximation and Projection for Dimension Reduction
UMI	Unique molecular identifier
WB	Western Blot
Y	Tyrosine

6.2.2 Gene abbreviations

Table 16: Gene names are listed with their corresponding protein name.

Gene name	Protein name
Abl1	Tyrosine-protein kinase ABL1
Ablim2	Actin-binding LIM protein 2
Abr	Active breakpoint cluster region-related protein
Acap3	ArfGAP with coiled-coil, ankyrin repeat and PH domains 3
Actn4	Alpha-Actinin-4
Add	Adducin
Afap1	Actin filament-associated protein 1
Ahctf1	Protein ELYS
Akt1	RAC-alpha serine/threonine-protein kinase
Aktip	AKT-interacting protein
Aldoc	Fructose-bisphosphate aldolase C
Alk	ALK tyrosine kinase receptor = Anaplastic lymphoma kinase
Angptl2	Angiopoietin-related protein 2
Ank	Ankyrin
Ankib1	Ankyrin repeat and IBR domain-containing protein 1
Anks1b	Ankyrin repeat and sterile alpha motif domain-containing protein 1B
Anpep	Aminopeptidase N
Ap3d1	AP-3 complex subunit delta-1
Apc	Adenomatous polyposis coli protein
Apod	Apolipoprotein D
Aqp4	Aquaporin-4
Arglu1	Arginine and glutamate-rich protein 1
Arhgef6	Rho guanine nucleotide exchange factor 6
Arhgef7 = βPix	Rho guanine nucleotide exchange factor 7 = Beta-Pix
Arp2/3 complex	Actin-related protein 2/3 complex
Asap1	Arf-GAP with SH3 domain, ANK repeat and PH domain-containing protein 1
Ask1 = Map3k5	Apoptosis signal-regulating kinase 1 = Mitogen-activated protein kinase kinase kinase 5
Atp1a3	Sodium/potassium-transporting ATPase subunit alpha-3
Atrx	Transcriptional regulator ATRX
Basp1	Brain acid soluble protein 1
Bcl7a	B-cell CLL/lymphoma 7 protein family member A
Bloc1s1	Biogenesis of lysosome-related organelles complex 1 subunit 1

c-src	Cellular proto-oncogene tyrosine-protein kinase Src
C1q	Complement C1q
Cacna1c	Voltage-dependent L-type calcium channel subunit alpha-1C
Cacna1i	Voltage-dependent T-type calcium channel subunit alpha
Cacnb	Voltage-dependent L-type calcium channel subunit beta
Cacng	Voltage-dependent calcium channel gamma subunit
Camk2a/b	Calcium/calmodulin-dependent protein kinase type II subunit alpha/beta
Car4	Carbonic anhydrase 4
Cask	Peripheral plasma membrane protein CASK
Cat	Catalase
Ccdc177	Coiled-coil domain-containing protein 177
Ccl5	C-C motif chemokine 5
Cdk	Cyclin-dependent kinase
Cebpb	CCAAT/enhancer-binding protein beta
Cfl	Cofilin
Chl1	Neural cell adhesion molecule L1-like protein
Clasp	CLIP-associating protein
Cldn5	Claudin-5
Clip3	CAP-Gly domain-containing linker protein 3
Clu	Clusterin
Cntnap2	Contactin-associated protein-like 2
Cops5	COP9 signalosome complex subunit 5
Cpe	Carboxypeptidase E
Crmp1 = Dpysl1	Collapsin response mediator protein 1 = Dihydropyrimidinase-related protein 1
Crmp2 = Dpysl2	Collapsin response mediator protein 2 = Dihydropyrimidinase-related protein 2
Ctss	Cathepsin S
Cwc22	Pre-mRNA-splicing factor CWC22 homolog
Cxcl2	C-X-C motif chemokine 2
Dact3	Dapper homolog 3
Dbnl	Drebrin-like protein
Dctn1	Dynactin subunit 1
Dcx	Neuronal migration protein doublecortin
Ddx17	Probable ATP-dependent RNA helicase DDX17
Dgcr6	Protein DGCR6
Dio2	Type II iodothyronine deiodinase
Dlg4	Disks large homolog 4
Dlgap1	Disks large-associated protein 1
Dmtn	Dematin
Dnajc8	DnaJ homolog subfamily C member 8
Dscam	Down syndrome cell adhesion molecule homolog
Dyrk2	Dual specificity tyrosine-phosphorylation-regulated kinase 2
Eef1d	Elongation factor 1-delta
Eftud2	116 kDa U5 small nuclear ribonucleoprotein component

Egr1	Early growth response protein 1
Ei24	Etoposide-induced protein 2.4
Enah	Protein enabled homolog
Ensa	Alpha-endosulfine
Epb4.1	Protein 4.1
Epb4.1l1	FERM domain-containing protein
Epb4.1l3	Band 4.1-like protein 3
Erbb2	Receptor tyrosine-protein kinase erbB-2
Ezr	Ezrin
Fak	Focal adhesion kinase 1
Fgb	Fibrinogen beta chain
Fgf13	Fibroblast growth factor 13
Flt1	Vascular endothelial growth factor receptor 1
Fmn2	Formin-2
Fmnl	Formin-like protein
Fosb	Protein FosB
Fus3	Mitogen-activated protein kinase FUS3
Fyn	Tyrosine-protein kinase Fyn
Gabra2	Gamma-aminobutyric acid receptor subunit alpha-2
Gad	Glutamate decarboxylase
Gas2l1	GAS2-like protein 1
Gdpd3	Lysophospholipase D GDPD3
Gfap	Glial fibrillary acidic protein
Git1	ARF GTPase-activating protein GIT1
GluA1 = Gria1	Glutamate receptor 1
Glul	Glutamine synthetase
Gm12166	Predicted gene 12166
Gnaz	Guanine nucleotide-binding protein G(z) subunit alpha
Gpc	Glypican
Gphn	Gephyrin
Grcc10	Protein C10
Grid2ip	Delphilin
Grin2a/b	Glutamate receptor ionotropic, NMDA 2A/B
Grlf1 = Arhgap35	Glucocorticoid receptor DNA-binding factor 1 =Rho GTPase-activating protein 35
Grn	Progranulin
Gsk3	Glycogen synthase kinase 3
Gsn	Gelsolin (actin-depolymerizing factor)
Gtf2e2	General transcription factor IIE subunit 2
H1	Histone H1
H3	Histone H3
Hecw1	E3 ubiquitin-protein ligase HECW1
Hgs	Hepatocyte growth factor-regulated tyrosine kinase substrate
Hist1h1c	Histone H1.2
Hist1h1d	Histone H1.3
Homer	Homer protein homolog

Hook3	Protein Hook homolog 3
Hopx	Homeodomain-only protein
Hsd17b4	Peroxisomal multifunctional enzyme type 2
Hsf1	Heat shock factor protein 1
Hsp70	Heat shock 70 kDa protein
Hspa1a/b	Heat shock 70 kDa protein 1A/B
Hsph1	Heat shock protein 105 kDa
Igf2bp1	Insulin-like growth factor 2 mRNA-binding protein 1
Ildr2	Immunoglobulin-like domain-containing receptor 2
Itm2c	Integral membrane protein 2C
Jakmip	Janus kinase and microtubule-interacting protein
Jnk1 = Mapk8	c-Jun N-terminal kinase 1 = Mitogen-activated protein kinase 8
Jun	Transcription factor Jun
Kalrn	Kalirin
Kcnj	ATP-sensitive inward rectifier potassium channel
Keap1	Kelch-like ECH-associated protein 1
Kidins220	Kinase D-interacting substrate 220
Kpnb1	Importin subunit beta-1
Kss1	Mitogen-activated protein kinase KSS1
LacZ	Beta-galactosidase
Lag3	Lymphocyte activation gene 3 protein
Ldb	LIM domain-binding protein
Limch1	LIM and calponin homology domains-containing protein 1
Limk1	LIM domain kinase 1
Lmo4	LIM domain transcription factor LMO4
Lok = Stk10	Lymphocyte-oriented kinase = Serine/threonine-protein kinase 10
Lrch2	Leucine-rich repeat and calponin homology domain-containing protein 2
Luzp2	Leucine zipper protein 2
Ly6c1	Lymphocyte antigen 6C1
Lyz2	Lysozyme C-2
Lzts1	Leucine zipper putative tumor suppressor 1
Magi3	Membrane-associated guanylate kinase, WW and PDZ domain-containing protein 3
Map	Microtubule-associated protein
Map2k	Dual specificity mitogen-activated protein kinase kinase
Map3k	Mitogen-activated protein kinase kinase kinase
Map4k	Mitogen-activated protein kinase kinase kinase kinase
Map4k4	Mitogen-activated protein kinase kinase kinase kinase 4
Mapk	Mitogen-activated protein kinase
Mapk8ip	C-Jun-amino-terminal kinase-interacting protein
Mapre = Eb	Microtubule-associated protein RP/EB family member
Mapt	Microtubule-associated protein tau
March7	E3 ubiquitin-protein ligase MARCHF7
Marcks	Myristoylated alanine-rich C-kinase substrate
Marcksl1	MARCKS-related protein

Mark1	Serine/threonine-protein kinase MARK1
Matr3	Matrin-3
Mbp	Myelin basic protein
Mecp2	Methyl-CpG-binding protein 2
Mig-15	Serine/threonine-protein kinase mig-15
Mink1	Misshapen-like kinase 1
Mprip	Myosin phosphatase Rho-interacting protein
Mrc1	Macrophage mannose receptor 1
Msn	Moesin
Mt-Nd3	NADH-ubiquinone oxidoreductase chain 3
Mtss1l = Mtss2	Protein MTSS 2
Myh10	Myosin-10
Myo5a	Unconventional myosin-Va
Nacc2	Nucleus accumbens-associated protein 2
Nav1/3	Neuron navigator 1/3
Ncam1	Neural cell adhesion molecule 1
Ndrg2	Protein NDRG2
Nefh	Neurofilament heavy polypeptide
Nefl	Neurofilament light polypeptide
Nefm	Neurofilament medium polypeptide
NeuN = Rbfox3	Neuronal nuclei antigen = RNA binding protein fox-1 homolog 3
Nf1	Neurofibromin
Ngdn	Neuroguidin
Ngef	Ephexin-1
Nlgn	Neuroligin
Nono	Non-POU domain-containing octamer-binding protein
Npl	N-acetylneuraminate lyase
Nrgn	Neurogranin
Nrxn	Neurexin
Nsfl1c	NSFL1 cofactor p47
Nup153	Nucleoporin 153
Ophn1	Oligophrenin-1
Otud3	OTU domain-containing protein 3
p38 Mapk	Mitogen-activated protein kinase p38
Pacs1	Phosphofurin acidic cluster sorting protein 1
Pak	Serine/threonine-protein kinase PAK
Pcdh	Protocadherin
Pclo	Protein piccolo
Pdgfra	Platelet-derived growth factor receptor alpha
Pex5l	PEX5-related protein
Pf4	Platelet factor 4
pGrlf1	Phosphorylated glucocorticoid receptor DNA-binding factor 1
Phf14	PHD finger protein 14
Pik3c3	Phosphatidylinositol 3-kinase catalytic subunit type 3
Pik3r1	Phosphatidylinositol 3-kinase regulatory subunit alpha
Pik3r4	Phosphoinositide 3-kinase regulatory subunit 4

Pja1	E3 ubiquitin-protein ligase Praja-1
Plcg1	1-phosphatidylinositol 4,5-bisphosphate phosphodiesterase gamma-1
Plk1	Serine/threonine-protein kinase PLK1
Pnn	Pinin
Ppp1r16a	Protein phosphatase 1 regulatory subunit 16A
Ppp1r9b	Neurabin-2
Ppp3ca	Protein phosphatase 3 catalytic subunit alpha
Ppp6r2	Serine/threonine-protein phosphatase 6 regulatory subunit 2
Pqbp1	Polyglutamine-binding protein 1
Prickle2	Prickle-like protein 2
Prka	cAMP-dependent protein kinase
Prkcg	Protein kinase C gamma type
Prrt2	Proline-rich transmembrane protein 2
pS6 = phosphorylated Rps6	Phosphorylated 40S ribosomal protein S6
Psd3	PH and SEC7 domain-containing protein 3
Psd95 = Dlg4	Postsynaptic density protein 95 = Disks large homolog 4
Ptgds	Prostaglandin-H2 D-isomerase
Pxn	Paxillin
Rab15	Ras-related protein Rab-15
Rac1	Ras-related C3 botulinum toxin substrate 1
Rap2b	Ras-related protein Rap-2b
Rars	Arginine--tRNA ligase, cytoplasmic
Rasgrf1	Ras-specific guanine nucleotide-releasing factor 1
Rcn2	Reticulocalbin-2
Rdx	Radixin
Reep1	Receptor expression-enhancing protein 1
Rgs5	Regulator of G-protein signaling 5
RhoA	Transforming protein RhoA
Rims1	Regulating synaptic membrane exocytosis protein 1
Rnaset2a	Ribonuclease T2-A
Rnps1	RNA-binding protein with serine-rich domain 1
Rock	Rho-associated protein kinase 1
Rorb	Nuclear receptor ROR-beta
Rpl17	60S ribosomal protein L17
Rpl27	60S ribosomal protein L27
Rps6	40S ribosomal protein S6
S100a9	Protein S100-A9
S6K1 = Rps6kb1	Ribosomal protein S6 kinase beta-1
Satb1	DNA-binding protein SATB1
Satb2	DNA-binding protein SATB2
Serinc3	Serine incorporator 3
Sfxn5	Sideroflexin-5
Sgip1	SH3-containing GRB2-like protein 3-interacting protein 1
Shank	SH3 and multiple ankyrin repeat domains protein

Shisa7	Protein shisa-7
Slc17a7	Vesicular glutamate transporter 1
Slc25a18	Mitochondrial glutamate carrier 2
Slc2a13	Proton myo-inositol cotransporter
Slc4a7	Sodium bicarbonate cotransporter 3
Slc7a5	Large neutral amino acids transporter small subunit 1
Slk	Ste20-like serine/threonine-protein kinase
Sltm	SAFB-like transcription modulator
Snap25	Synaptosomal-associated protein 25
Snap91	Clathrin coat assembly protein AP180
Snca	Alpha-Synuclein
Sphkap	A-kinase anchor protein SPHKAP
Spire1	Protein spire homolog 1
Sptbn1	Spectrin beta chain, non-erythrocytic 1
Src	Proto-oncogene tyrosine-protein kinase Src
Srcin1	SRC kinase signaling inhibitor 1
Srrm2	Serine/arginine repetitive matrix protein 2
Ste11	Serine/threonine-protein kinase Ste11
Ste7	Serine/threonine-protein kinase Ste7
Sult4a1	Sulfotransferase 4A1
Sv2a	Synaptic vesicle glycoprotein 2A
Syngap1	Ras/Rap GTPase-activating protein SynGAP
Synj1	Synaptojanin-1
Syt	Synaptotagmin
Taok2	Serine/threonine-protein kinase TAO2
Tbcd	Tubulin-specific chaperone D
Tenm1	Teneurin-1
Tgfβ	Transforming growth factor beta
Thrap3	Thyroid hormone receptor-associated protein 3
Timp1	Metalloproteinase inhibitor 1
Tjp1	Tight junction protein ZO-1
Tln1	Talin-1
Tmeff	Tomoregulin
Tnik	Traf2 and NCK-interacting protein kinase
Tomm70	Mitochondrial import receptor subunit TOM70
Tp53	Cellular tumor antigen p53
Tpm3-rs7	Tropomyosin 3, related sequence 7
Tppp	Tubulin polymerization-promoting protein
Tpr	Nucleoprotein TPR
Trio	Triple functional domain protein
Tsc1	Hamartin
Tsc2	Tuberin
Ttbk1	Tau-Tubulin kinase 1
Ttyh3	Protein tweety homolog 3
Tuba	α-Tubulin
Tyrobp	TYRO protein tyrosine kinase-binding protein

U2surp	U2 snRNP-associated SURP motif-containing protein
Uba52	Ubiquitin-60S ribosomal protein L40
Ubc	Polyubiquitin-C
Ubr5	E3 ubiquitin-protein ligase UBR5
v-src	Viral proto-oncogene tyrosine-protein kinase Src
Vtn	Vitronectin
Wipf2	WAS/WASL-interacting protein family member 2
Ylpm1	YLP motif-containing protein 1
Ywhag	14-3-3 protein gamma
Zap70	Tyrosine-protein kinase ZAP-70
Zdbf2	DBF4-type zinc finger-containing protein 2 homolog

6.3 Material

6.3.1 Equipment

Table 17: Equipment used in this study.

Equipment	Model	Company
Acrylamide electrophoresis system	Mini-PROTEAN Tetra Electrophoresis System	BioRad
Agarose electrophoresis power supply	PowerPac Basic	BioRad
Agarose electrophoresis system	Sub-Cell GT	BioRad
Autoclave	Laboclav	Steriltechnik AK
Balance	Analytical Balance	VWR
Balance	EG420-3NM	Kern EG
Biological Safety Cabinet	MSC-Advantage	ThermoFisher Scientific
Biological Safety Cabinet	HERA Safe KS	ThermoFisher Scientific
Cell counter	Countess 2 Automated Cell Counter	ThermoFisher Scientific
Centrifuge	Rotina 420R	Hettich
Centrifuge	Mikro200	Hettich
Centrifuge	Mikro22R	Hettich
Confocal laser scanning microscope	Eclipse Ti A1	Nikon
Confocal laser scanning microscope	LSM700	Zeiss
Controller	Micro4 Controller, 4-channel	World Precision Instruments
Electroporator	CUY21SC	NepaGene
Fluorescent Probe Flashlight	Dual Fluorescent Probe Flashlight Set	Electron Microscopy Sciences
Fractionator	3100 OFFGEL fractionator	Agilent
Gel imaging system	ChemiDoc MP System	Bio-Rad
Glass capillary puller	PC-10	Narishige

Homogenizer	Polytron 1200E	Kinematica
HPLC system	Dionex UltiMate 3000 RSLC nano HPLC system	ThermoFisher Scientific
Imaging system	Odyssey DLx	LI-COR
Incubator (bacteria)	Inkubator 1000, Unimax 1010	Heidolph
Incubator (cells)	Heracell 150/150i	ThermoFisher Scientific
Inverse microscope	Axio Observer A1	Zeiss
Inverse microscope	Axiovert 40CF	Zeiss
Ion source	Nanospray Flex Ion Source	ThermoFisher Scientific
Luminometer	GloMax 96 Microplate Luminometer	Promega
Lyophilisator	Alpha 1-2 LD Plus	Christ
Mass spectrometer	Q Exactive Plus Hybrid Quadrupole-Orbitrap	ThermoFisher Scientific
Mass spectrometer	Thermo Orbitrap Tribrid Fusion Lumos mass spectrometer	ThermoFisher Scientific
MEA	Maestro Edge	Axion Biosystems
Microinjector	Picospritzer III	Parker
MilliQ-Ultra pure water	Advantage A10	Millipore
Nanophotometer	Implen	ThermoFisher Scientific
PCR machine	MY Cycler	BioRad
PCR machine	T3000	Biometra
pH-Meter	SevenCompact	Mettler Toledo
Photometer	BioPhotometer	Eppendorf
Sequencer	NovaSeq6000	Illumina
Shaker	Polymax 1040	Heidolph
Sonicator	Sonopuls MS73	Bandelin
Sonicator	Ultrasonics Sonifier	Branson Ultrasonics
Spectrophotometer	NanoDrop 2000	ThermoFisher Scientific
Syringe	Hamilton Nanofil syringe 10 µl	World Precision Instruments
Thermo Shaker	Thermo Mixer Compact	Eppendorf
Thermo Shaker	MB-102 / MKR13	Bioer / HLC
Tissue dissociator	GentleMacs Octo Dissociator	Miltenyi Biotec
Tissue grinder	Potter-Elvehjem Tissue Grinder	DWK Life Sciences
Triple electrode		Constructed in workshop at University of Bonn
Ultracentrifuge	Sorvall WX Ultra Series	ThermoFisher Scientific
Ultracentrifuge	Optima XE-90	Beckman Coulter
Vaporizer	Anesthetic vaporizer (isoflurane)	Harvard Apparatus

Vibratome	Microm HM650V	ThermoFisher Scientific
Vortexer	Vortex-Genie 2	Scientific Industries

6.3.2 Software / databases

Table 18: Softwares and databases that were used for acquisition, analysis, and interpretation of data.

Software / database	Application	Company / URL
Allen Brain Map	Extraction of marker genes for scRNAseq	https://portal.brain-map.org/
AXiS Navigator 2.0.4	MEA recordings and analysis	Axion Biosystems
Cell Ranger	Read alignment and feature-barcode matrix generation for scRNAseq	10x Genomics
DAVID 6.8	Functional annotation analysis	https://david.ncifcrf.gov/
Fiji	Analysis of confocal microscopy images	https://imagej.net/software/fiji/
GraphPad Prism 9.1.1	Statistical testing	Graphstats
IgorPro 7.08	Creation of graphs	WaveMetrics
ImageStudio	Acquisition of immunoblots	LI-COR
ImageStudioLite	Analysis of immunoblots	LI-COR
Imaris 9.1.0	Tracing and analysis of dendrites	Oxford Instruments
Limma 3.36.5	Analysis of proteomics data	R package
Mascot server version 2.6.1	CoIP mass spectrometry analysis	Matrix Science Ltd.
MaxQuant v1.5.8.3	Phosphoproteomics analysis	https://www.maxquant.org/
MaxQuant v1.6.5.0	BioID analysis	https://www.maxquant.org/
Mouse Brain Atlas	Extraction of marker genes for scRNAseq	http://mousebrain.org/
NCBI Nucleotide	Extraction of gene information	https://www.ncbi.nlm.nih.gov/nuccore/
NeuroScore v2.1	EEG analysis	DSI
NIS-Elements AR 5.11.03	Acquisition software of the confocal microscope	Nikon
Paircoil2	Visualization of coiled-coil domain structure of Slk	http://cb.csail.mit.edu/cb/paircoil2/
phosphoprocessR 0.99.8	Phosphoproteomics analysis	R package
Proteome Discoverer 2.5.0.400	CoIP mass spectrometry analysis	ThermoFisher Scientific
R 3.6.3	Analysis of scRNAseq data	https://www.r-project.org/
Seurat 3.2.1	Analysis of scRNAseq data	R package
SnapGene 2.7.3	Plasmid design	Dotmatics
STRING Version 11.5	Analysis of protein networks	https://string-db.org/
SynGO	Synaptic protein annotation analysis	https://www.syngoportal.org/
UniProt	Extraction of protein information	https://www.uniprot.org/

6.3.3 Reagents / chemicals / enzymes

Table 19: Reagents, chemicals, and enzymes used in this study.

Reagents / chemicals / enzymes	Company
β-Glycerophosphate	Sigma-Aldrich
β-Mercaptoethanol	Carl Roth
10x restriction buffers G, O, R, Tango	ThermoFisher Scientific
5x HF Buffer	ThermoFisher Scientific
6x DNA Gel Loading Dye	ThermoFisher Scientific
Acetonitrile	Sigma-Aldrich
Acrylamide	Sigma-Aldrich
Acrylamide Rotiphorese Gel 40 (37,5:1)	Carl Roth
Agarose	Biozym
Ammonium persulfate (APS)	Carl Roth
Ampicillin	Carl Roth
Ampuwa water	Fresenius Kabi
Benzonase endonuclease	Sigma-Aldrich
Bovine Serum Albumin (BSA), fraction V	Carl Roth
Bromophenol Blue	Carl Roth
Buprenorphine	Bayer
Calcium chloride ($CaCl_2$)	Sigma-Aldrich
Colloidal Coomassie ROTI Blue	Carl Roth
cOmplete ULTRA-Mini EDTA-free Protease Inhibitor Cocktail	Roche
cOmplete-ULTRA Protease Inhibitor Cocktail	Roche
Coomassie Brilliant Blue R	Sigma-Aldrich
Dimethylsulfoxide (DMSO)	Sigma-Aldrich
Disodium hydrogen phosphate (Na_2HPO_4)	Sigma-Aldrich
dNTP	ThermoFisher Scientific
EDTA	Calbiochem
EGTA	Carl Roth
Ethanol	Carl Roth
Fast Green	Sigma-Aldrich
Fentanyl	Braun
Formic acid	Sigma-Aldrich
Gelatin from cold-water fish skin	Sigma-Aldrich
GeneRuler 1 kb DNA ladder	Invitrogen
GeneRuler 100 bp DNA ladder	Invitrogen
GFP-Trap Magnetic Agarose Beads	ChromoTek
Glucose	PanReac AppliChem
Glutathione-Agarose	Merck
Glycerol	ThermoFisher Scientific
Glycine	Carl Roth
GST Elution Buffer	G-Biosciences
HEPES	Carl Roth
Hydrogen chloride (HCl)	Carl Roth

Immersol W2010	Pulch + Lorenz
Isoflurane	Piramal Healthcare
Isopropanol	Carl Roth
Isopropyl β-D-thiogalactosid (IPTG)	Carl Roth
Kanamycin	Sigma-Aldrich
Ketamine 10%	WDT
Ketoprofen	Mibe
Luria Broth-Agar (Luria-Miller)	Carl Roth
Luria Broth-Medium (Luria-Miller)	Carl Roth
Lysozyme	Carl Roth
Lysyl endopeptidase	Fujifilm/Wako
Magnesium chloride ($MgCl_2$)	PanReac AppliChem
Magnesium sulfate ($MgSO_4$)	Sigma-Aldrich
Medetomidine	Zoetis
Methanol	Merck
Midazolam	Braun
Mowiol 4-88	Carl Roth
Myelin Removal Beads II, human, mouse, rat	Miltenyi Biotec
N-octyl-β-D-glucopyranoside	Merck
Normal goat serum (NGS)	Life Technologies
NuPAGE MOPS SDS Running Buffer	Invitrogen
PageRuler Plus Prestained Protein	ThermoFisher Scientific
Paraformaldehyde	Sigma-Aldrich
PeqGreen DNA/RNA Dye	VWR
Phenylmethylsulfonyl fluoride (PMSF)	Sigma-Aldrich
Phosphatase Inhibitor Cocktail II	Calbiochem
Phosphate buffered saline (PBS)	Millipore
PhosSTOP Phosphatase inhibitor cocktail	Roche
Phusion High-Fidelity DNA polymerase	ThermoFisher Scientific
Pierce Anti-HA Magnetic Beads	ThermoFisher Scientific
Potassium chloride (KCl)	Carl Roth
Red Blood Cell Lysis Solution (10x)	Miltenyi Biotec
Restriction enzymes	ThermoFisher Scientific
Ringer solution	Fresenius Kabi
RNaseZap RNase Decontamination Solution	Invitrogen
SOC Medium	Takara
Sodium carbonate ($NaHCO_3$)	PanReac AppliChem
Sodium chloride (NaCl)	Carl Roth
Sodium deoxycholate	Sigma-Aldrich
Sodium fluoride (NaF)	Sigma-Aldrich
Sodium hydroxide (NaOH)	Carl Roth
Sodium phosphate (NaH_2PO_4)	G-Biosciences
Sodiumdodecylsulfate (SDS)	Carl Roth
Sodiumhydrogenphosphate (Na_2HPO_4)	Merck
Spectinomycin	Sigma-Aldrich

Streptavidin Sepharose high-performance affinity resin	GE Healthcare
Sucrose	PanReac AppliChem
Tandem mass tag 10-plex reagents	ThermoFisher Scientific
Tetramethylethylenediamine (TEMED)	Carl Roth
TetraSpeck Microspheres 4.0 µm fluorescent	Invitrogen
Tris	Carl Roth
Tris-hydrochloride (Tris-HCl)	Carl Roth
TritonX-100	Roche
Trypsin (sequencing grade)	Promega
Tween	Sigma-Aldrich
Xylazine 2% vet.	Ceva Tiergesundheit

6.3.4 Cell culture media / reagents

Table 20: Cell culture media and reagents used in this study.

Media / Reagents	Company
B27 Supplement	Gibco
Basal Medium Eagle (BME)	Gibco
Biotin	Sigma-Aldrich
Dulbecco's Modified Eagle's Medium (DMEM)	Gibco
Dulbecco's Phosphate Buffered Saline (DPBS)	Gibco
Fetal bovine/calf serum (FBS/FCS)	Gibco
G418	Carl Roth
GenJet Plus DNA *in vitro* Transfection Reagent	SignaGen Laboratories
GlutaMAX DMEM	Gibco
Hank's Buffered Salt Solution (HBSS)	Gibco
Iscove's Modified Dulbecco's Medium (IMDM)	Gibco
L-Glutamine	Gibco
Neurobasal Medium (NB)	Gibco
OptiPrep Density Gradient Medium	Sigma-Aldrich
Penicillin-Streptomycin	Gibco
Poly-D-lysine	Sigma-Aldrich
Trypsin-EDTA (0.05%)	Gibco

6.3.5 Consumables

Table 21: Consumables used in this study.

Consumable	Company
100/20 mm cell culture dish Cellstar sterile	Greiner Bio-One
15 ml Falcon	Greiner Bio-One
50 ml Falcon	Greiner Bio-One
Amersham Protran 0.45 nitrocellulose membrane	GE Healthcare
Amicon Ultra Centrifugal filters	Merck Millipore
Cell Culture Flask	Greiner Bio-One

Cell Scraper	TPP
Coverslips	Hecht
CytoView MEA 6-well plate	Axion Biosystems
Feather Disposable Scalpel	ThermoFisher Scientific
Filter pipette tips	Nerbe Plus
Gel Saver Tip II 200 µl	Kisker Biotech
GentleMACS C tubes	Miltenyi Biotec
HiTrap heparin columns	GE Healthcare
LS columns	Miltenyi Biotec
MACS SmartStrainers 70 µm	Miltenyi Biotec
NuPAGE 4-12% Bis-Tris 1.5 mm gels	ThermoFisher Scientific
Object slide	Marienfeld
Pipette (5 ml, 10 ml, 25 ml)	Greiner Bio-One
Pipette tips	Greiner Bio-One
Protein LoBind Tubes	Eppendorf
Replacement Bores for Drummond Micropipettes	ThermoFisher Scientific
ReproSil Pur C18 AQ 1.9 µm resin column	Dr. Maisch
S2 flow cell	Illumina
Sep-Pak tC18 3 cc Vac Cartridge 200 mg	Sorbent, Water
Syringe filter 0.2 µm cellulose acetate	VWR
Syringe Filter Unit 0.45 µm PVDF 33 mm gamma sterilized	Merck Millipore
TA10ETA-F20 electrodes	DSI
ThermoScientific PA Microtube 1.5 ml Ultracentrifuge	ThermoFisher Scientific
TSKgel Amide-80 resin column	Tosoh
Wound clips (Michel, 7.5 x 1.75 mm)	VUBU

6.3.6 Kits

Table 22: Kits used in this study.

Kit	Company
ADP-Glo Kinase Assay Kit	Promega
Chromium Chip B Single Cell Kit	10xGenomics
Chromium i7 Multiplex Kit	10xGenomics
Chromium NextGEM Single Cell 3' GEM, Library & Gel Bead Kit v3.1	10xGenomics
DC Protein Assay	Bio-Rad
DNA Clean and Concentrator Kit	Zymo Research
EndoFree Plasmid Maxi Kit	Qiagen
GeneJET Plasmid Miniprep Kit	ThermoFisher Scientific
In-Fusion HD Cloning Plus Kit	Takara
Neural Tissue Dissociation Kit (P)	Miltenyi Biotec
NovaSeq S2 Reagent Kit (100 cycles)	Illumina
PureLink HiPure Plasmid Filter Maxiprep Kit	Invitrogen
PureLink HiPure Plasmid Filter Midiprep Kit	Invitrogen
SLK Kinase Enzyme System	Promega
Zymoclean Gel DNA Recovery Kit	Zymo Research

6.3.7 Primary antibodies

Table 23: Primary antibodies used for immunocytochemistry (ICC) and Western Blotting (WB) experiments.

Antibody	Dilution	Assay	Product No.	Company
Anti-β-actin mouse monoclonal	1:5000	WB	ab6276	Abcam
Anti-acetylated Tubulin mouse monoclonal	1:500	ICC	T7451	Sigma Aldrich
Anti-FAK rabbit monoclonal	1:500	ICC	ab40794	Abcam
Anti-gephyrin mouse monoclonal	1:250	ICC	147111	Synaptic Systems
Anti-gephyrin rabbit monoclonal	1:500	ICC	147008	Synaptic Systems
Anti-GFP mouse monoclonal	1:1000	WB	ab38689	Abcam
Anti-GRLF1 rabbit polyclonal	1:500	WB	PA5-38253	Invitrogen
Anti-GST rabbit polyclonal	1:500	WB	ab9085	Abcam
Anti-HA-tag (HA.C5) mouse monoclonal	1:1000	WB	ab18181	Abcam
Anti-paxillin rabbit monoclonal	1:250	ICC	ab32084	Abcam
Anti-pGRLF1 Y1105 rabbit polyclonal	1:500	WB	ab182636	Abcam
Anti-pS6 ribosomal protein (Ser240/244) rabbit monoclonal	1:500	ICC	5364	Cell Signaling
Anti-Slk rabbit polyclonal	1:1000	WB	MBS8233912	MyBioSource

6.3.8 Secondary antibodies

Table 24: Secondary antibodies used for immunocytochemistry (ICC) and Western Blotting (WB) experiments.

Antibody	Dilution	Assay	Product No.	Company
Goat Anti-Guinea pig IgG H&L (Alexa Fluor® 405)	1:200	ICC	ab175678	Abcam
Goat anti-Mouse IgG (H+L) Cross-Adsorbed Secondary Antibody, Alexa Fluor 568	1:200	ICC	A11004	Invitrogen
Goat Anti-Mouse IgG H&L (Alexa Fluor® 647)	1:200	ICC	ab150115	Abcam
Goat anti-Rabbit IgG (H+L) Cross-Adsorbed Secondary Antibody, Alexa Fluor 568	1:200	ICC	A11011	Invitrogen
Goat Anti-Rabbit IgG H&L (Alexa Fluor® 647)	1:200	ICC	ab150079	Abcam
IRDye 680LT Donkey anti-Mouse IgG(H+L)	1:10000	WB	926-68022	LI-COR Biotechnology
IRDye 680RD Goat anti-Mouse IgG (H+L)	1:10000	WB	926-68070	LI-COR Biotechnology
IRDye 680RD Streptavidin	1:5000	WB	926-32231	LI-COR Biotechnology
IRDye 800CW Goat anti-Rabbit IgG (H+L)	1:10000	WB	926-32211	LI-COR Biotechnology

IRDye 800CW Streptavidin	1:5000	WB	926-32230	LI-COR Biotechnology
Phalloidin-iFluor 647 Conjugate	1:500	ICC	23127	AAT Bioquest

6.3.9 Cloning primers

Table 25: Primers used to clone constructs.
fw: forward primer, rev: reverse primer, h: human, m: mouse, r: rat.

Primer	Internal ID	Sequence (5' to 3')	Cloned construct
EGFP_fw	c2974	CGTCAGATCCGCTAGCTAGCGCTACCGGTCGCC	pCMV-EGFP
EGFP_rev	c2975	CCGCGGTACCGTCGATTACTTGTACAGCTCGTCCATGCC	pCMV-EGFP
EGFP-hMap4k4_fw	c3226	CGGACTCAGATCTCGATGGCGAACGACTCCCC	pCMV-EGFP-hMap4k4
EGFP-hMap4k4_rev	c3227	CCGCGGTACCGTCGACTACCAGCTCAGAAGAGAAGTCC	pCMV-EGFP-hMap4k4
EGFP-hMink1_fw	c3095	CGGACTCAGATCTCGATGGGCGACCCAGCC	pCMV-EGFP-hMink1
EGFP-hMink1_rev	c3096	CCGCGGTACCGTCGATCACCAGTTCATGATGCAGTTACGGT	pCMV-EGFP-hMink1
EGFP-hPrkcg_fw	c3126	CGGACTCAGATCTCGATGGCTGGTCTGGGCC	pCMV-EGFP-hPrkcg
EGFP-hPrkcg_rev	c3127	CCGCGGTACCGTCGATTACATGACGGGCACAGGC	pCMV-EGFP-hPrkcg
EGFP-hTnik_fw	c3101	CGGACTCAGATCTCGATGGCGAGCGACTCCC	pCMV-EGFP-hTnik
EGFP-hTnik_rev	c3102	CCGCGGTACCGTCGATTACCAGTTCATCATGGAATTTCTGTTGAGG	pCMV-EGFP-hTnik
EGFP-mCrmp1_fw	c2976	CGGACTCAGATCTCGATGTCTCATCAGGGGAAGAAGAG	pCMV-EGFP-mCrmp1
EGFP-mCrmp1_rev	c2977	CCGCGGTACCGTCGATCAACCGAGGCTGGTGATGTTGGAG	pCMV-EGFP-mCrmp1
EGFP-mMap4k4_Fragment1_fw	c3246	CGGACTCAGATCTCGATGGCGAACGACTCTCCC	pCMV-EGFP-mMap4k4
EGFP-mMap4k4_Fragment1_rev	c3247	GGCACTTCCTCCTCCTCCTCCTCG	pCMV-EGFP-mMap4k4
EGFP-mMap4k4_Fragment2_fw	c3248	GGAGGAGGAAGTGCCTGAGCA	pCMV-EGFP-mMap4k4

EGFP-mMap4k4_Fragment2_rev	c3249	ACCAGCTTTTCCACTCTCTCCCCA	pCMV-EGFP-mMap4k4
EGFP-mMap4k4_Fragment3_fw	c3250	AGTGGAAAAGCTGGTCCCCAG	pCMV-EGFP-mMap4k4
EGFP-mMap4k4_Fragment3_rev	c3251	TTTCTTAGCCAGGATAAATAGTAGACACGTAACTT	pCMV-EGFP-mMap4k4
EGFP-mMap4k4_Fragment4_fw	c3252	ATCCTGGCTAAGAAATAAGATTCTTCATAATGATCCA	pCMV-EGFP-mMap4k4
EGFP-mMink1_Fragment1_rev	c3240	TCTTCCTCCTCACTGCCGCT	pCMV-EGFP-mMink1
EGFP-mMink1_Fragment2_rev	c3242	GACCCTCCGGCCCCACTGGT	pCMV-EGFP-mMink1
EGFP-mMink1_Fragment2_fw	c3241	CAGTGAGGAGGAAGACGACAGC	pCMV-EGFP-mMink1
EGFP-mMink1_Fragment3_rev	c3244	GTGATGAGCAAGTTGAGCCCTTCT	pCMV-EGFP-mMink1
EGFP-mMink1_Fragment3_fw	c3243	TGGGGCCGGAGGGTCCCGG	pCMV-EGFP-mMink1
EGFP-mMink1_Fragment4_fw	c3245	CAACTTGCTCATCACCATCTCAGGG	pCMV-EGFP-mMink1
EGFP-mShisa7_fw	c3128	CGGACTCAGATCTCGGGAGTCATCAGTTTCGCCCT	pCMV-EGFP-mShisa7 (194-558)
EGFP-mShisa7_rev	c3129	CCGCGGTACCGTCGAAACATCCCAAAAGGAGGCGT	pCMV-EGFP-mShisa7 (194-558)
EGFP-mTmeff1_fw	c3132	CGGACTCAGATCTCGGGCGACAGCATGGGCG	pCMV-EGFP-mTmeff1
EGFP-mTmeff1_rev	c3133	CCGCGGTACCGTCGACGTGGTCAGTGCGCATATAA	pCMV-EGFP-mTmeff1
EGFP-mTnik_Frag1_rev	c3220	CAGTGTTGACTCCCCTGGTAGG	pCMV-EGFP-mTnik
EGFP-mTnik_Frag2_fw	c3221	GGGGAGTCAACACTGCGAAGGGACTTCC	pCMV-EGFP-mTnik
EGFP-mTnik_Frag2_rev	c3222	TCCAAGTCTGGGGCCCAG	pCMV-EGFP-mTnik
EGFP-mTnik_Frag3_fw	c3223	CTGGGCCCCAGACTTGGATC	pCMV-EGFP-mTnik
EGFP-mTnik_Frag3_rev	c3224	TATTTCTGAATTGAAGCGTTT	pCMV-EGFP-mTnik
EGFP-mTnik_Frag4_fw	c3225	AAACGCTTCAATTCAGAAATACTTTGTGCA	pCMV-EGFP-mTnik

GST-mAcap3 (305-469)_fw	c3067	GTGGTGGAATTCTAGGAAAGGATGCACTCACTGTGGTG	pGEX-GST-mAcap3 (305-469)
GST-mAcap3 (305-469)_rev	c3068	TTGAGCTCGAGTCGACCTACTTTAGCAGCTCTGGCTCCC	pGEX-GST-mAcap3 (305-469)
GST-mChl1_fw	c2763	GTGGTGGAATTCTAGAAAAGAGGAACAGAGGTGGAAAGTATT	pGEX-GST-mChl1 (1105-1209)
GST-mChl1_rev	c2764	TTGAGCTCGAGTCGACTCATGCCCGGAGTGG	pGEX-GST-mChl1 (1105-1209)
GST-mCrmp1_fw	c2765	GTGGTGGAATTCTAGAAATGTCTCATCAGGGGAAGAAGAGC	pGEX-GST-mCrmp1
GST-mCrmp1_rev	c2766	TTGAGCTCGAGTCGACTCAACCGAGGCTGGTGATGTTG	pGEX-GST-mCrmp1
GST-mGit1 (375-546)_fw	c3069	GTGGTGGAATTCTAGGAAACCTTGAGCTGTCTGCACG	pGEX-GST-mGit1 (375-546)
GST-mGit1 (375-546)_rev	c3070	TTGAGCTCGAGTCGACCTACGTGCTGTGGAAAGGC	pGEX-GST-mGit1 (375-546)
GST-mMagi3 (581-773)_fw	c3071	GTGGTGGAATTCTAGGAACTATCCCTCTGATTAAGGGCCC	pGEX-GST-mMagi3 (581-773)
GST-mMagi3 (581-773)_rev	c3072	TTGAGCTCGAGTCGACCTAAGCAGCACGGAGCC	pGEX-GST-mMagi3 (581-773)
GST-mMap1b (1807-1982)_fw	c3073	GTGGTGGAATTCTAGGAGCAGCAGCTCACCAAGCCTC	pGEX-GST-mMap1b (1807-1982)
GST-mMap1b (1807-1982)_rev	c3074	TTGAGCTCGAGTCGACCTAGTCATCCAGGAGCCTTCTGG	pGEX-GST-mMap1b (1807-1982)
GST-mMap1b_402_fw	c2905	GTGGTGGAATTCTAGTAAGAAGTGTAGGCAATACCATTGAGCCTG	pGEX-GST-mMap1b (402-678)
GST-mMap1b_678_rev	c2906	TTGAGCTCGAGTCGATTACACCTCTTCCTTTCTTGGCT	pGEX-GST-mMap1b (402-678)
GST-mMap1b_fw	c2767	GTGGTGGAATTCTAGAAATTGGTGAGCTCCTAAGCACC	pGEX-GST-mMap1b (171-793)
GST-mMap1b_rev	c2768	TTGAGCTCGAGTCGACTTAGGCAGCTGCTTCTGTGGT	pGEX-GST-mMap1b (171-793)
GST-mMap2 (1582-1723)_fw	c3075	GTGGTGGAATTCTAGGAAGGTCAGAACCAATTCGCAGAG	pGEX-GST-mMap2 (1582-1723)
GST-mMap2 (1582-1723)_rev	c3076	TTGAGCTCGAGTCGACCTAACGTCCACCACCTGG	pGEX-GST-mMap2 (1582-1723)

GST-mMap4k4(139-315)_fw	c3218	GTGGTGGAATTCTAGGAGGATTGGCACATCTCCATATTCAC	pGEX-GST-mMap4k4 (139-315)
GST-mMap4k4(139-315)_rev	c3219	TTGAGCTCGAGTCGATTATTTCTCGCCTCTCTTCTTTCTGGTCC	pGEX-GST-mMap4k4 (139-315)
GST-mMapre3 (89-235)_fw	c3077	GTGGTGGAATTCTAGGAAAAATCATTCCCGTAGAGAAGTTAGTGAAAG	pGEX-GST-mMapre3 (89-235)
GST-mMapre3 (89-235)_rev	c3078	TTGAGCTCGAGTCGACCTACAGCTCGATGTCTCGCAATTTG	pGEX-GST-mMapre3 (89-235)
GST-mMink1 (140-316)_fw	c3079	GTGGTGGAATTCTAGAGGGTCTTGCCCATCTCCATGC	pGEX-GST-mMink1 (140-316)
GST-mMink1 (140-316)_rev	c3080	TTGAGCTCGAGTCGACCTATTTCTCACCCCGCTTCT	pGEX-GST-mMink1 (140-316)
GST-mNav1 (492-672)_fw	c3081	GTGGTGGAATTCTAGGAGGTAGCCTGAAGATGGAACCT	pGEX-GST-mNav1 (492-672)
GST-mNav1 (492-672)_rev	c3082	TTGAGCTCGAGTCGACACTACTGGATGTTGGACCGTGCT	pGEX-GST-mNav1 (492-672)
GST-mNav1_283_rev	c2739	ATGGAGTCTAGAATTTTATCGCAGGCTGGACATGGT	pGEX-GST-mNav1 (39-283)
GST-mNav1_fw	c2738	GGTGGTGGTGGAATTGGAGGAGGTGGGTCTGGAGGTGGAGCGGCGGACGGCAG	pGEX-GST-mNav1 (39-283)
GST-mNcam1 (730-875)_fw	c3083	GTGGTGGAATTCTAGGAGACATCACCTGCTACTTCCTGAACA	pGEX-GST-mNcam1 (730-875)
GST-mNcam1 (730-875)_rev	c3084	TTGAGCTCGAGTCGACCTAGGCCTGACCAGCGGG	pGEX-GST-mNcam1 (730-875)
GST-mNefh_412_fw	c2907	GTGGTGGAATTCTAGGCTTTGGTCCGAGTCCC	pGEX-GST-mNefh (412-807)
GST-mNefh_807_rev	c2908	TTGAGCTCGAGTCGATTTACGCCTCAGCTGGGGG	pGEX-GST-mNefh (412-807)
GST-mNefh_fw	c2769	GTGGTGGAATTCTAGAAATCCAGGGCTGCGGG	pGEX-GST-mNefh (243-892)
GST-mNefh_rev	C2770	TTGAGCTCGAGTCGACTTACTCCTTCACAGGGGACTTCA	pGEX-GST-mNefh (243-892)
GST-mRasgrf1 (635-749)_fw	c3085	GTGGTGGAATTCTAGGAAAAGTGCTTCAGATCCGCTATGCC	pGEX-GST-mRasgrf1 (635-749)
GST-mRasgrf1 (635-749)_rev	c3086	TTGAGCTCGAGTCGACCTAGGGGATGTTGAGGGACAGC	pGEX-GST-mRasgrf1 (635-749)
GST-mShisa7 (211-345)_fw	c3087	GTGGTGGAATTCTAGGAAGCAAGGCGTCACGTG	pGEX-GST-mShisa7 (211-345)

GST-mShisa7 (211-345)_rev	c3088	TTGAGCTCGAGTCGACCTACAGTCTCTTGAGGGAAGAGTATCG	pGEX-GST-mShisa7 (211-345)
GST-mTnik (140-316)_fw	c3089	GTGGTGGAATTCTAGAGGGCCTGAGTCACCTGCAC	pGEX-GST-mTnik (140-316)
GST-mTnik (140-316)_rev	c3090	TTGAGCTCGAGTCGACCTATTTTTCTCCTCGCTTCTTCTTTGTT	pGEX-GST-mTnik (140-316)
GST-rIgf2bp1_343_rev	c2734	ATGGAGTCTAGAATTTTAGATCTCCTGCTCAGCCCTG	pGEX-GST-rIgf2bp1 (1-343)
GST-rIgf2bp1_fw	c2733	GGTGGTGGTGGAATTGGAGGAGGTGGGTCTGGAGGTGGAATGAACAAGCTTTACATCGGCAACC	pGEX-GST-rIgf2bp1 / pGEX-GST-rIgf2bp1 (1-343)
GST-rIgf2bp1_rev	c2737	ATGGAGTCTAGAATTTCACTTCCTTCGTGCCTGGG	pGEX-GST-rIgf2bp1
GST-rSV2a_169_rev	c2736	ATGGAGTCTAGAATTTTAGTAGAGTGTCCACTGGAAGCGAC	pGEX-GST-rSv2a (1-169)
GST-rSv2a_fw	c2735	GGTGGTGGTGGAATTGGAGGAGGTGGGTCTGGAGGTGGAATGGAAGAAGGCTTTCGAGACCG	pGEX-GST-rSv2a (1-169)
HA_fw	c1976	AATTCACCAGGACCAACCATGTACCCATACGATGTTCCAGATTACGCTTAGGCGGCCGCG	pLenti-Ef1α-mCherry-T2A-HA
HA_rev	c1977	GATCCGCGGCCGCCTAAGCGTAATCTGGAACATCGTATGGGTACATGGTTGGTCCTGGTG	pLenti-Ef1α-mCherry-T2A-HA
mRFP_fw	c1644	TGGATCGATCCACCAATGGCCTCCTCCGAGG	pAAV-CMV/CBA-mRFP-U6-shSlk
mRFP_rev	c1645	ATAAGCTAGCTTGATTTAGGCGCCGGTGGAGTGG	pAAV-CMV/CBA-mRFP-U6-shSlk
mSlk-8AA_fw	c2038	GCCCTGCCTCGAATTGGATGTCCTTCTTCAATTTCCGTAAGATCT	pLenti-Ef1α-mCherry-T2A-mSlk-myc-BirA*
mSlk-8AA_rev	c2039	TCCACCTCCAGACCCACCTCCTCCTGACCCAGTGGAATGTAAGGT	pLenti-Ef1α-mCherry-T2A-mSlk-myc-BirA*
mSlk-HA_fw	c1974	GCCCTGCCTCGAATTCGATGTCCTTCTTCAATTTCCGTAAGATCTT	pLenti-Ef1α-mCherry-T2A-mSlk-HA
mSlk-HA_rev	c1975	TAGATCCGGTGGATCCGCGGCCGCCTAAGC	pLenti- EF1α-mCherry-T2A-mSlk-HA
myc-BioID_fw	c2036	GCCCTGCCTCGAATTGCATGGAACAAAAACTCATCTCAGAAGAG	pLenti-Ef1α-mCherry-T2A-myc-BirA*

myc-BioID_fw	c2040	TGGGTCTGGAGGTGGAGGATCCATGGAACAAAAACTCATCTCAG	pLenti-Ef1α-mCherry-T2A-mSlk-myc-BirA*
myc-BioID_rev	c2037	TAGATCCGGTGGATCTCTAGAAAACGCGTTAGATATCACCCGG	pLenti-Ef1α-mCherry-T2A-myc-BirA* / pLenti-Ef1α-mCherry-T2A-mSlk-myc-BirA*

6.3.10 Sequencing primers

Table 26: Primers used for sequencing.
Fw: forward, rev: reverse.

Target sequence	Primer	Internal ID	Sequence (5' to 3')
End of CMV promoter	fw	s155	CACCCCATTGACGTCAATG
End of CMV/CBA promoter	fw	s243	GGTTCGGCTTCTGGCGTG
End of EGFP	fw	s16	ATGGTCCTGCTGGAGTTC
End of EGFP	fw	s32	AAGTTCGAGGGCGACACC
End of EGFP	rev	s33	TCTTGTAGTTGCCGTCGTCC
End of GST tag	fw	s274	GTGCCTGGATGCGTTCCCAAA
End of H1 promoter	fw	s220	TCGCTATGTGTTCTGGGAAA
End of mCherry	fw	s17	CCGCCACTCCACCGG
End of mCherry	fw	s188	CACTACGACGCTGAGGTCAA
End of mSlk	fw	s68	CACCTGTTGGTTGAACATGAGA
End of U6 promoter	fw	s245	TGACGTAGAAAGTAATAATTTCTTGG
pGEX-GST vector	rev	s5	GGGAGCTGCATGTGTCAGAG
rIgf2bp1	fw	s356	CCTCGGCCTGTAAGATGATCTTGG
rIgf2bp1	fw	s357	CAGGAGATCATGAAGAAAGTTCG
rIgf2bp1	fw	s358	AGAGGCTCAGTTCAAGGCTC
WPRE element	rev	s247	GCATTAAAGCAGCGTATCCACA

6.3.11 Plasmids

Table 27: Plasmids that were used in this study.
RE: restriction enzyme; m: mouse; r: rat; h: human.

Plasmid	Resistance	RE1	RE2	Source
pAAV-U6-MCS-CMV/CBA-hrGFP	Ampicillin			Cloned by previous colleagues
pAAV-U6-MCS-CMV/CBA-mRFP	Ampicillin			Cloned by previous colleagues
pAAV-U6-shSlk-CMV/CBA-hrGFP	Ampicillin			Cloned by previous colleagues
pAAV-U6-shSlk-CMV/CBA-mRFP	Ampicillin	OliI	Eco 32I	Cloned in this study
pBABE_puro_DEST_Flag_TNIK	Ampicillin			Kindly provided by William Hahn (Addgene plasmid #45276)

pCAG_GPHN.FingR-eGFP-CCR5TC	Ampicillin			Kindly provided by Don Arnold (Addgene plasmid # 46296)
pCMV-EGFP	Kanamycin	NheI	SalI	Cloned in this study
pCMV-EGFP-hMap4k4	Kanamycin	SacI	SalI	Cloned in this study
pCMV-EGFP-hMink1	Kanamycin	SacI	SalI	Cloned in this study
pCMV-EGFP-hNav1	Kanamycin			Kindly provided by Dr. Niels Galjart, Rotterdam
pCMV-EGFP-hPrkcg	Kanamycin	SacI	SalI	Cloned in this study
pCMV-EGFP-hTnik	Kanamycin	SacI	SalI	Cloned in this study
pCMV-EGFP-mCrmp1	Kanamycin	SacI	SalI	Cloned in this study
pCMV-EGFP-mMap4k4	Kanamycin	SacI	SalI	Cloned in this study
pCMV-EGFP-mMink1	Kanamycin	SacI	SalI	Cloned in this study
pCMV-EGFP-mShisa7 (194-558)	Kanamycin	SacI	SalI	Cloned in this study
pCMV-EGFP-mTmeff1	Kanamycin	SacI	SalI	Cloned in this study
pCMV-EGFP-mTnik	Kanamycin	SacI	SalI	Cloned in this study
pCMV-EGFP-rGephyrin	Kanamycin			Kindly provided by Dr. Theofilos Papadopoulos, Göttingen
pCMV-EGFP-rIgf2bp1	Kanamycin			Kindly provided by Dr. Jacek Jaworski, Warsaw
pCMV-EGFP-rShank1	Ampicillin			Kindly provided by Dr. Carlo Sala, Milan
pCMV-EGFP-rShank2	Kanamycin			Kindly provided by Prof. Dr. Tobias Böckers, Ulm
pCMV-EGFP-rShank3	Ampicillin			Kindly provided by Prof. Dr. Tobias Böckers, Ulm
pDONR223-hMAP4K4	Spectino-mycin			Kindly provided by William Hahn & David Root (Addgene plasmid #23486)
pDONR223-hMINK1	Spectino-mycin			Kindly provided by William Hahn & David Root (Addgene plasmid #23522)
pDONR223-hPRKCG	Spectino-mycin			Kindly provided by William Hahn & David Root (Addgene plasmid #23486)
pFΔ6 VP179 (helper virus)	Ampicillin			Kindly provided by Matthias Klugmann
pFIV3.2-CMV-myc-BirA*	Ampicillin			Kindly provided by Dr. Shiva Ahmadi & Dr. Dominic Winter, Bonn
pGEX-GST-mAcap3 (305-469)	Ampicillin	XbaI	SalI	Cloned in this study
pGEX-GST-mChl1 (1105-1209)	Ampicillin	XbaI	SalI	Cloned in this study
pGEX-GST-mCrmp1	Ampicillin	XbaI	SalI	Cloned in this study
pGEX-GST-MCS	Ampicillin			Cloned by previous colleagues
pGEX-GST-mGit1 (375-546)	Ampicillin	XbaI	SalI	Cloned in this study

pGEX-GST-mMagi3 (581-773)	Ampicillin	XbaI	SalI	Cloned in this study
pGEX-GST-mMap1b (171-793)	Ampicillin	XbaI	SalI	Cloned in this study
pGEX-GST-mMap1b (1807-1982)	Ampicillin	XbaI	SalI	Cloned in this study
pGEX-GST-mMap1b (402-678)	Ampicillin	XbaI	SalI	Cloned in this study
pGEX-GST-mMap2 (1582-1723)	Ampicillin	XbaI	SalI	Cloned in this study
pGEX-GST-mMap4k4 (139-315)	Ampicillin	XbaI	SalI	Cloned in this study
pGEX-GST-mMapre3 (89-235)	Ampicillin	XbaI	SalI	Cloned in this study
pGEX-GST-mMink1 (140-316)	Ampicillin	XbaI	SalI	Cloned in this study
pGEX-GST-mNav1 (39-283)	Ampicillin	XbaI	SalI	Cloned in this study
pGEX-GST-mNav1 (492-672)	Ampicillin	XbaI	SalI	Cloned in this study
pGEX-GST-mNcam1 (730-875)	Ampicillin	XbaI	SalI	Cloned in this study
pGEX-GST-mNefh (243-892)	Ampicillin	XbaI	SalI	Cloned in this study
pGEX-GST-mNefh (412-807)	Ampicillin	XbaI	SalI	Cloned in this study
pGEX-GST-mRasgrf1 (635-749)	Ampicillin	XbaI	SalI	Cloned in this study
pGEX-GST-mShisa7 (211-345)	Ampicillin	XbaI	SalI	Cloned in this study
pGEX-GST-mTnik (140-316)	Ampicillin	XbaI	SalI	Cloned in this study
pGEX-GST-rIgf2bp1	Ampicillin	XbaI	SalI	Cloned in this study
pGEX-GST-rIgf2bp1 (1-343)	Ampicillin	XbaI	SalI	Cloned in this study
pGEX-GST-rSv2a (1-169)	Ampicillin	XbaI	SalI	Cloned in this study
pH21 VP181	Ampicillin			Kindly provided by Matthias Klugmann
pLenti-Ef1α-mCherry-T2A-HA	Ampicillin	XhoI	BamHI	Cloned in this study
pLenti-Ef1α-mCherry-T2A-mSlk-HA	Ampicillin	EcoRI	BamHI	Cloned in this study
pLenti-Ef1α-mCherry-T2A-mSlk-myc-BirA*	Ampicillin	EcoRI	BamHI	Cloned in this study
pLenti-Ef1α-mCherry-T2A-myc-BirA*	Ampicillin	EcoRI	BamHI	Cloned in this study
pLVTHM-EF1α-mRFP-H1-MCS	Ampicillin			Cloned by previous colleagues

pLVTHM-EF1α-mRFP-H1-shSlk	Ampicillin			Cloned by previous colleagues
pMD2.G	Ampicillin			Kindly provided by Didier Trono (Addgene plasmid #12259)
pNLrep / pRV1 VP180	Ampicillin			Kindly provided by Matthias Klugmann
psPAX2	Ampicillin			Kindly provided by Didier Trono (Addgene plasmid #12260)

6.3.12 Cells and animals

Table 28: Cells and mice used in this study.
Mice that were used for coordinated breedings were purchased from Charles River. CD1 females were mated with C57BL/6 males and timed pregnant mice were used for IUE.

Cell / mouse strain	Company
C57BL/6 (male) mice	Charles River
CD1 (female) mice	Charles River
E. coli DH5α	ThermoFisher Scientific
HEK293T cells	Takara
MAX Efficiency™ Stbl2™ Competent Cells	Takara
One Shot BL21 (DE3) pLysE Chemically Competent E. coli	ThermoFisher Scientific

6.4 List of figures

Fig. 1: Phosphorylation as a reversible process. 2
Fig. 2: Distribution of cytoskeletal elements within a neuron. 5
Fig. 3: Protein composition of postsynaptic sites. 6
Fig. 4: Structure of Slk. 12
Fig. 5: Functions of Slk in non-neuronal cells. 13
Fig. 6: Slk effects on neuron morphology. 17
Fig. 7: Slk expression in focal cortical malformations. 18
Fig. 8: No change of dendritic arborization after Slk knockdown (KD) in adulthood. 45
Fig. 9: Video/EEG monitoring of *in utero* electroporated mice. 46
Fig. 10: Procedure of MEA recordings from acute brain slices. 47
Fig. 11: No change in the number of spikes and bursts in MEA recordings of acute slices of control (Ctrl) and Slk knockdown (KD) animals. 50
Fig. 12: Effect of epileptiform aCSF$^{lowMg2+,highK+}$ on control and Slk knockdown (KD) brain slices. 51
Fig. 13: Increased activity in aCSF$^{lowMg2+,highK+}$ predominantly in control (Ctrl) brain slices. 52
Fig. 14: Preparation of a viable cell suspension for scRNAseq analysis. 53
Fig. 15: Marker identification in the cell clusters of the scRNAseq dataset. 56
Fig. 16: Clustering and cell-type annotation of the sequenced cells. 57
Fig. 17: scRNAseq cell cluster characterization 59
Fig. 18: Differential gene expression in scRNAseq dataset. 60
Fig. 19: Investigation of cytoskeleton-/scaffold-associated proteins at inhibitory synapses in cultured neurons with Slk knockdown (KD). 62
Fig. 20: Immunocytochemistry of cultured cortical neurons. 63
Fig. 21: No change in candidate proteins at inhibitory synapses in control and Slk knockdown (KD) neurons. 64
Fig. 22: Cytoskeletal changes in dendrites after Slk knockdown (KD) 66
Fig. 23: Screen for phosphorylation substrates of Slk in neurons 67
Fig. 24: Phosphorylation profile of cultured cortical neurons after Slk overexpression or knockdown. 68
Fig. 25: Annotation of significantly differentially phosphorylated proteins after Slk knockdown (KD). 70
Fig. 26: Annotation of the molecular function of differentially phosphorylated proteins after Slk knockdown (KD). 72
Fig. 27: *In vitro* phosphorylation motifs of Slk. 73
Fig. 28: KinSwing analysis of measured phosphorylation sites. 74

Fig. 29: Classification of proteins with phosphorylation sites matching the computed Slk motifs. 75
Fig. 30: Cloning of BirA* expression constructs for proximity-dependent biotinylation experiments. 76
Fig. 31: Proximity-dependent biotinylation in cultured HEK293T cells and primary neurons. 77
Fig. 32: BioID analysis. 78
Fig. 33: CoIP of brain proteins with Slk. 79
Fig. 34: Mass spectrometric analysis of co-immunoprecipitated proteins. 80
Fig. 35: Overlap of the three different proteomics approaches. 81
Fig. 36: GO analysis of proteins identified in phosphoproteomics and CoIP experiments. ... 85
Fig. 37: Proteins that are binding to Slk and less phosphorylated after Slk knockdown. 86
Fig. 38: No change of Grlf1 phosphorylation after Slk knockdown (KD) in cultured cortical neurons. 87
Fig. 39: CoIP with candidate proteins followed by immunoblotting. 90
Fig. 40: *In vitro* kinase reactions with potential candidate substrates of Slk. 92
Fig. 41: Structures and phosphorylation sites of the four candidate substrates of Slk. 95
Fig. 42: Potential mechanisms of Slk action in neurons based on proteomics experiments. 110
Fig. 43: Mutations in hSlk leading to a disruption of the coiled-coil domains. 113

6.5 List of tables

Table 1: Known functions of Slk in different cell types and tissues..... 14
Table 2: Known phosphorylation substrates of Slk. 19
Table 3: Known binding partners of Slk. 21
Table 4: PCR protocol for amplification of insert..... 24
Table 5: Restriction digest of vector DNA and recombination with PCR fragments. 25
Table 6: Transfection of HEK293T cells in 100 mm cell culture dishes. 27
Table 7: Transfection of HEK293T cells for lentivirus preparation. 28
Table 8: Proteins that were found in all of the proteomics approaches. 82
Table 9: Comparison of proteomics results with known substrates and interaction partners of Slk. 83
Table 10: Identification of Grlf1 in phosphoproteomics and CoIP experiments. 87
Table 11: Proteins chosen for CoIP verification experiments. 88
Table 12: Mass spectrometric screen of candidate proteins after *in vitro* kinase reactions with Slk. 93
Table 13: New phosphorylation sites identified by *in vitro* kinase reactions followed by mass spectrometric analysis. 94
Table 14: Neurodevelopmental risk genes affecting structural plasticity. 114
Table 15: Abbreviations that are used in this study. 117
Table 16: Gene names are listed with their corresponding protein name..... 120
Table 17: Equipment used in this study. 127
Table 18: Softwares and databases that were used for acquisition, analysis, and interpretation of data. 129
Table 19: Reagents, chemicals, and enzymes used in this study. 130
Table 20: Cell culture media and reagents used in this study. 132
Table 21: Consumables used in this study. 132
Table 22: Kits used in this study. 133
Table 23: Primary antibodies used for immunocytochemistry (ICC) and Western Blotting (WB) experiments..... 134
Table 24: Secondary antibodies used for immunocytochemistry (ICC) and Western Blotting (WB) experiments..... 134
Table 25: Primers used to clone constructs. 135
Table 26: Primers used for sequencing. 140
Table 27: Plasmids that were used in this study. 140
Table 28: Cells and mice used in this study..... 143

7 References

Allison, D. W. et al. (2000) Postsynaptic scaffolds of excitatory and inhibitory synapses in hippocampal neurons: maintenance of core components independent of actin filaments and microtubules. *The Journal of Neuroscience*. 20 (12), 4545–4554.

Al-Zahrani, K. N. et al. (2014) Essential Role for the SLK Protein Kinase in Embryogenesis and Placental Tissue Development. *Developmental Dynamics*. 243 (5), 640–651.

Al-Zahrani, K. N. et al. (2020) Loss of the Ste20-like kinase induces a basal/stem-like phenotype in HER2-positive breast cancers. *Oncogene*. 39 (23), 4592–4602.

Al-Zahrani, K. N. et al. (2013) Ste20-like kinase SLK, at the crossroads: A matter of life and death. *Cell Adhesion and Migration*. 7 (1), 1–10.

Ammann, S. et al. (2016) Mutations in AP3D1 associated with immunodeficiency and seizures define a new type of Hermansky-Pudlak syndrome. *Blood*. 127 (8), 997.

Anazi, S. et al. (2017) Expanding the genetic heterogeneity of intellectual disability. *Human Genetics*. 136 (11–12), 1419–1429.

de Anda, F. C. et al. (2012) Autism spectrum disorder susceptibility gene TAOK2 affects basal dendrite formation in the neocortex. *Nature neuroscience*. 15 (7), 1022–1031.

Andoh, M. et al. (2019) Synaptic Pruning by Microglia in Epilepsy. *Journal of Clinical Medicine 2019*. 8 (12), 2170.

Andrade, C. S. & da Costa Leite, C. (2011) Malformations of cortical development: current concepts and advanced neuroimaging review. *Arquivos de neuro-psiquiatria*. 69 (1), 130–138.

Apta-Smith, M. J. et al. (2018) Evidence for the nuclear import of histones H3.1 and H4 as monomers. *The EMBO Journal*. 37 (19), e98714.

Ardito, F. et al. (2017) The crucial role of protein phosphorylation in cell signaling and its use as targeted therapy (Review). *International Journal of Molecular Medicine*. 40 (2), 271–280.

Aronica, E. et al. (2012) Malformations of cortical development. *Brain pathology*. 22 (3), 380–401.

Asquith, C. R. M. et al. (2020) Design and Analysis of the 4-Anilinoquin(az)oline Kinase Inhibition Profiles of GAK/SLK/STK10 Using Quantitative Structure-Activity Relationships. *ChemMedChem*. 15 (1), 26–49.

Bagci, H. et al. (2020) Mapping the proximity interaction network of the Rho-family GTPases reveals signalling pathways and regulatory mechanisms. *Nature cell biology*. 22 (1), 120–134.

Ballman, K. v. et al. (2004) Faster cyclic loess: normalizing RNA arrays via linear models. *Bioinformatics*. 20 (16), 2778–2786.

Baron, K. D. et al. (2015) Recruitment and activation of SLK at the leading edge of migrating cells requires Src family kinase activity and the LIM-only protein 4. *Biochimica et biophysica acta*. 1853 (7), 1683–1692.

von Bartheld, C. S. et al. (2016) The Search for True Numbers of Neurons and Glial Cells in the Human Brain: A Review of 150 Years of Cell Counting. *The Journal of comparative neurology*. 524 (18), 3865.

Bartholome, O. et al. (2017) Puzzling Out Synaptic Vesicle 2 Family Members Functions. *Frontiers in molecular neuroscience*. 10148.

Bateman, A. et al. (2021) UniProt: the universal protein knowledgebase in 2021. *Nucleic acids research*. 49 (D1), D480–D489.

Bearce, E. A. et al. (2015) TIPsy tour guides: How microtubule plus-end tracking proteins (+TIPS) facilitate axon guidance. *Frontiers in Cellular Neuroscience*. 9241.

Becker, A. J. et al. (2008) Transcriptional upregulation of Cav3.2 mediates epileptogenesis in the pilocarpine model of epilepsy. *The Journal of Neuroscience*. 28 (49), 13341–13353.

Bemben, M. A. et al. (2015) Autism-associated mutation inhibits protein kinase C-mediated neuroligin-4X enhancement of excitatory synapses. *Proceedings of the National Academy of Sciences of the United States of America*. 112 (8), 2551–2556.

Benjamini, Y. & Hochberg, Y. (1995) Controlling the False Discovery Rate: A Practical and Powerful Approach to Multiple Testing. *Journal of the Royal Statistical Society: Series B (Methodological)*. 57 (1), 289–300.

Berkovic, S. F. et al. (2006) Human epilepsies: interaction of genetic and acquired factors. *Trends in Neurosciences*. 29 (7), 391–397.

Bertling, E. et al. (2016) Actin tyrosine-53-phosphorylation in neuronal maturation and synaptic plasticity. *The Journal of Neuroscience*. 36 (19), 5299–5313.

Blümcke, I. & Wiestler, O. D. (2002) Gangliogliomas: an intriguing tumor entity associated with focal epilepsies. *Journal of neuropathology and experimental neurology*. 61 (7), 575–584.

Boersema, P. J. et al. (2009) Multiplex peptide stable isotope dimethyl labeling for quantitative proteomics. *Nature Protocols*. 4 (4), 484–494.

Borovac, J. et al. (2018) Regulation of actin dynamics during structural plasticity of dendritic spines: Signaling messengers and actin-binding proteins. *Molecular and Cellular Neuroscience*. 91122–130.

Bozzi, Y. et al. (2018) Neurobiological bases of autism–epilepsy comorbidity: a focus on excitation/inhibition imbalance. *European Journal of Neuroscience*. 47 (6), 534–548.

Bramwell, M. E. (1987) Characterization of biotinylated proteins in mammalian cells using 125I-streptavidin. *Journal of biochemical and biophysical methods*. 15 (3–4), 125–132.

Bright, D. P. & Smart, T. G. (2013) Protein kinase C regulates tonic GABAA receptor-mediated inhibition in the hippocampus and thalamus. *European Journal of Neuroscience*. 38 (10), 3408–3423.

Bruining, H. et al. (2020) Measurement of excitation-inhibition ratio in autism spectrum disorder using critical brain dynamics. *Scientific Reports*. 10 (1), 1–15.

Burakov, A. v. et al. (2005) LOSK (SLK) protein kinase activity is necessary for microtubule organization in the interphase cell centrosome. *Doklady Biological Sciences*. 403 (1–6), 317–319.

Burakov, A. v et al. (2008) Ste20-related protein kinase LOSK (SLK) controls microtubule radial array in interphase. *Molecular biology of the cell*. 19 (5), 1952–1961.

Butler, K. M. et al. (2018) De novo variants in GABRA2 and GABRA5 alter receptor function and contribute to early-onset epilepsy. *Brain*. 141 (8), 2392–2405.

Calderwood, D. A. et al. (1999) The Talin head domain binds to integrin beta subunit cytoplasmic tails and regulates integrin activation. *The Journal of biological chemistry*. 274 (40), 28071–28074.

Caserta, F. et al. (1995) Determination of fractal dimension of physiologically characterized neurons in two and three dimensions. *Journal of Neuroscience Methods*. 56 (2), 133–144.

Caserta, F. et al. (1990) Physical Mechanisms Underlying Neurite Outgrowth: A Quantitative Analysis of Neuronal Shape. *Physical Review Letters*. 64 (1), 95–98.

Cases-Cunillera, S. et al. (2022) Heterogeneity and excitability of BRAF V600E-induced tumors is determined by Akt/mTOR-signaling state and Trp53-loss. *Neuro-oncology*. 24 (5), 741–754.

Chaar, Z. et al. (2006) *v-Src-dependent Down-regulation of the Ste20-like Kinase SLK by Casein Kinase II*. 281 (38), 28193–28199.

Chen, X. et al. (2018) Rap2 and TNIK control Plexin-dependent tiled synaptic innervation in C. elegans. *eLife*. 7e38801.

Chen, Y. et al. (2012) Ankyrin repeat-rich membrane spanning protein (kidins220) is required for neurotrophin and ephrin receptor-dependent dendrite development. *The Journal of Neuroscience*. 32 (24), 8263–8269.

Chklovskii, D. B. (2004) Synaptic Connectivity and Neuronal Morphology: Two Sides of the Same Coin. *Neuron*. 43 (5), 609–617.

Choi, K. et al. (2020) Bayesian model selection reveals biological origins of zero inflation in single-cell transcriptomics. *Genome Biology*. 21 (1), 1–16.

Collins, M. O. et al. (2005) Proteomic analysis of in vivo phosphorylated synaptic proteins. *Journal of Biological Chemistry*. 280 (7), 5972–5982.

Conway, J. et al. (2017) Transforming growth factor β-induced epithelial to mesenchymal transition requires the Ste20-like kinase SLK independently of its catalytic activity. *Oncotarget*. 8 (58), 98745–98756.

Cornett, E. M. et al. (2021) VALTOCO® (Diazepam Nasal Spray) for the Acute Treatment of Intermittent Stereotypic Episodes of Frequent Seizure Activity. *Neurology International*. 13 (1), 64–78.

Cortes-Canteli, M. et al. (2008) CCAAT/enhancer binding protein beta deficiency provides cerebral protection following excitotoxic injury. *Journal of cell science*. 121 (Pt 8), 1224–1234.

Cossu, M. et al. (2013) Epilepsy surgery of focal cortical dysplasia–associated tumors. *Epilepsia*. 54 (SUPPL. 9), 115–122.

Crino, P. B. (2015) Focal cortical dysplasia. *Seminars in Neurology*. 35 (3), 201–208.

Cueille, N. et al. (2007) Characterization of MAP1B heavy chain interaction with actin. *Brain research bulletin*. 71 (6), 610–618.

Cybulsky, A. v et al. (2017) Regulation of Ste20-like kinase, SLK, activity: Dimerization and activation segment phosphorylation. *PLoS One*. 12 (5), e0177226.

Cybulsky, A. v. et al. (2004) Renal expression and activity of the germinal center kinase SK2. *American journal of physiology. Renal physiology*. 286 (1), F16–F25.

Cybulsky, A. v. et al. (2009) The Ste20-like kinase SLK promotes p53 transactivation and apoptosis. *American journal of physiology. Renal physiology*. 297 (4), F971–F980.

Dan, I. et al. (2001) The Ste20 group kinases as regulators of MAP kinase cascades. *Trends in cell biology*. 11 (5), 220–230.

Datta, D. et al. (2020) Classical complement cascade initiating C1q protein within neurons in the aged rhesus macaque dorsolateral prefrontal cortex. *Journal of Neuroinflammation*. 17 (1), 1–15.

Davis, R. J. (1993) The mitogen-activated protein kinase signal transduction pathway. *Journal of Biological Chemistry*. 268 (20), 14553–14556.

Delarosa, S. et al. (2011) Activity of the Ste20-like kinase, SLK, is enhanced by homodimerization. *American journal of physiology. Renal physiology*. 301 (3), F554–F564.

Delgado, J. Y. et al. (2020) Pin1 Binding to Phosphorylated PSD-95 Regulates the Number of Functional Excitatory Synapses. *Frontiers in molecular neuroscience*. 13 (10).

Desiniotis, A. & Kyprianou, N. (2011) Significance of talin in cancer progression and metastasis. *International review of cell and molecular biology*. 289117–147.

Dohlman, H. G. & Thorner, J. W. (2001) Regulation of G protein-initiated signal transduction in yeast: paradigms and principles. *Annual review of biochemistry*. 70703–754.

Dossi, E. et al. (2014) Multi-electrode array recordings of human epileptic postoperative cortical tissue. *Journal of visualized experiments*. (92), e51870.

Dudoit, S. & Fridlyand, J. (2002) A prediction-based resampling method for estimating the number of clusters in a dataset. *Genome biology*. 3 (7), 0036.

Dukay, B. et al. (2019) Heat-shock proteins in neuroinflammation. *Frontiers in Pharmacology*. 10920.

Duncan, B. W. et al. (2021) Molecular Mechanisms of L1 and NCAM Adhesion Molecules in Synaptic Pruning, Plasticity, and Stabilization. *Frontiers in Cell and Developmental Biology*. 910.

Ekdahl, C. T. (2012) Microglial Activation – Tuning and Pruning Adult Neurogenesis. *Frontiers in Pharmacology*. 341.

Ellinger-Ziegelbauer, H. et al. (2000) Ste20-like kinase (SLK), a regulatory kinase for polo-like kinase (Plk) during the G2/M transition in somatic cells. *Genes to Cells*. 5 (6), 491–498.

Engholm-Keller, K. et al. (2019) The temporal profile of activity-dependent presynaptic phospho-signalling reveals long-lasting patterns of poststimulus regulation. *PLoS biology*. 17 (3), e3000170.

Fagiani, F. et al. (2020) Targeting dementias through cancer kinases inhibition. *Alzheimer's and Dementia: Translational Research and Clinical Interventions*. 6 (1), e12044.

Fan, R. & Lai, K. O. (2022) Understanding how kinesin motor proteins regulate postsynaptic function in neuron. *The FEBS Journal*. 289 (8), 2128–2144.

Ferreira, T. et al. (2014) Dendrite architecture organized by transcriptional control of the F-actin nucleator Spire. *Development*. 141 (3), 650–660.

Ferrer, I. et al. (2021) Dysregulated protein phosphorylation: A determining condition in the continuum of brain aging and Alzheimer's disease. *Brain Pathology*. 31 (6), e12996.

Ferrer-Ferrer, M. & Dityatev, A. (2018) Shaping synapses by the neural extracellular matrix. *Frontiers in Neuroanatomy*. 1240.

Fokin, A. I. et al. (2016) SLK/LOSK kinase regulates cell motility independently of microtubule organization and Golgi polarization. *Cytoskeleton*. 73 (2), 83–92.

Forrest, M. P. et al. (2018) Dendritic structural plasticity and neuropsychiatric disease. *Nature reviews. Neuroscience*. 19 (4), 215.

Fortuna, T. R. et al. (2021) DDX17 is involved in DNA damage repair and modifies FUS toxicity in an RGG-domain dependent manner. *Acta neuropathologica*. 142 (3), 515.

Fossati, M. et al. (2016) SRGAP2 and its human-specific paralog co-regulate the development of excitatory and inhibitory synapses. *Neuron*. 91 (2), 356.

Frias, C. P. et al. (2019) Semaphorin4D Induces Inhibitory Synapse Formation by Rapid Stabilization of Presynaptic Boutons via MET Coactivation. *The Journal of Neuroscience*. 39 (22), 4221–4237.

Fu, C. A. et al. (1999) TNIK, a Novel Member of the Germinal Center Kinase Family That Activates the c-Jun N-terminal Kinase Pathway and Regulates the Cytoskeleton. *Journal of Biological Chemistry*. 274 (43), 30729–30737.

Garrett, A. M. et al. (2012) γ-Protocadherins Control Cortical Dendrite Arborization by Regulating the Activity of a FAK/PKC/MARCKS Signaling Pathway. *Neuron*. 74 (2), 269.

Gleichman, A. J. et al. (2012) Anti-NMDA Receptor Encephalitis Antibody Binding Is Dependent on Amino Acid Identity of a Small Region within the GluN1 Amino Terminal Domain. *The Journal of Neuroscience*. 32 (32), 11082.

Goikolea-Vives, A. & Stolp, H. B. (2021) Connecting the Neurobiology of Developmental Brain Injury: Neuronal Arborisation as a Regulator of Dysfunction and Potential Therapeutic Target. *International Journal of Molecular Sciences*. 22 (15), 8220.

de Groot, C. et al. (2017) RhoGEF9 splice isoforms influence neuronal maturation and synapse formation downstream of α2 GABAA receptors. *PLOS Genetics*. 13 (10), e1007073.

Guilluy, C. et al. (2008) Ste20-related kinase SLK phosphorylates Ser188 of RhoA to induce vasodilation in response to angiotensin II Type 2 receptor activation. *Circulation research*. 102 (10), 1265–1274.

Han, W. et al. (2019) Shisa7 is a GABA A receptor auxiliary subunit controlling benzodiazepine actions. *Science*. 366 (6462), 246–250.

Hao, W. et al. (2006) Induction of apoptosis by the Ste20-like kinase SLK, a germinal center kinase that activates apoptosis signal-regulating kinase and p38. *Journal of Biological Chemistry*. 281 (6), 3075–3084.

van Haren, J. et al. (2014) Dynamic microtubules catalyze formation of navigator-TRIO complexes to regulate neurite extension. *Current biology*. 24 (15), 1778–1785.

Hast, B. E. et al. (2014) Cancer-derived mutations in KEAP1 impair NRF2 degradation but not ubiquitination. *Cancer research*. 74 (3), 808–817.

Havugimana, P. C. et al. (2012) A census of human soluble protein complexes. *Cell*. 150 (5), 1068–1081.

Heffron, T. P. (2018) Challenges of developing small-molecule kinase inhibitors for brain tumors and the need for emphasis on free drug levels. *Neuro-Oncology*. 20 (3), 307–312.

Heffron, T. P. (2016) Small Molecule Kinase Inhibitors for the Treatment of Brain Cancer. *Journal of Medicinal Chemistry*. 59 (22), 10030–10066.

Herculano-Houzel, S. (2012) The remarkable, yet not extraordinary, human brain as a scaled-up primate brain and its associated cost. *Proceedings of the National Academy of Sciences of the United States of America*. 109 (SUPPL.1), 10661–10668.

Hernández, S. E. et al. (2004) Adhesion-dependent regulation of p190RhoGAP in the developing brain by the Abl-related gene tyrosine kinase. *Current biology*. 14 (8), 691–696.

Higuero, A. M. et al. (2010) Kidins220/ARMS modulates the activity of microtubule-regulating proteins and controls neuronal polarity and development. *The Journal of biological chemistry*. 285 (2), 1343–1357.

Hill, S. L. et al. (2012) Statistical connectivity provides a sufficient foundation for specific functional connectivity in neocortical neural microcircuits. *Proceedings of the National Academy of Sciences of the United States of America*. 109 (42), E2885–E2894.

Hoersting, A. K. & Schmucker, D. (2021) Axonal branch patterning and neuronal shape diversity: roles in developmental circuit assembly: Axonal branch patterning and neuronal shape diversity in developmental circuit assembly. *Current Opinion in Neurobiology*. 66158–165.

Hu, C. et al. (2020) Conserved Tao Kinase Activity Regulates Dendritic Arborization, Cytoskeletal Dynamics, and Sensory Function in Drosophila. *The Journal of Neuroscience*. 40 (9), 1819–1833.

Humphrey, S. J. et al. (2015) Protein Phosphorylation: A Major Switch Mechanism for Metabolic Regulation. *Trends in Endocrinology & Metabolism*. 26 (12), 676–687.

Hussain, N. K. et al. (2010) MINK and TNIK Differentially Act on Rap2-Mediated Signal Transduction to Regulate Neuronal Structure and AMPA Receptor Function. *The Journal of Neuroscience*. 30 (44), 14786–14794.

Huttlin, E. L. et al. (2017) Architecture of the human interactome defines protein communities and disease networks. *Nature*. 545 (7655), 505–509.

Itoh, S. et al. (1997) Molecular cloning and characterization of a novel putative STE20-like kinase in guinea pigs. *Archives of biochemistry and biophysics*. 340 (2), 201–207.

Jaberi, A. et al. (2015) Identification of Tpr and α-actinin-4 as two novel SLK-interacting proteins. *Biochimica et biophysica acta*. 1853 (10 Pt A), 2539–2552.

Jaworski, J. et al. (2009) Dynamic Microtubules Regulate Dendritic Spine Morphology and Synaptic Plasticity. *Neuron*. 61 (1), 85–100.

Jenö, P. et al. (1995) Internal sequences from proteins digested in polyacrylamide gels. *Analytical biochemistry*. 224 (1), 75–82.

Jeste, S. S. & Tuchman, R. (2015) Autism Spectrum Disorder and Epilepsy: Two Sides of the Same Coin? *Journal of child neurology*. 30 (14), 1963.

Jiang, R. et al. (2022) Statistics or biology: the zero-inflation controversy about scRNA-seq data. *Genome Biology*. 23 (1), 1–24.

Jiang, Y. H. et al. (2013) Detection of clinically relevant genetic variants in autism spectrum disorder by whole-genome sequencing. *American journal of human genetics*. 93 (2), 249–263.

Jin, J. K. et al. (2015) Talin1 phosphorylation activates β1 integrins: a novel mechanism to promote prostate cancer bone metastasis. *Oncogene*. 34 (14), 1811–1821.

Johnson, G. V. W. & Stoothoff, W. H. (2004) Tau phosphorylation in neuronal cell function and dysfunction. *Journal of Cell Science*. 117 (Pt 24), 5721–5729.

Johnson, T. M. et al. (2008) Plk1 activation by Ste20-like kinase (Slk) phosphorylation and polo-box phosphopeptide binding assayed with the substrate translationally controlled tumor protein (TCTP). *Biochemistry*. 47 (12), 3688–3696.

Johnson, W. E. et al. (2007) Adjusting batch effects in microarray expression data using empirical Bayes methods. *Biostatistics*. 8 (1), 118–127.

Juric-Sekhar, G. & Hevner, R. F. (2019) Malformations of Cerebral Cortex Development: Molecules and Mechanisms. *Annual review of pathology*. 14293–318.

Käll, L. et al. (2008) Assigning significance to peptides identified by tandem mass spectrometry using decoy databases. *Journal of proteome research*. 7 (1), 29–34.

Kang, K. W. et al. (2019) Genetic characteristics of non-familial epilepsy. *PeerJ*. 7e8278.

Kawabata Galbraith, K. et al. (2018) MTSS1 Regulation of Actin-Nucleating Formin DAAM1 in Dendritic Filopodia Determines Final Dendritic Configuration of Purkinje Cells. *Cell Reports*. 24 (1), 95-106.e9.

Keeler, A. B. et al. (2015) Protein Kinase C Phosphorylation of a γ-Protocadherin C-terminal Lipid Binding Domain Regulates Focal Adhesion Kinase Inhibition and Dendrite Arborization. *Journal of Biological Chemistry*. 290 (34), 20674–20686.

Kendrick, A. A. et al. (2019) Hook3 is a scaffold for the opposite-polarity microtubule-based motors cytoplasmic dynein-1 and KIF1C. *Journal of Cell Biology*. 218 (9), 2982–3001.

Khosravani, H. et al. (2003) The Control of Seizure-Like Activity in the Rat Hippocampal Slice. *Biophysical Journal*. 84 (1), 687.

Kim, D. I. et al. (2014) Probing nuclear pore complex architecture with proximity-dependent biotinylation. *Proceedings of the National Academy of Sciences of the United States of America*. 111 (24), E2453-61.

Kise, Y. & Schmucker, D. (2013) Role of self-avoidance in neuronal wiring. *Current Opinion in Neurobiology*. 23 (6), 983–989.

Koh, H. Y. et al. (2021) Non–Cell Autonomous Epileptogenesis in Focal Cortical Dysplasia. *Annals of Neurology*. 90 (2), 285–299.

Konietzny, A. et al. (2017) Dendritic actin cytoskeleton: Structure, functions, and regulations. *Frontiers in Cellular Neuroscience*. 11147.

Koyama, R. & Ikegaya, Y. (2015) Microglia in the pathogenesis of autism spectrum disorders. *Neuroscience Research*. 1001–5.

Krause, M. et al. (2003) Ena/VASP Proteins: Regulators of the Actin Cytoskeleton and Cell Migration. *Annual Review of Cell and Developmental Biology*. 19541–564.

Kurochkina, N. & Guha, U. (2013) SH3 domains: Modules of protein-protein interactions. *Biophysical Reviews*. 5 (1), 29–39.

Larhammar, M. et al. (2017) The Ste20 Family Kinases MAP4K4, MINK1, and TNIK Converge to Regulate Stress-Induced JNK Signaling in Neurons. *The Journal of Neuroscience*. 37 (46), 11074–11084.

Larimore, J. et al. (2011) The schizophrenia susceptibility factor dysbindin and its associated complex sort cargoes from cell bodies to the synapse. *Molecular biology of the cell*. 22 (24), 4854–4867.

de Las Rivas, J. & Fontanillo, C. (2010) Protein-protein interactions essentials: Key concepts to building and analyzing interactome networks. *PLoS Computational Biology*. 6 (6), e1000807.

Lasser, M. et al. (2018) The role of the microtubule cytoskeleton in neurodevelopmental disorders. *Frontiers in Cellular Neuroscience*. 12165.

Lebrand, C. et al. (2004) Critical Role of Ena/VASP Proteins for Filopodia Formation in Neurons and in Function Downstream of Netrin-1. *Neuron*. 42 (1), 37–49.

Lechuga, L. & Franz, D. N. (2019) Everolimus as adjunctive therapy for tuberous sclerosis complex-associated partial-onset seizures. *Expert Review of Neurotherapeutics*. 19 (10), 913–925.

Leclaire, L. L. et al. (2008) Phosphorylation of the Arp2/3 complex is necessary to nucleate actin filaments. *Journal of Cell Biology*. 182 (4), 647–654.

Lee, H. K. (2006) Synaptic plasticity and phosphorylation. *Pharmacology and Therapeutics*. 112 (3), 810–832.

Lee, J. et al. (2015) Shank3-mutant mice lacking exon 9 show altered excitation/inhibition balance, enhanced rearing, and spatial memory deficit. *Frontiers in cellular neuroscience*. 994.

Lee, S. et al. (2017) Distinct structural mechanisms determine substrate affinity and kinase activity of protein kinase Cα. *The Journal of Biological Chemistry*. 292 (39), 16300.

Leek, J. T. & Storey, J. D. (2007) Capturing heterogeneity in gene expression studies by surrogate variable analysis. *PLoS genetics*. 3 (9), 1724–1735.

Leterrier, C. (2021) A pictorial history of the neuronal cytoskeleton. *The Journal of Neuroscience*. 41 (1), 11–27.

Lewis, S. (2021) Microglia prune inhibitory synapses, too. *Nature Reviews Neuroscience*. 22 (9), 517–517.

Li, J. et al. (2016) Long-term potentiation modulates synaptic phosphorylation networks and reshapes the structure of the postsynaptic interactome. *Science signaling*. 9 (440), rs8.

Li, J. et al. (2017) Spatiotemporal profile of postsynaptic interactomes integrates components of complex brain disorders. *Nature neuroscience*. 20 (8), 1150–1161.

Li, S. et al. (2013) The Neural Cell Adhesion Molecule (NCAM) Associates with and Signals through p21-Activated Kinase 1 (Pak1). *The Journal of Neuroscience*. 33 (2), 790.

Li, W. et al. (2005) Abelson, enabled, and p120catenin exert distinct effects on dendritic morphogenesis in Drosophila. *Developmental Dynamics*. 234 (3), 512–522.

Lin, Y. C. & Koleske, A. J. (2010) Mechanisms of synapse and dendrite maintenance and their disruption in psychiatric and neurodegenerative disorders. *Annual Review of Neuroscience*. 33349–378.

Liu, J. et al. (2014) Evidence for mTOR pathway activation in a spectrum of epilepsy-associated pathologies. *Acta Neuropathologica Communications*. 271.

van Loo, K. M. J. et al. (2012) Transcriptional regulation of T-type calcium channel CaV3.2: Bi-directionality by early growth response 1 (Egr1) and repressor element 1 (RE-1) protein - silencing transcription factor (REST). *Journal of Biological Chemistry*. 287 (19), 15489–15501.

López Tobón, A. et al. (2018) The guanine nucleotide exchange factor Arhgef7/βPix promotes axon formation upstream of TC10. *Scientific Reports*. 8 (1), 1–12.

López-Colomé, A. M. et al. (2017) Paxillin: a crossroad in pathological cell migration. *Journal of Hematology & Oncology*. 10 (1), 1–15.

Loureiro, J. J. et al. (2002) Critical Roles of Phosphorylation and Actin Binding Motifs, but Not the Central Proline-rich Region, for Ena/Vasodilator-stimulated Phosphoprotein (VASP) Function during Cell Migration. *Molecular Biology of the Cell*. 13 (7), 2533.

Lovestone, S. et al. (2015) A phase II trial of tideglusib in alzheimer's disease. *Journal of Alzheimer's Disease*. 45 (1), 75–88.

Lu, H. et al. (2020) Recent advances in the development of protein–protein interactions modulators: mechanisms and clinical trials. *Signal Transduction and Targeted Therapy*. 5 (1), 213.

Luhovy, A. Y. et al. (2012) Regulation of the Ste20-like kinase, SLK: involvement of activation segment phosphorylation. *The Journal of biological chemistry*. 287 (8), 5446–5458.

Lynch, B. A. et al. (2004) The synaptic vesicle protein SV2A is the binding site for the antiepileptic drug levetiracetam. *Proceedings of the National Academy of Sciences of the United States of America*. 101 (26), 9861–9866.

Maas, C. et al. (2009) Synaptic activation modifies microtubules underlying transport of postsynaptic cargo. *Proceedings of the National Academy of Sciences of the United States of America*. 106 (21), 8731.

Machicoane, M. et al. (2014) SLK-dependent activation of ERMs controls LGN-NuMA localization and spindle orientation. *Journal of Cell Biology*. 205 (6), 791–799.

Malacrida, A. et al. (2019) Chemotherapy-induced peripheral neuropathy and changes in cytoskeleton. *International Journal of Molecular Sciences*. 20 (9), 2287.

Malinová, A. et al. (2017) Assembly of the U5 snRNP component PRPF8 is controlled by the HSP90/R2TP chaperones. *The Journal of cell biology*. 216 (6), 1579–1596.

Marchionni, I. et al. (2009) New insights on the role of gephyrin in regulating both phasic and tonic GABAergic inhibition in rat hippocampal neurons in culture. *Neuroscience*. 164 (2), 552–562.

Mathern, G. W. et al. (2000) *Neurons Recorded from Pediatric Epilepsy Surgery Patients with Cortical Dysplasia*. 41 (Suppl 6), 162–167.

McDermott, J. E. et al. (2018) Class 4 Semaphorins and Plexin-B receptors regulate GABAergic and glutamatergic synapse development in the mammalian hippocampus. *Molecular and cellular neurosciences*. 9250–66.

McDonnell, A. v. et al. (2006) Paircoil2: improved prediction of coiled coils from sequence. *Bioinformatics*. 22 (3), 356–358.

Meier, J. et al. (2003) GABA(A) receptor activity and PKC control inhibitory synaptogenesis in CNS tissue slices. *Molecular and cellular neurosciences*. 23 (4), 600–613.

Mitchison, T. & Kirschner, M. (1984) Dynamic instability of microtubule growth. *Nature*. 312 (5991), 237–242.

Mitsogiannis, M. D. et al. (2021) Subtle Roles of Down Syndrome Cell Adhesion Molecules in Embryonic Forebrain Development and Neuronal Migration. *Frontiers in cell and developmental biology*. 8624181.

Müller, J. A. et al. (2022) A presynaptic phosphosignaling hub for lasting homeostatic plasticity. *Cell reports*. 39 (3), 110696.

Müller, T. et al. (2010) ASAP1 promotes tumor cell motility and invasiveness, stimulates metastasis formation in vivo, and correlates with poor survival in colorectal cancer patients. *Oncogene*. 29 (16), 2393–2403.

Myers, J. P. & Gomez, T. M. (2011) Focal Adhesion Kinase Promotes Integrin Adhesion Dynamics Necessary for Chemotropic Turning of Nerve Growth Cones. *The Journal of Neuroscience*. 31 (38), 13585–13595.

Nadezhdina, E. et al. (2001) [Spermatozoa of the loach Misgurnus fossilis as a test system for identification of new centromere proteins]. *Ontogenez*. 32 (1), 41–50.

Nakamura, F. et al. (2020) Collapsin Response Mediator Proteins: Their Biological Functions and Pathophysiology in Neuronal Development and Regeneration. *Frontiers in Cellular Neuroscience*. 14188.

Nakamura, Y. et al. (2016) Proteomic characterization of inhibitory synapses using a novel phluorin-tagged γ-aminobutyric acid receptor, type a (GABAA), α2 subunit knock-in mouse. *Journal of Biological Chemistry*. 291 (23), 12394–12407.

Ndoja, A. et al. (2020) Ubiquitin Ligase COP1 Suppresses Neuroinflammation by Degrading c/EBPβ in Microglia. *Cell*. 182 (5), 1156-1169.e12.

Ohno, Y. & Tokudome, K. (2017) Therapeutic Role of Synaptic Vesicle Glycoprotein 2A (SV2A) in Modulating Epileptogenesis. *CNS & neurological disorders drug targets*. 16 (4), 463–471.

Okazawa, H. (2018) PQBP1, an intrinsically disordered/denatured protein at the crossroad of intellectual disability and neurodegenerative diseases. *Neurochemistry International*. 11917–25.

Olsen, R. W. & Sieghart, W. (2009) GABAA Receptors: Subtypes Provide Diversity of Function and Pharmacology. *Neuropharmacology*. 56 (1), 141.

Onore, C. et al. (2017) Dynamic Akt/mTOR signaling in children with autism spectrum disorder. *Frontiers in Pediatrics*. 543.

van Ooyen, A. et al. (2014) Independently outgrowing neurons and geometry-based synapse formation produce networks with realistic synaptic connectivity. *PloS one*. 9 (1), e85858.

O'Reilly, P. G. et al. (2005) The Ste20-like kinase SLK is required for cell cycle progression through G2. *The Journal of biological chemistry*. 280 (51), 42383–42390.

Orlova, K. A. et al. (2010) Early progenitor cell marker expression distinguishes type II from type i focal cortical dysplasias. *Journal of Neuropathology and Experimental Neurology*. 69 (8), 850–863.

Pallud, J. et al. (2014) Cortical GABAergic excitation contributes to epileptic activities around human glioma. *Science translational medicine*. 6 (244), 244ra89.

Panzanelli, P. et al. (2011) Distinct mechanisms regulate GABAA receptor and gephyrin clustering at perisomatic and axo-axonic synapses on CA1 pyramidal cells. *The Journal of Physiology*. 589 (Pt 20), 4959.

Paolicelli, R. C. et al. (2011) Synaptic pruning by microglia is necessary for normal brain development. *Science*. 333 (6048), 1456–1458.

Perucca, P. & Scheffer, I. E. (2021) Genetic Contributions to Acquired Epilepsies. *Epilepsy Currents*. 21 (1), 5.

Pitsch, J. et al. (2017) Circadian clustering of spontaneous epileptic seizures emerges after pilocarpine-induced status epilepticus. *Epilepsia*. 58 (7), 1159–1171.

Pitsch, J. et al. (2007) Functional role of mGluR1 and mGluR4 in pilocarpine-induced temporal lobe epilepsy. *Neurobiology of Disease*. 26 (3), 623–633.

Pitsch, J. et al. (2012) The Presynaptic Active Zone Protein RIM1α Controls Epileptogenesis following Status Epilepticus. *The Journal of Neuroscience*. 32 (36), 12384.

Pollscheit, J. et al. (2012) Phosphorylation of serine 774 of the neural cell adhesion molecule is necessary for cyclic adenosine monophosphate response element binding protein activation and neurite outgrowth. *Journal of neuroscience research*. 90 (8), 1577–1582.

Poopal, A. C. et al. (2016) Increased expression of the PI3K catalytic subunit p110δ underlies elevated S6 phosphorylation and protein synthesis in an individual with autism from a multiplex family. *Molecular Autism*. 7 (1), 1–12.

Potekhina, E. S. et al. (2003) Enzymatic activity of protein kinase LOSK: possible regulatory role of the structural domain. *Biochemistry. Biokhimiia*. 68 (2), 188–195.

Pourhaghighi, R. et al. (2020) BraInMap Elucidates the Macromolecular Connectivity Landscape of Mammalian Brain. *Cell systems*. 10 (4), 333-350.e14.

Pryce, B. R. et al. (2017) Deletion of the Ste20-like kinase SLK in skeletal muscle results in a progressive myopathy and muscle weakness. *Skeletal Muscle*. 7 (1), 3.

Pytowski, B. et al. (1998) Identification and Initial Characterization of mSLK , a Murine Member. *Archives of Biochemistry and Biophysics*. 359 (2), 310–319.

Quizi, J. et al. (2013) SLK-mediated phosphorylation of paxillin is required for focal adhesion turnover and cell migration. *Oncogene*. 32 (39), 4656–4663.

Raju, T. N. (2000) The Nobel chronicles. 1992: Edmond H Fischer (b 1920) and Edwin G Krebs (b 1918). *The Lancet*. 355 (9219), 2004.

Ramkumar, A. et al. (2018) ReMAPping the microtubule landscape: How phosphorylation dictates the activities of microtubule-associated proteins. *Developmental Dynamics*. 247 (1), 138–155.

Rappsilber, J. et al. (2003) Stop And Go Extraction tips for matrix-assisted laser desorption/ionization, nanoelectrospray, and LC/MS sample pretreatment in proteomics. *Analytical Chemistry*. 75 (3), 663–670.

Read Montague, P. & Friedlander, M. J. (1991) Morphogenesis and Territorial Coverage by Isolated Mammalian Retinal Ganglion Cells. *The Journal of Neuroscience*. 1 (5), 1440–1457.

Ribeiro, A. et al. (2013) β1-integrin Cytoskeletal Signaling Regulates Sensory Neuron Response to Matrix Dimensionality. *Neuroscience*. 24867–78.

Riccomagno, M. M. & Kolodkin, A. L. (2015) Sculpting Neural Circuits by Axon and Dendrite Pruning. *Annual review of cell and developmental biology*. 31779–805.

Richter, M. et al. (2018) Altered TAOK2 activity causes autism-related neurodevelopmental and cognitive abnormalities through RhoA signaling. *Molecular Psychiatry*. 24 (9), 1329–1350.

Ridley, A. J. (2006) Rho GTPases and actin dynamics in membrane protrusions and vesicle trafficking. *Trends in Cell Biology*. 16 (10), 522–529.

Ripley, B. D. (2014) *Pattern recognition and neural networks*. Cambridge University Press.

Ritchie, M. E. et al. (2015) limma powers differential expression analyses for RNA-sequencing and microarray studies. *Nucleic acids research*. 43 (7), e47.

Robens, B. K. (2016) *Mechanisms of epileptogenesis in animal models of developmental brain lesions*. Doctoral dissertation thesis. Rheinische Friedrich-Wilhelms-Universität Bonn.

Ronning, K. E. et al. (2019) Molecular profiling of resident and infiltrating mononuclear phagocytes during rapid adult retinal degeneration using single-cell RNA sequencing. *Scientific Reports*. 9 (1), 1–12.

Roovers, K. et al. (2009) The Ste20-like kinase SLK is required for ErbB2-driven breast cancer cell motility. *Oncogene*. 28 (31), 2839–2848.

Rosenfeld, J. et al. (1992) In-gel digestion of proteins for internal sequence analysis after one- or two-dimensional gel electrophoresis. *Analytical biochemistry*. 203 (1), 173–179.

Rosina, E. et al. (2019) Disruption of mTOR and MAPK pathways correlates with severity in idiopathic autism. *Translational Psychiatry*. 9 (1), 1–10.

Rossini, L. et al. (2021) Dendritic pathology, spine loss and synaptic reorganization in human cortex from epilepsy patients. *Brain*. 144 (1), 251–265.

Roux, K. J. et al. (2018) BioID: A Screen for Protein-Protein Interactions. *Current protocols in protein science*. 91 (19.23), 1–15.

Royero, P. (2022) *Participation of Ste20-like kinase-deficient neurons in the abnormal circuitry of focal epileptogenic lesions*. Doctoral dissertation thesis. Bonn: Rheinische Friedrich-Wilhelms-Universität Bonn.

von Rüden, E. L. et al. (2018) Genetic Modulation of HSPA1A Accelerates Kindling Progression and Exerts Pro-convulsant Effects. *Neuroscience*. 386108–120.

Sabourin, L. A. et al. (2000) Caspase 3 cleavage of the Ste20-related kinase SLK releases and activates an apoptosis-inducing kinase domain and an actin-disassembling region. *Molecular and cellular biology*. 20 (2), 684–696.

Sabourin, L. A. & Rudnicki, M. A. (1999) Induction of apoptosis by SLK, a Ste20-related kinase. *Oncogene*. 18 (52), 7566–7575.

Sánchez-Huertas, C. & Herrera, E. (2021) With the Permission of Microtubules: An Updated Overview on Microtubule Function During Axon Pathfinding. *Frontiers in Molecular Neuroscience*. 14759404.

Sathe, G. et al. (2020) Multiplexed Phosphoproteomic Study of Brain in Patients with Alzheimer's Disease and Age-Matched Cognitively Healthy Controls. *OMICS A Journal of Integrative Biology*. 24 (4), 216–227.

Schmitz, L. J. M. et al. (2017) The AMPA receptor-associated protein Shisa7 regulates hippocampal synaptic function and contextual memory. *eLife*. 6e24192.

Schoch, S. et al. (2021) Ste20-like Kinase Is Critical for Inhibitory Synapse Maintenance and Its Deficiency Confers a Developmental Dendritopathy. *The Journal of Neuroscience*. 41 (39), 8111–8125.

Schonkeren, S. L. et al. (2019) Nervous NDRGs: the N-myc downstream–regulated gene family in the central and peripheral nervous system. *Neurogenetics*. 20 (4), 173.

Schroeder, C. M. & Vale, R. D. (2016) Assembly and activation of dynein-dynactin by the cargo adaptor protein Hook3. *The Journal of cell biology*. 214 (3), 309–318.

Schuemann, A. et al. (2013) Structural plasticity of GABAergic axons is regulated by network activity and GABAA receptor activation. *Frontiers in Neural Circuits*. 7113.

Sepp, M. et al. (2017) The Intellectual Disability and Schizophrenia Associated Transcription Factor TCF4 Is Regulated by Neuronal Activity and Protein Kinase A. *The Journal of Neuroscience*. 37 (43), 10516–10527.

Serafim, R. A. M. et al. (2021) Discovery of a Potent Dual SLK/STK10 Inhibitor Based on a Maleimide Scaffold. *Journal of medicinal chemistry*. 64 (18), 13259–13278.

Serenó, L. et al. (2009) A novel GSK-3β inhibitor reduces Alzheimer's pathology and rescues neuronal loss in vivo. *Neurobiology of Disease*. 35 (3), 359–367.

Shao, Y. et al. (2022) Pathological Networks Involving Dysmorphic Neurons in Type II Focal Cortical Dysplasia. *Neuroscience Bulletin*. 1–18.

Sharma, R. et al. (2016) Activity-Based Protein Pro fi ling Shows Heterogeneous Signaling Adaptations to BRAF Inhibition. *Journal of Proteome Research*. 15 (12), 4476–4489.

Sharma, S. et al. (2018) Role of the Fyn-PKCδ signaling in SE-induced neuroinflammation and epileptogenesis in experimental models of temporal lobe epilepsy. *Neurobiology of Disease*. 110102–121.

Shen, C. H. et al. (2008) Breast tumor kinase phosphorylates p190RhoGAP to regulate rho and ras and promote breast carcinoma growth, migration, and invasion. *Cancer research*. 68 (19), 7779–7787.

Sheng, M. & Kim, E. (2011) The postsynaptic organization of synapses. *Cold Spring Harbor perspectives in biology*. 3 (12), a005678.

Sihag, R. K. et al. (2007) Role of phosphorylation on the structural dynamics and function of types III and IV intermediate filaments. *Experimental Cell Research*. 313 (10), 2089–2109.

Smith, J. H. et al. (2021) How neurons exploit fractal geometry to optimize their network connectivity. *Scientific Reports*. 11 (1), 2332.

Smith, K. R. et al. (2014) GIT1 and βPIX Are Essential for GABAA Receptor Synaptic Stability and Inhibitory Neurotransmission. *Cell Reports*. 9 (1), 298.

Sowers, L. P. et al. (2013) Disruption of the non-canonical Wnt gene PRICKLE2 leads to autism-like behaviors with evidence for hippocampal synaptic dysfunction. *Molecular psychiatry*. 18 (10), 1077.

Steinlein, O. K. (2008) Genetics and epilepsy. *Dialogues in Clinical Neuroscience*. 10 (1), 29.

Storbeck, C. J. et al. (2013) Distinct roles for Ste20-like kinase SLK in muscle function and regeneration. *Skeletal muscle*. 3 (1), 16.

Storbeck, C. J. et al. (2004) Ste20-like kinase SLK displays myofiber type specificity and is involved in C2C12 myoblast differentiation. *Muscle & nerve*. 29 (4), 553–564.

Storbeck, C. J. et al. (2009) The Ldb1 and Ldb2 transcriptional cofactors interact with the Ste20-like kinase SLK and regulate cell migration. *Molecular biology of the cell*. 20 (19), 4174–4182.

Strange, K. et al. (2006) Ste20-type kinases: evolutionarily conserved regulators of ion transport and cell volume. *Physiology*. 21 (1), 61–68.

Stürner, T. et al. (2022) The branching code: A model of actin-driven dendrite arborization. *Cell Reports*. 39 (4), 110746.

Sun, T. et al. (2012) Grb2 mediates semaphorin-4D-dependent RhoA inactivation. *Journal of cell science*. 125 (Pt 15), 3557–3567.

Swiercz, J. M. et al. (2008) ErbB-2 and met reciprocally regulate cellular signaling via plexin-B1. *Journal of Biological Chemistry*. 283 (4), 1893–1901.

Szczurkowska, J. et al. (2016) Targeted in vivo genetic manipulation of the mouse or rat brain by in utero electroporation with a triple-electrode probe. *Nature protocols*. 11 (3), 399–412.

Szklarczyk, D. et al. (2021) The STRING database in 2021: customizable protein-protein networks, and functional characterization of user-uploaded gene/measurement sets. *Nucleic acids research*. 49 (D1), D605–D612.

Tailby, C. et al. (2005) Activity-dependent maintenance and growth of dendrites in adult cortex. *Proceedings of the National Academy of Sciences of the United States of America*. 102 (12), 4631–4636.

Tamura, N. et al. (2021) Intellectual-disability-associated mutations in the ceramide transport protein gene CERT1 lead to aberrant function and subcellular distribution. *Journal of Biological Chemistry*. 297 (5), 101338.

Tanaka, H. et al. (2018) The intellectual disability gene PQBP1 rescues Alzheimer's disease pathology. *Molecular Psychiatry*. 23 (10), 2090–2110.

Taniguchi, Y. et al. (2012) In utero electroporation as a tool for genetic manipulation in vivo to study psychiatric disorders: from genes to circuits and behaviors. *The Neuroscientist*. 18 (2), 169–179.

Tedeschi, A. et al. (2019) ADF/Cofilin-Mediated Actin Turnover Promotes Axon Regeneration in the Adult CNS. *Neuron*. 103 (6), 1073-1085.e6.

Teng, J. et al. (2001) Synergistic effects of MAP2 and MAP1B knockout in neuronal migration, dendritic outgrowth, and microtubule organization. *Journal of Cell Biology*. 155 (1), 65–76.

Tenreiro, S. et al. (2014) Protein phosphorylation in neurodegeneration: Friend or foe? *Frontiers in Molecular Neuroscience*. 742.

Terunuma, M. et al. (2008) Deficits in phosphorylation of GABAA receptors by intimately associated protein kinase C activity underlie compromised synaptic inhibition during status epilepticus. *The Journal of Neuroscience*. 28 (2), 376–384.

Todd, P. K. & Mack, K. J. (2001) Phosphorylation, CREB, and mental retardation. *Pediatric Research*. 50 (6), 672.

Tretter, V. et al. (2012) Gephyrin, the enigmatic organizer at GABAergic synapses. *Frontiers in Cellular Neuroscience*. 623.

Tyagarajan, S. K. et al. (2013) Extracellular signal-regulated kinase and glycogen synthase kinase 3β regulate gephyrin postsynaptic aggregation and GABAergic synaptic function in a calpain-dependent mechanism. *Journal of Biological Chemistry*. 288 (14), 9634–9647.

Tyagarajan, S. K. et al. (2011) Regulation of GABAergic synapse formation and plasticity by GSK3β-dependent phosphorylation of gephyrin. *Proceedings of the National Academy of Sciences of the United States of America*. 108 (1), 379–384.

Tyanova, S. et al. (2016) The MaxQuant computational platform for mass spectrometry-based shotgun proteomics. *Nature protocols*. 11 (12), 2301–2319.

Uezu, A. et al. (2016) Identification of an elaborate complex mediating postsynaptic inhibition. *Science*. 353 (6304), 1123–1129.

Urbanska, A. S. et al. (2017) ZBP1 phosphorylation at serine 181 regulates its dendritic transport and the development of dendritic trees of hippocampal neurons. *Scientific Reports*. 7 (1), 1–11.

Urbanska, M. et al. (2019) GSK3β activity alleviates epileptogenesis and limits GluA1 phosphorylation. *EBioMedicine*. 39377–387.

Varnaitė, R. & MacNeill, S. A. (2016) Meet the neighbors: Mapping local protein interactomes by proximity-dependent labeling with BioID. *Proteomics*. 16 (19), 2503–2518.

Viswanatha, R. et al. (2012) Local phosphocycling mediated by LOK/SLK restricts ezrin function to the apical aspect of epithelial cells. *Journal of Cell Biology*. 199 (6), 969–984.

Wagner, S. et al. (2002) Association of the Ste20-like Kinase (SLK) with the Microtubule. *Journal of Biological Chemistry*. 277 (40), 37685–37692.

Wagner, S. et al. (2008) FAK/src-family dependent activation of the Ste20-like kinase SLK is required for microtubule-dependent focal adhesion turnover and cell migration. *PLoS ONE*. 3 (4), e1868.

Wagner, S. M. & Sabourin, L. A. (2009) A novel role for the Ste20 kinase SLK in adhesion signaling and cell migration. *Cell Adhesion and Migration*. 3 (2), 182–184.

Wan, C. et al. (2015) Panorama of ancient metazoan macromolecular complexes. *Nature*. 525 (7569), 339–344.

Wang, K. et al. (2018) Ste20-like kinase is upregulated in glioma and induces glioma invasion. *Neoplasma*. 65 (2), 185–191.

Wang, Q. et al. (2016) Identification of Phosphorylation Consensus Sequences and Endogenous Neuronal Substrates of the Psychiatric Risk Kinase TNIK. *The Journal of pharmacology and experimental therapeutics*. 356 (2), 410–423.

Wang, Q. et al. (2011) The psychiatric disease risk factors DISC1 and TNIK interact to regulate synapse composition and function. *Molecular psychiatry*. 16 (10), 1006–1023.

Wang, Y. et al. (2020) Ste20-like Kinase-mediated Control of Actin Polymerization Is a New Mechanism for Thin Filament-associated Regulation of Airway Smooth Muscle Contraction. *American journal of respiratory cell and molecular biology*. 62 (5), 645–656.

Wessel, D. & Flügge, U. I. (1984) A method for the quantitative recovery of protein in dilute solution in the presence of detergents and lipids. *Analytical biochemistry*. 138 (1), 141–143.

Willige, D. van de et al. (2019) Cytolinker Gas2L1 regulates axon morphology through microtubule-modulated actin stabilization. *EMBO reports*. 20 (11), e47732.

Wilson, C. et al. (2020) Protocol for Evaluating Neuronal Polarity in Murine Models. *STAR Protocols*. 1 (3), 100114.

Winkelman, J. D. et al. (2014) Ena/VASP Enabled is a highly processive actin polymerase tailored to self-assemble parallel-bundled F-actin networks with Fascin. *Proceedings of the National Academy of Sciences of the United States of America*. 111 (11), 4121–4126.

Winkler, S. C. et al. (2020) PKCγ-Mediated Phosphorylation of CRMP2 Regulates Dendritic Outgrowth in Cerebellar Purkinje Cells. *Molecular Neurobiology*. 57 (12), 5150–5166.

Winter, D. et al. (2009) Citrate boosts the performance of phosphopeptide analysis by UPLC-ESI-MS/MS. *Journal of proteome research*. 8 (1), 418–424.

Witke, W. (2004) The role of profilin complexes in cell motility and other cellular processes. *Trends in Cell Biology*. 14 (8), 461–469.

Wong, M. (2008) Stabilizing dendritic structure as a novel therapeutic approach for epilepsy. *Expert review of neurotherapeutics*. 8 (6), 907–915.

Wong, M. & Crino, P. B. (2012) mTOR and Epileptogenesis in Developmental Brain Malformations. *Jasper's Basic Mechanisms of the Epilepsies*.

Woolfenden, S. et al. (2012) A systematic review of two outcomes in autism spectrum disorder - epilepsy and mortality. *Developmental medicine and child neurology*. 54 (4), 306–312.

Woychyshyn, B. et al. (2020) Genetic ablation of SLK exacerbates glomerular injury in adriamycin nephrosis in mice. *American journal of physiology. Renal physiology*. 318 (6), F1377–F1390.

Wu, K. et al. (2022) Shisa7 phosphorylation regulates GABAergic transmission and neurodevelopmental behaviors. *Neuropsychopharmacology*.

Wuchter, J. et al. (2012) A Comprehensive Small Interfering RNA Screen Identifies Signaling Pathways Required for Gephyrin Clustering. *The Journal of Neuroscience*. 32 (42), 14821–14834.

Yamada, E. et al. (2000) Molecular cloning and characterization of a novel human STE20-like kinase, hSLK. *Biochimica et biophysica acta*. 1495 (3), 250–262.

Yang, L. et al. (2014) The mTORC1 effectors S6K1 and 4E-BP play different roles in CNS axon regeneration. *Nature Communications*. 5 (1), 1–7.

Yang, M. et al. (2012) The role of microtubule-associated protein 1B in axonal growth and neuronal migration in the central nervous system. *Neural Regeneration Research*. 7 (11), 842.

Yang, X. et al. (2014) Intercellular protein-protein interactions at synapses. *Protein and Cell*. 5 (6), 420–444.

Yi, J. J. et al. (2015) An Autism-Linked Mutation Disables Phosphorylation Control of UBE3A. *Cell*. 162 (4), 795–807.

Yu, J. et al. (2016) Metastasis suppressor 1 regulates neurite outgrowth in primary neuron cultures. *Neuroscience*. 333123–131.

Yu, L. et al. (2017) c-Maf inducing protein inhibits cofilin-1 activity and alters podocyte cytoskeleton organization. *Molecular medicine reports*. 16 (4), 4955–4963.

Yu-Kemp, H. C. et al. (2017) CRMP-1 enhances EVL-mediated actin elongation to build lamellipodia and the actin cortex. *Journal of Cell Biology*. 216 (8), 2463–2479.

ben Zablah, Y. et al. (2020) The Role of ADF/Cofilin in Synaptic Physiology and Alzheimer's Disease. *Frontiers in Cell and Developmental Biology*. 8594998.

Zacchi, P. et al. (2014) Gephyrin phosphorylation in the functional organization and plasticity of GABAergic synapses. *Frontiers in Cellular Neuroscience*. 8103.

Zaman, R. et al. (2021) Effector-mediated ERM activation locally inhibits RhoA activity to shape the apical cell domain. *The Journal of cell biology*. 220 (6), e202007146.

Zamoner, A. & Pessoa-Pureur, R. (2017) Intermediate Filaments as a Target of Signaling Mechanisms in Neurotoxicity. *Cytoskeleton - Structure, Dynamics, Function and Disease*.

Zeisel, A. et al. (2015) Brain structure. Cell types in the mouse cortex and hippocampus revealed by single-cell RNA-seq. *Science*. 347 (6226), 1138–1142.

Zhang, L. et al. (2008) The MeCP2-null mouse hippocampus displays altered basal inhibitory rhythms and is prone to hyperexcitability. *Hippocampus*. 18 (3), 294–309.

Zhang, S. & Qi, Q. (2015) MTSS1 suppresses cell migration and invasion by targeting CTTN in glioblastoma. *Journal of neuro-oncology*. 121 (3), 425–431.

Zhang, Y. H. et al. (2002) Expression of the Ste20-like kinase SLK during embryonic development and in the murine adult central nervous system. *Developmental Brain Research*. 139 (2), 205–215.

Zhapparova, O. N. et al. (2013) Ste20-like protein kinase SLK (LOSK) regulates microtubule organization by targeting dynactin to the centrosome. *Molecular biology of the cell*. 24 (20), 3205–3214.

Zürner, M. et al. (2011) Analyses of the spatiotemporal expression and subcellular localization of liprin-α proteins. *Journal of Comparative Neurology*. 519 (15), 3019–3039.

8 Acknowledgements

First and foremost, I would like to thank Prof. Dr. Susanne Schoch McGovern for giving me the opportunity to work in the lab under her supervision. I really appreciate her guidance, patience, and constant support throughout all the years starting from the master thesis. It was very helpful that she always had an open door to discuss questions, challenges, and future steps! Over the last years, I have learned a lot about science and scientific thinking and this has been made possible by her mentorship!

A deep “Thank you” also goes to Prof. Dr. Albert Becker who always supported and guided the project and who has always opened up new possibilities!

I would like to thank my second supervisor Prof. Dr. Witke for taking the time to supervise this thesis and for being a member of the IMPRS advisory committee! Thank you to Prof. Dr. Schmucker and Prof. Dr. Lamprecht for agreeing to join the thesis defense committee and for taking the time to evaluate this thesis!

Thank you very much to Prof. Dr. Dietrich and Prof. Dr. Beck for all the fruitful collaborations, and the helpful and guiding scientific discussions on different aspects of the project!

Furthermore, I would like to thank the International Max Planck Research School (IMPRS) for Brain and Behavior, especially Ezgi Bulca, for their academic and financial support throughout the PhD years!

I am very grateful to Dr. Julika Pitsch, for always sharing her knowledge and expertise and for giving helpful advice! A big thank you to the past and current TAs of the AG Schoch/Becker, especially to Pia Trebing, Shayne Gilgenbach, Katrin Krischer, and Sanja Markovic without whom the lab would not be running. A huge thank you goes to Sabine Opitz for the reliable preparation of cultured neurons over the past years! Thank you to Vivian Ludwig and Anna Dorißen for preparing and purifying viruses.

Thank you very much to all the past and current members of the AG Schoch/Becker/Dietrich, especially to Annachiara, Annika, Despina, Felipe, Gunther, Idil, and Katia - we spent most of the years together and dealt with minor and major challenges. It was always a great atmosphere in and outside of the lab!

I also wanted to especially thank the lab members with whom I shared offices over the years. Thank you to Alex, Arlind, Aya, Chrysa, Marie, and Polina for all the good times and the fun we had! My longest office mate is Silvia – and I am incredibly grateful to her! We went through so many different phases in the lab together and I could always count on her for scientific support, mental encouragement, honest feedback, and passionate discussions!

I would also like to thank my outside-the-lab friends, especially Polina, Catia, Lena, Zakaria, and Javier for sharing many special moments during our years here in Bonn!

Finally, a big thank you goes to my family that always supported me, by actions, by words, and by being always there! I really appreciate their unconditional support and encouragement in all life situations!